# X-ray Spectroscopy to Study Lytic Polysaccharide Monooxygenases

Abbey Jane Telfer

PhD

University of York

Department of Chemistry

September 2024

# Abstract

Lytic polysaccharide monooxygenase (LPMO) is a family of mono-copper metalloenzymes that can perform oxidative saccharification of naturally abundant polysaccharides. The LPMO mechanism is of great interest because of the possible applications in the production of biofuels and in crop protection, however this mechanism remains largely uncharacterised.

This work aims to investigate the LPMO electronic structure over three key genomic families: AA9, AA10 and AA11, using conventional XAS and HERFD-XANES. The X-ray spectroscopy data presented is supported by EPR, UV-vis spectroscopy and TD-DFT calculations.

Changes to the electronic structure of the copper ion on the addition of substrate in both the Cu(I) and Cu(II) oxidation states have been evaluated. The main finding of this work is that the addition of PASC to Cu(II) *An*AA9 does not yield any significant changes in the active site, whereas in the Cu(I) oxidation state the addition of phosphoric acid swollen cellulose induced changes consistent with a decrease in coordination number, which were observed spectroscopically and computationally. ICP-MS was used to detect the presence of metal contaminants in commonly used LPMO substrates, which found significant quantities of iron and zinc.

A Cu(II)-histidyl radical species has been observed and characterised. The radical intermediate was trapped for spectroscopic measurements using an anaerobic rapid freeze quenching technique. The Cu(II)-histidyl radical species has been found to be part of an LPMO oxidative damage protection mechanism.

Insights into the photodamage/ photoreaction mechanism of LPMOs were gained in the presence and absence of substrate. The spectra of intermediates were extracted using Multivariate Curve Resolution - Alternating Least Squares and linear combination fitting. It was found that there are discrepancies between chemically reduced and photoproduced LPMO samples and the most observed photodamage mechanisms were found to be specific primary and secondary reactions.

The main findings include direct comparisons of Cu(I) and Cu(II) LPMO-substrate interactions, the characterisation of a Cu(II)-histidyl intermediate species thought to be part of an oxidative damage protection mechanism, and a comprehensive investigation into X-ray radiation damage of LPMOs in the presence and absence of substrate.

Abstract

List of Contents

# List of Figures

# List of Tables

# Acknowledgements

I would firstly like to thank Professor Sofia Diaz-Moreno and Professor Paul Walton for giving me the opportunity and guidance to undertake this research. Beyond the findings reported in this thesis you have also been inspirational role models, for which I will be forever grateful.

It has been a privilege to have been able to work with the Spectroscopy Group at Diamond Light Source and the PHW group at the University of York. I am grateful to everyone who has shared their time, knowledge and experience with me. Especially thanks to those who have been present on beamtimes; the outstanding beamline scientists on I20-Scanning and B18, and particularly Dr João Cairo for dedicating so much time and patience, being on every beamtime and helping with protein preparations. Thank you to Dr Joshua Elliott for providing help and education on TD-DFT simulations. A special gracias also goes to Professor Irene Diaz-Moreno's group at the Universidad de Sevilla for welcoming me to their lab whilst teaching me about their research and un poco de español along the way!

Contrary to popular belief; life is long, and I am lucky to be surrounded by such wonderful people to share it with. As I draw a close to this chapter, I would like to express my gratitude and appreciation to my friends and family, old and new, for their encouragement, support and joy throughout this process.

To Dr Armando Ibraliu, Dr Tom Pidgeon, Dr Connor Sherwin, Dr Carissa Ponan and Dr Georgie Roberts, thank you for sharing the highs and lows of the PhD experience with me, now for the post-doctoral experience!

To Beth, Hannah and Holly, thank you for your unwavering friendship throughout school and beyond, having you just a message away makes everywhere feel like home.

To Melissa and Alex, thank you for your friendship throughout undergraduate onwards. The memories we have made are cherished highlights of my time at university.

To Liv, Jack, Georgia, Jordan, Lauren, Harry, Fran, Ben, Alex, Taryn, Imi, Kurt, Hayley, Ross, Cate, Dave, Danni, Sam, Paul and Benja, thank you for giving encouragement, fun and the best escapes.

To my family, parents and brother, thank you for everything! For supporting me in my ambitions and encouraging me to be big whenever I meet with Triumph or Disaster. Every step of the way you have been instrumental in making me who I am today, my achievements continually come back to the love and support you have always generously given to me.

To Sammy, thank you for being on this adventure with me and filling each day with love and laughter. Throughout long distance, late nights in the lab, experiments gone wrong and self-doubt you have always been a sanctuary. Continuing to build a life together has been the greatest motivation, but can we call a truce on degrees now?

# Author's Declaration

Presented in this thesis is original work undertaken by the author unless otherwise stated. This work has not previously been presented for a degree or other qualification at this University or elsewhere. All sources are acknowledged as references.

The data presented in Chapter 4: Rapid freeze quenching to trap LPMO intermediates, were published in Zhao *et al*., *J. Am. Chem. Soc*. 2023, 145, 37, 20672-20682.

Work carried out by other persons:

Chapter 3: LPMO substrate interactions

- ICP-MS of the LPMO substrates was collected by Dr. Niall Donaldson
- The *An*AA9 LPMO was produced and purified by Dr. César Terrasan
- The EPR spectrum of Cu(II) *An*AA9 in the presence and absence of substrate was collected and simulated by Dr. Thammy Correa
- TD-DFT calculations were undertaken by Dr. Joshua Elliott

Chapter 4: Rapid freeze quenching to trap LPMO intermediates

- The *Ls*AA9 Y164F LPMO for the HERFD-XANES measurement was produced and purified by Dr. Jingming Zhao
- TD-DFT calculations were undertaken by Dr. Peter Lindley

Chapter 5: X-ray induced photoreactions in LPMOs

- The *An*AA9 LPMO was produced and purified by Dr. César Terrasan

# 1 Introduction

## 1.1 An introduction to LPMOs

The discovery of the inaugural LPMO genomic classes; AA9 and AA10 (formerly GH61 and CBM33) was preceded by the observation of oxidative enzymatic activity on polysaccharides in white rot fungi and soil bacteria.[2–7] Since then, LPMOs have become a topic of research with growing interest and many milestones have been achieved in the pursuit of gaining insight into their structures and functions, including their assignment as mono-copper monooxygenases[8–10], the characterisation of the histidine brace[11,12] and the more recent discovery of their peroxygenase activity[12] (Figure 1.1).

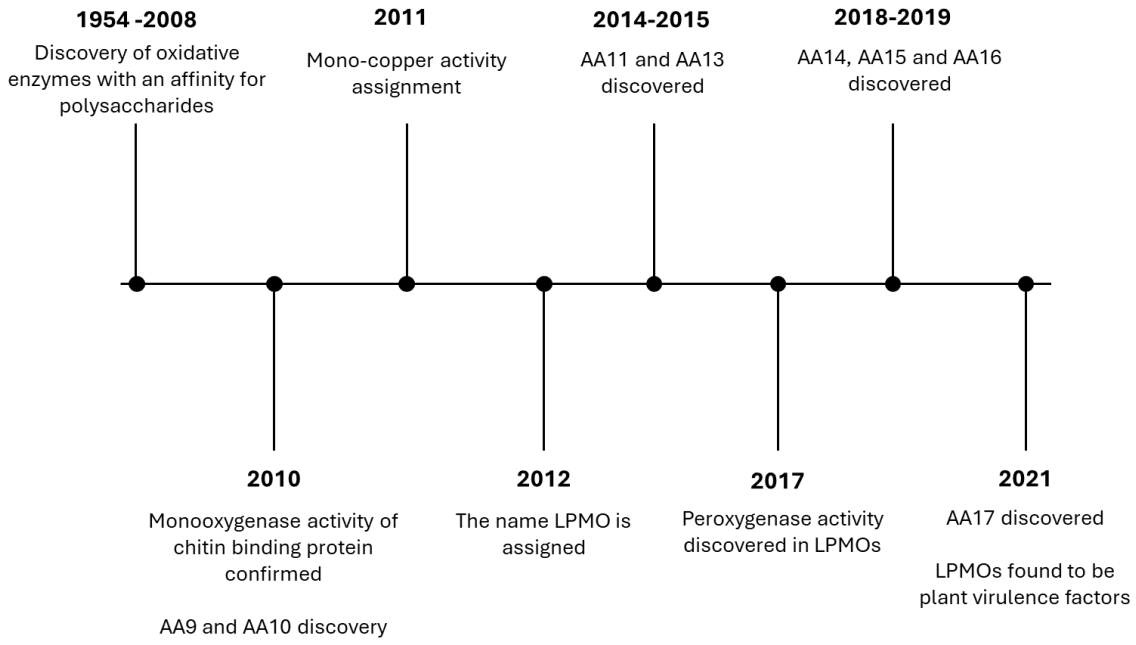


Figure 1.1: A brief history of LPMO milestones.

LPMOs were initially of interest because their ability to perform oxidative saccharification of naturally abundant polysaccharides, which holds potential applications in the biofuel industry. The recent discovery of LPMOs as plant virulence factors has unlocked further potential applications in crop protection.[13]

The breakdown of polysaccharides is complex, their chemical and physical properties such as strong glycosidic bonds and intermolecular interactions contribute to their recalcitrance. Nature's ability to solve the problem of the resistance of polysaccharides to degradation is of great interest.[14] Current enzymatically catalysed biofuel production relies on a combination of oxidase and

hydrolase enzymes including amylases, protease, cellulase, xylanase, xylosidase, xylose-isomerase and lipase to cleave and solubilise the individual saccharidic units of different polysaccharide feedstocks. Whilst enzymatically catalysed biofuel production is performed regularly in industry, its profitability is limited by the high costs of production, of which the cost of enzymes contributes up to 50 %.[15] Lytic polysaccharide monooxygenases can act on the surface of polysacchrides to cleave glycosidic bonds which improves accesibity for hydrolase enzymes resulting in a boost in efficiency. In this regard, LPMOs have the potential to reduce the cost of biofuel production making it a more viable operation. Whilst the exact mechanism and intermediates formed during the LPMO catalytic mechanism are still debated, it is known that the Cu(I) oxidation state is the active oxidation state and the reduction from the Cu(II) resting state often results in the loss of an exogenous ligand. It has also been shown that LPMO reactions proceed with either oxygen or peroxide and it is thought that they occur *via* an elusive Cu(I)-oxyl intermediate which can activate the glycosidic bonds of polysaccharides, as shown in the general mechanism presented in Figure 1.2.[16]

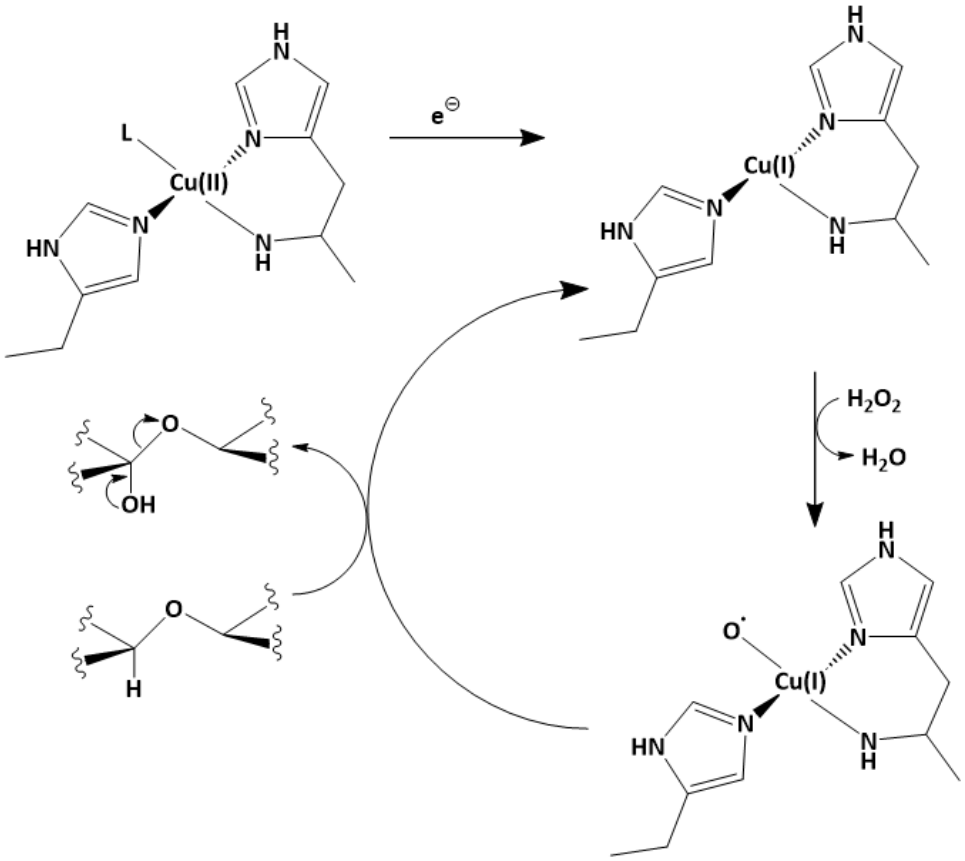


Figure 1.2: A general mechanism for LPMOs featuring the reduction from the Cu(II) resting state to the Cu(I) active oxidation state and the subsequent reaction with peroxide (although it is noted that activity also occurs with oxygen), forming a Cu(I)-oxyl intermediate which is able to activate the

glycosidic bond of polysaccharides resulting in saccharification. “L” is used to represent an exogenous ligand.

Insights into LPMO structures, functions and mechanisms have the potential to discover futher LPMO applications as well as enhace their applications in the production of biofuels and in crop protection.

### 1.1.1 LPMO substrates

Cellulose is the most abundant organic polymer on Earth, found in plant cell walls as well as in algae and bacteria. It exists as a linear chain of β(1→4) linked D-glucose units (Figure 1.3).[17–20] The swelling of cellulose results in the same gross structure and solid cellulosic phase, but the uptake of a swelling agent, such as phosphoric acid, causes changes in the physical properties such as an increase in sample volume which makes cellulose more easily digestible.[21] This is why phosphoric acid swollen cellulose (PASC) is commonly used in activity assays. Hemicellulose typically exists as shorter chains than cellulose (500 – 3,000 units compared to 7,000 – 15,000 units), and they are often branched polymers. Hemicelluloses include xylans, mannans and xyloglucans and are commonly found in plant cell walls.[22] Oligosaccharides are polysaccharides with shorter chain lengths again; typically between three and ten sugar units.

Chitin is also a long chain polysaccharide and is the second most abundant polysaccharide in nature.[23] Chitin is made up of repeating N-acetyl-D-glucosamine units. The presence of the amine group results in more hydrogen bonding between chains than in cellulose, which creates a strong polymer matrix. Chitin is found in cell walls as well as in exoskeletons and has also been found to be produced by some fish. [24,25] The abundance of cellulose and chitin make these LPMO substrates ideal feedstocks for biofuel production.

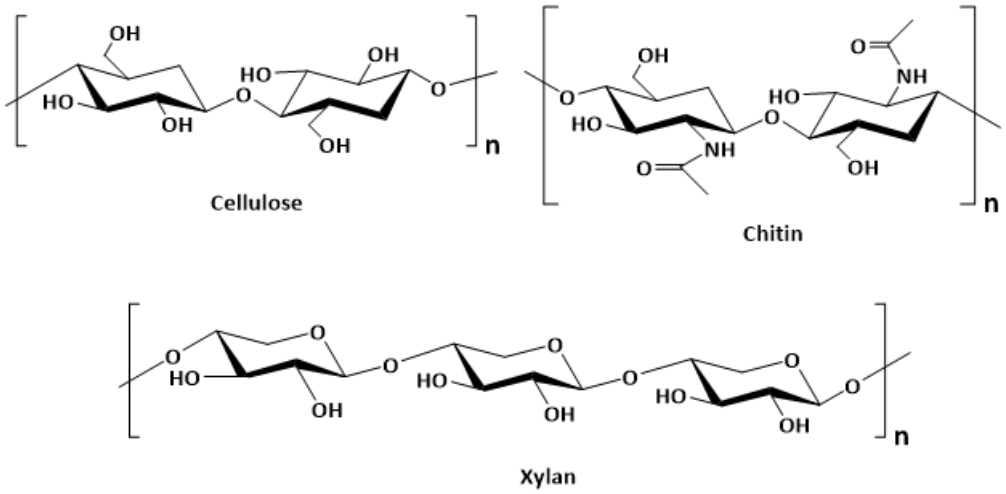


Figure 1.3: Chemical structures of common naturally occuring polysaccharide substrates for LPMOs.

### 1.1.2 Protein sequence classifications

The amino acid sequences of LPMOs can be found in several databases, the most authoritative of which is the carbohydrate active enzyme (CAZy) database.[26] The CAZy database correlates the sequences of carbohydrate-active proteins to their catalytic and carbohydrate-binding activities. [26,27] The first LPMO proteins to be catalogued in the CAZy database were originally categorised as glycoside hydrolases (GH61) and carbohydrate-binding modules (CBM33). Following the discovery of their oxidative activity, the CAZy database reclassified LPMOs as Auxiliary Activity (AA) enzymes, and currently account for eight distinct sequence classes: AA9-11 and AA13-17, each of which can be loosely associated with activity on different saccharidic substrates (Table 1.1).

Table 1.1: LPMO classes (CAZy) and the broad substrate classes upon which they have been found to be active.

| **CAZy Genomic Class** | **Substrate activity** |
|---|---|
| AA9 | Cellulose, hemicellulose, oligosaccharides [28] |
| AA10 | Cellulose [28–30], α and β chitin[31–43] |
| AA11 | α and β chitin [44,45] |
| AA13 | Starch [46,47] |
| AA14 | Xylan [48] |
| AA15 | α and β chitin [49] |
| AA16 | Cellulose and oligosaccharides [50] |
| AA17 | Pectin [13] |

Note: when naming LPMOs, the CAZy genomic class of LPMOs is prefixed with two letters denoting the organism from which the LPMO was produced, e.g. *Ls*AA9 refers to the AA9 LPMO from the organism *Lentinus similis*.

### 1.1.3 Role of LPMO enzymes

Within a biological context, LPMOs are found in the genomes across Monera, Plant, Fungi and Animalia kingdom.[8,13,49,51] As described above, organisms have utilised the ability of LPMOs to perform oxidative saccharification of polysaccharides during the breakdown of biomass.[8,10,49] Over time, however, other functions and uses of LPMOs are continuously being discovered. For instance, the use of LPMOs has revolutionised the production of second generation biofuels as they offer the opportunity to use abundantly available feedstocks such as cellulose in biorefineries.[50] LPMOs have also been found as virulence factors in fungal pathogens which are linked with crop diseases as well as in insect pests; a better understanding of LPMOs and the ability to control their expression in plant pathogens could have applications in crop protection and food security. [13,52]

LPMOs are enzymes which are notable from two perspectives. The first is that these enzymes catalyse the oxidative cleavage of polysaccharides by $O_2$ (or $H_2O_2$) in the reaction depicted in Figure 1.4.[53–57] This oxidative mode of action is in contrast to the usual hydrolytic action of cellulase or chitinase enzymes acting on saccharidic biomass. Most importantly, by acting in concert with hydrolytic enzymes, the oxidative action of LPMOs provides a significant boost (*ca.* 25 %) to the overall degradation of biomass into its soluble sugar units - thus creating a highly efficient enzymatic degradation system. [58] The second is that the strength of the C-H bond in the substrate which is cleaved by the action of LPMOs has been calculated to be >95 kcal/mol, a value which necessitates that LPMOs generate highly reactive intermediates at their active sites to cleave the bond.[59]

There is significant research into LPMOs which seeks to harness their oxidative power, not only for biomass utilisation but for the possible application to the degradation/conversion of a wide range of other recalcitrant materials. Therefore, studies to elucidate the structure and the reactivity of the intermediates in the catalytic cycle have become the focus of multiple research efforts. A key factor in these studies is the utilisation of several spectroscopic techniques.

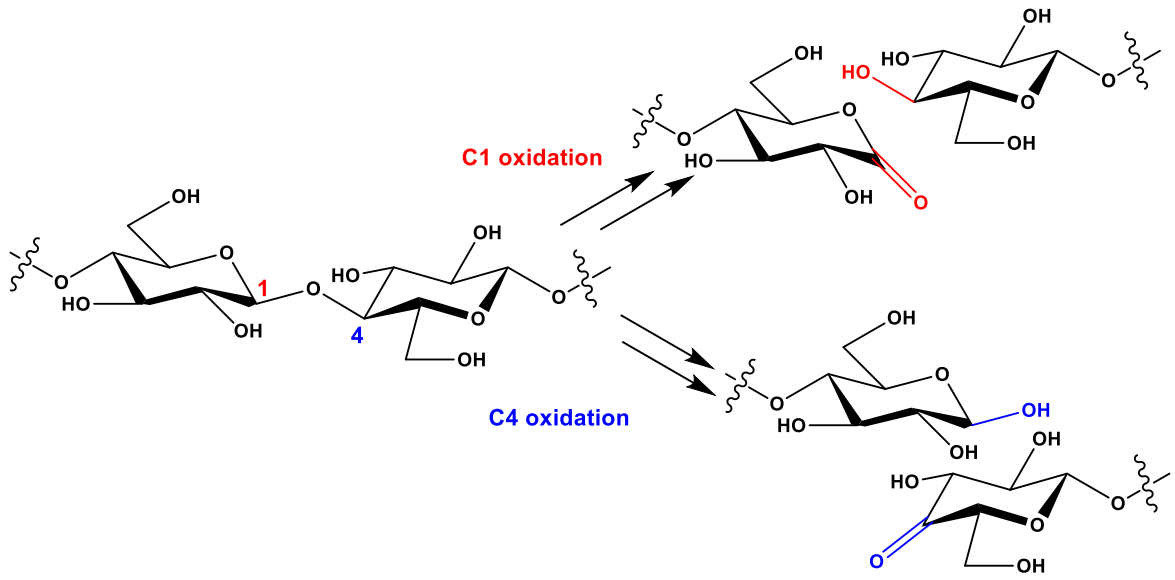


Figure 1.4: Reactivity of LPMOs, C1 and C4 oxidative cleavage routes of LPMOs and the resulting products. [53,54]

High-performance liquid chromatography (HPLC) and mass spectrometry experiments have deduced that different genomic classes of LPMOs display different regioselectivity resulting in C1 and/or C4 oxidation of polysaccharides. C1 oxidation of polysaccharides yields an unstable δ-lactone which forms an aldonic acid in the presence of water whereas C4 oxidation produces a 4-ketoaldose (Figure 1.4).

### 1.1.4 Crystal structures

The structures of several LPMOs have been determined by using X-rays and neutrons to measure their crystal structures. It is generally accepted that LPMOs have a highly conserved "histidine brace" active site (Figure 1.5).[11] Two histidine residues coordinate to the single copper ion, one of which is found at the N-terminus of the peptide chain; chelating the metal centre through both the nitrogen atom of the amino terminus $NH_2$ and the *p*-N atom of the imidazole side chain. The second histidine coordinates to the copper *via* the *t*-N atom of the imidazole ring, giving an overall arrangement around the $CuN_3$ as a T-shape.[8,11] In the Cu(II) form, the protein usually has an exogenous ligand (typically a water molecule) occupying the position *trans* to the amino terminus $NH_2$ group to give a roughly square planar coordination geometry. This arrangement is conserved across all LPMOs with the exception of some bacterial AA10 LPMOs where two exogenous ligands (Figure 1.6) are found above and below the equatorial plane. It is important to note that some LPMO structures are methylated at the τ-N on the N-terminal histidine, a feature that may be important in preventing oxidation of the histidine brace structure.[8,60]

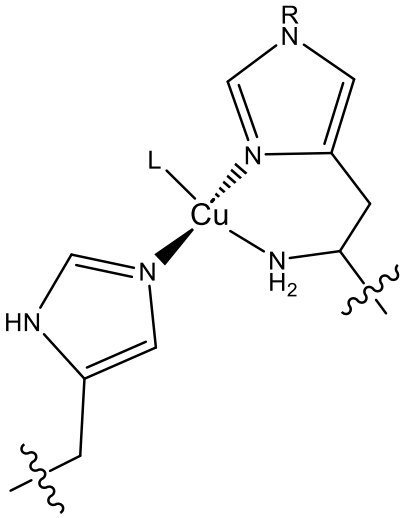


Figure 1.5: Histidine brace coordinated to copper ion (R = Me or H, L = exogenous ligands e.g $H_2O/OH^-/Cl^-$).

The histidine brace motif is also found across several classes of copper proteins, including the copper transport protein (CopC) and particulate methane monooxygenases (pMMOs). [11,61] There is significant diversity in the amino acid residues and their relative positions in the copper ion secondary coordination spheres, which also correlates with how LPMO proteins are divided into their genomic classes (Figure 1.6).

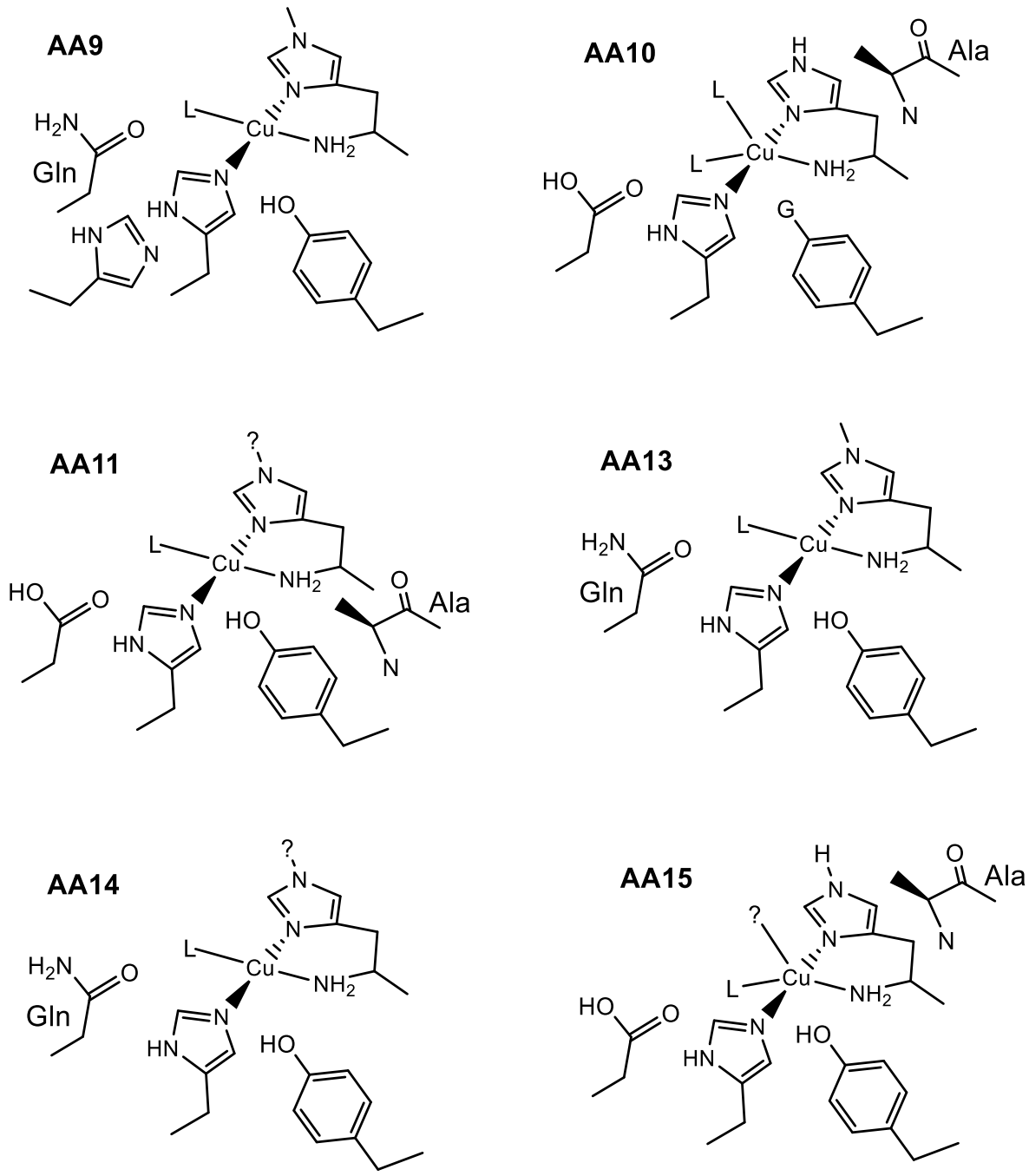


Figure 1.6: LPMO active site structures from currently characterised genomic classes. L is an exogenous ligand, G can be H or OH in AA10, ? is used to denote that the histidine brace in AA11 and AA14 may be methylated and the second exogenous ligand may be present in AA15.

### *1.1.4.1 X-ray crystallography*

Single crystal X-ray diffraction (XRD) has been used extensively to evaluate the structure of LPMOs. Examples of the XRD crystallographic structures from the currently known LPMO genomic classes (Figure 1.7) show the conservation of the histidine brace throughout.

It is important to highlight that obtaining crystallographic structures of the resting state Cu(II) LPMOs is challenging due to the fast rate of photoreduction experienced by Cu(II) samples, particularly when samples are measured using synchrotron radiation with high photon density. It has been shown that both water ligands are lost (successively) from the copper centre with continuous exposure to X-ray radiation, showing continual change in geometry from trigonal bipyramidal to T-shaped. [62] The active site structures of an AA10 LPMO that was photoreduced using the X-ray beam and reduced chemically using ascorbate have been found to be the same concluding that it can be assumed that the XRD structures obtained reflect the accurate structure of Cu(I) LPMOs. [33] The rapid rate of photoreduction means that both experimental and analytical precautions must be considered in studying the crystal structure of Cu(II) LPMOs. The application of other complementary spectroscopic techniques are required in order to be able to characterise the Cu(II) active site and its interactions.

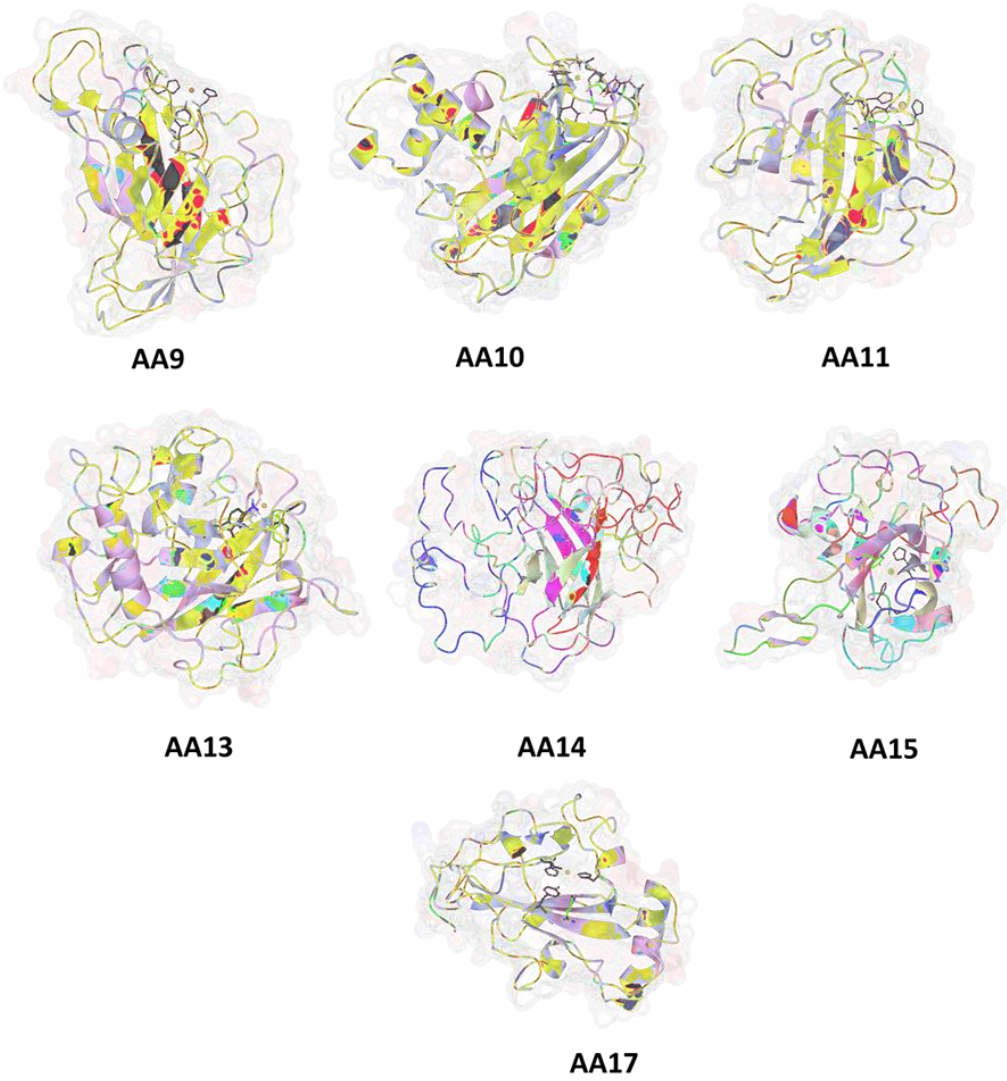


Figure 1.7: Crystallographic structures of LPMO proteins across different genomic classes: AA9 (PDB: 7NTL) [63], AA10 (PDB: 5OPF) [42], AA11 (PDB: 4MAI) [64], AA13 (PDB: 6TBQ) [65], AA14 (PDB: 5NO7) [48], AA15 (PDB: 5MSZ) [49], AA17 (PDB: 6Z5Y) [13]. A crystal structure for AA16 was not available at the time of writing.

Cu(II) LPMO crystal structures typically demonstrate a copper ion in a Jahn-Teller tetragonally distorted coordination geometry due to the degeneracy of the d-orbitals.[66] Jahn-Teller distortion is not applicable in Cu(I) structures due to the $d^{10}$ electronic configuration resulting in no d-orbital degeneracy. As such, the presence of Jahn-Teller distortion at the Cu active site of LPMO crystal structures can be used as a proxy for assigning the copper oxidation state. In addition to the histidine brace, the Cu(II) ion is usually coordinated to one or two exogenous ligands depending on the genomic class and experimental factors such as pH and substrate presence. When in the reduced state, the Cu(I) centre has no additional ligands and such is coordinated by the histidine

brace alone. Most LPMOs exhibit a flat binding surface which exposes the copper active site to the substrate and thought to facilitate binding (Figure 1.7). Somewhat in contrast, AA13 LPMOs demonstrate a shallow dip in this flat surface which is thought to better accommodate polysaccharide substrates (Figure 1.8). [47] Similarly, AA14 LPMOs have demonstrated a ripple shaped surface with two surface loops which form a clamp. [48] How the shape of the binding site influences the LPMO interaction with substrate and mechanism of action remains unclear.

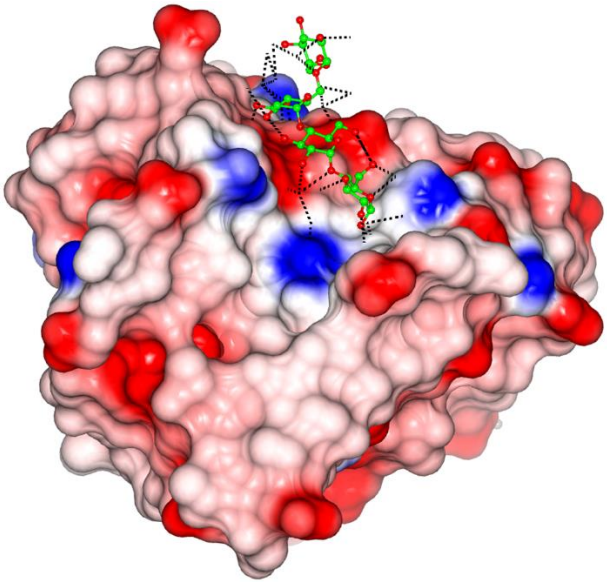

Figure 1.8: Crystal structure of an AA13 LPMO (PDB: 5T7N) interaction with a polysaccharide, showing a shallow dip in the usually flat LPMO active surface.

Interestingly, crystallographic studies have shown that even within the same genomic classes LPMOs interact differently with substrates (Figure 1.9). Simmons *et al.* soaked crystalline LPMO in polysaccharide solutions and thus characterised *Cv*AA9 and *Ls*AA9 with various polysaccharide substrates. Whilst both *Cv*AA9 and *Ls*AA9 have very similar overall structures, including copper active site coordination and folds, XRD has highlighted distinct differences in binding cleft interactions. [67] Furthermore, crystal structures published by Frandsen *et al.* demonstrate that at lower pH (3.5) *Ls*AA9 exhibits more disorder in the histidine brace than at higher pH (5.5), and this translates to observable structural differences in substrate bound *Ls*AA9. This is significant as the optimum pH of most commercial cellulases is around pH 5.[68] In substrate bound *Ls*AA9, the histidine brace is ordered and the cellohexaose substrate binding at subsites -1 to +2 is almost identical for both pH 3.5 and 5.5. However, conformational differences exist in binding at subsites -2 and -3, which at pH 5.5 results in fewer hydrogen bonds being formed. [54,69]

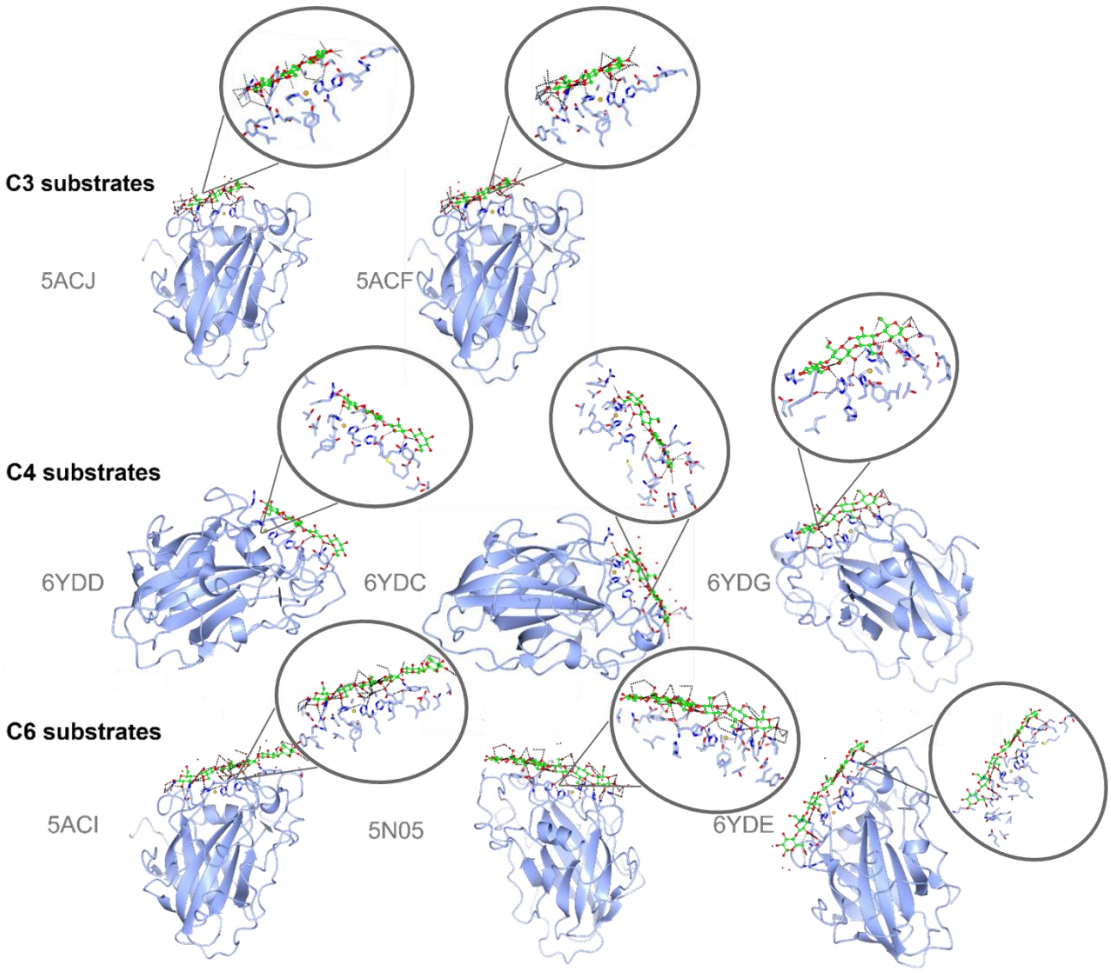


Figure 1.9: X-ray crystallography structures of AA9 LPMOs with various substrates, shown with their PDB codes.

Many carbohydrate active enzymes, including LPMOs, are tethered to a carbohydrate binding module (CBM). Crouch *et al.* found that deletion of the CBM inhibited the enzymatic activity of an AA10 LPMO. [70] Following from this discovery, Chalak *et al.,* demonstrated that the deletion of the CBM from an AA9 LPMO did not reduce the enzymatic activity on cellulose, but did affect substrate binding and release. [71] However, the linkers used to tether the catalytic domains of LPMOs to the CBM are flexible and thus cannot be well resolved in X-ray crystallography, which means the mechanism by which CBMs are involved in polysaccharide degradation is not well understood. [72]

### *1.1.4.2 Neutron crystallography*

Neutron crystallography is emerging as a popular technique in structural biology and as such there are a growing number of LPMO neutron crystallographic structures. X-ray diffraction is caused by scattering by electrons, which means that isotopes of the same element cannot be differentiated,

whereas in neutron crystallography diffraction occurs through neutron interactions with the nucleus and therefore isotopes of the same element have different scattering factors and can be differentiated. Hydrogen and particularly deuterium atom occupancy in crystal structures can be resolved using neutron crystallography as the coherent scattering lengths of hydrogen and deuterium are similar in magnitude to those of carbon, oxygen and nitrogen. The ability to discern hydrogen atoms using neutron diffraction gives a more complete view of LPMO structure and reactivity through a more accurate understanding of coordination number, hydrogen-bond interactions, protonation states and electrostatic interactions. Furthermore, neutrons do not cause radiative damage, which is a significant drawback of X-ray techniques, particularly as the copper ion in LPMOs is prone to photoreduction. However, due to the intrinsically low flux of neutron beams compared to synchrotron X-ray beams, LPMO crystals need to be *ca.* three times larger than crystals used in XRD studies, and particularly well ordered to achieve a good quality structure. Further to this, significantly longer exposure times on the order of hours/days are required for neutron crystallography in contrast to seconds/minutes for XRD.[73]

Bacik *et al*. used a combination of neutron and X-ray diffraction to study the structure of a Cu(II) AA10 LPMO and found the amino terminus of the histidine brace motif His157 to be an $ND_2$ doubly protonated state, giving a net positive charge to the structure.[74,75] This finding is consistent with a study by O'Dell *et al*. which similarly found that the His157 amino acid is doubly protonated in an AA9 LPMO and suggests that this structural feature favours $O_2$ binding and therefore activation at *ca*. pH 5, the pH at which other cellulases have also demonstrated maximum activity.[76] Schröder *et al*. also collected a neutron crystal structure for an AA9 LPMO but in this experiment the crystal was soaked in a low pH buffer (pH 4.4) before collection. In this study, the His157 amino acid is $N_\epsilon$-singly protonated. [77]

At the time of writing, there are three LPMO neutron diffraction structures deposited in the Protein Data Bank (PDB), the structures of which are shown in Figure 1.10. [78]

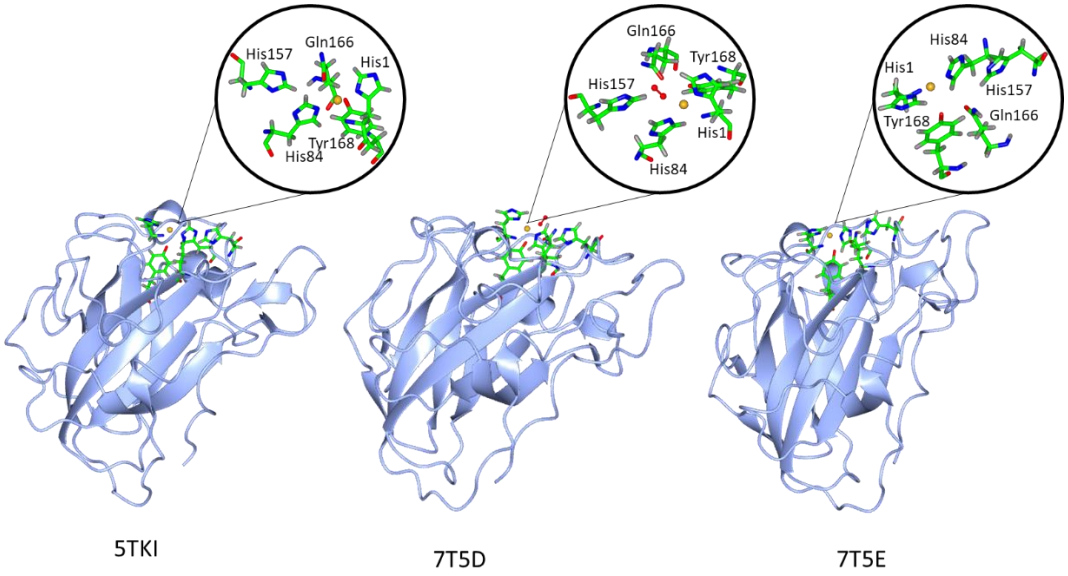


Figure 1.10: Neutron crystal structures of a AA9 LPMOs. PDB 5TKI, 7T5D (structure shown with dioxygen) and 7T5E.

## 1.2 Spectroscopic Analysis of LPMOs

Whilst extensive crystallographic studies on LPMOs have been undertaken to elucidate their structures, spectroscopic techniques have also been applied to gain further insight into LPMO structures and reactivity. Without the need for long range order many spectroscopic techniques have been used to study LPMOs in solution, arguably giving a more representative picture of LPMO structure, reactivity, and dynamics.

### 1.2.1 Continuous wave electron paramagnetic resonance

Continuous wave electron paramagnetic resonance (cw-EPR) has been applied extensively to study the structure and reactivity of LPMOs. Only paramagnetic species are EPR active, which in the application of LPMOs means that it is a useful technique to study the Cu(II) oxidation state but not the Cu(I) oxidation state of LPMOs. EPR measurements of LPMOs are commonly recorded on frozen solutions (*ca*. 150 K) to reduce the tumbling rate and, involve irradiation of the sample by a microwave source whilst varying the magnetic field strength, $B_0$.

EPR is an advantageous spectroscopic technique to analyse LPMOs because we can track reactions through the formation and degradation of radical species in close proximity to the active site as well as observing changes in the copper environment. Whilst relatively low concentrations of protein (ca. 0.15 mM) can be used to prepare EPR samples, significant volumes are required (ca.

80-120 µL). However, EPR is a non-destructive technique and therefore the LPMO samples can be recovered for further applications. Using simulations, structural information can be gained through the calculation of Hamiltonian parameters, namely *g* and A values (Figure 1.11). The *g* values obtained from EPR are defined by the position of the signal and provide information on the geometry around the Cu(II) active site which is useful to characterise the resting state of LPMOs as well as probing reaction mechanisms. The A value is related to the hyperfine slitting and is influenced by atoms in the primary coordination sphere of the metal, and therefore can also provide information on the coordinating ligands and geometry around the copper active site.

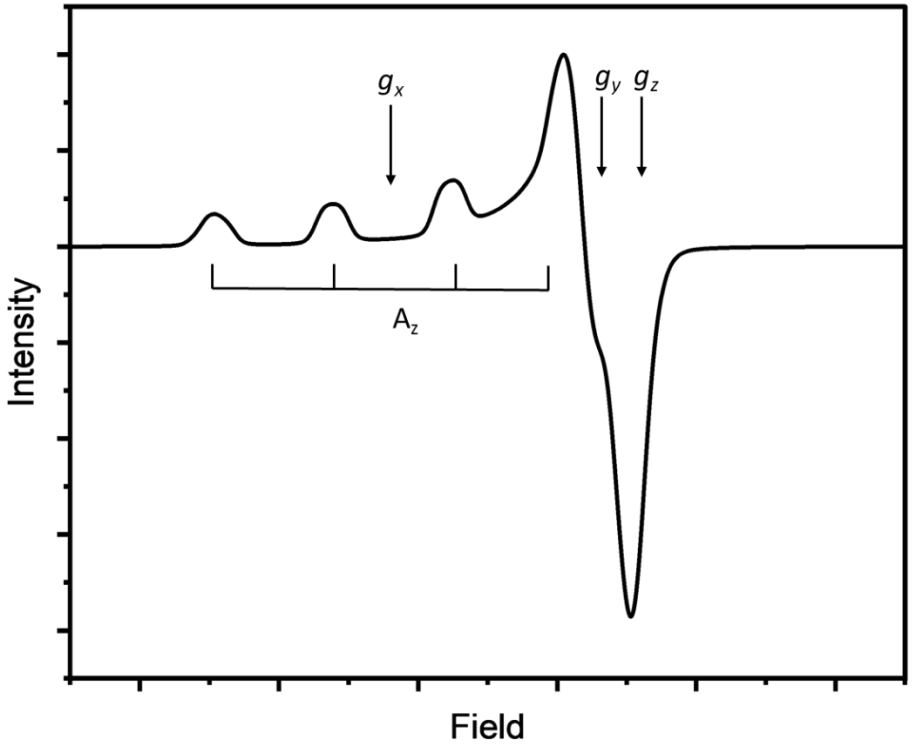


Figure 1.11: Example of a typical continuous wave EPR (cw-EPR) spectrum for a LPMO protein, showing the hyperfine interaction on the $g_z$ feature.

Cu(II) proteins can be classified as Type I and Type II depending on the nature of their donor atoms (Figure 1.12).[79] As defined by Peisach-Blumberg classifications; Type II Cu(II) proteins have larger $A_z$ values and smaller molar extinction coefficients (< 3000 $M^{-1}$ $cm^{-1}$).[51,80] EPR studies have shown that LPMOs can be generally classed as Type II copper proteins with axially distorted structures as a result of Jahn-Teller distortion of Cu(II) coordinated to two water molecules; one equatorial and one axial to an amino acid residue.[13,33,35,38,47,48,64,81–83] There are discrepancies as to where LPMOs lie within the Peisach-Blumberg Type II classification. For example, Cu(II) *Ba*AA10 lies between the

Type I and Type II classifications, however its overall axial envelope ($g_x \neq g_y \neq g_z$ ) still justifies a Type II classification.[33,35] The relationship between the $A_z$ and $g_z$ spin Hamiltonian parameters of copper proteins can be correlated to their coordination geometry (Figure 1.12). The spectral envelopes in LPMO EPR suggest a near square planar geometry where the SOMO is majority d($x^2 - y^2$ ).[82,84]

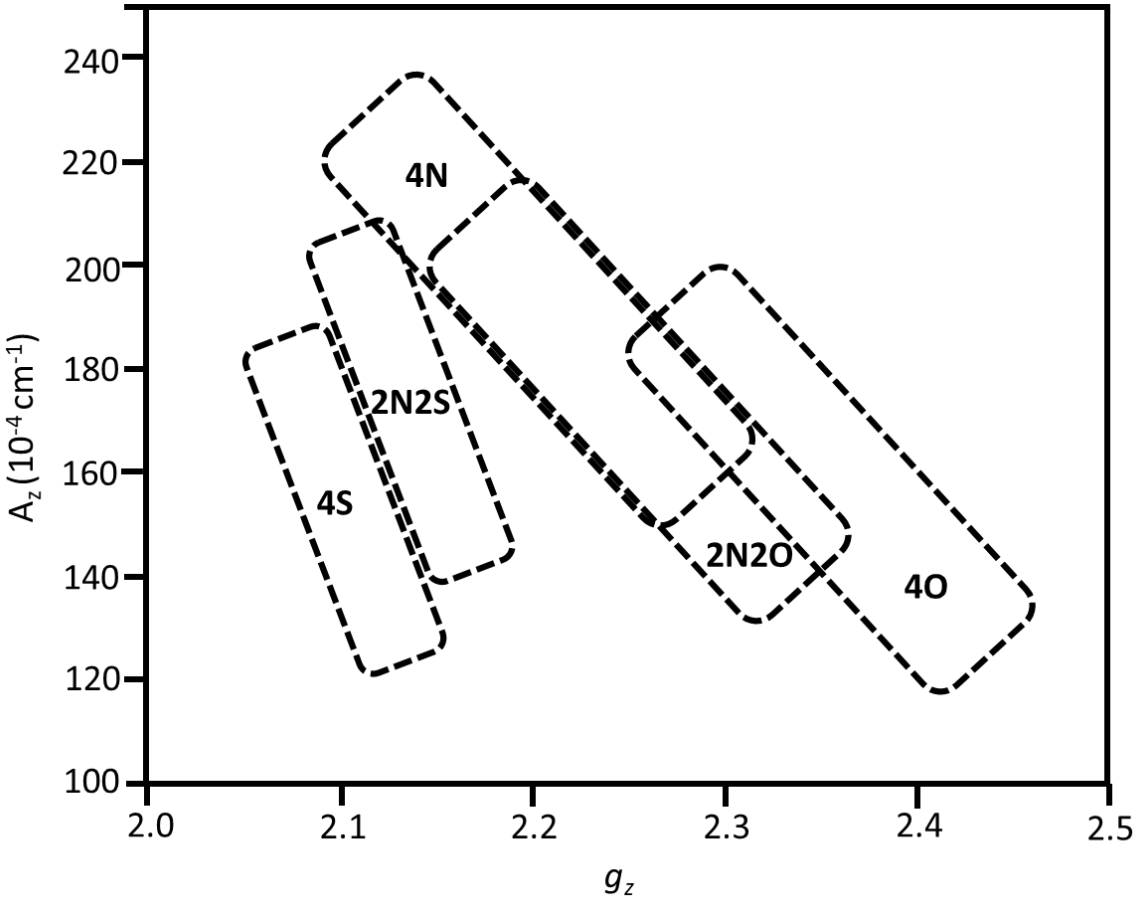


Figure 1.12: Peisach-Blumberg chart showing the correlation between different coordination geometries of copper proteins and their spin Hamiltonian parameters. This figure was adapted from Peisah *et al* (1974) with permission from Elsevier. [51]

The *g* values of LPMOs are interrelated with the sample conditions used. X-band cw-EPR demonstrates that LPMOs are sensitive to chloride ions in solution, with the formation of a new copper species occurring in a solution of an AA9 LPMO in the presence of ~ 200 mM chloride ions.[54] It has also been found that when sodium azide was added to an AA11 LPMO a significant change in the $g_z$ value from 2.27 to 2.06 was observed, which suggests that azides have the ability to coordinate to LPMOs resulting in a shift towards axial geometry, this trend has also been observed in AA9 and AA10 LPMOs.[33,54,64] The Hamiltonian parameters calculated from EPR data reflect the

differences in amino acid residues in the copper active sites of different LPMOs and their diverse range of interactions with substrate, protonation states and ion interactions.

A significant barrier to obtaining spectroscopic data on substrate binding of LPMOs is that the polysaccharide substrates used are predominantly insoluble. However, several studies have been published using innovative ideas to overcome this barrier. Ciano *et al.* developed a method to use natural semi crystalline cellulose fibrils to partially orientate the LPMO-substrate interaction with the magnetic field of the spectrometer, giving dimensional data analogous to a crystalline LPMO-substrate sample. X-band cw-EPR was used to determine that the N-Cu-N direction of two different AA9 LPMO active site histidine braces are situated parallel to the plane of the glucose rings in the cellulose fibrils and concluded that there are no apparent electronic active site structure changes on binding of AA9 LPMOs to a natural cellulose substrate.[85]

Unlike many spectroscopic techniques, slurries can be used to gain structural information using EPR.[85] Bissaro *et al.* investigated insoluble substrate activation by an AA10 LPMO using EPR and found that the copper active site is altered on substrate activation. Using a strategy of combining molecular modelling and EPR data led the authors to the conclusion that the changes in the EPR signal they observed are attributed to a reorganisation of water molecules coordinated to the copper ion.[86] Correspondingly Courtade *et al*, investigated the structure of a chitin bound AA10 LPMO using a slurry and found agreement in the data obtained in the X and Q band cw-EPR that on addition of substrate there is a rearrangement of the copper active site from 5-coordinate square pyramidal geometry to a 4-coordinate square planar geometry.[87]

LPMOs within the AA9 classification have been found to be active on soluble cellooligosaccharides, which opens further spectroscopic possibilities. There is an apparent connection between AA9 LPMO ability to bind cellooligosaccharides and the presence of hydrogen bond forming amino acids, specifically Asn28, His66 and Asn67.[54,67] Using this finding, Borisova *et al.* found that on substrate binding AA9 LPMOs show a change in spin Hamiltonian parameters as well as observable changes in the superhyperfine splitting, which they suggest to be indicative of an enhanced interaction between the Cu(II) ion and lone pair electron of nitrogen on the histidine brace.[66] Similarly, Simmons *et al.* observed that on addition of soluble substrates to various AA9 LPMOs where the LPMOs demonstrated activity with the substrate there were deviations in the in the $g_z$ and $A_z$ values corresponding to changes in the Cu(II) active site on substrate activation.[67]

Lindley *et al*. used a combination of EPR and density functional theory (DFT) to characterise three species formed successively as the pH of an AA10 LPMO was increased from 6.5 to 12.5 (Figure 1.13). Through the changes observed in the hyperfine coupling and *g* values it was proposed that the first species formed at pH 6.5 is a 5-coordinate ($N_3O_2$), which forms a 4-coordinate species which is fully formed at pH 10.5 by deprotonating the water ligands and protonating the histidine amino terminus. The species at pH 6.5 and 10.5 are formed within a biologically relevant pH range and therefore could be significant in the LPMO catalytic cycle. The third species identified at pH 12.5 is a four-coordinate complex.[88]

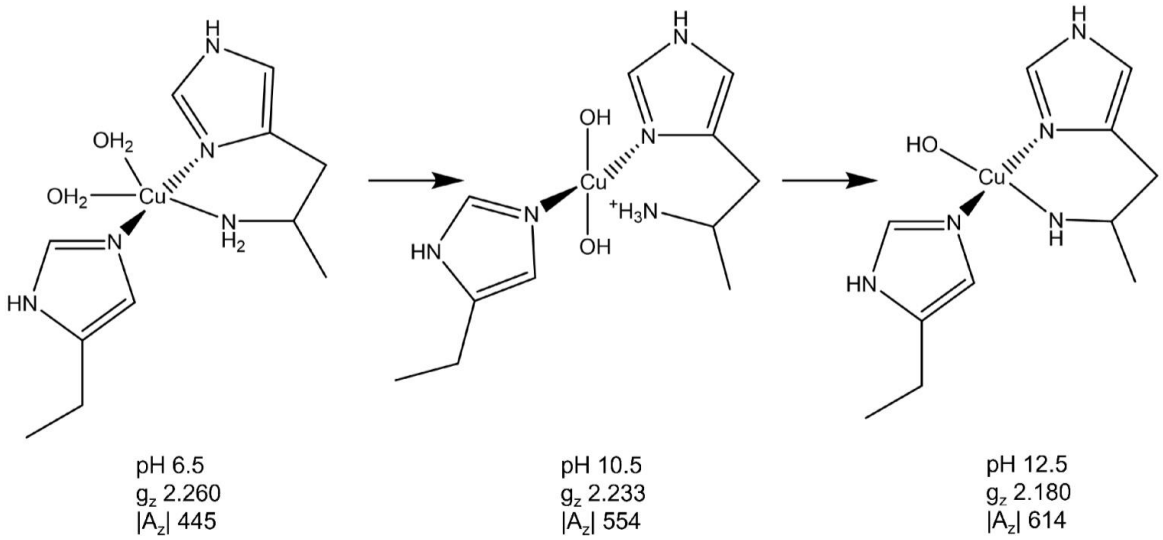


Figure 1.13: Suggested characterisation of AA10 LPMO species formed of an increasing pH range with their respective $g_z$ and $|A_z|$ values. $|A_z|$ values are given in MHz.[88]

EPR has been applied to study the structure of Cu(II) LPMOs and has uncovered the structure of substrate bound LPMOs and the effects of different LPMO buffer conditions such as pH and salt concentration. Further EPR application is required to deduce how LPMO-substrate interactions differ among the genomic classes giving rise to their structure-function relationship, substrate and regio-specificity. The EPR data on Cu(II)-LPMO substrate interactions should be integrated with other spectroscopic techniques to investigate Cu(I)-LPMO substrate interactions, which is thought to be an integral component of the catalytic mechanism.

### 1.2.2 Nuclear magnetic resonance

Nuclear magnetic resonance (NMR) of LPMOs is most commonly undertaken in solution at a particular magnetic field strength whilst varying the radio frequency applied. The atoms in the

protein will experience different chemical environments depending on their nature and the nature of adjacent atoms giving rise to different chemical shifts. The sensitivity of chemical shifts given in NMR spectroscopy mean that it is possible to assess the structural changes which occur at specific sites of proteins during reaction. [89,90] This has made NMR very valuable in solving the structures of LPMOs and also to gain insights into LPMO-substrate interactions.

In the case of copper proteins, and more specifically LPMOs, the paramagnetism of Cu(II) causes hyperfine coupling with nuclei within close proximity. Hyperfine coupling with the Cu(II) $d^9$ unpaired electron increases the relaxation rate in an effect called paramagnetic relaxation enhancement (PRE). Following the Heisenberg uncertainty principle, NMR signal linewidth is proportional to the nuclear longitudinal and transverse relaxation rate, therefore spectra of Cu(II) LPMOs experience signal broadening and thereby signal reduction, which decreases detectability. For this reason, Type II copper proteins were once considered inaccessible by proton NMR, hence many LPMO NMR studies are of the *apo* or Cu(I) structures.[91]

Using the often-problematic PRE effects of Cu(I) as a result of its unpaired 4s electron to their advantage, Courtade *et al.* found that other than structural effects attributed to copper binding at the active site, there is very little observable difference in the NMR of the *apo* and Cu(I) in *Bl*AA10, suggesting LPMO coordination to Cu(I) ions has little impact on the overall protein structure.[87]

A $^{13}C$ heteronuclear single quantum coherence (HSQC) investigation found that the histidine brace of LPMOs is able to coordinate a range of divalent ions including Zn(II), but confirmed the strongest affinity for copper ions with an even greater preference for Cu(I) ions over Cu(II) ions.[92] Using $^{15}N$ HSQC NMR to track signal changes from the amide hydrogen atom, it has been shown that the CBM linker is indeed disordered and extended, which is proposed to function to create distance between the catalytic and carbohydrate-binding domains. Furthermore, this study found a correlation between the presence of the CBM and promoted LPMO catalysis.[93]

An *apo-Nc*AA9 LPMO showed a significant chemical shift change in the presence of soluble polysaccharides: cellulose hexasaccharide ($Glc_6$), a mixture of longer xyloglucan oligomers (XG14), and Polymeric xyloglucan (polyXG). The chemical shift has also been observed in the presence of cellobiose dehydrogenase (CDH), a known natural source of electrons. The chemical shift changes observed in all the $^{15}N$-HSQC and $^{13}C$-aromatic-HSQC spectra with different substrates are consistent with binding at the histidine brace, evidenced by changes in the chemical shifts of the

His1, Ala80, His83 and His155 residues. Furthermore, there is variation in the changes in the chemical shifts of other amino acid residues with different substrates. The polysaccharide substrates were also found to cause changes in a surface loop, known as L3. The addition of CDH did not afford a change in this surface loop.[94] The NMR data collected is inconsistent with the XRD structure for the substrate interaction of *Ls*AA9 with $Glc_6$; where the NMR data suggests substrate binding from the -3 to +3 or -2 to +4 subsites, the XRD suggests substrate interaction is from -2 to +2 subsites.[54,94] It is important to note that these differences could be attributed to substrate binding variation within the AA9 genomic class or different substrate interactions between the *apo* and copper bound LPMOs.

To circumvent the issue of NMR silent copper(II), Aachmann *et al.* used a Zn(II) bound AA10 LPMO to study LPMO interaction with cyanide as a molecular oxygen mimic. No changes were observed in the $^{15}N$ or $^{13}C$ HSQC NMR of the *apo*-LPMO where the Zn-LPMO saw significant changes at the histidine brace on addition of cyanide, leading to the conclusion that the oxygen mimic directly coordinates the metal ion.[92]

Using NMR, it has been determined that LPMOs have a high affinity for copper ions and the structure of apo and Cu(I) structures of LPMOs have been solved. LPMOs that are active on soluble substrates have been studied using NMR although these interactions do not replicate the findings of XRD LPMO-substrate structures. As more LPMOs are discovered, NMR is a useful spectroscopic tool to elucidate their structures without the requirement for crystallisation. There is still more to understand about LPMO-substrate interactions and NMR as a spectroscopic technique could be integral to this.

### 1.2.3 Ultraviolet-visible spectroscopy

Ultraviolet-visible spectroscopy (UV-vis) is a spectroscopic technique widely used during the production of LPMO proteins. During the purification of LPMOs the UV-vis absorption at 280 nm can be used in conjunction with a molar extinction coefficient calculated by the number of tyrosine and tryptophan amino acid residues in the protein sequence to be able to determine the protein concentration of a sample.[95] Similarly, UV-vis can also be used to evaluate the presence of DNA in LPMO samples by measuring the absorbance at 260 nm, which is inversely related to the purity of the LPMO sample.

The accessibility and swiftness of UV-vis as a spectroscopic technique makes it ideal for LPMO activity assays, as opposed to conventional techniques such as mass spectrometry and high-performance liquid chromatography. As such, E. Breslmayr *et al.* developed a simple assay using a solution of 2,6-dimethoxyphenol (2,6-DMP) at a suitable pH (pH 5-8) and a short incubation time (15 minutes, 30 °C) with the LPMO. In the presence of an active LPMO, coerulignone will be produced giving an absorbance peak in the UV-vis region at 469 nm (Figure 1.14).[96] This assay is currently the most sensitive LPMO UV-vis activity assay, but builds on the work of R. Kittl *et al.,* in which Amplex Red was used and fluorescence was applied to measure the formation of products.[97]

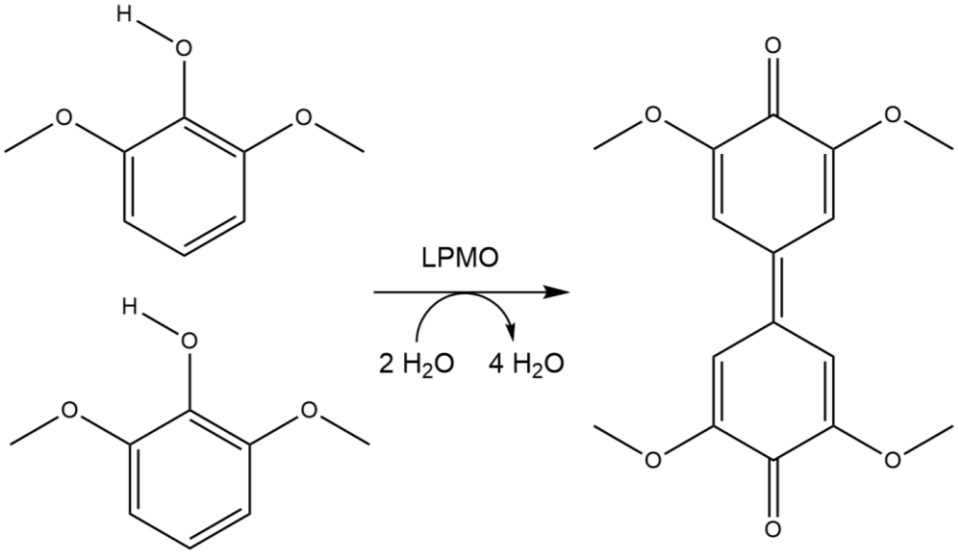


Figure 1.14: Reaction of 2,6-DMP assay to determine LPMO activity.[96]

UV-vis has been successfully applied to study the kinetics of LPMO oxidation mechanisms and radical intermediates using stopped flow. Jones *et al.* used UV-vis coupled with stopped flow methodologies to investigate the role of peroxide in the reactivity of LPMOs by monitoring the absorbance at 650 nm, attributed to a Cu(II) ligand field band. In an aerated buffer the re-oxidation rate of a Cu(I) *Hj*AA9 LPMO was found to be second order with a rate of 12 $M^{-1}$ $s^{-1}$, with no intermediates observed. Conversely, re-oxidation of Cu(I) *Hj*AA9 with hydrogen peroxide showed a significant increase in rate to 4 x$10^4$ $M^{-1}$ $s^{-1}$ and exhibited the formation and decay of absorbance at 520 and 420 nm, both dependent on peroxide concentration. The peak at 420 nm was attributed as a neutral tyrosyl radical with a slow rate of decay (0.04 $s^{-1}$). The peak at 520 nm decayed slower than the peak at 420 nm (*ca.* 5 $s^{-1}$) and was assigned as a neutral tryptophanyl radical. The formation and decay of these intermediates has been suggested by Jones *et al.* to exist as part of a homolytic O-O bond cleavage major pathway alongside a minor heterolytic O-O pathway which would involve an elusive cupryl intermediate.[98] Singh *et al.* also observed a peak at 420 nm in the reaction of Cu(I)-

*Ta*AA9 and hydrogen peroxide which was attributed to a tyrosyl radical. In this study there was an absence of a peak at 520 nm, suggesting a tryptophanyl radical does not form part of the Cu(I)-*Ta*AA9 reaction with peroxide.[99] These findings confirm that peroxide is able to drive an LPMO catalytic reaction in the absence of substrate and provide insights into intermediate LPMO species which could be formed, including alternative mechanisms which are present in different LPMOs within the same genomic class.

Whilst UV-vis is limited in the structural information that can be extracted for LPMOs, it is an accessible and quick spectroscopic technique to study LPMO concentration, kinetics activity and radicals. UV-vis has been used in the exploration of LPMO reactivity to study the formation and decay of LPMO intermediates, assess activity, and to elucidate possible LPMO co-substrates.

### 1.2.4 Magnetic circular dichroism

Magnetic circular dichroism (MCD) is a form of electronic spectroscopy concerned with the differential absorption of left and right polarised light induced by an external magnetic field, parallel to the direction of light. [100–102] MCD can be used to probe electronic and magnetic properties as well as optical transitions of metal ions and therefore can be applied to the study of the ligand-field bands at the copper active site in LPMO proteins.[101] Applying a magnetic field induces interaction between molecular orbitals causing mixing and allowing absorption, which MCD probes using X-rays (XMCD) or visible light with higher resolution than UV-vis. Few studies have used MCD spectroscopy to evaluate LPMO structures, despite being a powerful means of evaluating the local electronic structure in the copper active site. Currently, only visible light MCD LPMO investigations have been published and therefore herein visible light MCD will be the focus of this discussion.

MCD has been successfully used to characterise the structure of LPMO active sites and when used in tandem with EPR can offer important information on the electronic structure and ground state magnetic properties of copper in LPMOs. MCD is particularly useful to gain further information from UV-vis spectroscopy as the transitions appear at the same energy in each spectroscopic technique. MCD allows the separation of A, B and C terms from which insights into the geometry and interactions of molecular orbitals can be ascertained.

Paradisi *et al.,* used MCD to determine the spin state of a Cu(II)-*Ls*AA9 tyrosine radical intermediate.[1] The MCD spectrum for Cu(II)-*Ls*AA9 found bands at 14300 and 1700 $cm^{-1}$ and shoulders at 14300, 18000, 25700 and 28400 $cm^{-1}$ which were insensitive to both changes in

temperature and electric field and therefore were attributed to a singlet *S*=0 ground state, with no C-term bands to be assigned. [1] Jones *et al.,* used a combination of EPR and MCD spectroscopy to identify the optically active intermediates in the reaction of an AA9 LPMO with peroxide as tyrosyl and tryptophanyl radicals, to conclude that peroxide has an enhanced ability to drive a catalytic LPMO reaction over $O_2$, though this was once again in the absence of a discernible C-term because of low spin-orbit coupling. [98] A further study with an AA9 LPMO (*Hj*AA9) used MCD to evaluate the structure of the LMPO when a carbohydrate binding module had been removed. The MCD spectrum contained two C-term features of opposite signs which were assigned as spin orbit coupled $d_{xz/yz}$ to $d_{x2-y2}$ ligand field transitions. A combination of MCD and EPR spectroscopy was used to determine that the removal of this module did not change the structure of the binding site, even though the catalytic activity of the modified LPMO decreased. Based on these findings, Hansson *et al.* concluded that the CBM module increases the LPMO substrate affinity. [103]

### 1.2.5 Resonance Raman spectroscopy

Resonance Raman is undertaken by irradiating the sample using a laser with an excitation frequency close to that of the electronic transitions of the sample. Using resonance Raman, information on LPMO vibrational states can be gleaned. Resonance Raman spectroscopy has been used to study the vibrational bands of several metalloproteins such as hemoglobin, cytochrome c, rubredoxin, hemerythrin, hemocyanin, adrenodoxin, and transferrin. [104–111] Unlike other vibrational spectroscopies such as IR, Raman requires that the molecular vibrations induce a change in polarizability. Resonance Raman is an ameliorated form of Raman spectroscopy whereby the energy of the incident beam is selected to specifically initiate a particular electronic transition and as such the vibrational states surrounding the copper ion in the LPMO active site can be selectively studied.

There are very few examples of studies which have applied resonance Raman to LPMOs. Paradisi *et al.* characterised the "purple species", a Cu(II) tyrosyl-radical AA9 LPMO species, using resonance Raman (Figure 1.15). Different isotopic conditions were used by preparing the samples in combinations of $H_2{}^{18}O$, $H_2{}^{16}O$ and $D_2O$ with no differences observed between these samples, concluding that copper-peroxide and superoxide species could be ruled out. Spectra were recorded using 532 nm and 785 nm laser excitations and gave peaks which correspond with those observed in a Cu(II)-tyrosyl galactose oxidase enzyme. [1] Also in the pursuit of characterising an LPMO-tyrosyl radical, Singh *et al*. observed a peak in the resonance Raman of Cu(I)-*Ta*AA9 treated with peroxide at 1505 $cm^{-1}$ which they assign to the tyrosyl radical. The authors also cite difficulty in obtaining this

data as exposure to the laser causes very fast decay of intermediate LPMO species, offering an explanation as to why there are so few resonance Raman LPMO studies and a word of caution for future studies.[99]

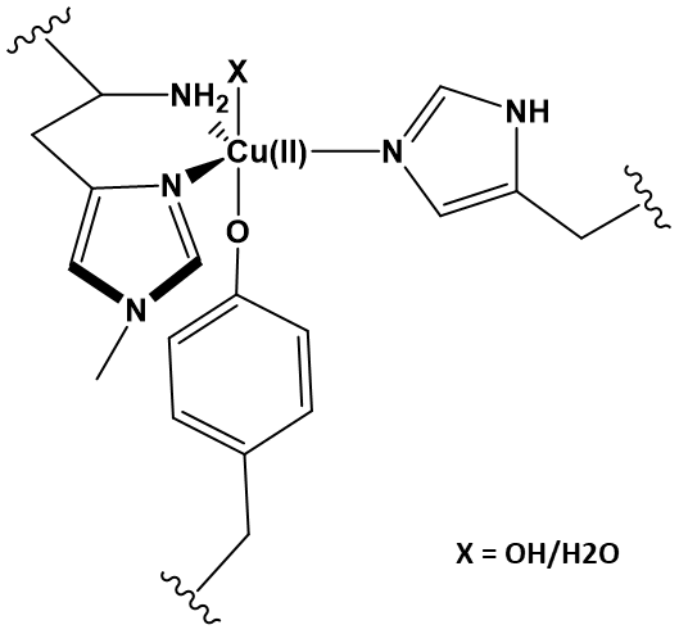


Figure 1.15: *Ls*AA9 "purple species" Cu(II)-tyrosyl radical structure characterised by Paradisi *et al*.[1]

### 1.2.6 X-ray spectroscopy

X-ray spectroscopy encompasses techniques which analyse the interaction between X-rays and matter to characterise its chemical properties. Some of those techniques have been used to get different insights into the structure and mechanism of LPMOs, providing complementary information.

#### *1.2.6.1 XAS*

X-ray absorption spectroscopy (XAS) is a powerful element-selective tool which provides local structural and electronic information around an absorbing atom. In the case of LPMOs, XAS is used to probe the copper active site. Whilst there are increasingly available laboratory options to perform XAS, synchrotron radiation is still required to obtain high quality XAS data with dilute LPMO samples. The requirement for access to synchrotron radiation is a significant barrier to the accessibility of recording XAS data for LPMOs. Furthermore, under the conditions of synchrotron radiation, the copper(II) ion in LPMOs is very susceptible to photoreduction, which causes electronic and coordination changes to the active site. [33,112] The use of filters and the careful choice of scanning parameters is essential in Bio-XAS experiments. This will reduce the exposure to the full photon flux

and will curb the photodamage of copper(II) LPMO samples, although this often has an impact on the signal-to-noise ratio of the collected data.

XAS utilises the photoelectric effect for the excitation of a core electron to the continuum (Figure 1.16). By tuning the energy of the X-ray beam it is possible to dictate which electron is excited, resulting in different electronic transitions being studied.

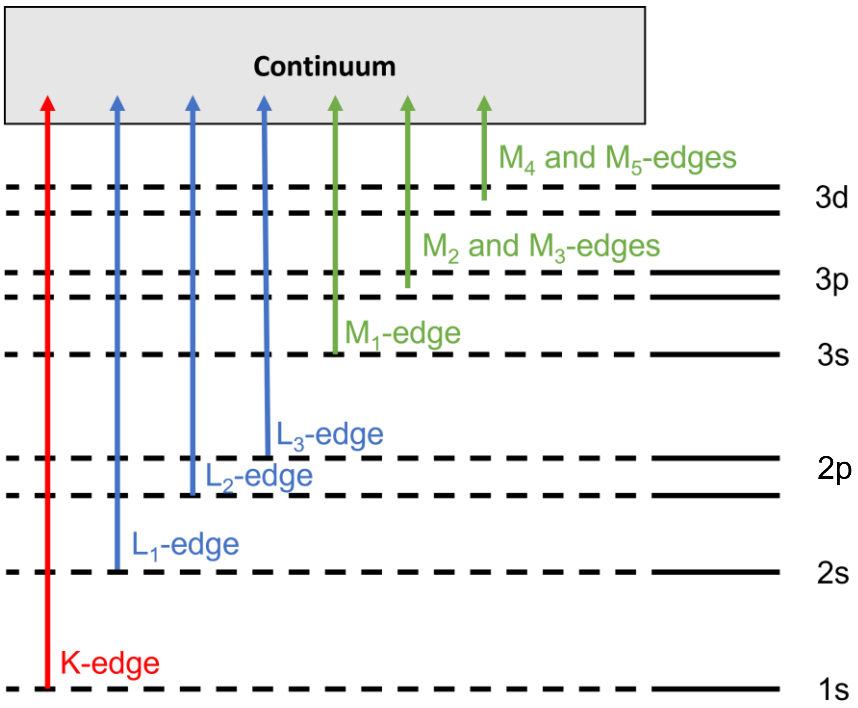


Figure 1.16: Energy level diagram showing the electronic transitions resulting in different absorption edges.

Transmission mode is the standard way to measure XAS, however for dilute samples such as the case for LPMOs, fluorescence mode is recommended. The intensity of the fluorescence XAS signal ($\mu(E)$) is measured by:

$$\mu(E) \propto {I_f}/{I_0}$$

Where $I_0$ is the incident flux and $I_f$ is the fluorescence emitted from the electronic excitation in the sample. When absorption of the incident X-ray photon occurs a core electron can be excited which results in a core-hole. The core-hole is then filled by an electron through the relaxation of an

electron from a higher energy shell, the energy difference is then emitted as fluorescence which can be measured as the intensity of radiation as a function of energy ($I_f$) (Figure 1.17).

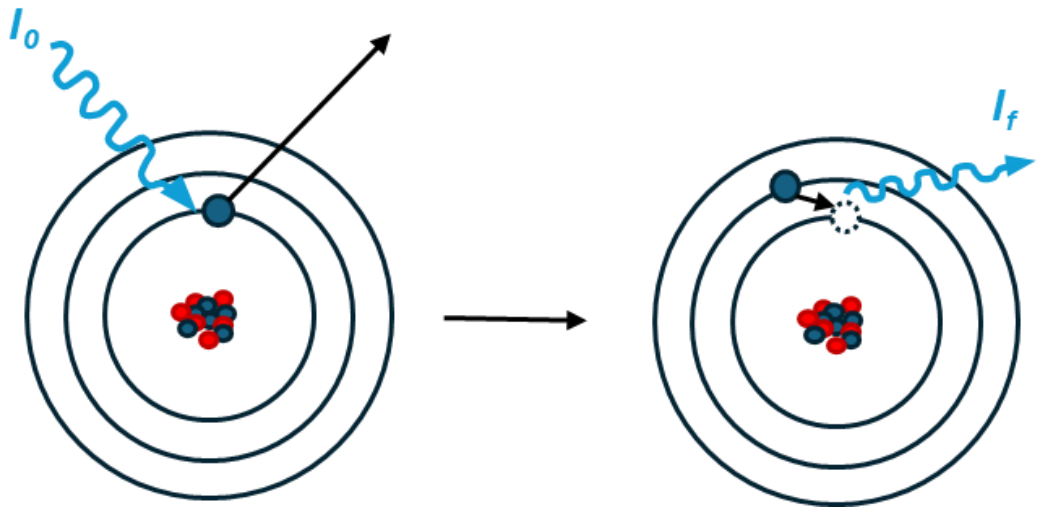


Figure 1.17: An atomic diagram showing the absorption of an X-ray photon ($I_0$) resulting in the ejection of a core electron. An electron from a shell of higher energy fills the core-hole that has been created which results in fluorescence emission ($I_f$).

Fluorescence exists as several emission lines depending on which electron fills the core-hole (Figure 1.18). The most probable transitions correspond to the Kα emission lines: $K\alpha_1$ and $K\alpha_2$ which are the lowest energy emission lines and are sensitive to the oxidation states of the absorbing atom. The Kβ emission lines can be sub-divided into the Kβ mainlines: $K\beta_1$ and $K\beta_3$, and valence-to-core: $K\beta_2$ and $K\beta_5$. The Kβ emission lines are sensitive to the oxidation state and spin state of the absorbing atom as well as the ligand environment. The lower probability of the Kβ transitions compared to Kα transitions correspond to the relatively weaker Kβ spectra intensity.

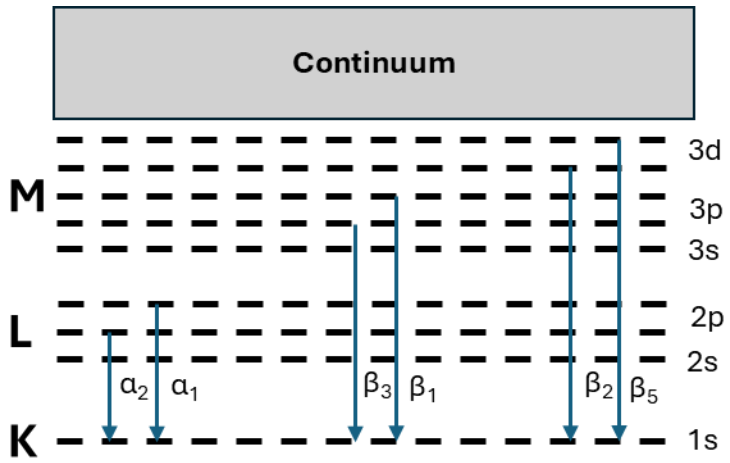


Figure 1.18: Energy level diagram showing the transitions corresponding to the Kα and Kβ fluorescence emission lines.

For fluorescence detection, the sample is angled at 45° to the incident beam and the fluorescence emission is measured by a detector perpendicular to the incident beam. Fluorescence detection is preferable for dilute samples as it is more sensitive than transmission, however fluorescence detection is unsuitable for concentrated samples due to self-absorption.

High energy resolution fluorescence detected XAS (HERFD-XAS) is an advancement of conventional XAS. When performing HERFD-XAS, the energy of the emitted photons is measured in fluorescence mode with an energy bandwidth on the order of the core-hole lifetime broadening of the inner-shell electron hole, increasing the resolution of the measurement and enhancing the spectral features in the XANES region of the spectrum. To measure HERFD-XAS an emission spectrometer consisting of analyser crystals is used to select a narrow energy band from the sample's emission line. For HERFD-XAS the sample, emission spectrometer and detector are arranged in a Rowland circle configuration (Figure 1.19).

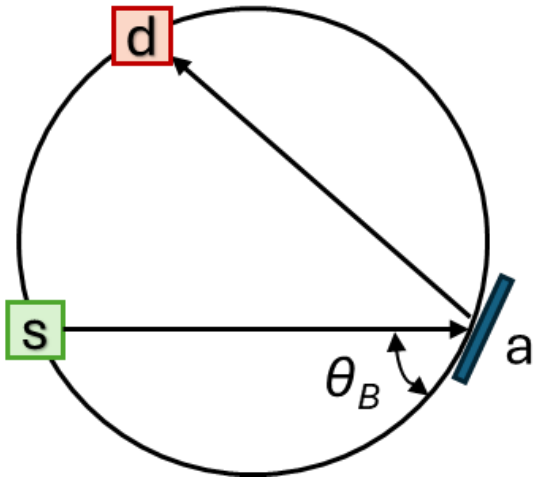


Figure 1.19: Schematic illustration of the Rowland circle geometry set up used in HERFD-XAS. The sample position is represented by "s", the analyser crystal is represented by "a" and the detector is represented by "d". The Bragg angle is shown as $\theta_B$.

The oxidation state, ligand interactions and geometry affect the relative energies of the copper orbitals, thus X-ray spectroscopy is sensitive to these conditions. The relatively high energy of the K-edge transition means that it is measured using hard X-rays whereas the L and M-edges require the use of soft X-ray beams (Table 1.2). At the time of writing there are no published studies of LPMOs using soft X-rays and therefore the focus of this section will be on K-edge XAS of LPMOs.

Table 1.2: copper absorption edges and their corresponding energies.[113]

| **Absorption edge** | **Energy (eV)** |
|---|---|
| K | 8979.0 |
| L1 | 1096.7 |
| L2 | 952.3 |
| L3 | 932.7 |
| M1 | 122.5 |
| M2 | 77.3 |
| M3 | 75.1 |
| M4 | 5.0 |
| M5 | 5.0 |

Two distinct regions can be defined in the absorption spectrum; the X-ray absorption near edge structure (XANES) and the extended X-ray absorption fine structure (EXAFS) (Figure 1.20). [114–116] The

XANES region extends about 30 eV above the absorption edge which includes pre-edge peaks and the rising edge (sometimes referred to as the white line). The XANES region contains information about the electronic structure of the absorbing atom (oxidation state, density of states), coordination symmetry (tetrahedron, octahedron, etc) and orbital occupancy. In particular, the energy position of the rising edge has been used to diagnose the oxidation state of copper in LPMOs.[117] The EXAFS region, beginning around 30 eV above the absorption threshold and extending for hundreds of electronvolts, is the oscillatory structure that modulates the absorption spectrum. It contains detailed structural information about the atoms around the absorbing centre, including nature of the coordinating atoms, coordination numbers, bond lengths and order/disorder.

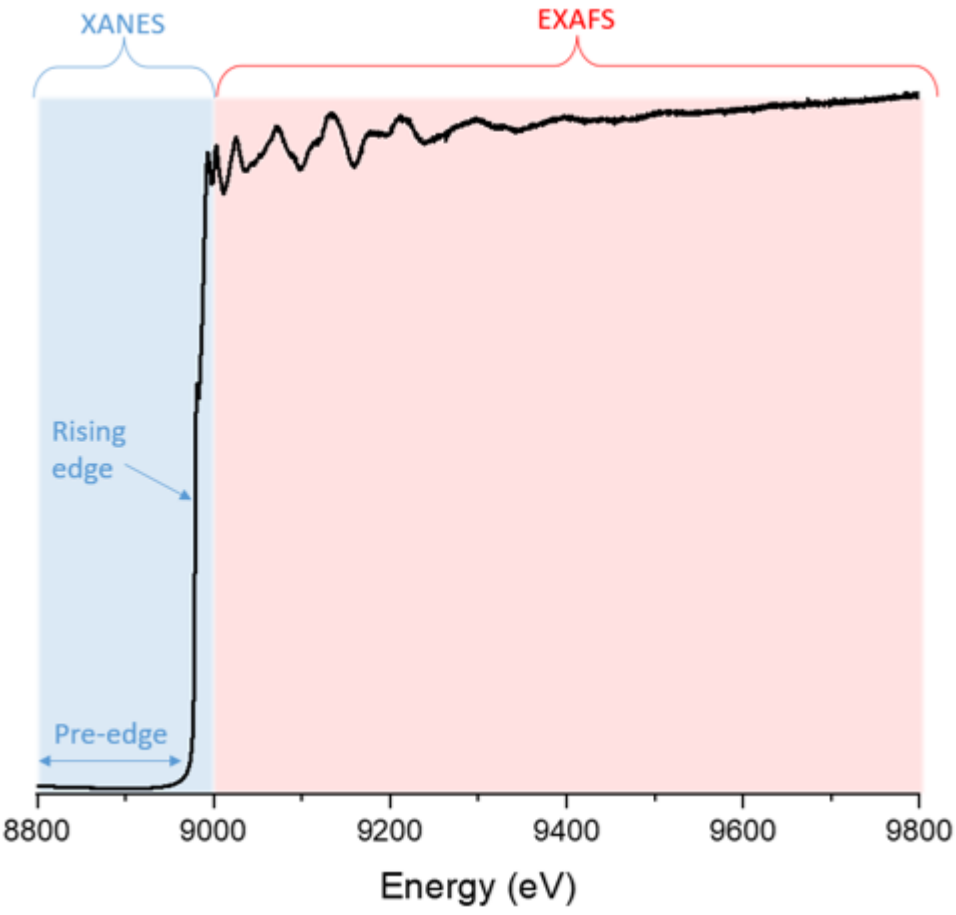


Figure 1.20: Copper K-edge XAS spectrum showing the XANES and EXAFS regions.

### *1.2.6.2 XANES*

The copper K-edge XANES region of copper complexes is sensitive to changes in oxidation state and coordination environment. Copper K-edge XANES spectra are usually comprised of a weak pre edge transition in the case of Cu(II), a rising edge peak which varies in intensity and the white line absorption peak. The energy and intensity of the white line as well as the presence of a pre-edge

peak can be used to assign the oxidation state of copper complexes. In Cu(II) complexes the pre-edge peak which is assigned as a dipole forbidden quadrupole allowed 1s to *3d* transition has been found to be sensitive in energy to ligand contributions to the lowest unoccupied molecular orbital (LUMO).[118] The rising edge peak in Cu(I) and Cu(II) complexes assigned as a 1s to *4p* transition changes in intensity and energy position not only on changes in oxidation state but also with changes to the coordination environment. An experiment by Kau *et al* found that in a range of Cu(I) compounds measured, the normalised intensity and energy of the 1s to *4p* transitions were correlated to their coordination number (Figure 1.21). The sensitivity of the copper K-edge XANES region to changes in copper coordination means that XANES is a suitable technique to use to study changes in the LPMO primary coordination sphere.

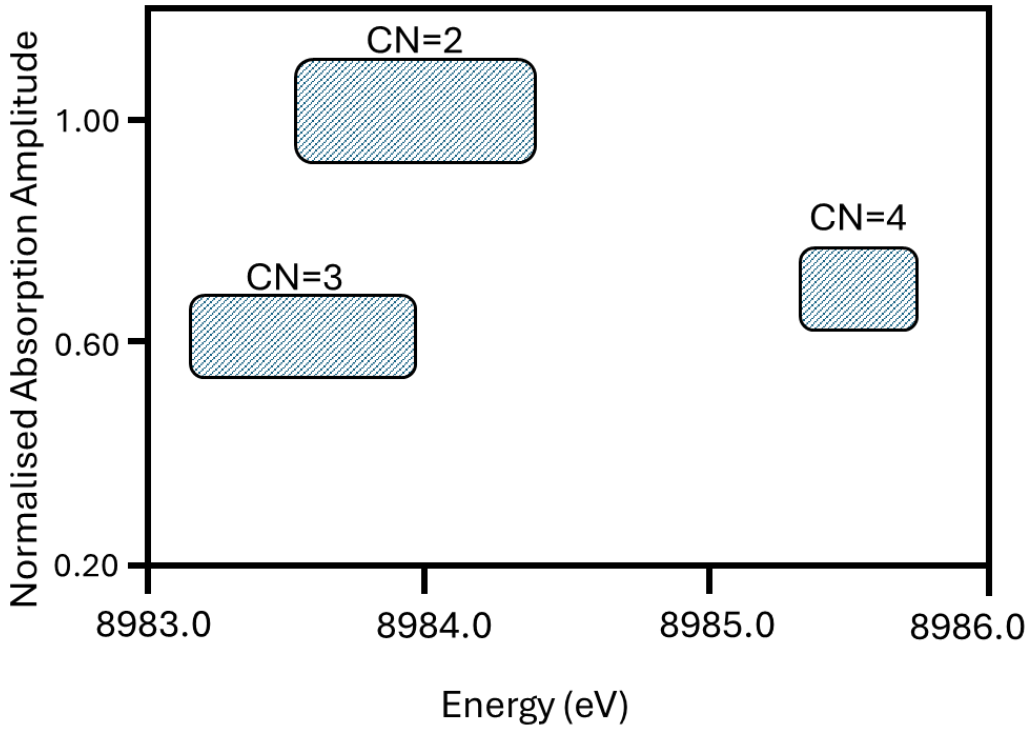


Figure 1.21: The ranges for the normalised amplitudes and energy of the 1s to 4*p* transition in various Cu(I) compounds with different coordination numbers (CN-2, 3, 4). This figure was adapted from the publication by Kau *et al*.[117]

'Shakedown' transitions are also reportedly observed in Cu(II) XANES spectra whereby the excitation of the core 1s electron lowers the energy of the *3d* Cu(II) orbital, facilitating the metal-to-ligand charge transfer (MLCT) from the *3p* ligand orbital (Figure 1.22). [119]

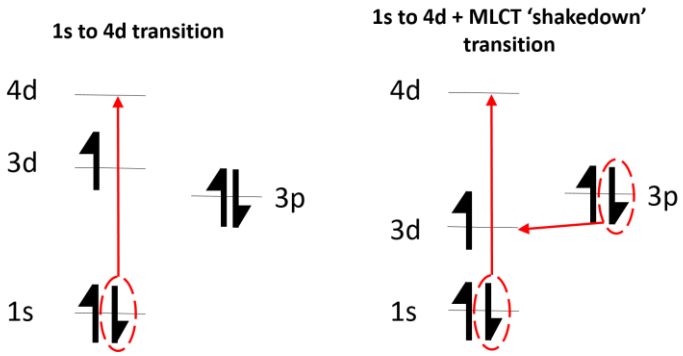


Figure 1.22: Schematic diagram of the electronic transitions in a 1s to 4d transition (*left*) and a multi-electron 1s to 4d + MLCT 'shakedown' transition, which occurs due to the lowering in energy of the Cu(II) *3d* orbital (*right*) commonly observed in Cu(II) XANES spectra.

In early LPMO experiments Cu K-edge XANES was used to determine the oxidation state of the copper active site. A pre-edge feature was assigned as a 1s to non-bonded *4p* transition of a coordinatively unsaturated Cu(I) ion, consistent with a coordination number of less than four. [33,120] A similar XANES spectrum was also observed when sodium ascorbate, a chemical reductant, was added to the LPMO, which demonstrates the photoreduction caused by XAS. [33]

A further study which measured the XANES spectra of an *Ls*AA9 species with indefinite stability in the LPMO catalytic cycle, coined as the "purple species" was found to be almost identical to the resting state Cu(II) LPMO XANES spectra with the exception of an additional pre-edge feature at 8982.8 eV, leading to the conclusion that this species is formally a Cu(II) ion, but with an additional metal-ligand interaction attributed to a 1s to singularly occupied molecular orbital (SOMO) with tyrosyl character. [1]

Munzone *et al*., have used the enhanced resolution properties of HERFD-XANES along with TD-DFT to probe the electronic structure and coordination geometry of the Cu(I) and Cu(II) active site of *Sm*AA10.[121]

### *1.2.6.3 EXAFS*

The EXAFS region of the XAS spectrum gives structural information about the neighbouring atoms around the absorbing atom as a result of the scattering photoelectron according to the equation below.[122] The term $\sum_j$ refers to the sum of scattering pathways; the ejected photoelectron from the absorbing atom is scattered by neighbouring atoms, the extent of which depends on the electrons and distance of the neighbouring atom. Multiple scattering events can also occur when

the photoelectron is scattered by a series of atoms in close proximity to the absorbing atom. The scattering pathways are given by the terms $N_j$ which is the number of neighbouring atoms, $R_j$ which is the distance between the absorbing atom and the scattering atom, and $S_0^2$ is the amplitude reduction factor which corrects for phase shifts, incoherent scattering and inelastic scattering.

$$x(k) = \sum_j \frac{N_j S_0^2}{kR_j^2} F_j(k) e^{-2R_j/\lambda_j(k)} e^{-2k^2\sigma_j^2} \sin\left[2kR_j + \delta_j(k)\right]$$

By using the EXAFS equation to fit experimental data useful information about the system can be extracted including the coordination number of the absorbing atom and the scatting path lengths. Because of the large number of scattering interactions that are possible in the LPMO active site, including multiple scattering pathways, care must be taken in the interpretation of the EXAFS signal. XANES and EXAFS have confirmed the presence of three nitrogen ligands which are conserved in both Cu(I) and Cu(II) LPMO oxidation states, however a labile hydroxide ligand present in the Cu(II) species is uncoordinated on reduction to give a three coordinate Cu(I) species. Cryoreduction of a Cu(II) AA9 protein using γ-emitting $^{137}$Cs at 77 K also resulted in a change in geometry as diagnosed by XANES, which is evidence of limited rearrangement of the LPMO protein structure. [120]

Whilst few LPMO studies using XAS have been published due to the challenges of these techniques previously discussed, the papers presented demonstrate the high-quality data that can be obtained. As such there remains scope for further application of XAS techniques in the quest to learn more about the mechanism and function of LPMO intermediate species. So far, XANES has allowed for the characterisation of the oxidation states and electronic configurations of LPMO species whilst EXAFS has afforded structural information concerning the labile ligands at the copper active site.

## 1.3 An introduction to the beamlines

The X-ray spectroscopy data presented in this thesis were collected using synchrotron radiation at Diamond Light Source, the UK's national synchrotron facility. Diamond Light Source is a third-generation light source with a typical set up (Figure 1.23) comprising of an injection system, booster synchrotron, storage ring and beamlines. In the injection system an electron gun is used to produce electrons which are accelerated by the linear accelerator (LINAC) to a relativistic energy of 100 MeV. From the linear accelerator, electrons with an energy of 1 GeV are injected into the booster synchrotron where a series of magnets and a radio frequency voltage are used to increase the

electron energy to a final extraction energy of 3 GeV at which point the electrons are directed into the storage ring. The storage ring is comprised of bending magnets and insertion devices. The flux density available at the beamline depends on whether it is based on an insertion device (and depending on the type of insertion device) or a on bending magnet.

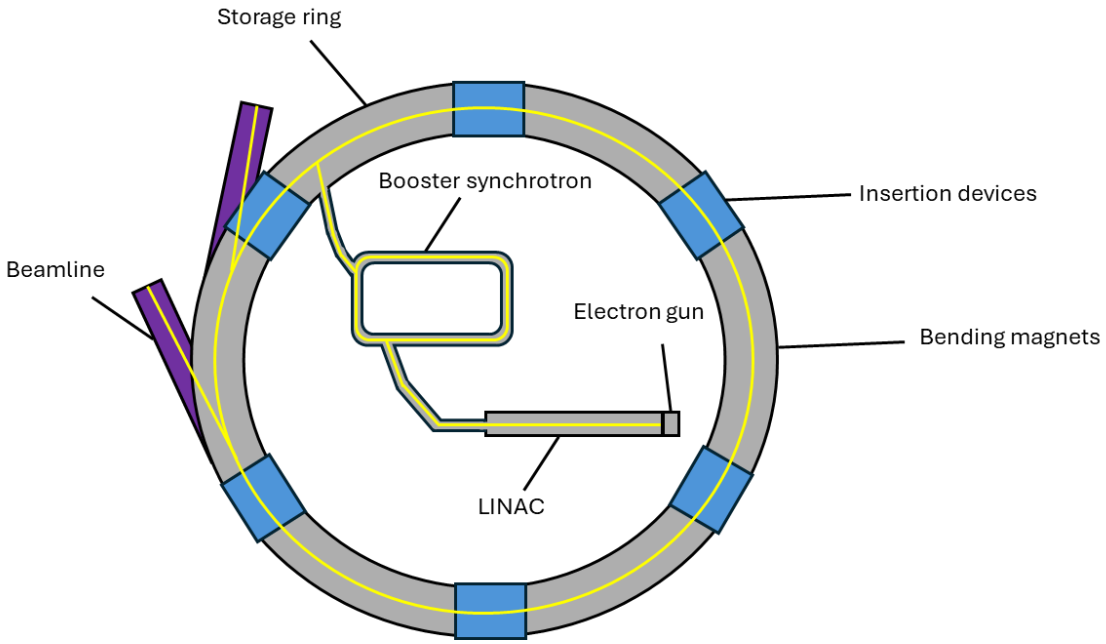


Figure 1.23: Schematic diagram of the main components of a synchrotron. The LINAC is a linear accelerator.

Deciding on a suitable beamline for the experiments proposed is crucial when planning X-ray spectroscopy experiments. Different beamlines offer variations of energy ranges, flux, beam size and collection time scales, as well as sample environment equipment. In the work presented in this Thesis, a dual beamline approach was used to collect both HERFD-XANES and conventional XAS. HERFD-XANES spectra were collected on I20-Scanning and conventional XAS was collected on B18 due to their different set ups which are discussed further below.

### 1.3.1 The Versatile Spectroscopy Beamline, I20-Scanning

The I20-Scanning beamline at Diamond Light Source is based on a wiggler (insertion device) source, and as such offers a high total flux of > $10^{12}$ ph/s. The energy range covered by I20-Scanning is from 4.5 – 20 keV and a beam size of 400 (V) x 400 (H) µm FWHM. The optics hutch includes a collimating mirror, a flat mirror, two focusing mirrors and an in-house designed four-bounce monochromator

consisting of two pairs of counter rotating crystals which offers high stability and reproducibility (Figure 1.24). The experimental hutch contains a pair of harmonic rejection mirrors and both XAS and XES end stations. The X-ray emission spectrometer in the end station can be used to measure HERFD-XANES, as well as resonant and non-resonant XES.[123,124]

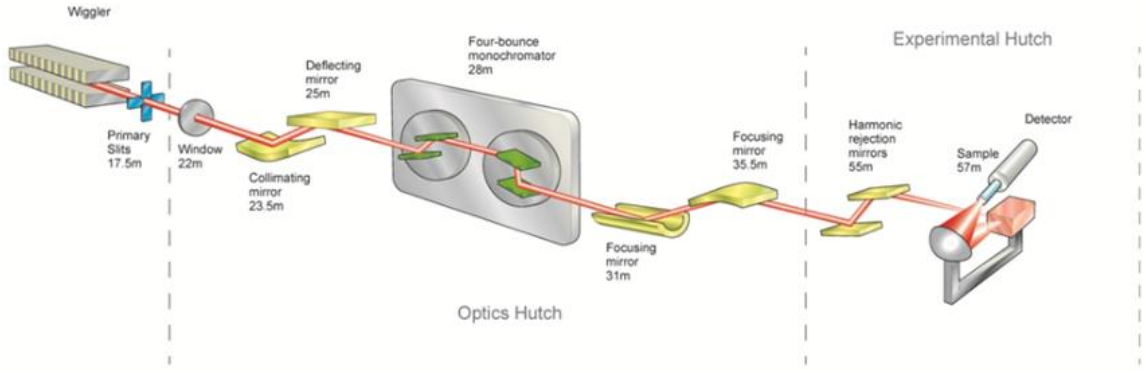


Figure 1.24: Schematic diagram of the I20-Scanning beamline at Diamond Light Source showing the XES end-station.[124]

I20-Scanning was chosen to measure the HERFD-XANES spectra of the samples because of its high flux and spectral purity which is ideal for measuring high resolution spectra of dilute samples. The compromise with this technique and using I20-Scanning is the risk of radiation induced damage to the sample because of the high flux and long scan times (this was mitigated by measuring the samples at 10 K, measuring spectra in different sample positions, and suitably attenuating the X-ray beam – further details are given in section 2.3.1).

### 1.3.2 The Core EXAFS beamline, B18

The B18 beamline at Diamond Light Source is based on a bending magnet source which means it offers a comparatively lower total flux of *ca*. $5 \times 10^{11}$ ph/s. The energy range covered by B18 is from 2.05keV to 35 keV and the beam size is 1000 (H) x 1000 (V) µm FWHM. The optics for B18 include a collimating mirror, a water-cooled double crystal monochromator and a focusing mirror (Figure 1.25).

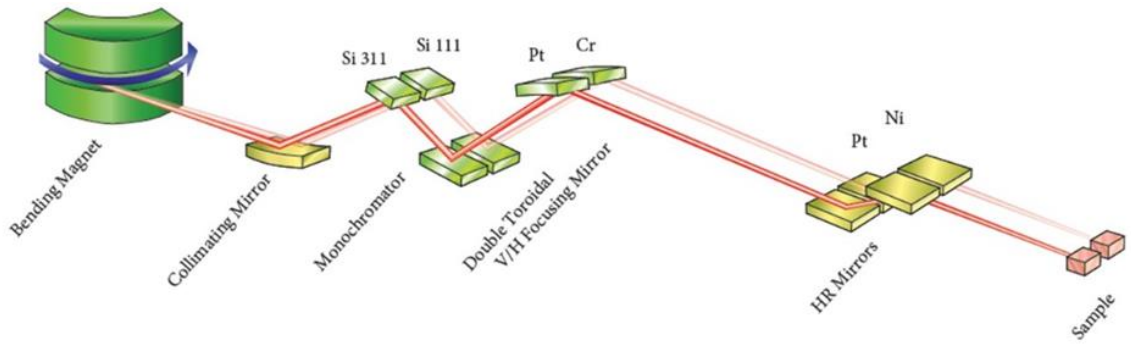


Figure 1.25: Schematic diagram of the B18 beamline at Diamond Light Source.[124]

B18 was chosen to carry out the conventional XAS experiments presented because of its quick scanning monochromator which allows for a faster rate of scanning and faster spectrum collection times than I20-Scanning. This means that a full XAS spectrum including the EXAFS region could be measured without inciting prolonged X-ray exposure which could result in an increased risk of radiation induced sample damage. The compromise with this technique is the lower spectral resolution and lower signal-to-noise ratio than the HERFD-XANES collected on I20-Scanning. This was mitigated by increasing the number of spectra recorded per sample to create merged spectra with increased statistics.

## 1.4 Aims

The overarching aim of this work is to use X-ray absorption spectroscopy to characterise a range of LPMO genomic classes in three different conditions. XAS offers a unique spectroscopic ability to study both the Cu(I) and Cu(II) oxidation states of LPMOs, LPMO-substrate slurries and freeze quenched LPMO intermediates.

The first condition presented aims to explore the interactions of *An*AA9, *Ls*AA9, *Bl*AA10 and *Ao*AA11 interactions with substrates in both the Cu(I) and Cu(II) oxidation states. The aim of this investigation is to determine the structural changes that occur in the initial stages of the LPMO reaction mechanism, and to compare how this differs between different genomic classes as well as within the same genomic class.

The second condition investigated uses rapid freeze quenching to trap LPMO intermediates from reactions initiated by an oxygen-atom “shunt”. The aim of this experiment is to outline a method for trapping and characterising a metalloenzyme intermediate, using LPMOs as a case study.

The third condition explored is the reaction of the LPMO copper active site to prolonged exposure to X-rays. Radiation damage is a challenging consequence of measuring metalloenzymes with XAS. The aim of these experiments is to explore the effects of different radiation doses on LPMOs measured at 10 K on the oxidation state and copper coordination/ geometry, and to determine if X-ray radiation is a feasible route to initiate reduction/ formation of intermediates in LPMOs.

# 2 Methods

## 2.1 LPMO synthesis and purification

### 2.1.1 *Ls*AA9 Y154F

*Ls*AA9 Y164F was prepared following reported procedures.[125] The Y164F mutation was introduced into the pET22b_LsAA9 construct using QuikChange site-directed mutagenesis. Chemically competent *E. coli* C43 (DE3) cells were transformed with the Y164F LPMO construct and plated onto Luria-Bertani (LB) agar with Ampicillin (100 µg/mL). A preculture consisting of 5 mL of LB medium with Ampicillin (100 µg/mL) inoculated with a single colony from the Y164F transformed *E. coli* cells was incubated overnight for 18 hours at 37 °C, shaking at 180 rpm. The following morning 400 mL 2XYT autoinduction medium with Ampicillin (100 µg/mL) was inoculated with 4 mL of preculture and incubated for 2 hours at 37 °C shaking at 180 rpm, before lowering the temperature to 25 °C for further incubation for 20 hours. The cells were then harvested by centrifugation at 6000 g for 10 minutes at 5 °C. The supernatant was discarded, and the cell pellet was resuspended in 50 mL ice-cold buffer (50 mM $NaH_2PO_4$, 300 mM NaCl, pH 8, 1 mg/mL lysozyme, 10 µg/mL DNase). The suspension was then sonicated in an ice bath for 2 x 5 min (1 s sonication, 1 second rest) and then centrifuged at 20000 g for 1 hour at 4 °C. The supernatant was removed and passed through a 0.2 µm filter before being passed through a 5 mL Strep-Tactin XT column. The column was washed with 75 mL of buffer (50 mM $NaH_2PO_4$, 300 mM NaCl, pH 8) to remove unbound protein before passing through 18 mL of elution buffer (50 mM $NaH_2PO_4$, 300 mM NaCl, 50 mM biotin, pH 8). The fractions containing LPMO were concentrated using a 10 kDa filter and then desalted by passing through a 10DG desalting column with elution buffer (50 mM $NaH_2PO_4$, pH 6). The resulting *Ls*AA9 Y164F solution was then copper loaded by the addition of a $CuCl_2$ solution (10 mM in MilliQ water, 0.75 equiv.) and incubated on ice for two hours.

### 2.1.2 *An*AA9

*An*AA9 was expressed and purified following a previously reported method.[126] *Aspergillus nidulans* transformants expressing *An*AA9 were grown in Erlenmeyer flasks (2 L) with minimal medium (200 mL, pH 6.5) with 1% (wt/vol) glucose and 2% (wt/vol) maltose and was incubated for 36 h at 37 °C under static conditions. The supernatant was then centrifuged at 5,000 g for 40 minutes at 4 °C and then filtered using a 0.45 µm syringe filter. The resulting suspension was passed through a HiPrep DEAE FF 16/10 column (equilibrated in 50 mM Tris-HCl, pH 7). A linear elution gradient from 0 to 100% with the elution buffer (50 mM Tris-HCl, pH 7, 1 M NaCl) was used and the fractions identified by SDS-page to contain LPMO were pooled and concentrated using a 10 kDa filter. The

concentrated fractions were then passed through a HiTrap Phenyl HP 1 mL column and eluted using a gradient of 1.5 to 0.0 M ammonium sulphate. The fractions identified using SDS-page to contain LPMO were combined. The LPMO fractions were incubated with three molar equivalents of $CuSO_4$ overnight at 4 °C and then concentrated and washed with MES buffer (50 mM, pH 6). The solution was then passed through a Superdex 75 column (equilibrated in 50 mM MES, pH 6). Fractions containing LPMO were concentrated using a 10 kDa filter to the desired concentration.

### 2.1.3 *Ao*AA11

*Ao*AA11 LPMO was expressed in E. coli BL21* (DE3) competent cells. Overnight, 2 x 50 mL falcon tubes each containing 15 mL of LB medium were shaken at 180 rpm, 37 °C. 30 mL of the resulting suspension was evenly divided to inoculate 3 x 1000 mL LB cultures, the cell growth was continued at 37 °C, shaking at 180 rpm. When the absorbance at 600 nm reached 0.4, the temperature was lowered to 16 °C. When the absorbance at 600nm = 0.6 – 0.8, isopropyl βD-1-thiogalactopyranoside (IPTG) was added to a final concentration of 1 mM, and the cell culture was continued to be shaken at 180 rpm, 16 °C overnight. The cells were then harvested by centrifugation at 11,000 g for 20 min at 4 °C. The cell pellets were resuspended in three volumes (by mass) of ice-cold 50 mM Tris-HCl, 20 % w/v sucrose, pH 8. Lysozyme (40 µL of 10 mg $mL^{-1}$ for every gram of cell paste), benzenase, and DNAase-I (both to a final concentration of 1 µg/mL) were added to the suspension. The suspension was then stirred in an ice bath for one hour. A solution of $MgSO_4$ (60 µL, 1 M per gram of cell paste) was added to the suspension and then the suspension was stirred in an ice bath for a further 30 minutes. The suspension was then centrifuged at 10000 g for 20 min at 4 °C. The supernatant was decanted into a separate tube and the pellet was resuspended on ice-cold MilliQ water and stirred in an ice bath for one hour. The resulting suspension was centrifuged at 10000 g for 20 min at 4 °C, the supernatant was removed and added to the previously removed supernatant. The combined supernatant was sonicated in an ice bath to reduce viscosity with 20 s of sonication and 90 s of resting over 20 min. A sodium acetate solution (1 M, pH 5) was added until the supernatant reached pH 6. The resulting solution was then passed through a HiTrap SP HP 5 mL column, the flow through this was then filtered through a 0.2 µm syringe filter and then solid $(NH_4)_2SO_4$ was added to a final concentration on 1 M. The resulting solution was passed through a 5 mL phenyl sepharose HP column (equilibrated in 50 mM Na-acetate, 1 M $(NH_4)_2SO_4$, pH 5. Ammonium sulfate was then added to the flow through to make an 85% saturated solution, which was stirred for 30 min. The solution was then centrifuged at 38000 g for 45 min and the supernatant was discarded. The pellet was resuspended in ten volumes of buffer (20 mM Na−acetate, 250 mM NaCl, pH 5.0) and concentrated to a volume of 2 mL using a 10 kDa filter. The concentrate was then

copper-loaded by adding a $CuSO_4$ solution (1 M) to a final concentration of 5 mM. The copper-loaded solution was then loaded onto a HiLoad 16/60 Superdex 75 column (GE Healthcare) (equilibrated with 20 mM Na-acetate, 250 mM NaCl, pH 5). Fractions containing *Ao*AA11 were combined and concentrated using a 10 kDa filter.

### 2.1.4 *Bl*AA10

The synthesis and purification of BlLPMO10A used the method previously reported.[127]. For each incubation flask, a preculture was prepared with Pm/XylS_*Bl*AA10 containing BL21 cells in 5 mL LB medium with Ampicillin (100 µg/ mL). The preculture was incubated overnight at 30 °C, shaking at 220 rpm. The preculture was then added to autoclaved flasks of LB medium (500 mL) with Ampicillin (100 µg/ mL), before being incubated at 30 °C and shaken at 220 rpm until the absorbance at 600 nm reached 0.6-0.8. At this point, the flasks were incubated on ice for five minutes and then induced with *m*-Toluic acid (in ethanol) to a final concentration of 0.1 mM, before further incubating at 16 °C, shaking at 220 rpm overnight. The resulting culture was then harvested by centrifugation at 5000 g at 4 °C. The supernatant was discarded and the pellet was gently resuspended in 30 mL spheroplast buffer (100 mM Tris-HCl, 500 mM sucrose, 500 µM EDTA, pH 8.5 with a protease inhibitor). The resuspended cells were then incubated on ice for five minutes before undergoing gentrification at 6150 g at 4 °C. The supernatant was discarded, and the pellet was incubated at room temperature for ten minutes. The pellet was then gently resuspended in 25 mL of ice-cold MilliQ water with protease inhibitors before the addition of $MgCl_2$ solution (1.5 mL, 20 mM), and then centrifuged at 15000 g at 4 °C for 30 min. The supernatant was then filtered through a 0.2 µm syringe filter before being passed through a HiTrap DEAE FF column (equilibrated in 50 mM Tris-HCl, pH 8.5), with a 0 – 50 % gradient with the elution buffer (50 mM Tris-HCl, 1 M NaCl, pH 8.5) over 90 CV. The LPMO fractions were identified by SDS-PAGE and concentrated using a 10 kDa spin column. The purified LPMO was copper loaded by adding a 3-fold excess of $CuSO_4$ and incubating the solution at room temperature for 30 min before removing excess copper using a 10/300 SEC column equilibrated in 50 mM Tris-HCl, 200 mM NaCl, pH 7.5.

## 2.2 EPR measurements

X-band CW-EPR measurements were made on a BRUKER EMXmicro™ spectrometer. The parameters were set with a microwave frequency of *ca.* 9.3 GHz over a magnetic field range of 2300 – 3700 G, a modulation amplitude of 4 G, a modulation frequency of 931 kHz, and a microwave power of 10.02 mW. LPMO CW-EPR samples were prepared in quartz tubes with *ca.* 80 µL of sample, and measured at 150 K using a liquid nitrogen cryostat. Annealing experiments were

executed by placing the sample into a bath of the required temperature for 3 min before the sample was remeasured at 150 K. The resulting spectrum was the average of three scans. Simulation of CW-EPR spectra to obtain Hamiltonian parameters and normalisation was performed using EasySpin (v 5.2.28) in Matlab (R2023a). [128] The EPR simulations were produced using a heuristic fitting approach, whereby the *g* and A parameters were manually adjusted by using starting values typical of the system being fitted and altering until the simulated spectrum resembled the experimental spectrum. It is therefore acknowledged that the values given are not the only possible *g* and *A* values for the system and there is an unquantified uncertainty in these values.

## 2.3 X-ray Spectroscopy measurements

X-ray spectroscopy gives a spectrum which represents the average of all of the absorbing atom systems in the sample, therefore the fits of these data are representative of a population of LPMO copper ions which are likely to be in different vibrational/ rotational configurations.

### 2.3.1 Kα HERFD-XANES

Kα HERFD-XANES measurements were recorded on the I20-Scanning beamline at Diamond Light Source (UK), at the time of measuring the synchrotron was operating at 3 GeV ring energy, with a current of 300 mA (Figure 2.1).[124] The samples were frozen in pure aluminium sample holders with a thickness of 2 mm. Rapid freeze quenched samples were frozen directly onto pre-cooled sample holders. Cu(I) and Cu(II)LPMO samples were frozen by placing the liquid-filled (*ca*. 120 µL) sample holders onto a liquid nitrogen cooled metal block. LPMO samples with substrates were prepared by making a slurry with excess substrate and then the sample was frozen in the same way as the standard Cu(I) and Cu(II) LPMO samples. The samples were measured in a liquid helium cryostat at 10 K and with a 0.2 mm Al filter to attenuate the beam (*ca.* $1x10^{11}$ ph/s), to reduce the rate of photoreduction. Beam damage tests were carried out for each of the samples by measuring several spectra in the same sample position continuously and comparing changes that are observed over increased beam exposure, the results from these tests for each sample are reported in the results. The calculated dose per scan under these conditions is $2x10^5$ Gy. The I20-Scanning beamline is set up with an in-house designed four-bounce scanning Si(111) monochromator and two dedicated Rh-coated mirrors operating at 4.5 mrad incidence angle were used to reject higher harmonics.[123] The measurements used the X-ray emission spectrometer available in I20-Scanning, based on a 1 m diameter Rowland circle operating in the Johann configuration in the vertical plane.[129,130]

Using three 100 mm diameter Si(444) spherically bent analyser crystals, HERFD-XANES spectra were recorded utilising the Cu Kα1 emission line (8048 eV), which was recorded by a four element Medipix-Merlin photon-counting pixel detector.[131] The ionization chamber was filled with a mixture of He and Ar gases to absorb 20% of the X-ray beam; this was used as an incident intensity monitor. From the width of the elastic peaks measured, the energy resolution was measured to be 1 eV. Each scan was measured in a different sample position to mitigate photoreduction in a single sample position, each scan took *ca.* six minutes, with longer acquisition time and shorter step sizes being used in the pre-edge to edge region. The beam size at the sample was 400 µm (H) x 300 µm (V) FWHM. All the HERFD-XANES data collected underwent calibration, alignment, background removal and normalisation before the spectra measured on each sample were merged to improve the signal to noise ratio. All processing was performed with Athena (v 0.9.26), part of the Demeter software, following standard procedures.[132]

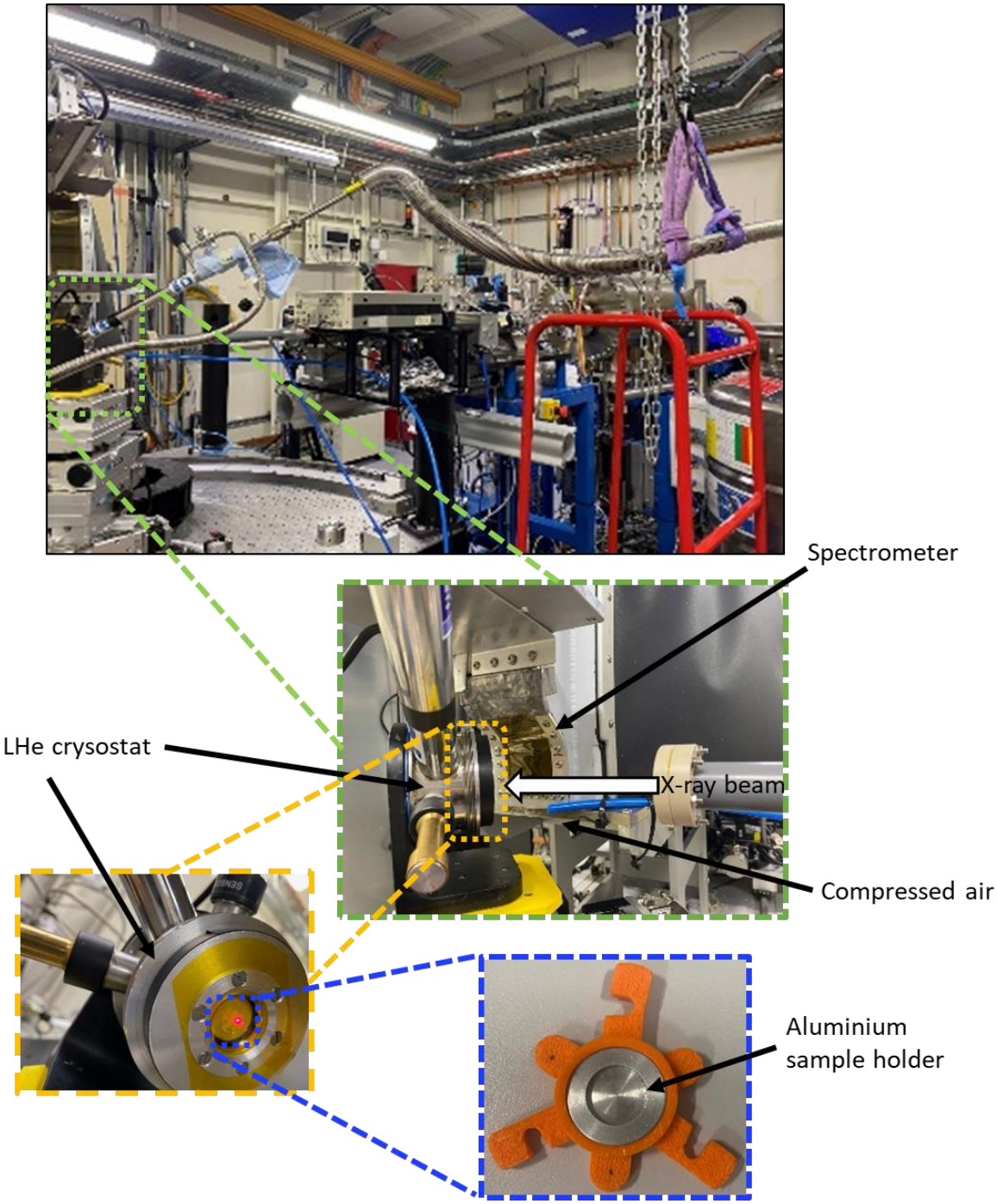


Figure 2.1: HERFD-XANES with a liquid helium cryostat set up in I20-Scanning at Diamond Light Source.

### 2.3.1 XAS

Conventional XAS spectra to obtain EXAFS and XANES of the LPMO samples were measured on the Core EXAFS beamline, B18, at Diamond Light Source (UK).[124] The samples were mounted in pure aluminium sample holders in a liquid helium cryostat in the same way as the HERFD-XANES measurements and the copper K-edge was measured *ca*. 8980 eV. The beamline was set up with a

Pt-coated branch of collimating, focusing mirrors, a Si(111) double crystal monochromator and a pair of Pt coated harmonic rejection mirrors. Spectra were acquired in quick-EXAFS mode at 10 K, using a 36-element solid state monolithic Ge fluorescence detector. As before, each scan was measured in a different sample position to mitigate radiation damage in a single sample position, with each scan taking *ca*. three minutes. Beam damage tests were carried out for each of the samples by measuring several spectra in the same sample position continuously and comparing changes that are observed over increased beam exposure, the results from these tests for each sample are reported in the results. The Cu(II) spectral regions that are particularly sensitive to beam damage are the 1s to 3d pre edge region, 1s to 3p rising edge transition, and the position/ intensity of the white line. The flux is $5x10^{11}$ ph/s, which means the calculated dose per scan is $6x10^{5}$ Gy. The beam-size at the sample was 1000 µm (H) x 1000 µm (V) FWHM. All data underwent calibration, alignment, background removal and normalisation before the spectra measured on each sample were merged to improve the signal to noise ratio. All XANES processing was performed with Athena (v 0.9.26) and all EXAFS processing and fitting was done in Artemis (v 0.9.26), both of which are part of the Demeter software. [132]

### 2.3.2 Data processing

For both the conventional XAS and HERFD-XANES data, the initial steps of data processing are the same. For each sample, the spectra were imported into Athena and any anomalous spectra were removed i.e. spectra that had a significantly lower signal-to-noise ratio or which contained Bragg peaks or glitches. The remaining spectra for each sample were then normalised and background subtracted to account for any differences in the sample thickness in the sample position each spectrum was collected in. To normalise the spectra $E_0$ is defined as the first maximum in the XAS derivative spectrum, and the pre-edge and post edge regions are chosen (Figure 2.2). The normalised spectra are then generated by subtracting the extrapolated pre-edge line from the entire sample and then diving through by the edge step. The normalised spectra for each sample were then averaged using the merging tool in Athena to produce a single normalised spectrum for each sample.

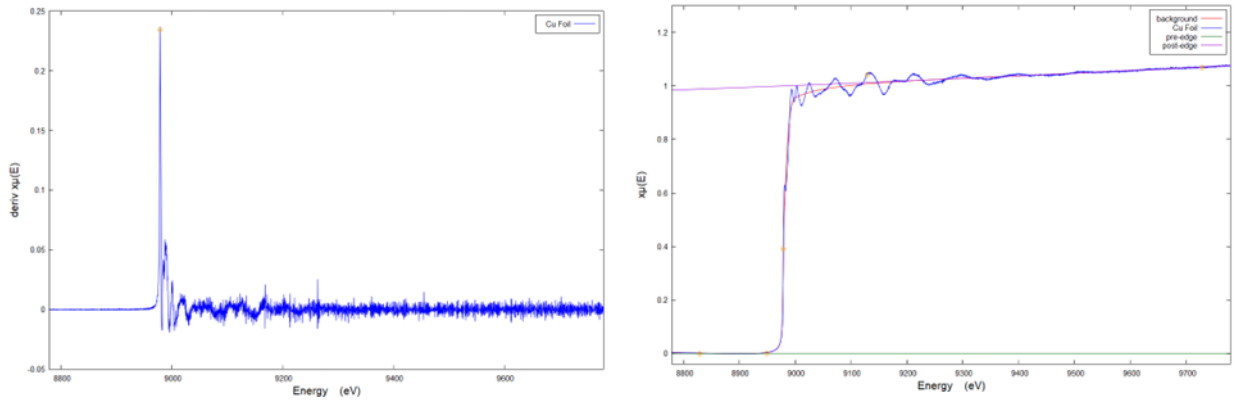


Figure 2.2: (Left) the first derivative of the XAS spectrum of a copper foil, with $E_0$ marked with a yellow circle. (Right) The XAS spectrum of a copper foil with the pre-edge, post-edge and background shown.

For the XAS spectra, the normalised spectrum for each sample was then imported into Artemis where EXAFS fitting could be undertaken. A file with the atomic coordinates either from experimental or simulated data can be imported into Artemis which is used to run a feff calculation to give the scattering pathways. Fits can then be generated using these scattering pathways along with parameters from the EXAFS equation such as N which is the degeneracy of the path, the amplitude reduction factor $S_0^2$, the path length ΔR, and the mean squared displacement $\sigma^2$. The fit is given for only a region of the data that is defined within a window (Figure 2.3)

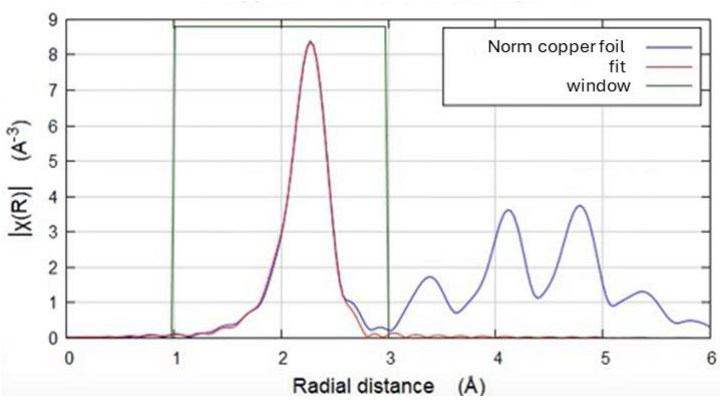


Figure 2.3: An EXAFS fit in Artemis for a copper foil.

Along with the fit Artemis will also give statistics to evaluate how good the fit is, such as a reduced Chi-squared value and a R-factor. The best fit values are also given and should be checked to make sure they are feasible to assess the validity of the fit to the experimental data.

# 3 LPMO substrate interactions

## 3.1 Introduction

This chapter details the spectroscopic investigation into the electronic and structural effects of substrate interaction in AA9, AA10 and AA11 LPMOs, to examine if there are differences between these genomic classes in the way they interact with substrates.

AA9, AA10 and AA11 were the first three genomic families to be classified as LPMOs, therefore there have been several studies pertaining to these three families which means they have well characterised crystal structures, providing a good starting point for spectroscopic interpretations (Figure 3.1). Although the structures of substrate bound AA9, AA10 and AA11 have been previously studied using techniques such as NMR, EPR and X-ray crystallography, to date there are no X-ray spectroscopy studies of the substrate interactions of these genomic classes of LPMOs. Whilst the histidine brace is conserved across the AA9, AA10 and AA11 LPMO active sites, these three genomic classes of LPMOs demonstrate differences in amino acid residues in the secondary coordination sphere of the copper active site (Figure 3.3). These three genomic classes of LPMOs also demonstrate differences in their combinations of substrate specificity and regioselectivity, but how the active site structure and substrate specificity/regioselectivity differences are correlated is largely unknown.

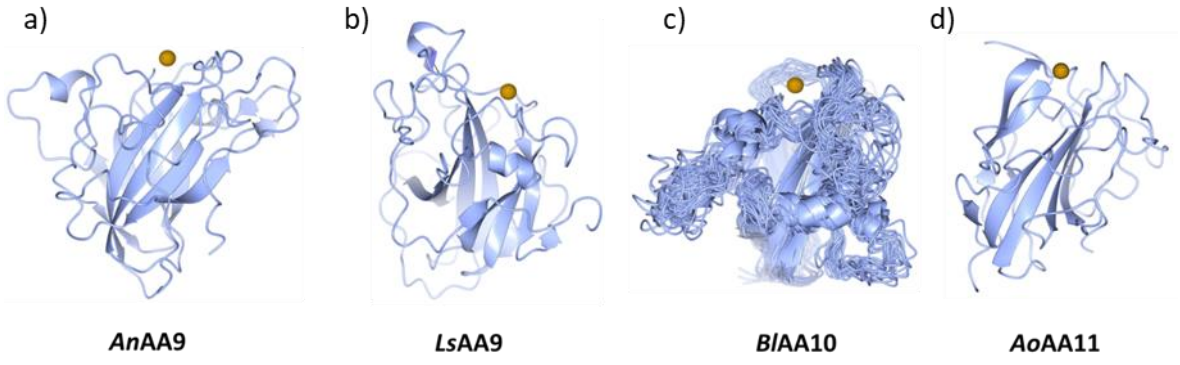


Figure 3.1: X-ray crystal structures of a) *An*AA9, b) *Ls*AA9 (PDB: 5NO4) and c) *Ao*AA11 (PDB: 4MAI) and an d) NMR structure of *Bl*AA10 (6TWE). All structures show the copper ion as a sphere.

AA9 LPMOs were previously classified (and have previously been referred to in the literature) as glycoside hydrolases (GH61).[8,133] AA9 LPMOs have been shown to oxidise the C1, C4 or C6 carbons of glycosidic rings and have activity on cellulose, hemicelluloses and oligosaccharides such as cello-oligos.[28,55,134,135] AA10 LPMOs were previously classified as carbohydrate binding modules (CBM33)

and have demonstrated reactivity with cellulose as well as α and β chitin, with most activity being in the form of C1 oxidation and some instances of C4 oxidation. [10,29,30,40,42,92] AA11 LPMOs are active on α and β chitin with primarily C1 oxidation.[45,64]

From crystal structures it is known that AA9 and AA10 both have relatively flat binding sites which has been suggested to be consistent with specificity for crystalline substrates. The AA9 active site is thought to interact with substrates through stacking with planar aromatic residues as it contains a conserved tyrosine aromatic amino acid and commonly contains other aromatic amino acids, several of these aromatic rings are almost parallel to the planar substrate interacting surface. Crystal structures of AA9 LPMOs soaked with substrates also show aromatic stacking interactions between the LPMO active site and the substrate (Figure 3.2). Whereas the lack of aromatic amino acid residues in the AA10 active site and presence of more hydrophilic amino acid residues suggests that substrate interaction occurs primarily through hydrogen bonding.[40,42,43,92,136] The H-bonding interaction proposed in AA10 LPMOs is consistent with the AA10 chitin activity as the acetamido group which replaces the hydroxyl group on the cellulose ring in chitin creates a more hydrophilic environment which is more favourable for polar interactions.

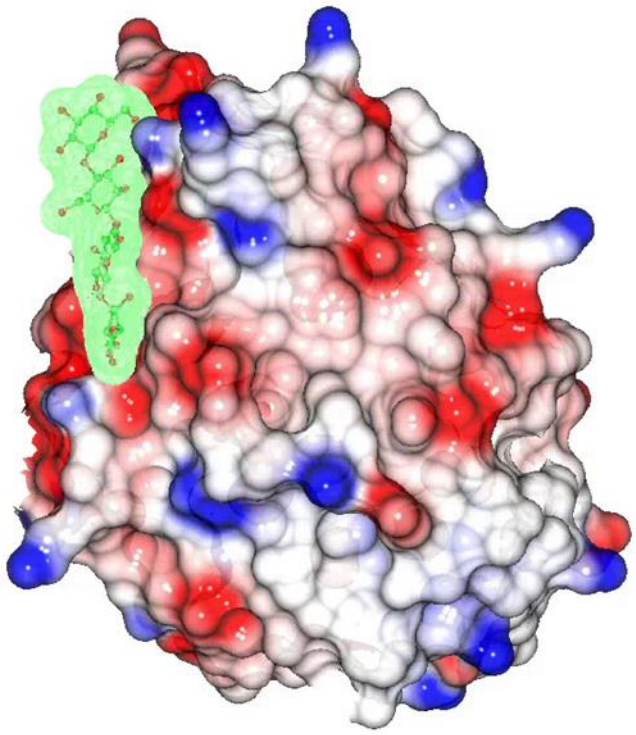

Figure 3.2: space filled crystal structure of *Cv*AA9 with $Cell_5$ substrate (PDB 6YDD).[137]

Crystal structures of AA11 LPMOs demonstrate little structural similarity to AA9 and AA10 and have more of a concave active site stricture (Figure 3.1).[33,92] Fewer aromatic amino acid residues in the AA11 active site suggest that AA11s also primarily interact with substrates through H-bonding, which is also consistent with AA11-chitin substrate activity.

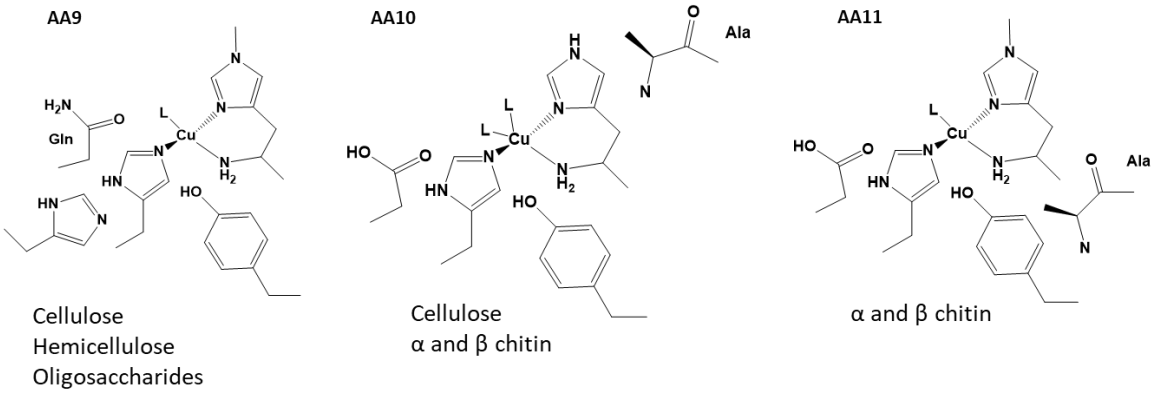


Figure 3.3: Active site structures and substrate specificity for AA9, AA10 and AA11 genomic classes of LPMOs.

The AA9 LPMOs used in this study are *An*AA9, from *Aspergillus nidulans*, and *Ls*AA9, from *Lentinus similis*. *An*AA9 has shown activity on cellulose in the form of phosphoric acid swollen cellulose (PASC) and xyloglucan, with C4 regioselectivity.[138] *Ls*AA9 has been found to have activity on PASC as well as soluble oligosachharides; cellotriose (G3) and cellohexaose (G6), all of which were cleaved with C4 regioselectivity.[54] The AA10 LPMO used in this investigation is *Bl*AA10, a bacterial LPMO from *Bacillus licheniformis*. *Bl*AA10 is active on β-chitin, with limited activity on α-chitin.[87] *Ao*AA11 is a bacterial LPMO from *Aspergillus oryzae* which demonstrates C1 and C4 cleavage.[64] The CBM is not included in any of the LPMOs used in this study as it is not included in the reported synthesis/ purification methods that were followed for the LPMO sample preparations. The CBM in LPMOs is thought to be non-catalytic and to have a non-conserved role in LPMOs.[70]

The following structural investigations into LPMO-substrate interactions were undertaken in a bid to gain insights into the initial step of the LPMO oxidative cleavage of polysaccharides mechanism.

## 3.2 Methods

### 3.2.1 Inductively coupled plasma mass spectrometry (ICP-MS)

To promote homogeneity in the samples, the solid substrates were ground in a pestle and mortar with ethanol (approximately 50 ml, HPLC grade, Thermofisher) and solvent removed *in vacuo* to produce a fine white powder.

To digest the chitin sample, chitin (26.4 mg) was suspended in 6.00 mL $HNO_3$ (70%, AR grade, Thermofisher) and 3.00 mL HCl (37%, AR grade, Thermofisher) in an acid washed digestion tube. For the digestion of the other substrate samples (approx. 50 mg), digestion blank (1.00 mL ultrapure water), and an interference check standard solution (1.00 mL 100 ppm CCS-6 standard supplied by Inorganic Ventures), were suspended in 3.00 mL $HNO_3$ (70%, AR grade, Thermofisher) and 1.50 mL HCl (37%, AR grade, Thermofisher) in separate tubes. Samples were digested by microwave-assisted acid digestion in an Anton Paar Microwave Go Plus system, ramp rate 12 °C $min^{-1}$, ultimate temperature 180 °C, dwell time 20 minutes. No solid residue was notable after digestion. The chitin sample was diluted with ultrapure water (Milli-Q® Type 1 Ultrapure Water System supplied by Merck) in a 50 mL volumetric flask. All other samples were diluted to 25 mL.

The samples were analysed with an Agilent ICP-OES 5800 VDV spectrometer, by comparison to commercial reference standard CCS-6 transition element standard for ICP-MS supplied by inorganic ventures, traceable to NIST certified reference materials. All standards were matrix matched to the digestion media. Samples were analysed with internal standard $^{89}Y$ (371.029 nm). All measurements were made in axial configuration, RF power 1.2 kW, plasma flow 12.0 L/min, nebuliser flow 0.70 L/min, auxiliary flow 1.00 L/min, sample read time 5 seconds.

### 3.2.2 LPMO-substrate X-ray spectroscopy samples

All LPMOs were produced and purified following the procedures described in section 2.1. The X-ray spectroscopy measurements and analysis were undertaken following the procedures in section 2.3.

XAS and HERFD-XANES samples were prepared by making a slurry with solutions of the LPMOs and their respective substrates before freezing in aluminium liquid helium cryostat holders. Cu(I) samples were prepared by adding stoichiometric quantities of ascorbate solution ($C_6H_7O_6Na$, 100 mM) before the addition of the substrate. The concentrations of the X-ray spectroscopy LPMO samples were as follows:

- HERFD-XANES of *An*AA9 was measured on 0.65 mM samples.
- XAS of *Ls*AA9 was measured on 0.8 mM samples.
- XAS and HERFD-XANES of *Bl*AA10 were measured on 0.8 mM samples.
- HERFD-XANES of *Ao*AA11 was measured of 0.8 mM samples.

### 3.2.3 LPMO-substrate EPR samples

EPR data collection and fitting was done following the procedure described in section 2.2.

## 3.3 Results and Discussion

### 3.3.1 Substrate metal content

The metal content of common LPMO substrates was investigated using XAS and ICP. The presence of metal impurities in LPMO substrates has the potential to skew reactivity studies by facilitating Fenton-like reactions[139] (Scheme 3.1), which would be detrimental as LPMO reactivity is often described as a Fenton-like reaction.[140–144] Furthermore, the presence of metal impurities in the substrates can result in additional signals in spectroscopic characterisations including in the XANES and EXAFS XAS regions, which may lead to incorrect conclusions on LPMO-substrate structures. Every effort is made to ensure a high purity of LPMO samples through several rounds of purification including by fractionation through various size exclusion and affinity columns. However, when investigating LPMO-substrate activity and structural interactions, a major part of the sample is the substrate which is often less rigorously tested for impurities.

Scheme 3.1

$$Fe^{2+} + H_2O_2 \rightarrow Fe^{3+} + HO\bullet + HO^-$$

$$Fe^{3+} + H_2O_2 \rightarrow Fe^{2+} + HOO\bullet + H^+$$

$$2\ H_2O_2 \rightarrow HO\bullet + HOO\bullet + H_2O$$

LPMO substrates are particularly prone to metal contamination as their structures often contain chelating functional groups such as hydroxyl, amino, and carboxylic acid groups (Figure 3.4).[145] Substrates such as cellulose and chitin are such effective metal chelators that they have been studied for water purification applications.[145–147]

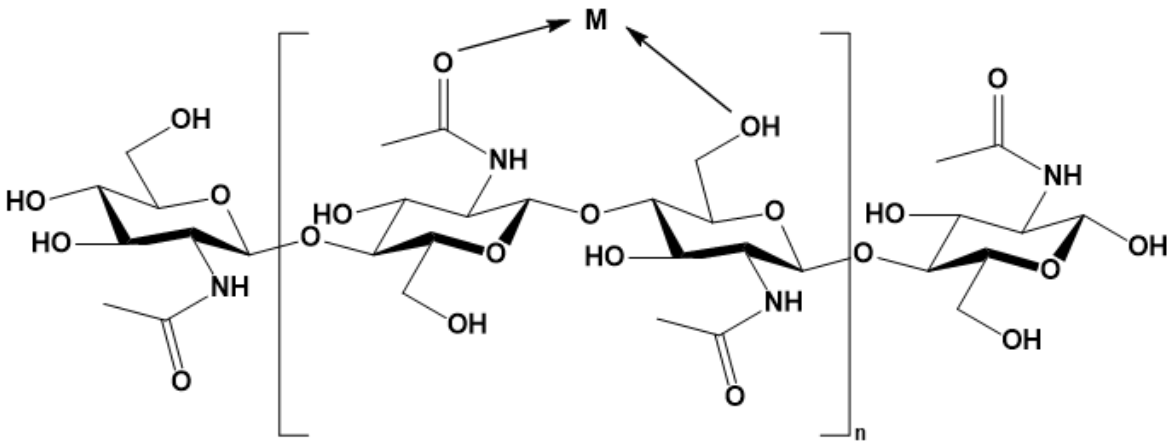


Figure 3.4: structure of potential metal chelating functional groups in chitin.[148]

LPMO substrate interactions

ICP results from several commonly used LPMO substrates; avicel, starch, pectin, xylan, chitosan and chitin were used to determine the amount of metals in these substrates (Table 3.1). The main metal contaminant of concern for LPMO studies is copper, as a copper contaminant would interfere with element selective spectroscopic techniques used to study the LPMO copper active site. ICP suggests that there is trace or less copper contamination in all of the LPMO substrates that were tested, which means we can be confident in the assignment of copper signals in our spectroscopy results.

Another metal of concern is iron because of its ability to perform Fenton reactions. ICP results show that there is a significant amount of iron contamination in the LPMO substrate samples tested, particularly in chitosan and chitin. The use of an iron catalyst to produce oxidative hydroxyl radicals and hydroperoxyl radicals through a Fenton reaction has been shown to promote LPMO oxidative activity on polysaccharides. Therefore, care must be taken when conducting and interpreting LPMO activity assays with these substrates.[140]

Zinc contamination must be taken into consideration when looking at the EXAFS region of LPMO-substrate samples as the zinc K-edge is at 9658.6 eV, which means that it can interfere with the copper EXAFS region which is *ca.* 9008.9 eV – 9978.9 eV. Out of the LPMO substrates tested, avicel, starch, pectin and xylan contained significant amounts of zinc.

Other metal contaminants such as chromium, mercury and manganese were also found in some of the LPMO substrates tested.

Table 3.1: ICP results for a range of LPMO substrates.

| Substrate | Co /ppm | Cr /ppm | Cu /ppm | Fe /ppm | Hg /ppm | Mn /ppm | Ni /ppm | Pb /ppm | Tl /ppm | V /ppm | Zn /ppm |
|---|---|---|---|---|---|---|---|---|---|---|---|
| **Avicel** | <LOD | Trace | <LOD | Trace | **18.09** | <LOD | <LOD | <LOD | <LOD | <LOD | **4.40** |
| **Starch** | <LOD | <LOD | <LOD | **2.07** | <LOD | **0.59** | <LOD | <LOD | <LOD | <LOD | **2.79** |
| **Pectin** | <LOD | Trace | Trace | **26.90** | <LOD | **4.62** | <LOD | <LOD | <LOD | <LOD | **6.45** |
| **Xylan** | <LOD | Trace | Trace | **66.92** | <LOD | **24.05** | <LOD | <LOD | <LOD | <LOD | **47.64** |
| **Chitosan** | Trace | **9.21** | <LOD | **166.13** | <LOD | **1.78** | Trace | <LOD | <LOD | <LOD | Trace |
| **Chitin** | <LOD | **7.79** | <LOD | **163.08** | **57.53** | Trace | Trace | <LOD | <LOD | <LOD | Trace |
| **Check std 4 ppm CCS6** | 3.90 | 3.87 | 3.87 | 3.88 | 3.91 | 3.92 | 3.92 | 3.92 | 3.75 | 3.92 | 3.88 |
| **Check std %** | 97 | 97 | 97 | 97 | 98 | 98 | 98 | 98 | 94 | 98 | 97 |

To investigate the nature of the metal contaminants found by ICP in the LPMO substrates, pellets of the substrates were measured by XAS at the zinc K-edge (9658.6 eV) and the iron K-edge (7112.0 eV). The zinc K-edge spectra of avicel, starch, xylan and pectin all have the same edge position of *ca*. 9664 eV and have spectral shapes consistent with a Zn(II) oxidation state (Figure 3.5). The spectral features of avicel and starch are very similar with a post-edge shoulder at 9675.9(3) eV, which differs from the zinc K-edge spectrum of xylan which has a post edge shoulder at 9684.6(3) eV. Due to the low signal to noise ratio it is more difficult to discern the features for the zinc K-edge for pectin. From the zinc K-edge it can be concluded that the zinc contaminant in avicel and starch are chemically similar and differ from the zinc contaminant in xylan.

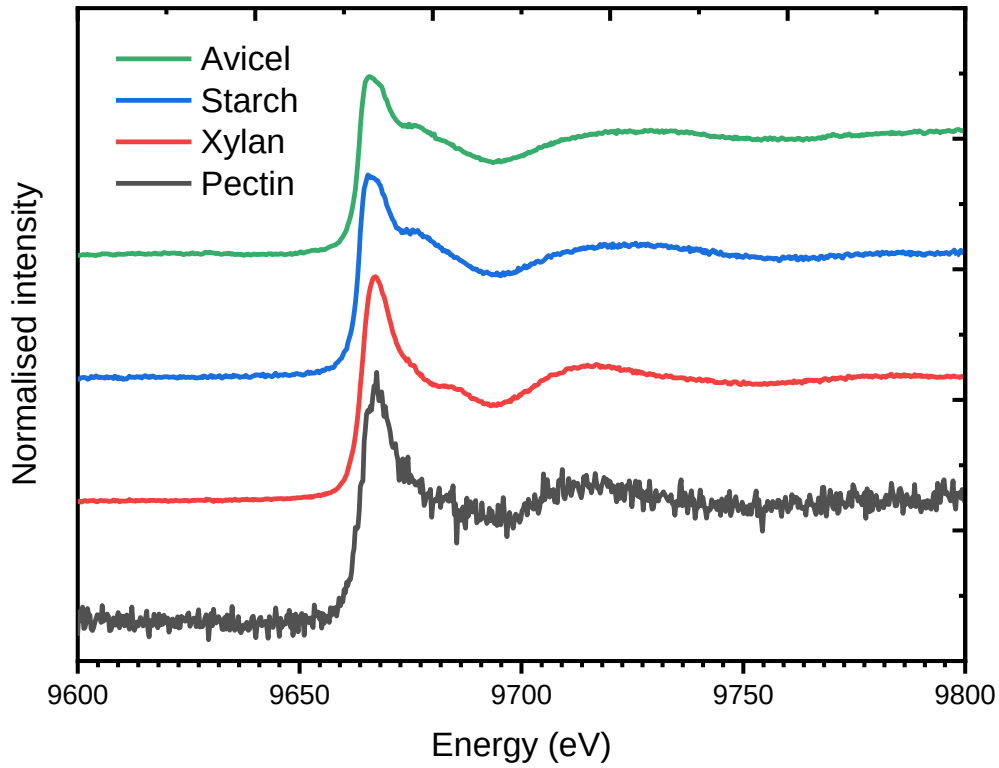


Figure 3.5: XANES region from the normalised zinc K-edge XAS spectrum from pellets of avicel (green), starch (blue), xylan (red) and pectin (black), plotted with a y-offset.

The iron K-edge positions of chitin and pectin are 7122 eV and have similar spectral shapes, with both iron K-edges showing a shoulder at 7113.4(3) eV (Figure 3.6). The iron K-edge positions of chitosan and xylan are both 7124 eV, suggesting the iron present in chitosan and xylan is of a higher oxidation state than the iron in chitin and pectin. The iron K-edge of chitosan and xylan also have similar spectral shapes to each other with both having weak rising edge shoulders at 7112.9(3) eV.

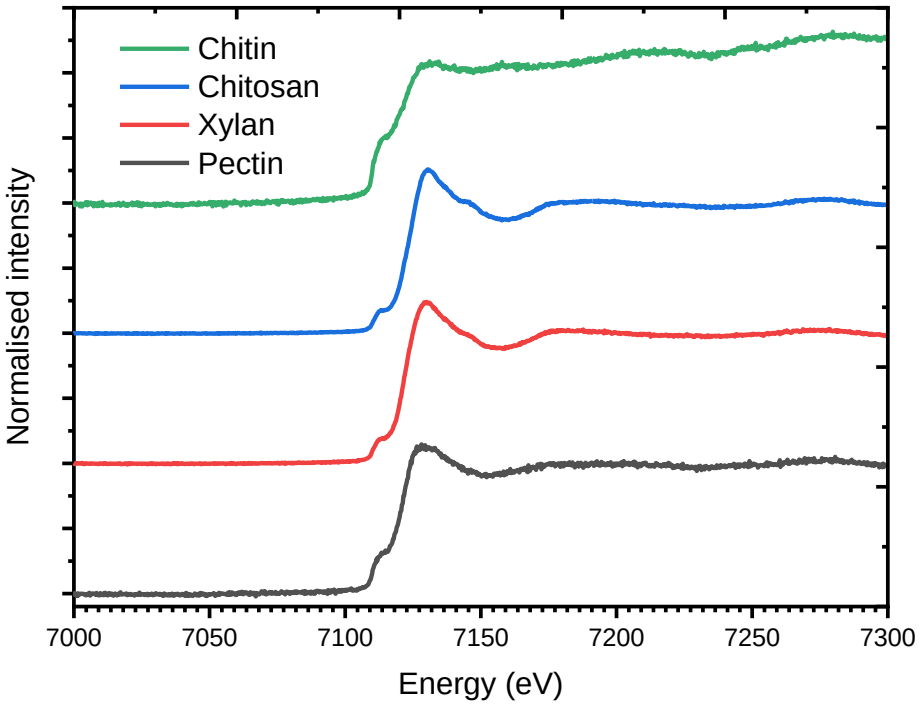


Figure 3.6: XANES region from the normalised iron K-edge XAS spectrum from pellets of chitin (green), chitosan (blue), xylan (red) and pectin (black), plotted with a y-offset.

To gain further information on the metal contaminants in LPMO substrates iron and zinc standards should be measured to be able to assign the K-edge XAS spectra.

It has previously been shown that overtime the LPMO substrate β-chitin becomes contaminated with copper which has significant impacts on LPMO activity assays.[149] The ICP and XAS results described in this section show that other metal contaminants could be present in common LPMO substrates, most concerningly iron which could result it Fenton reactions which skew the results of activity assays and also zinc which can impact spectroscopic measurements of LPMO-substrate interactions.

### 3.3.2 *An*AA9 with PASC

A combination of EPR and copper K-edge HERFD-XANES was used to investigate how PASC interacts with *An*AA9 in the Cu(I) and Cu(II) oxidation states.

#### *3.3.2.1 HERFD-XANES of Cu(II) AnAA9 with PASC*

As Cu(II) LPMOs are known from single-crystal X-ray diffraction studies to be prone to photoreduction, preliminary photoreduction checks by measuring several HERFD-XANES spectra in

the same sample position were undertaken to decide on the suitable level of attenuation of the X-ray beam (Figure 3.7).[62,150] It was decided that a 0.2 mm Al filter and scan time of 250 s gave a suitable signal to noise ratio whilst sufficiently minimising the rate of photoreduction. Photoreduction effects are observed at 8983.0(3) eV therefore care must be taken in the interpretation of this region. To reduce the influence of photoreduction on the interpretation of the experimental results several scans were collected with the Al filter attenuating the beam and were averaged to improve the signal to noise ratio through the central limit theorem. , and each was measured in a different point in the sample.

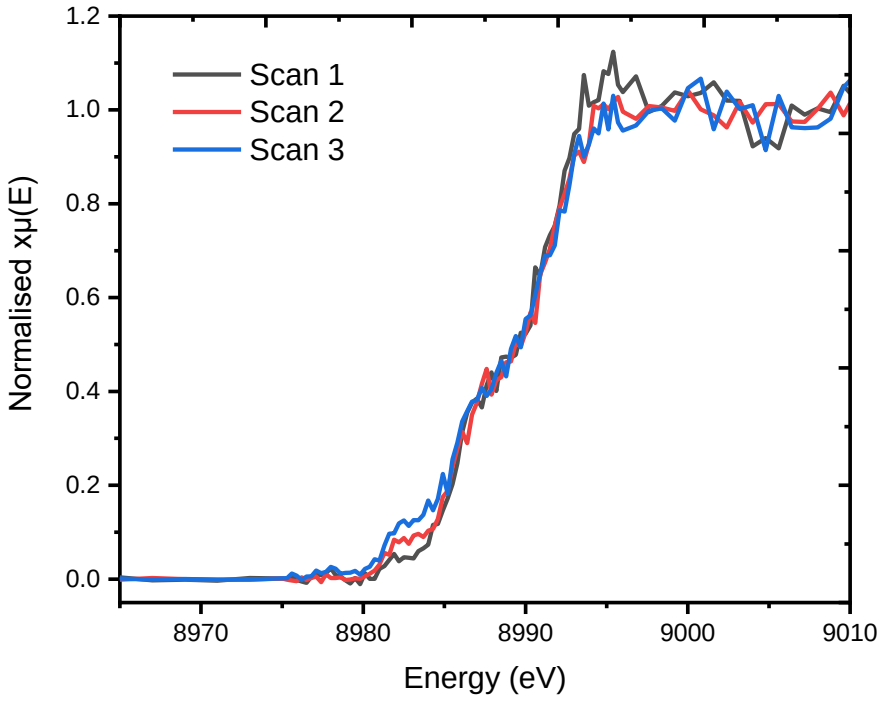


Figure 3.7: HERFD-XANES spectra of three consecutive scans in the same sample position to test for photoreduction under the experimental conditions with an attenuated beam (as detailed in section 2.3.1).

The copper K-edge HERFD-XANES spectra of Cu(II) *An*AA9 displays the characteristic features of a Cu(II) species. At 8977.7(3) eV there is a weak peak consistent with a Cu(II) 1s to $3d(x^2\text{-}y^2)$ dipole disallowed, quadrupole allowed transition and an edge position of 8985.8(3) eV.[1,117,151] The copper K-edge HERFD-XANES spectrum of Cu(II) *An*AA9 with and without PASC are superimposable and do not show any discernible peaks in the difference spectrum (Figure 3.8), which suggests that the addition of PASC does not afford any electronic or structural changes within the immediate vicinity of the Cu(II) ion in the *An*AA9 active site.

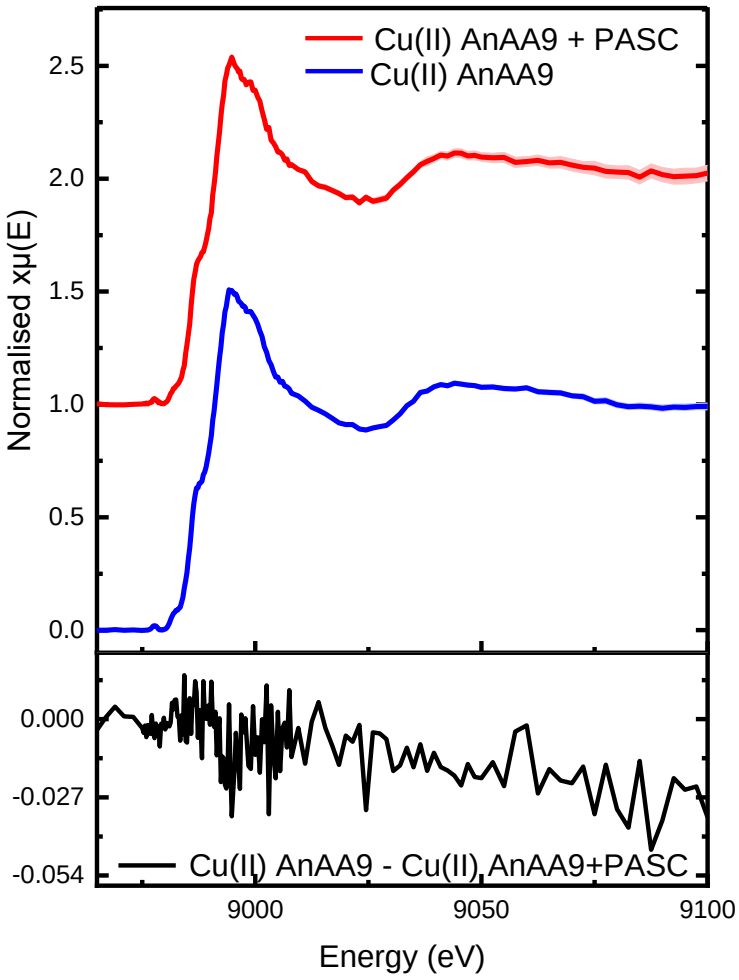


Figure 3.8: (top) HERFD-XANES K-edge of Cu(II) *An*AA9 (blue) and Cu(II) *An*AA9 with PASC (red), plotted with their respective standard deviations in their lighter colours with a y-offset, plotted within the spectral line. (bottom) difference spectrum of Cu(II) *An*AA9 minus Cu(II) *An*AA9 with PASC.

### *3.3.2.2 CW-EPR of Cu(II) AnAA9 with PASC*

The absence of change to the Cu(II) LPMO active site in *An*AA9 on the addition of PASC is corroborated in the EPR spectra of Cu(II) *An*AA9 with and without PASC, (data provided by Dr. Thamy Correa). The EPR spectrum of Cu(II) *An*AA9 does not show any significant change when PASC is added, which further supports the conclusions of the K-edge HERFD-XANES spectra that the presence of PASC does not result in electronic or geometric changes around the copper active site. The simulated spin-Hamiltonian parameters for both the EPR spectrum of Cu(II) *An*AA9 and Cu(II) *An*AA9 with PASC are the same (Figure 3.9, Table 3.2).

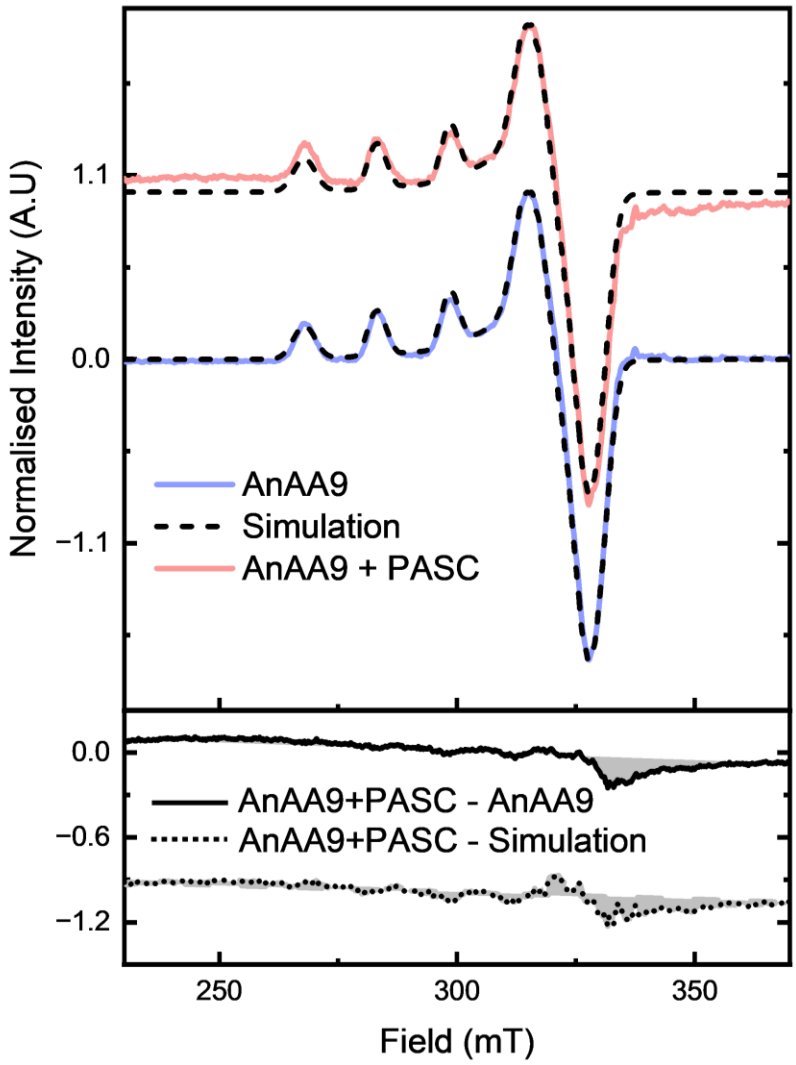


Figure 3.9: (top) Cu(II) EPR spectrum of AnAA9 in the presence and absence of PASC, plotted with simulated spectrum from EasySpin with y-offset. (bottom) Difference spectrum of Cu(II) AnAA9 with and without PASC.

Table 3.2: Hamiltonian parameters from the simulation of the EPR spectra of Cu(II) AnAA9 with and without PASC. A values given in MHz.

| | **Cu(II) *An*AA9** | **Cu(II) *An*AA9+PASC** |
|---|---|---|
| $\boldsymbol{g_{x,y,z}}$ | 2.048, 2.080, 2.284 | 2.048, 2.080, 2.284 |
| $\boldsymbol{\lvert A_{x,y,z}\rvert}$ | 70, 63, 480 | 70, 63, 480 |

The spin-Hamiltonian parameters from the simulation of the Cu(II) *An*AA9 EPR spectra are indicative of a structure in which $g_x < g_y << g_z$, this condition is met when there is a variation from four fold

axial symmetry to a structure more synonymous with a $D_{2h}$ point group symmetry. The non-equivalence of $g_x$ and $g_y$ arises from mixing of $d_z^2$ and $d(x^2\text{-}y^2)$ wavefunctions because of the reduction in axial symmetry, as governed by the equations below. ζ represents the one-electron quasi-atomic copper spin-orbit coupling constant, $k_n$ is the orbital reduction factor, and $b$ is the orbital coefficient for the $d_z^2$ wavefunction which mixes into the $d(x^2\text{-}y^2)$ wavefunction as a result of the reduction in axial symmetry. Due to their sensitivity to changes in $b$, changes are observed to the $g_x$ and $g_y$ spin-Hamiltonian parameter when there are changes in $d_z^2$ mixing but are not observed in $g_z$.

$$g_x = g_e + \frac{2\zeta k_x \left(a - \sqrt{3b}\right)^2}{E_{d_{x^2-y^2}} - E_{d_{yz}}}$$

$$g_y = g_e + \frac{2\zeta k_y \left(a - \sqrt{3b}\right)^2}{E_{d_{x^2-y^2}} - E_{d_{xz}}}$$

$$g_z = g_e + \frac{8\zeta k_z \ a^2}{E_{d_{x^2-y^2}} - E_{xy}}$$

These EPR traits are commonly observed in Cu(II) LPMOs and are consistent with a Type II classification. EPR also confirms the successful copper loading of Cu(II) *An*AA9 and shows only a single copper signal in the sample which means there is not a significant amount of free copper in the sample which would skew spectroscopic measurements.

#### *3.3.2.3 HERFD-XANES OF Cu(I) AnAA9 with PASC*

HERFD-XANES of the copper K-edge of Cu(I) *An*AA9 shows a rising edge peak at 8982.2(3) eV attributed to a 1s to $4p_z$ transition and an edge position at lower energy relative to the Cu(II) *An*AA9 spectra at 8981.2(3) eV, both of these features are typical of a Cu(I) oxidation state (Figure 3.10).[117]

The inclusion of PASC to Cu(I) *An*AA9 results in distinct spectral changes. The Cu(I) *An*AA9 with PASC spectrum also has an edge position of 8981.3(3) eV, confirming the Cu(I) oxidation state. However, the 1s to *4p* transition appears at slightly higher energy relative to that of Cu(I) *An*AA9 in the absence of substrate at 8982.4(3) eV. The addition of PASC to Cu(I) *An*AA9 also results in an increase in the intensity of the 1s to *4p* transition. Furthermore, the intensity of the white line is reduced in the Cu(I) *An*AA9 with PASC sample relative to that of the Cu(I) *An*AA9 sample (Figure 3.10).

A previously reported crystallographic study of AA9 LPMO-substrate interactions deposited PDB structures of Cu(I) *Ls*AA9 LPMO active site consisting of a T-shaped coordination geometry around the copper ion, from the histidine brace motif and an additional water ligand with 0.5 occupancy. Conversely, the Cu(I) *Ls*AA9 active site in the presence of G3 substrate showed a similar T-shaped histidine brace but with a notable absence of a water ligand (Figure 3.10).[54]

The crystal structures discussed formed the basis of our models for TD-DFT calculations of the XANES region. To simulate Cu(I) *An*AA9 in the absence of substrate a combination of models **1** and **2** (Figure 3.10) in equal weighting were used. For the model of Cu(I) *An*AA9 in the presence of PASC model **2** was used. The simulated spectra show the same spectral trends as the experimental data; an intensity increase and a small shift to higher energy of the 1s to *4p* transition on the addition of PASC as well as a decrease in white line intensity.

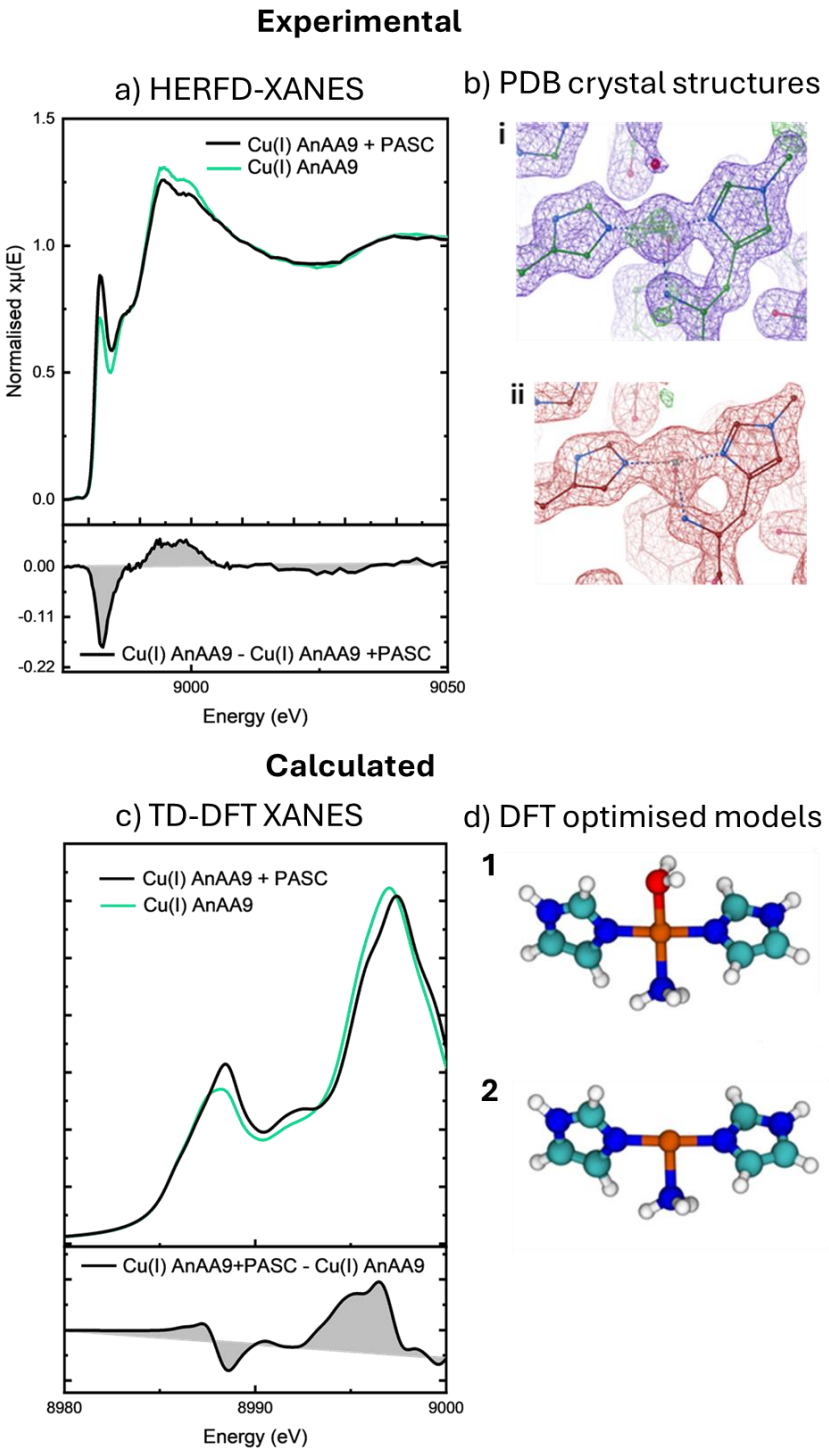


Figure 3.10: (*a*) experimental HERFD-XANES data of Cu(I) *An*AA9 with and without PASC and (b) TD-DFT modelled data from models **1** and **2** (c). (b) electron density contour plots from PDB deposited crystal structures of (i) Cu(I) AA9 LPMO active site in the absence of substrate (PDB 5ACH), and (ii) Cu(I) AA9 LPMO active site in the presence of G3 substrate (PDB 5ACJ) [54] and (d) DFT optimised models **1** and **2** used for the TD-DFT calculated spectra. A combination of models **1** (50 %) and **2** (50 %) were used to represent Cu(I) *An*AA9 and model **2** was used to represent Cu(I) *An*AA9 in the presence of PASC.

The assignment of the rising edge transition in the experimental data as a 1s to *4p* transition is corroborated in the TD-DFT calculated XANES spectra for models **1** and **2**, in which the oscillator with the greatest contribution to this peak corresponds to the *4p* orbital (Figure 3.11). The *4p* orbital in model **1** is more elongated indicating that the copper ion has more *p*-character than in model **2** which could explain the lower intensity of the 1s to *4p* associated peak in Cu(I) *An*AA9 in the absence of substrate.

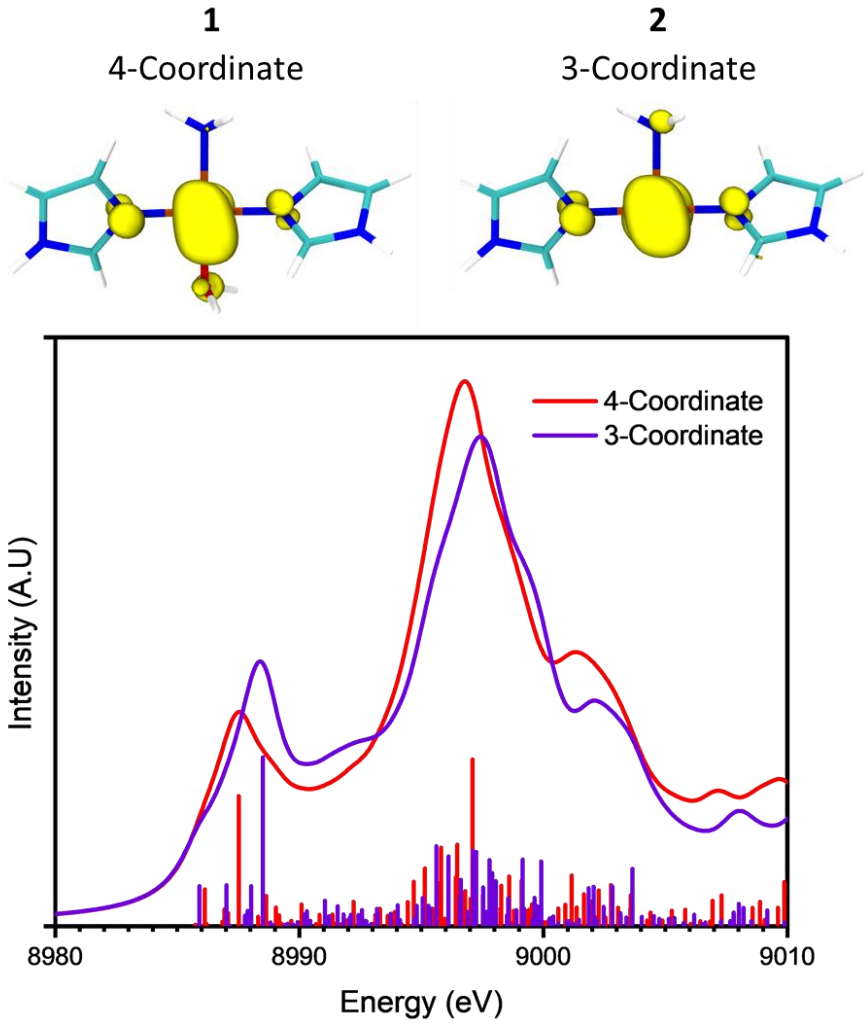


Figure 3.11: (Top) The copper *4p* orbitals for models **1** and **2**. The TD-DFT calculated XANES spectra for models **1** (4 coordinate) and **2** (3 coordinate) along with the oscillator contributions for the transitions used in the calculation.

#### *3.3.2.4 Summary*

HERFD-XANES and cw-EPR are in agreement that Cu(II) *An*AA9 does not undergo electronic or structural active site changes in the presence of PASC. However, in the Cu(I) oxidation state, HERFD-XANES and TD-DFT characterisation leads to the conclusion that on the addition of PASC, Cu(I) *An*AA9 changes from a T-shaped histidine brace with a 0.5 occupancy of water at the Cu(I) ion to the Cu(I) T-shaped histidine brace, through the loss of the 0.5 occupancy water ligand. The resulting loss of a ligand at the Cu(I) active site in the presence of substrate may spatially facilitate the interaction between the ligand and the copper active site, which is in agreement with Cu(I) being the active LPMO oxidation state.

### 3.3.3 *Ls*AA9 with cellohexaose

XAS was used to investigate the interaction of cellohexaose (G6) with *Ls*AA9 Y164F in both the Cu(I) and Cu(II) oxidation states. The *Ls*AA9 Y164F mutant was used for the following experiments. The Y164F mutation should not have a significant impact on substrate binding as this mutant has been shown to be active on cellohexaose but it should still be taken into consideration that the Y164F mutant is structurally different to the wild type.[125]

#### *3.3.3.1 XAS of Cu(II) LsAA9 Y164F with cellohexaose*

The photoreduction of Cu(II) *Ls*AA9 Y164F under the experimental conditions was checked by measuring several XAS spectra consecutively in the same sample position. After five consecutive scans in the same sample position there was no significant change in the XAS spectrum attributable to photoreduction (Figure 3.12). Based on the results of this photoreduction check it was decided that three XAS spectra could be recorded in each sample position confidently without incurring effects from photoreduction.

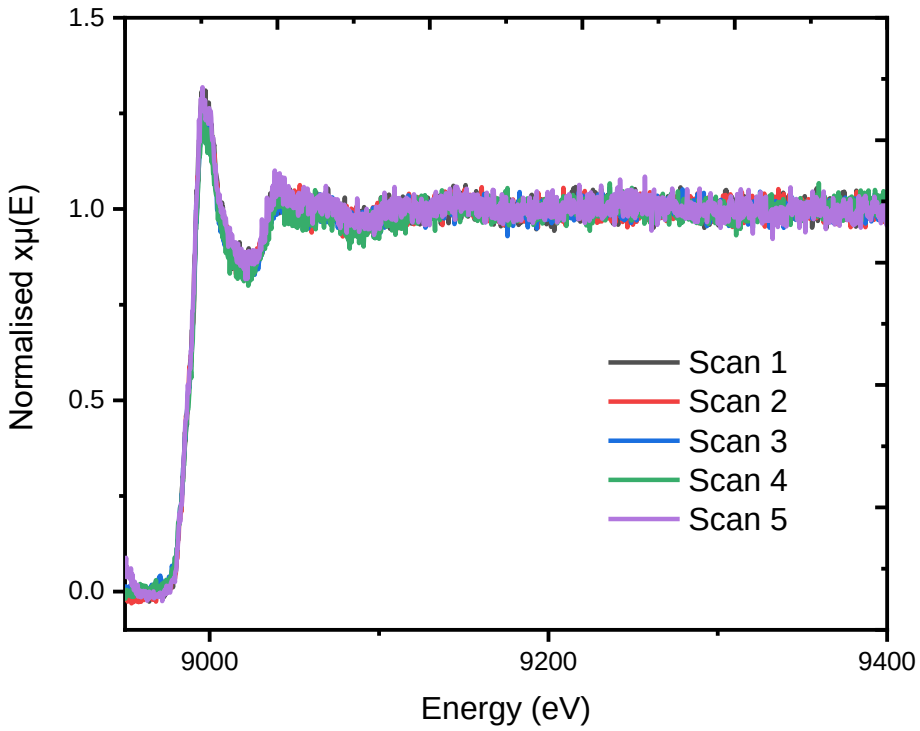


Figure 3.12: Five XAS spectra of Cu(II) *Ls*AA9 Y164F recorded consecutively in the same sample position.

The copper K-edge of Cu(II) *Ls*AA9 Y164F has the typical profile for a Cu(II) oxidation state with an edge position of 8990.4(3) eV and a slight shoulder at 8981.9(3) eV, consistent with a 1s to *4p* transition. The weak pre-edge peak associated with a 1s to *3d* transition in Cu(II) complexes is below the signal-to-noise level of these spectra. The addition of cellohexaose to Cu(II) *Ls*AA9 Y164F results in distinct changes to the copper K-edge XAS spectrum; there is an emergence of two shoulders in on the rising edge at 8981.9(3) eV and 8995.5(3) eV and a decrease in the white line intensity (Figure 3.13). The shoulder at 8981(3) eV is significantly more intense in Cu(II) *Ls*AA9 Y164F in the presence of cellohexaose. The edge position of Cu(II) *Ls*AA9 Y164F with cellohexaose is the same as that of Cu(II) *Ls*AA9 Y164F, confirming that the addition of substrate has not changed the oxidation state of the copper ion.

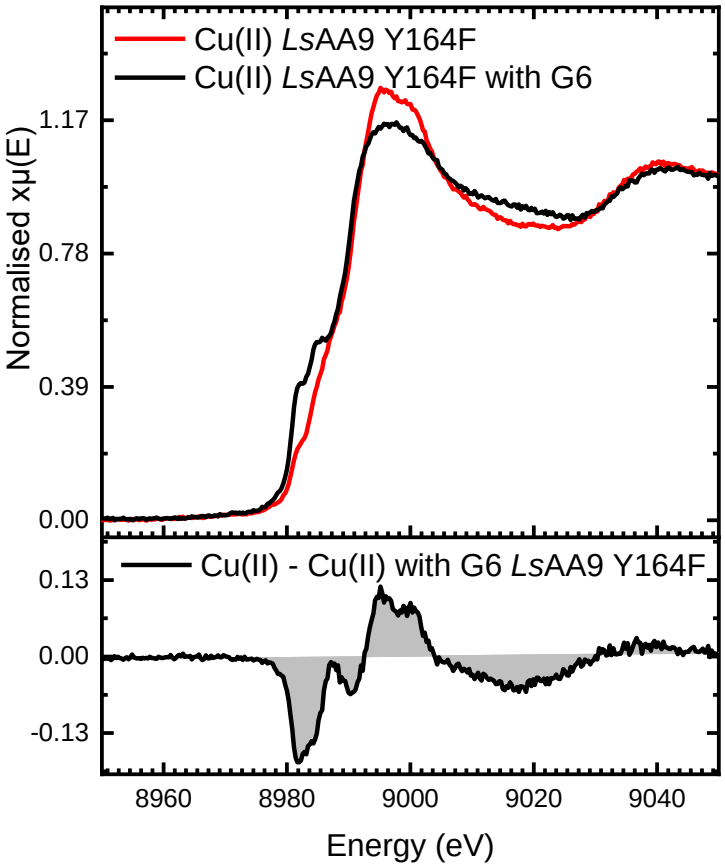


Figure 3.13: (top) copper K-edge XAS spectra of Cu(II) *Ls*AA9 Y164F (red) and Cu(II) *Ls*AA9 Y164F with cellohexaose (black). (Bottom) difference spectrum of Cu(II) *Ls*AA9 Y164F minus Cu(II) *Ls*AA9 Y164F with cellohaxaose.

The changes observed in the Cu(II) *Ls*AA9 Y164F copper K-edge XAS spectrum on addition of cellohexaose indicate that Cu(II) *Ls*AA9 Y164F undergoes a structural change in the presence of the substrate. A structural change in the Cu(II) LPMO oxidation state on the addition of substrate in *Ls*AA9 Y164F differs to the observations of Cu(II) *An*AA9 on the addition of PASC whereby there was no indication of a structural nor an electronic change. The increase in intensity of the peaks relating to 1s to *4p* transitions in the copper K-edge XAS spectrum on the addition of substrate follows the same pattern as that observed in Cu(I) *An*AA9 on the addition of PASC, which suggests that the presence of substrate results in a reduction in coordination number in Cu(II) *Ls*AA9 Y164F.

The EXAFS fit in R-space of Cu(II) *Ls*AA9 Y164F is consistent with a four coordinate Cu(II) structure with an average bond length of 1.89(3) Å, which most likely corresponds to three Cu-N bonds from the highly conserved histidine brace and an oxygen based ligand in the form of OH or $H_2O$ (Figure 4.23, Table 3.3). Conversely, the EXAFS fit in R-space of Cu(II) *Ls*AA9 Y164F with cellohexaose show

a three coordinate copper structure with an average Cu-N bond length of 1.95(5) Å, which would be consistent with a copper ion bound to a histidine brace (Figure 3.14, table 3.3).

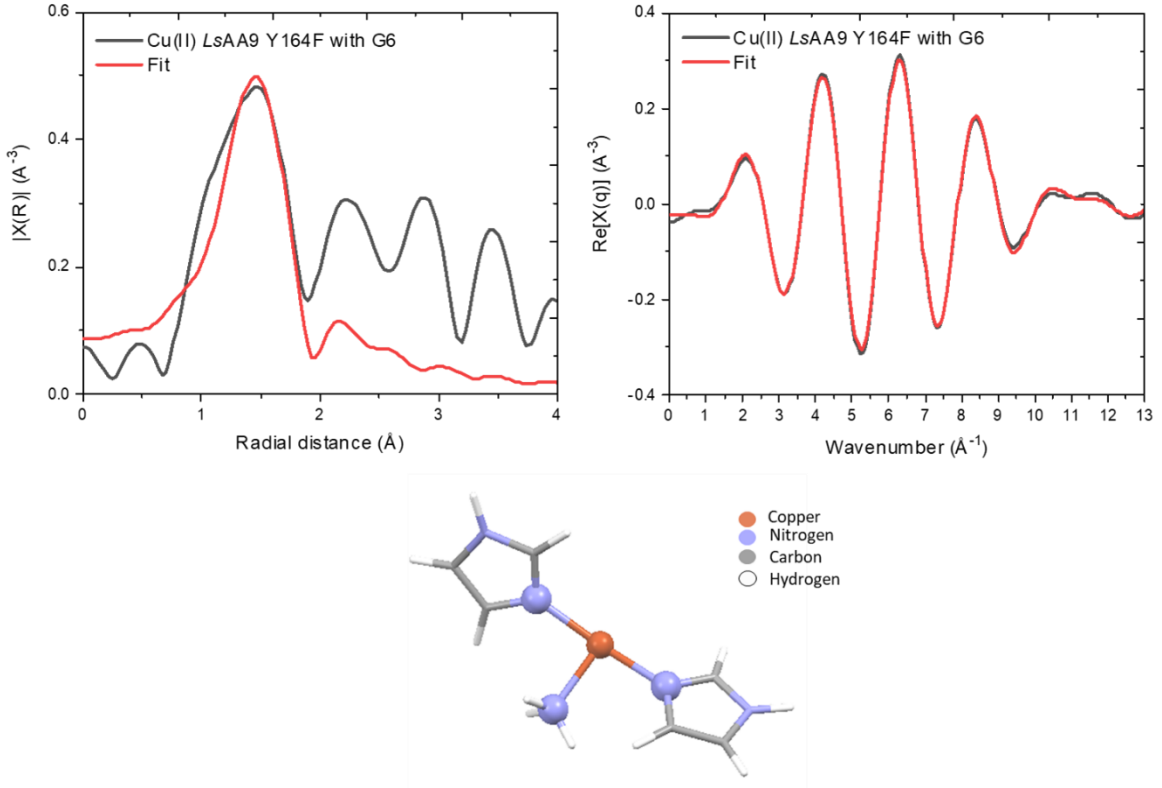


Figure 3.14: Copper K-edge magnitude of the Fourier transform from the extracted EXAFS signal for Cu(II) *Ls*AA9 Y164F with cellohexaose (k-range 3.4 – 10.4 $Å^{-1}$) (top *left*), q-space (R-range 1.15 – 1.90 Å) (*top right*) and the model used in the fitting (*bottom*). Experimental data is plotted in black and the corresponding fit is plotted in red, the fits were performed in R-space using the parameters in Table 3.2. The atoms used in the fit are represented as ball and stick.

Table 3.3: Best fit parameters obtained from the EXAFS fits of Cu(II) LsAA9 Y164F with and without G6. The $S_0^2$ value was fixed to 0.902.

| | **N and path** | **R-space fitting range** | **R / Å** | **$\sigma^2$ / $Å^2$** | **$\Delta E_0$ / eV** |
|---|---|---|---|---|---|
| **Cu(II) *Ls*AA9 Y164F** | 4 Cu-N/O | 1.16 – 2.00 Å | 1.89±0.03 | 0.009±0.001 | -11±5 |
| **Cu(II) *Ls*AA9 Y164F with G6** | 3 Cu-N | 1.15 – 1.90 Å | 1.95±0.05 | 0.007±0.003 | -4±8 |

The loss of a ligand on the addition of substrate in the R-space EXAFS fit of Cu(II) *Ls*AA9 Y164F coincides with the inference that the increase in 1s to *4p* transition intensity in the copper K-edge XANES region is attributable to a decrease in coordination number. The finding that cellohexaose induces a structural change to the Cu(II) *Ls*AA9 active site from this XAS (albeit in the Y164F mutant) is also consistent with a previously reported EPR study of Cu(II) *Ls*AA9 in the presence of cellohexaose which found that the addition of cellohexaose resulted in perturbations in the spin-Hamiltonian parameters and super hyperfine coupling, however the changes in the spin-Hamiltonian parameters were consistent with a change in geometry rather than a change in coordination number.[54] Whilst a change in the copper coordination number from four to three on the addition of G6 to *Ls*AA9 is in contradiction to the 4-coordinate structure characterised by Frandsen *et al.*, a reasonable fit could not be obtained with a four coordinate structure for the EXAFS data presented here. This discrepancy may have arisen due experimental differences such as the Y164F mutation, radiation damage or different incubation times.

#### *3.3.3.2 XAS of Cu(I) LsAA9 Y164F with cellohexaose*

The copper K-edge spectrum of Cu(I) *Ls*AA9 Y164F demonstrates the typical features of a Cu(I) spectrum; an intense rising edge peak attributed to a 1s to *4p* transition at 8982.4(3) eV and an edge position of 8981.4(3) eV. The addition of cellohexaose to Cu(I) *Ls*AA9 Y164F results in an increase in the intensity of the rising edge peak at 8982.4(3) eV, as well as a small increase in the white line intensity. The edge position does not change on addition of cellohexaose to Cu(I) *Ls*AA9 Y164F (Figure 3.15).

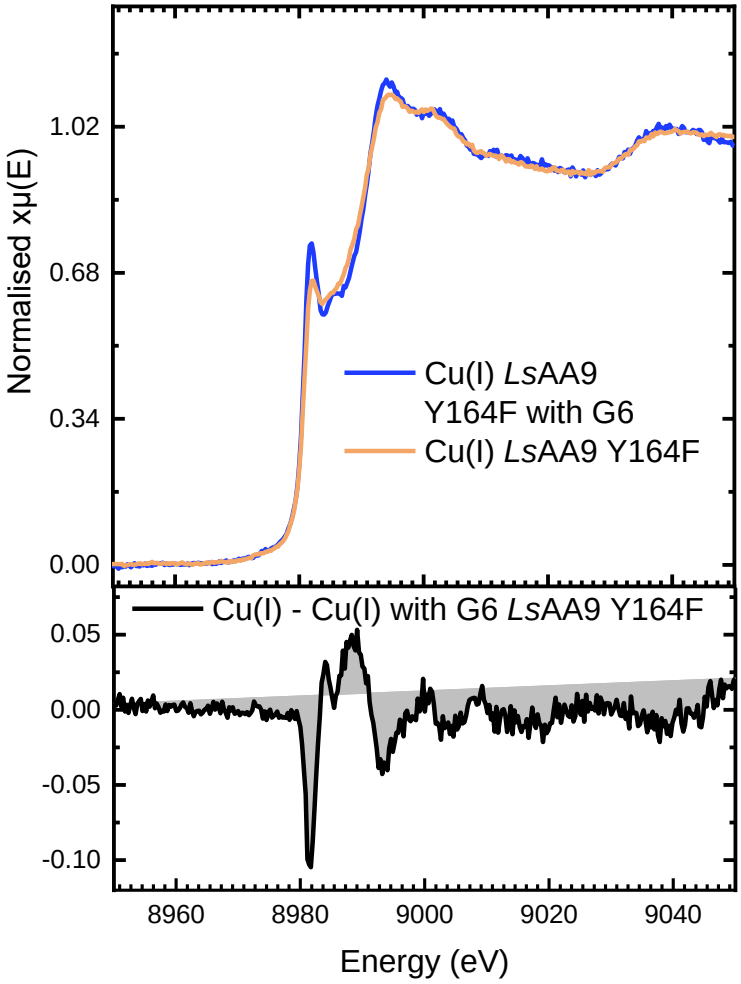


Figure 3.15: (top) copper K-edge XAS spectra of Cu(I) *Ls*AA9 Y164F (orange) and Cu(I) *Ls*AA9 Y164F with cellohexaose (blue). (Bottom) the difference spectrum of Cu(I) *Ls*AA9 Y164F minus Cu(I) *Ls*AA9 Y164F with cellohexaose.

The EXAFS fit in R-space of Cu(I) *Ls*AA9 Y164F shows a structure consistent with a copper ion bound to three nitrogen atoms with an average bond length of 1.93(3) Å (Figure 4.22, Table 3.4). The EXAFS fit in R-space for Cu(I) *Ls*AA9 Y164F with cellohexaose also shows a three coordinate Cu-N structure consistent with a copper coordinated histidine brace (Figure 3.16, Table 3.4). The average Cu-N bond length is marginally shorter in the fit of Cu(I) *Ls*AA9 Y164F with cellohexaose than in the absence of substrate (1.93±0.03 Å compared to 1.86±0.07 Å), but otherwise the EXAFS signal of *Ls*AA9 Y164F in the absence and presence of cellohexaose is very similar. It should be noted that the model used for the EXAFS fit does not include a methylated histidine residue, this is because the *E. coli* heterologous overexpression system used to express *Ls*AA9 results in non-methylated histidine in the histidine brace motif.

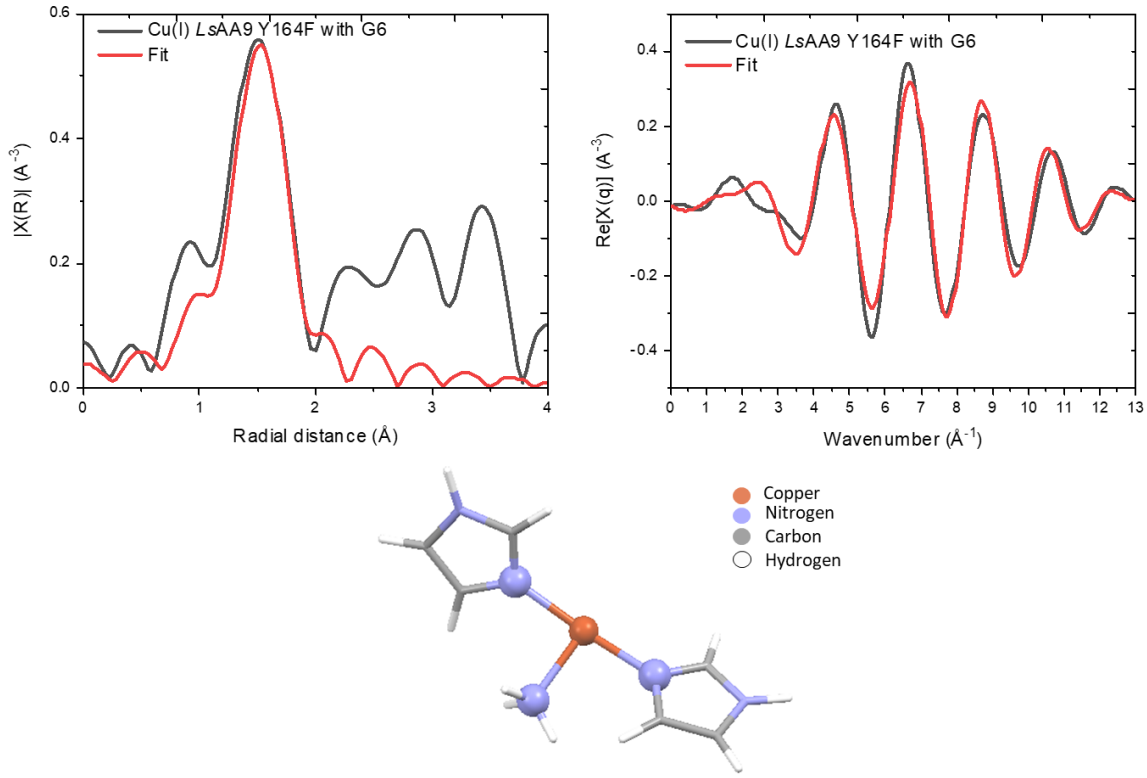


Figure 3.16: Copper K-edge magnitude of the Fourier transform from the extracted EXAFS signal for Cu(I) *Ls*AA9 Y164F with cellohexaose (k-range 3.4 – 11.3 $Å^{-1}$) (top *left*), q-space (R-range 1.15 – 1.90 Å) (*top right*) and the model used in the fitting (*bottom*). Experimental data is plotted in black and the corresponding fit is plotted in red. The fits were performed in R-space using the parameters in Table 3.3. The atoms used in the fit are represented as ball and stick.

Table 3.4: Best fit parameters obtained from the EXAFS fits of Cu(I) LsAA9 Y164F with and without G6. The $S_0^2$ value was fixed for both to 0.902.

| | **N and path** | **R-space fitting range** | **R / Å** | **$\sigma^2$ / $Å^2$** | **$\Delta E_0$ / eV** |
|---|---|---|---|---|---|
| **Cu(I) *Ls*AA9 Y164F** | 3 Cu-N | 1.01 – 1.87 Å | 1.93±0.03 | 0.008±0.002 | -5±4 |
| **Cu(I) *Ls*AA9 Y164F with G6** | 3 Cu-N | 1.00 – 2.20 Å | 1.86±0.07 | 0.006±0.004 | -10±13 |

The increase in intensity of the 1s to *4p* rising edge transition in Cu(I) *Ls*AA9 Y164F with cellohexaose is an observation which has been made in both the addition of PASC to Cu(I) *An*AA9 and the addition of cellohexaose to Cu(II) *Ls*AA9 Y164F. In the latter cases the increase in 1s to *4p* intensity has been attributable to a decrease in coordination number, but as the EXAFS fit in R-space of Cu(I) *Ls*AA9

Y164F both with and without cellohexaose shows a three coordinate structure consistent with a copper bound histidine brace, it is not evident that a change in coordination number is attributable to the change in the XANES region. The small change in the average Cu-N bond length from the EXAFS fits of *Ls*AA9 Y164F with and without cellohexaose is not significant enough to bring about the significant increase in the 1s to *4p* transition in the XANES region. As we have ruled out a change in coordination number and changes in bond length, it stands to reason that the changes observed on substrate addition in the Cu(I) *Ls*AA9 Y164F XANES region result from either a change in geometry at the copper active site or a change to the ligands effecting the metal-ligand covalency.

The intensity of the transitions measured in the XANES region is correlated with the probability of the transition occurring, an electronic transition has a higher probability of occurring if it is "allowed", that is to say that it satisfies the selection rules. In a copper ion with a trigonal planar geometry with $C_{2v}$ symmetry there is no *s*-*p* mixing and the $4p_z$ orbital is non-bonding and localised on the copper ion, which means that the 1s to $4p_z$ transition involves a change in parity and therefore fulfils the symmetry selection rule resulting in an intense rising edge peak in the copper K-edge XANES spectrum (Figure 3.17). A distortion in the trigonal planar geometry towards a trigonal pyramidal geometry with $C_{3v}$ symmetry whereby the copper ion is out of the plane of the three nitrogen ligands of the histidine brace causes the 4s and $4p_z$ orbitals to belong to the same $A_1$ representation. The subsequent *s*-*p* mixing results in a bonding orbital with *s* and $p_z$ character which is lower in energy than the $4p_z$ orbital, thus the 1*s* to *4p* transition becomes less probable as the transition becomes Laporte forbidden, which experimentally translates to a weaker rising edge transition in the copper K-edge absorption spectrum.[152] The ligand field diagram in Figure 3.17 also predicts a small change in energy between the two symmetry configurations, however this was not observed spectroscopically. It also cannot be ruled out that the changes observed in the 1s to *4p* transition are influenced by changes in the metal-ligand covalency.

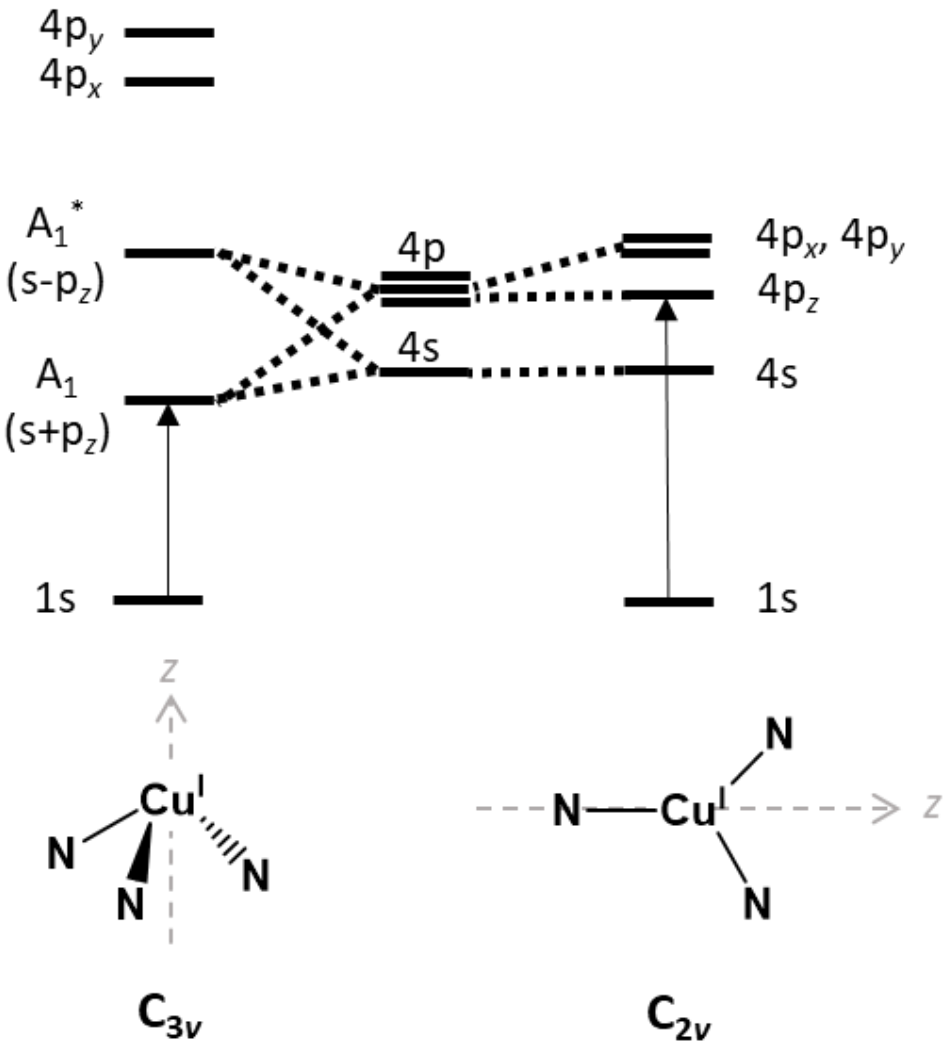


Figure 3.17: Ligand field diagram demonstrating the differences in the 1s to *4p* transition in three coordinate Cu(I) molecules with $C_{3v}$ and $C_{2v}$ symmetries.

The increase in intensity of the rising edge 1s to *4p* transition in the Cu(I) *Ls*AA9 Y164F K-edge XAS spectrum on the addition of cellohexaose is likely due to a change in geometry of the histidine brace coordinated to the Cu(I) ion. An increase in the intensity of the 1s to *4p* transition on addition of substrate is consistent with a change from a distorted trigonal pyramidal geometry with $C_{3v}$ symmetry to a more planar geometry with a more trigonal planar geometry with $C_{2v}$ symmetry. The sensitivity of the 1s to *4p* transition to changes in the copper geometry cannot be deconvoluted from the changes in intensity observed in this transition and therefore may influence all of the XAS spectra presented.

#### *3.3.3.3 Summary*

Unlike in *An*AA9, the addition of substrate to Cu(II) *Ls*AA9 Y164F instigates a change in the copper K-edge XAS spectrum in both the XANES and EXAFS regions, which is corroborated by literature EPR data. The changes observed in the Cu(II) *Ls*AA9 Y164F K-edge XAS spectrum on the addition of cellohexaose are consistent with a decrease in coordination number from four coordinate to three coordinate through the loss of an exogenous $OH/H_2O$ ligand, the histidine brace remains conserved.

The Cu(I) K-edge XAS spectra of *Ls*AA9 Y164F also changes on addition of cellohexaose, but this change is most likely attributed to a change in geometry from a distorted trigonal pyramidal structure to a more trigonal planar geometry with increased symmetry.

### 3.3.4 *Bl*AA10 with chitin

A combination of copper K-edge HERFD-XANES and conventional XAS was used to investigate the interaction of *Bl*AA10 with chitin in both the Cu(I) and Cu(II) oxidation states.

#### *3.3.4.1 CW-EPR Cu(II) BlAA10*

The X-band cw-EPR spectrum of Cu(II) *Bl*AA10 and simulated spin-Hamiltonian parameters are comparable to those of Courtade *et al* (Figure 3.18, Table 3.5).[87] The Cu(II) *Bl*AA10 cw-EPR spectrum shows a single copper species. The spin-Hamiltonian parameters from the simulation of the Cu(II) *Bl*AA10 cw-EPR spectrum are consistent with a spectral envelope with a SOMO with mainly $d(x^2-y^2)$ character. The rhombic *g* values from the simulation are typical of square-pyramidal copper complex, which is consistent with the crystal structures of Cu(II) AA10 LPMOs. [32]

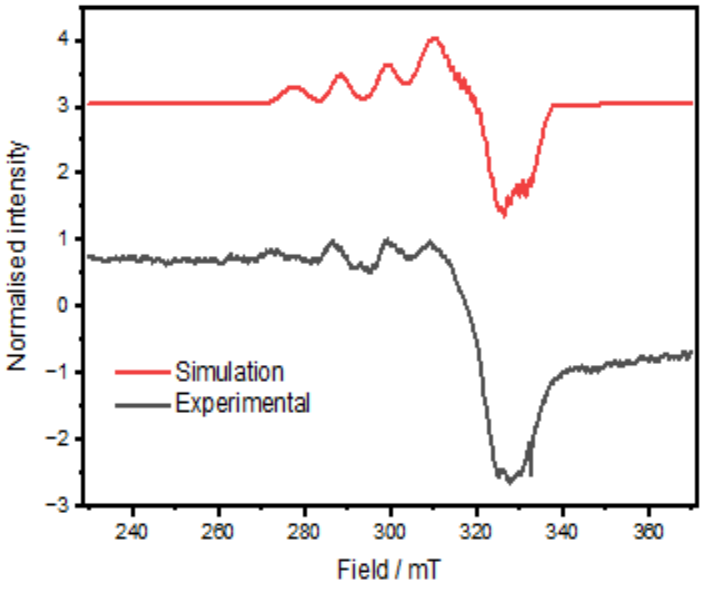


Figure 3.18: CW-EPR spectrum of Cu(II) *Bl*AA10 experimental data measured at 150 K (black) and simulation (red).

Table 2.5: Spin-Hamiltonian parameters used for the simulated CW-EPR spectrum of Cu(II) *Bl*AA10. A values given in MHz.

| | $g_{x,y,z}$ | $\lvert A_{x,y,z} \rvert$ |
|---|---|---|
| ***Bl*AA10** | 2.027, 2.095, 2.261 | 90, 110, 336 |

The aforementioned study by Courtade *et al* also found that addition of chitin Cu(II) *Bl*AA10 caused significant changes in the cw-EPR spectrum (both X-band and Q-band), that are consistent with a change in coordination number from five coordinate to four coordinate through the loss of an exogenous ligand ($OH/H_2O$).[32]

### *3.3.4.2 HERFD-XANES spectra of Cu(II) BlAA10 with chitin*

To check for effects of photoreduction in the HERFD-XANES spectrum of Cu(II) *Bl*AA10 three scans in the same sample position were measured consecutively, there was no significant difference between each spectrum so a single scan in each sample position can be measured and interpreted with confidence under these experimental conditions (Figure 3.19).

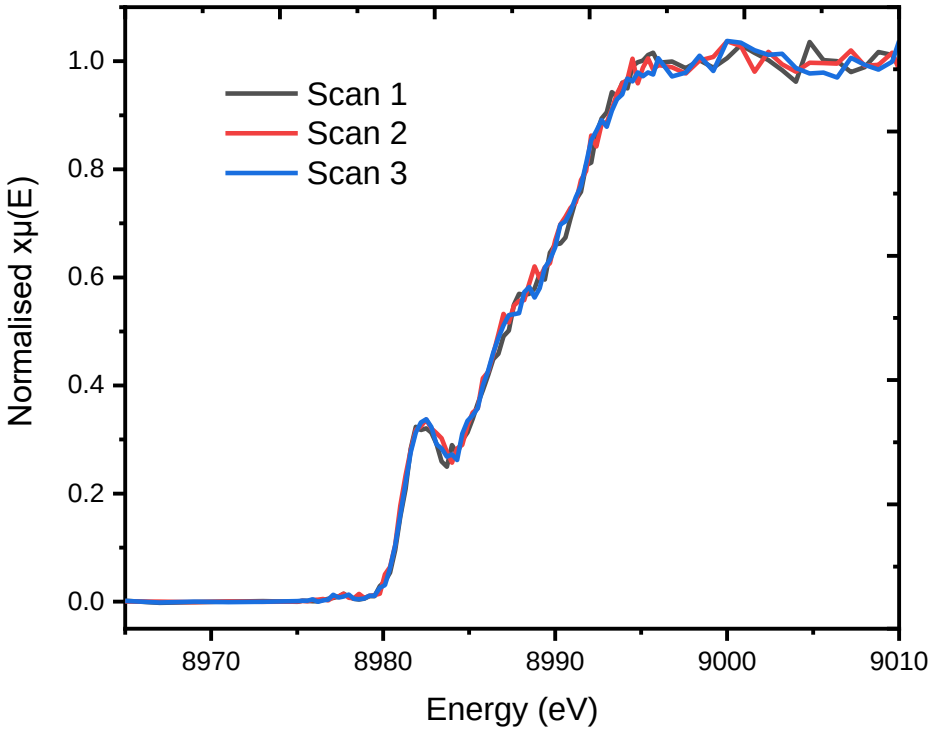


Figure 3.19: Three HERFD-XANES spectra of Cu(II) *Bl*AA10 measured consecutively in the same sample position.

The Cu(II) *Bl*AA10 K-edge HERFD-XANES spectrum demonstrates typical Cu(II) spectral features such as a weak pre-edge peak at 8977.7(3) eV consistent with a 1s to *3d* transition and two rising edge shoulders at 8982.7(3) eV and 8987.8(3) eV consistent with 1s to *4p* transitions. The K-edge position of the Cu(II) *Bl*AA10 HERFD-XANES spectrum is 8990.5(3) eV (Figure 3.20). The addition of chitin to Cu(II) *Bl*AA10 afforded changes to the copper K-edge HERFD-XANES spectrum with a decrease in intensity of the rising edge shoulders at 8982.7(3) eV and 8987.8(3) eV assigned as 1s to *4p* transitions, as well as an increase in the white line intensity. The addition of chitin to Cu(II) *Bl*AA10 did not bring about significant changes in the 1s to *3d* transition at 8977.7(3) eV nor the copper K-edge position. A decrease in the intensity of the 1s to *4p* transition in the Cu(II) K-edge on addition of substrate is in contrast to the previous observations in both *An*AA9 whereby there was no change, and *Ls*AA9 Y164F whereby there was an increase in the 1s to *4p* transition intensity. To give a decrease in intensity of the 1s to *4p* intensity in the copper K-edge one of the following effects must have been induced by the addition of chitin: an increase in coordination number, a shortening of the average bond length at the copper ion or a change in geometry from a square planar structure to a more distorted square pyramidal structure. To gain further insight into the effect that the addition of chitin to Cu(II) *Bl*AA10 has on the active site further investigation using conventional XAS was undertaken.

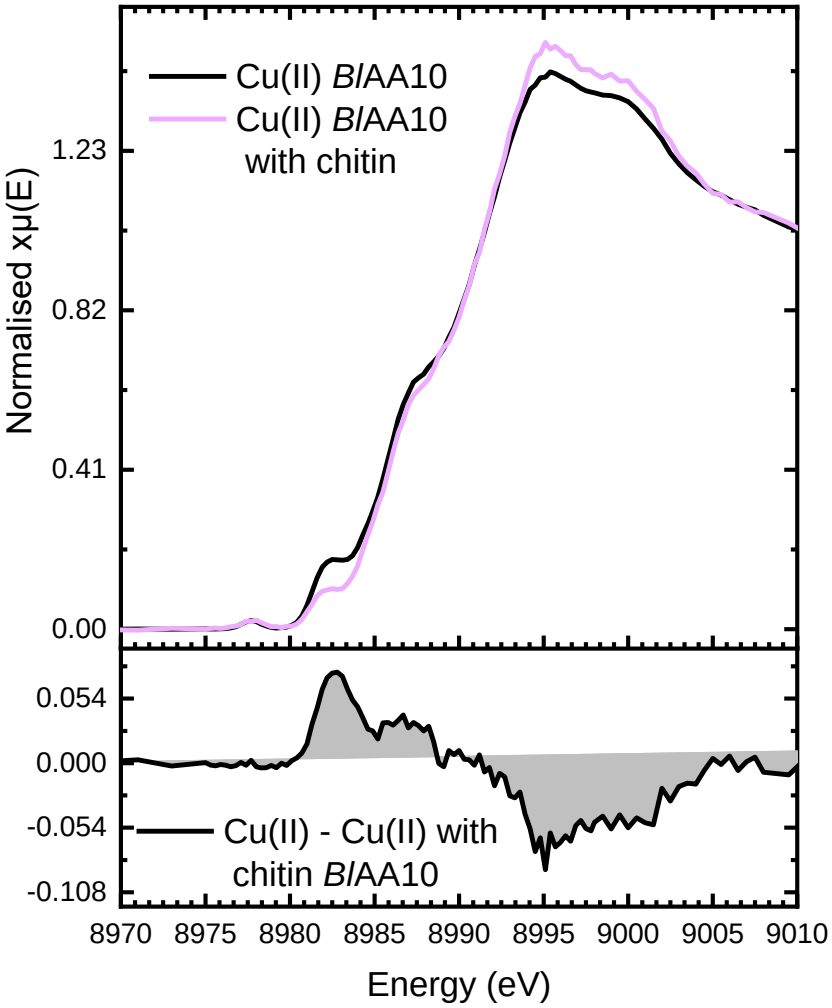


Figure 3.20: (Top) HERFD-XANES spectra of Cu(II) *Bl*AA10 (black) and Cu(II) *Bl*AA10 with chitin (pink). (Bottom) difference spectrum of Cu(II) – Cu(II) with chitin *Bl*AA10.

### *3.3.4.3 XAS of Cu(II) BlAA10 with chitin*

To check for any changes in the Cu(II) *Bl*AA10 XAS spectrum under the experimental conditions due to photoreduction, four consecutive XAS spectra were measured in the same sample position (Figure 3.21). There was no significant difference between the four scans, therefore three scans in each sample position could confidently be measured and averaged to improve the signal to noise ratio through the central limit theorem. .

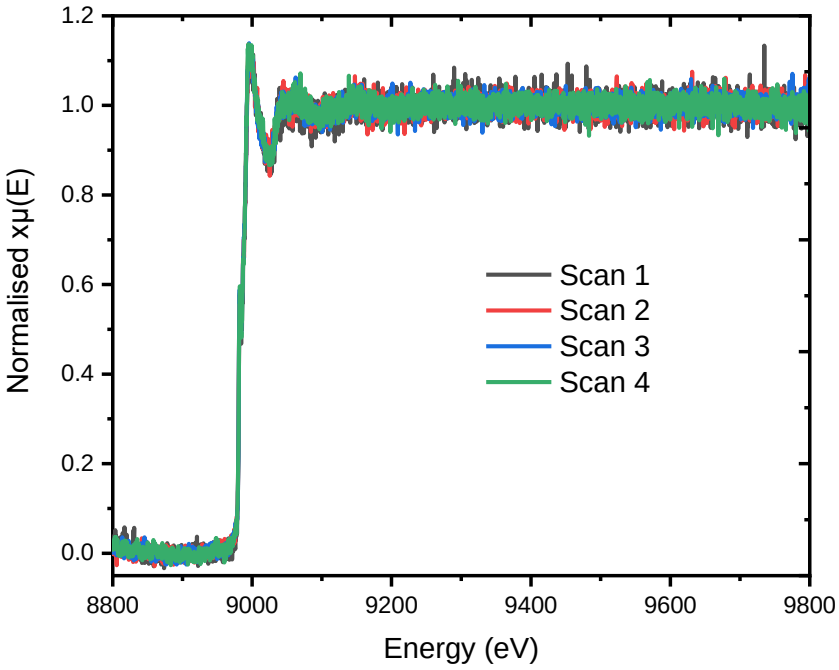


Figure 3.21: Four XAS spectra of Cu(II) *Bl*AA10 measured consecutively in the same sample position.

The XANES region of the conventional XAS copper K-edge spectra of Cu(II) *Bl*AA10 with and without chitin show the same spectral features as the HERFD-XANES spectra however the change in the intensity of the 1s to *4p* transition is much smaller than expected in the conventional XAS spectra (Figure 3.22). The discrepancy between the HERFD-XANES and conventional XAS XANES regions may be due to differences in sample preparation such as different substrate incubation times resulting in a weaker LPMO-substrate interaction in the conventional XAS samples, or potentially the presence of multiple Cu(II) *Bl*AA10 species being present in the conventional XAS samples.

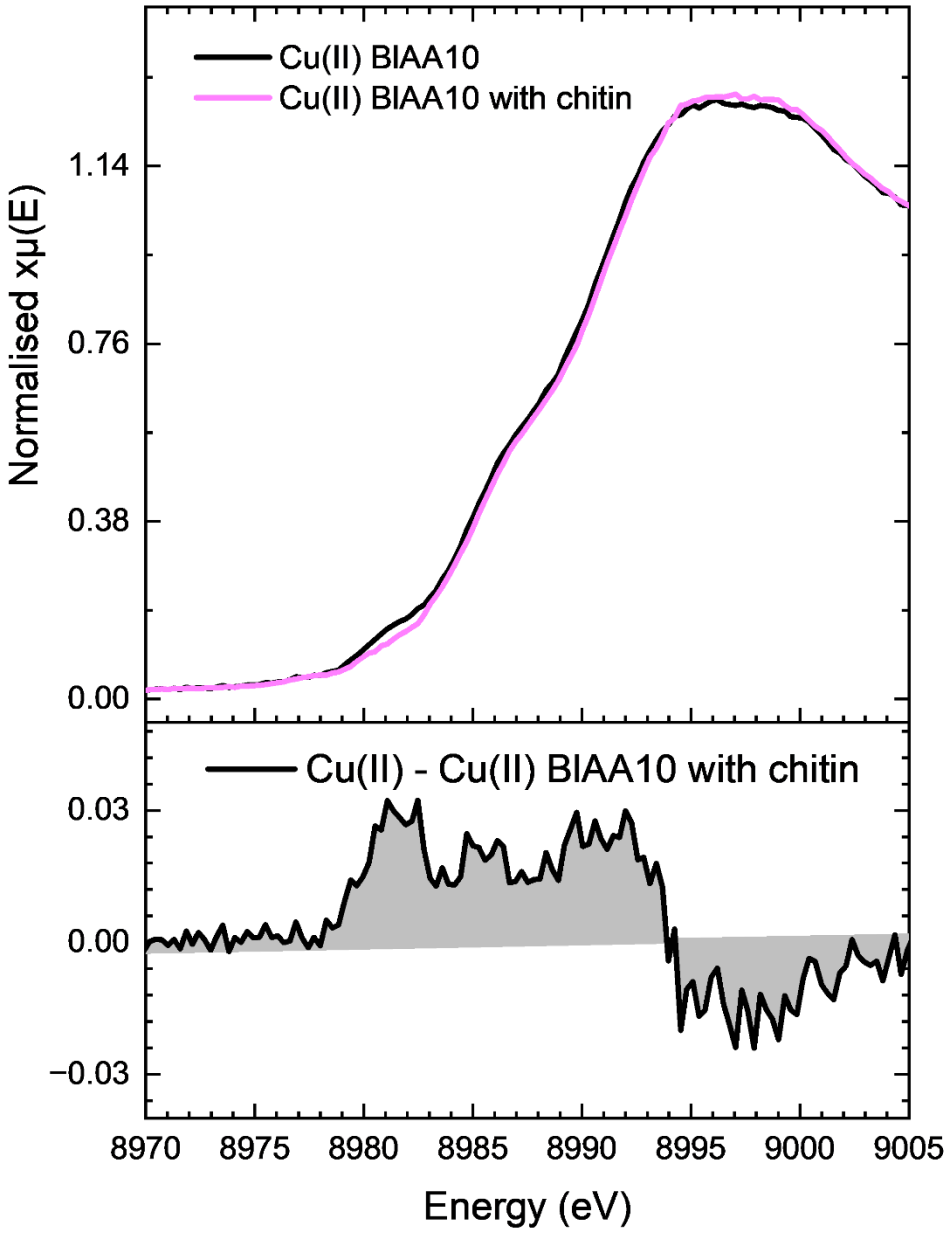


Figure 3.22: Conventional XAS copper K-edge spectrum XANES region of Cu(II) *Bl*AA10 with and without chitin, plotted with the difference spectrum (bottom).

Conventional XAS was used to collect the EXAFS region for Cu(II) *Bl*AA10 with and without chitin in order to gain insights into any changes in the coordination number and average bond length at the copper active site induced by the addition of chitin. The EXAFS region of *Bl*AA10 with and without chitin are very similar (Figure 3.23).

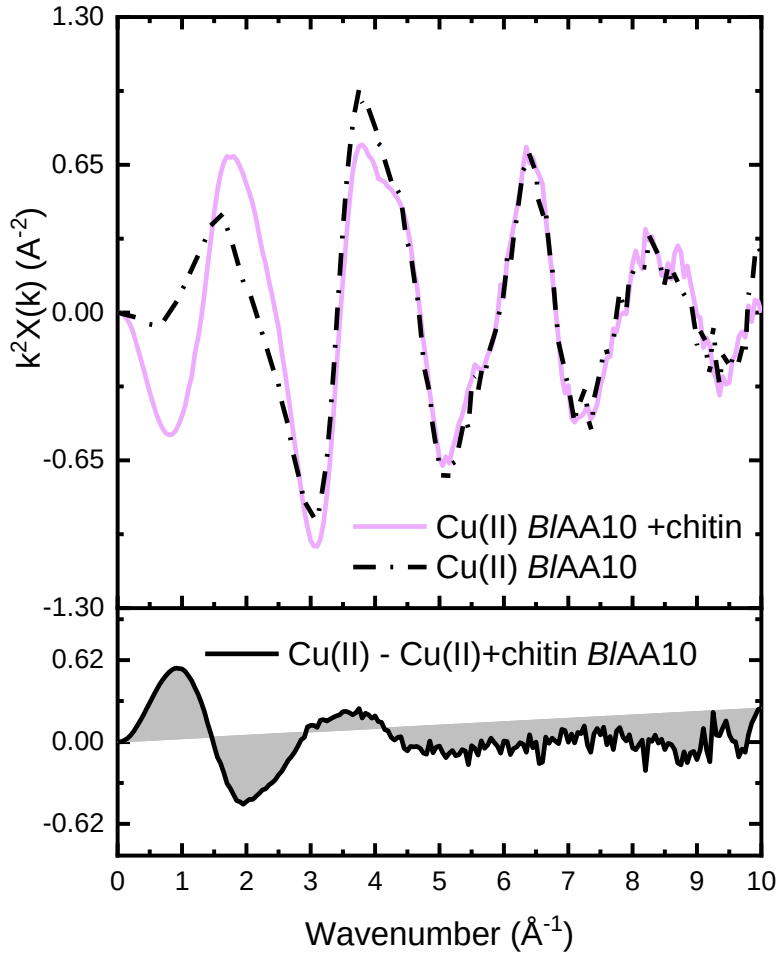


Figure 3.23: (Top) extracted EXAFS spectra of Cu(II) *Bl*AA10 with and without chitin. (Bottom) the difference spectrum of Cu(II) *Bl*AA10 minus Cu(II) *Bl*AA10 with chitin.

A fit of the Cu(II) *Bl*AA10 EXAFS spectrum in R-space suggests that the copper ion is four coordinate, which likely relates to three nitrogen ligands from the histidine brace and an exogenous ligand such as OH/ $H_2O$, with an average bond length of 1.96(2) Å (Figure 3.24, Table 3.6), but this is contradictory to the EPR spectrum measured for this sample which was consistent with a five coordinate structure.[32,87] A reasonable fit of the EXAFS region could not be achieved with a coordination number of five. The discrepancy between the EXAFS fit and the EPR spin-Hamiltonian parameters could be due to a mixture of species being present in the sample.

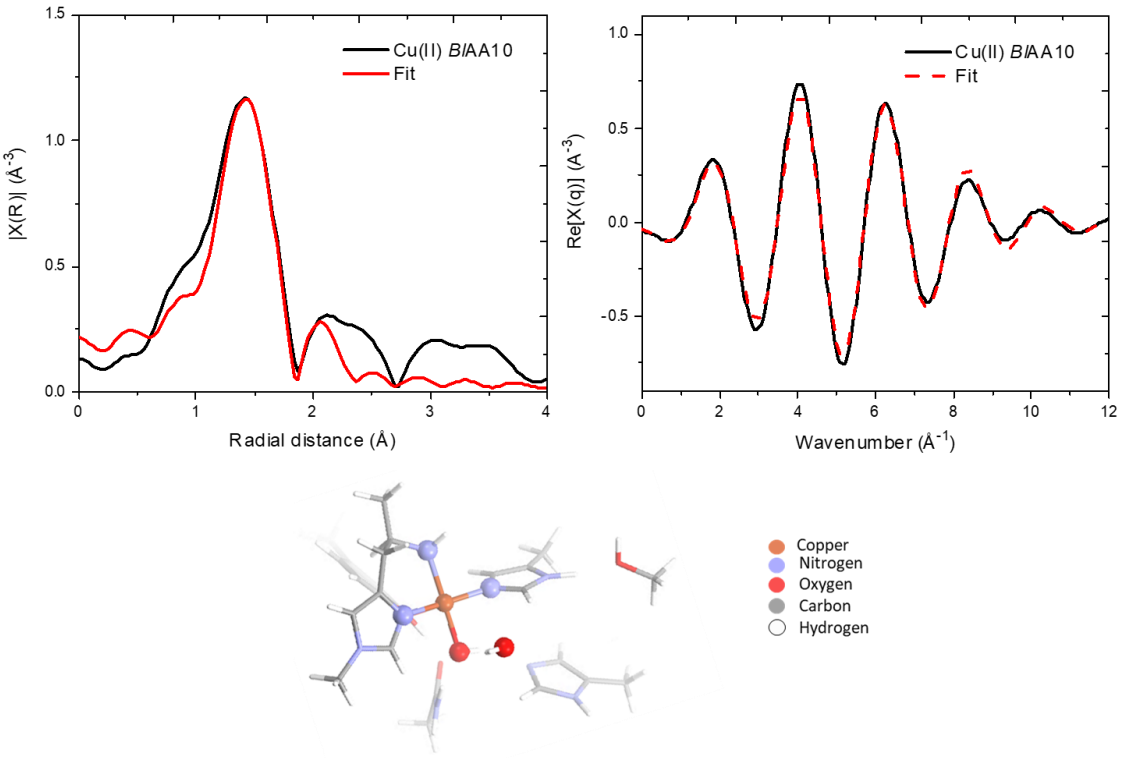


Figure 3.24: Copper K-edge magnitude of the Fourier transform from the extracted EXAFS signal for Cu(II) *Bl*AA10 (k-range 2.0 – 9.0 $Å^{-1}$) (top *left*), q-space (R-range 1.00 – 1.85 Å) (*top right*) and the model used in the fitting (*bottom*). Experimental data is plotted in black and the corresponding fit is plotted in red, the fits were performed in R-space using the parameters in Table 3.6. The atoms used in the fit are represented as ball and stick.

The fit of EXAFS spectrum in R-space for the Cu(II) *Bl*AA10 with chitin unsurprisingly gave similar results to that of Cu(II) *Bl*AA10 in the absence of substrate. In the presence of chitin the Cu(II) *Bl*AA10 EXAFS fit in R-space gave a coordination number of four, which is most likely representative of three nitrogen ligands from the histidine brace and an exogenous OH/$H_2O$ ligand (Figure 3.25, Table 3.6). A Cu(II) *Bl*AA10 with a coordination number of four in the presence of chitin is consistent with the EPR spin-Hamiltonian parameters reported by Courtade *et al*.[87] A coordination number of four in the presence of chitin should rule out the decrease in 1s to *4p* intensity in the HERFD-XANES spectra of Cu(II) *Bl*AA10 in the presence and absence of chitin being from an increase in coordination number. The conservation of coordination number on the addition of chitin to Cu(II) *Bl*AA10 also contradicts the findings of Courtade *et al*, who through an EPR study found that the addition of chitin to Cu(II) *Bl*AA10 causes the loss of the exogenous ligand resulting in a change in coordination number from five to four. There is also no change in the average bond length across the four Cu-N(O) bonds in Cu(II) *Bl*AA10 with and without chitin, which also rules out a decrease in

average bond length as a cause for the decrease in intensity of the 1s to *4p* transition in the HERFD-XANES spectra of Cu(II) *Bl*AA10 upon chitin addition.

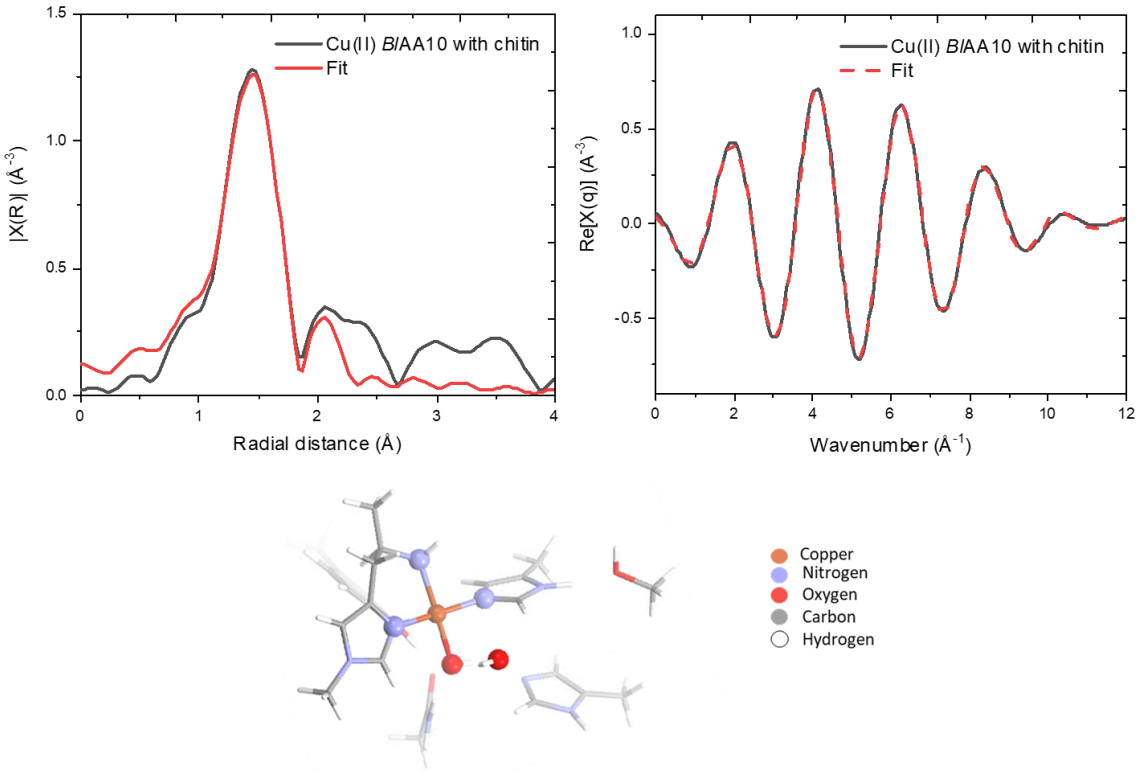


Figure 3.25: Copper K-edge magnitude of the Fourier transform from the extracted EXAFS signal for Cu(II) *Bl*AA10 with chitin (k-range 2.0 – 9.0 Å$^{-1}$) (top *left*), q-space (R-range 1.10 – 1.85 Å) (*top right*) and the model used in the fitting (*bottom*). Experimental data is plotted in black and the corresponding fit is plotted in red, the fits were performed in R-space using the parameters in Table 3.6. The atoms used in the fit are represented as ball and stick.

Table 3.6: Best fit parameters obtained from the EXAFS fits of Cu(II) *Bl*AA10 with and without chitin. The $S_0^2$ value was fixed to 0.902 for both fits.

| | **N and path** | **R-space fitting range** | **R / Å** | **$\sigma^2$ / Å$^2$** | **$\Delta E_0$ / eV** |
|---|---|---|---|---|---|
| **Cu(II) *Bl*AA10** | 4 Cu-N/O | 1.00 – 1.85 Å | 1.96±0.02 | 0.004±0.001 | -4±2 |
| **Cu(II) *Bl*AA10 with chitin** | 4 Cu-N/O | 1.10 – 1.85 Å | 1.966±0.007 | 0.0039±0.0006 | -1.5±0.9 |

Discarding a change in coordination number and average bond length at the copper ion as the cause for the decrease in 1s to *4p* intensity in the HERFD-XANES spectrum of *Bl*AA10 on the addition of chitin leaves a change in geometry at the copper ion or changes in the metal-ligand covalency as the most probable explanation. For a decrease in 1s to *4p* intensity there could be a reduction in symmetry at the copper ion on the addition of chitin. However, the possibility of mixed species in the sample and potential differences in the sample preparation reduces the confidence with which conclusions can be made.

#### *3.3.4.4 HERFD-XANES spectra of Cu(I) BlAA10 with chitin*

The Cu(I) *Bl*AA10 K-edge HERFD-XANES spectrum is in accordance with a Cu(I) spectrum with features including an intense rising edge 1s to *4p* transition at 8982.2(3) eV and an edge position of 8981.0(3) eV. The addition of chitin to Cu(I) *Bl*AA10 resulted in the same K-edge HERFD-XANES spectral shape, white line intensity and edge position as Cu(I) *Bl*AA10 in the absence of substrate, but a significant decrease in the 1s to *4p* transition intensity at 8982.2(3) eV can be observed (Figure 3.26). A decrease in 1s to *4p* rising edge transition intensity on the addition of chitin to Cu(I) *Bl*AA10 is the same trend as was observed on the addition of chitin to Cu(II) *Bl*AA10, but is the opposite of the change observed in both Cu(I) *An*AA9 and Cu(I) *Ls*AA9 on the addition of substrate which saw an increase in 1s to *4p* intensity.

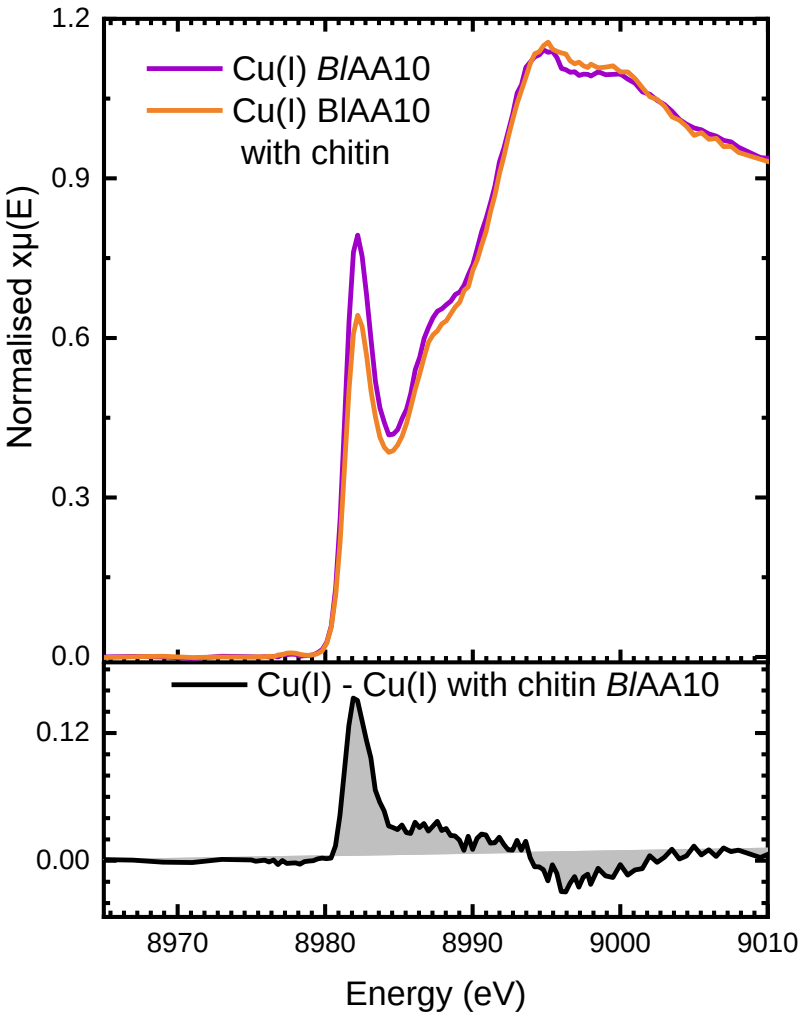


Figure 3.26: (Top) HERFD-XANES spectra of Cu(I) *Bl*AA10 (purple) and Cu(I) *Bl*AA10 with chitin (orange). (Bottom) difference spectrum of Cu(I) – Cu(I) with chitin *Bl*AA10.

In the same case as Cu(II) *Bl*AA9 with chitin, further investigation to explain this decrease in 1s to *4p* intensity on the addition of chitin to Cu(I) *Bl*AA10 was undertaken using conventional XAS.

### *3.3.4.5 XAS of Cu(I) BlAA10 with chitin*

Conventional XAS was undertaken to assess the changes to the EXAFS region induced by the addition of chitin to Cu(I) *Bl*AA10, to ascertain whether there are changes in the coordination number and average bond lengths in the primary coordination sphere of the copper active site. The XANES region of the XAS spectrum shows similar changes on the addition of chitin to Cu(I) *Bl*AA10 as was observed in the HERFD-XANES spectrum such as a decrease in the intensity of the 1s to *4p* transition at 8982 eV (Figure 3.27). However, the changes observed in the conventional XAS Cu(I) *Bl*AA10 spectrum on addition of chitin are significantly smaller than those observed in the HERFD-

XANES spectrum. These changes may have arisen due to differences in the incubation period with the substrate between the samples.

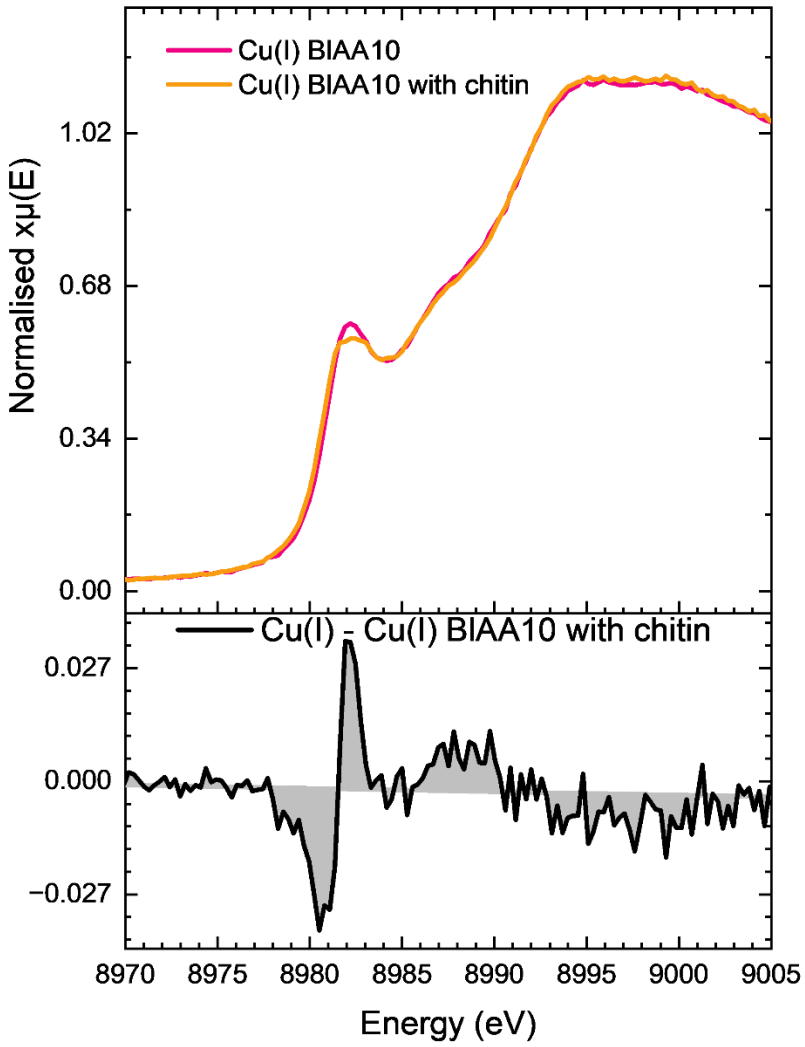


Figure 3.27: XANES region from the conventional XAS spectra of Cu(I) *Bl*AA10 with and without chitin. The difference spectrum for the two XAS spectra is shown at the bottom.

The extracted EXAFS spectra of Cu(I) *Bl*AA10 with and without chitin do not show significant differences (Figure 3.28).

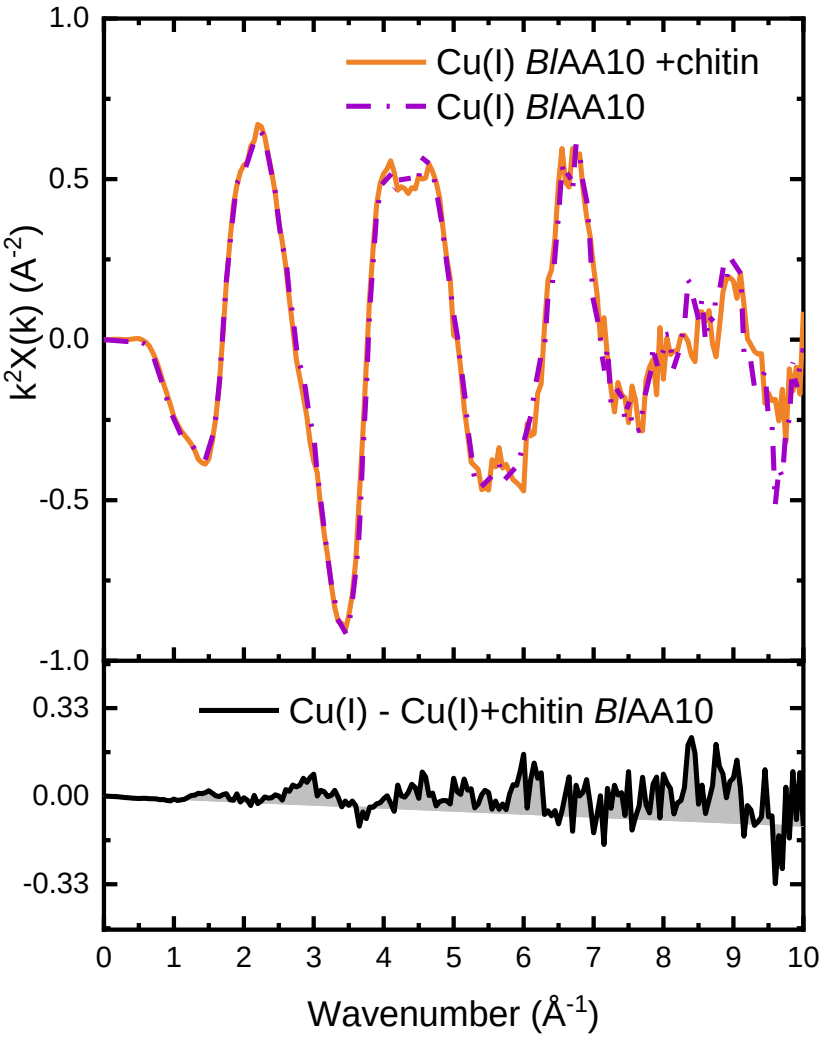


Figure 3.28: (Top) extracted EXAFS spectra of Cu(I) *Bl*AA10 with and without chitin. (Bottom) the difference spectrum of Cu(I) *Bl*AA10 minus Cu(I) *Bl*AA10 with chitin.

The fit in R-space suggests that Cu(I) *Bl*AA10 has a three coordinate structure consistent with a copper bound histidine brace motif, with an average Cu-N bond length of 1.91(1) Å (Figure 3.29, Table 3.7).

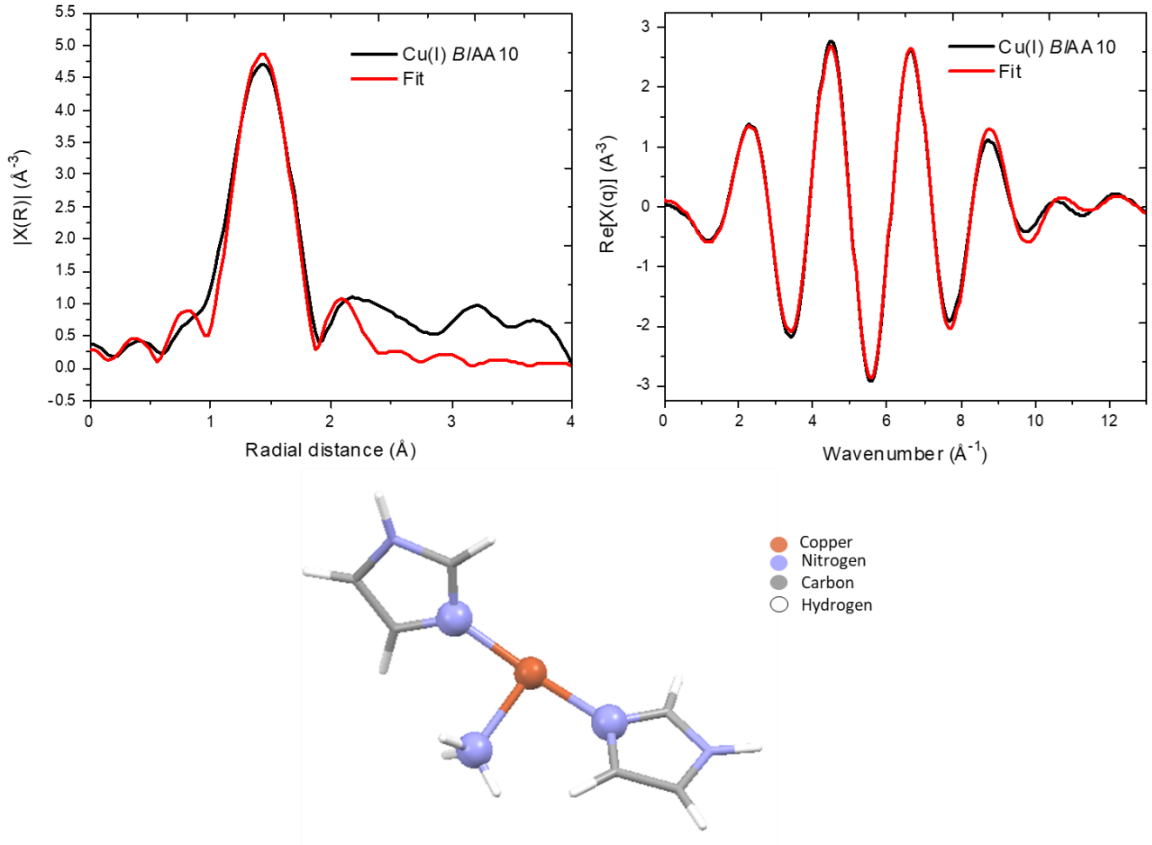


Figure 3.29: Copper K-edge magnitude of the Fourier transform from the extracted EXAFS signal for Cu(I) *Bl*AA10 (k-range 1.8 – 9.2 $Å^{-1}$) (top *left*), q-space (R-range 1.05 – 1.85 Å) (*top right*) and the model used in the fitting (*bottom*). Experimental data is plotted in black and the corresponding fit is plotted in red. The fits were performed in R-space using the parameters in Table 3.7. The atoms used in the fit are represented as ball and stick.

Given the similarity between the EXAFS spectra of Cu(I) *Bl*AA10 with and without chitin, it is as predicted that there is little difference in the fit of Cu(I) *Bl*AA10 with and without chitin. The fit in R-space of Cu(I) *Bl*AA10 with chitin gives a three coordinate structure that could be attributable to a copper bound histidine brace, with an average bond length of 1.90(2) Å (Figure 3.30, Table 3.7).

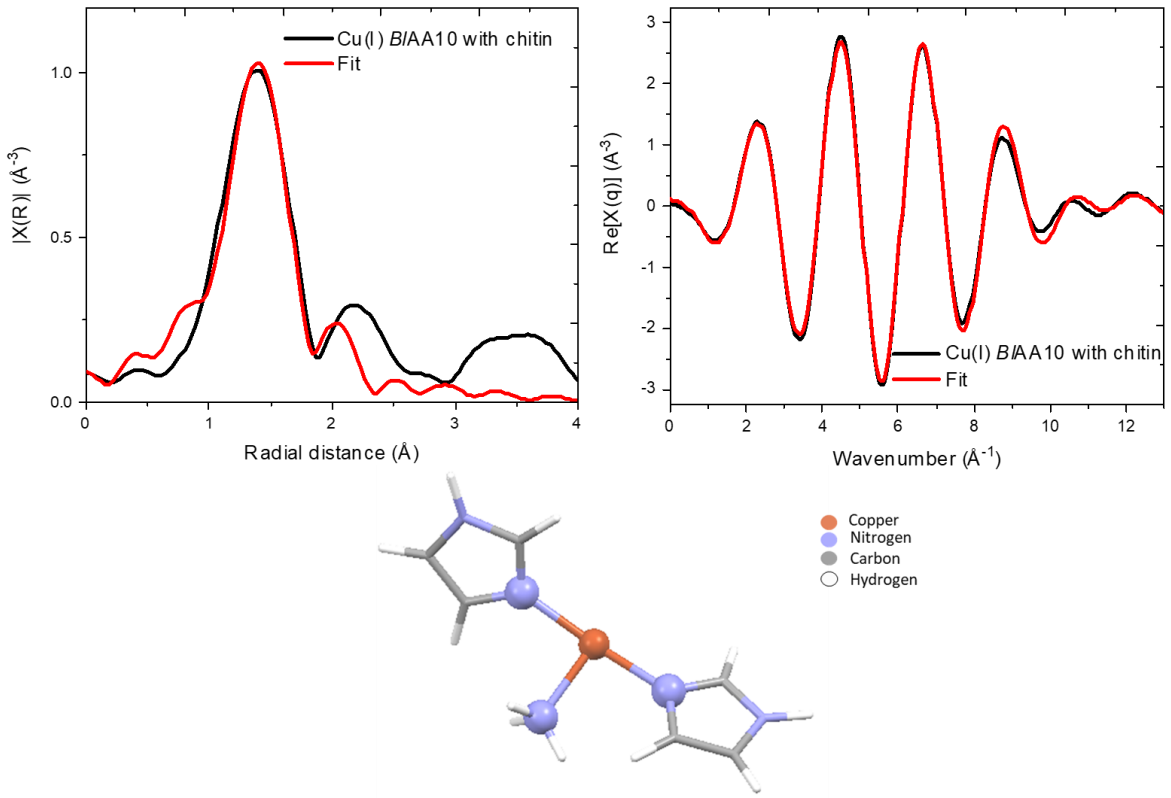


Figure 3.30: Copper K-edge magnitude of the Fourier transform from the extracted EXAFS signal for Cu(I) *Bl*AA10 (k-range 1.8 – 9.2 $Å^{-1}$) (top *left*), q-space (R-range 1.05 – 1.85 Å) (*top right*) and the model used in the fitting (*bottom*). Experimental data is plotted in black and the corresponding fit is plotted in red. The fits were performed in R-space using the parameters in Table 3.7. The atoms used in the fit are represented as ball and stick.

Table 3.7: Best fit parameters obtained from the EXAFS fits of Cu(II) *Bl*AA10 with and without chitin. The $S_0^2$ value was fixed to 0.902 for both fits.

| | **N and path** | **R-space fitting range** | **R / Å** | **$\sigma^2$ / $Å^2$** | **$\Delta E_0$ / eV** |
|---|---|---|---|---|---|
| **Cu(I) *Bl*AA10** | 3 Cu-N | 1.05 – 1.85 Å | 1.91±0.01 | 0.005±0.001 | 4±1 |
| **Cu(I) *Bl*AA10 with chitin** | 3 Cu-N | 1.05 – 1.85 Å | 1.90±0.02 | 0.005±0.001 | 2±2 |

Like the addition of chitin to Cu(II) *Bl*AA10, the decrease in 1s to *4p* intensity in the HERFD-XANES spectrum of Cu(I) *Bl*AA10 on the addition of chitin cannot be explained by a change in coordination number nor a change in bond length as these changes have been ruled out by a lack of change in their EXAFS spectra. Therefore the likely explanation for the observations in the 1s to *4p* region of

the HERFD-XANES spectra of Cu(I) *Bl*AA10 in the absence and presence of chitin could once again be a change in geometry, with chitin causing a decrease in symmetry at the copper active site or a change in metal-ligand covalency.

#### *3.3.4.6 Summary*

A combination of X-ray spectroscopy techniques was used to gain insights into the effects of chitin addition to *Bl*AA10 in the Cu(I) and Cu(II) oxidation states. The findings from this investigation indicate that the addition of chitin causes a decrease in intensity of the copper K-edge rising edge peaks attributed to 1s to *4p* transitions for both Cu(I) and Cu(II) *Bl*AA10. Through ruling out a change in coordination number/ average bond lengths through fitting of the EXAFS region, it is likely that the observed spectral changes occur due to a change in copper geometry induced by the addition of chitin to Cu(I) and Cu(II) *Bl*AA10.

Based on literature studies it was expected that chitin would induce a change in the Cu(II) *Bl*AA10 active site which could be observed spectroscopically using HERFD-XANES, however the changes observed in this study are not in accordance with a change in coordination number previously reported in an EPR study of *Bl*AA10 with chitin.[87] The discrepancy between the findings presented and literature findings could be due to differences in incubation periods of *Bl*AA10 and chitin, perhaps differences in the chitin used or the presence of multiple Cu(II) *Bl*AA10 species present in the some of the samples.

### 3.3.5 *Ao*AA11 with chitin

Copper K-edge HERFD-XANES was used to assess the changes to the *Ao*AA11 active site in both the Cu(I) and Cu(II) oxidation states induced by the addition of chitin.

#### *3.3.5.1 CW-EPR Cu(II) AoAA11*

The X-band CW-EPR spectrum of Cu(II) *Ao*AA11 is consistent with a single copper species with significant d($x^2$-$y^2$) SOMO character (Figure 3.31, Table 3.8). The *g*-values from the simulation of the CW-EPR spectrum of Cu(II) *Ao*AA11 are commensurate with those previously reported for Cu(II) *Ao*AA11.[64]

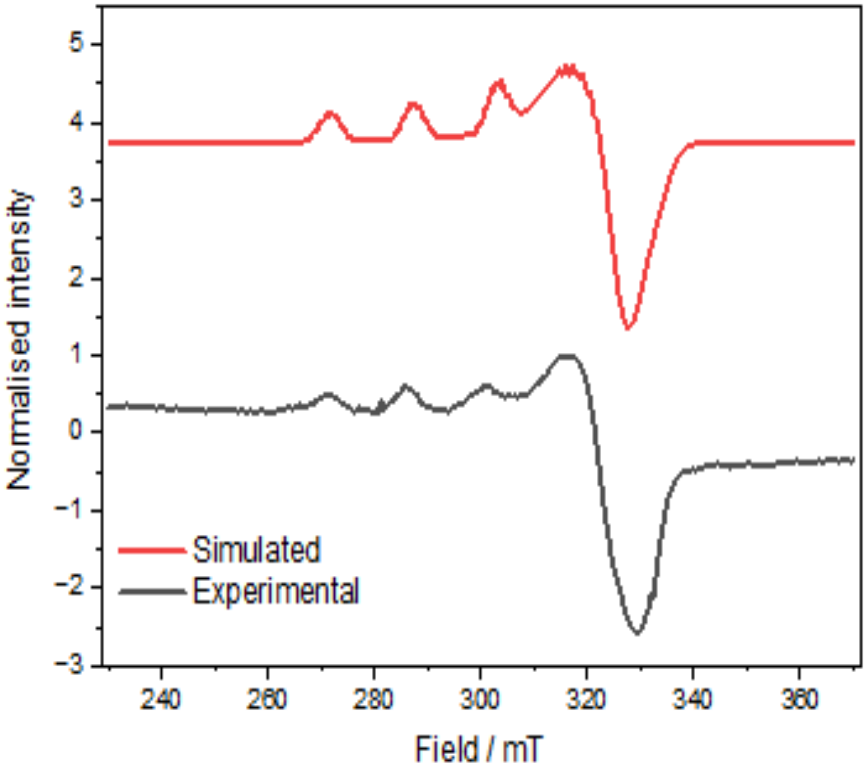


Figure 3.31: CW-EPR spectrum of Cu(II) *Ao*AA11 (black) and simulation (red).

Table 3.8: Spin-Hamiltonian parameters used for the simulated CW-EPR spectrum of Cu(II) *Ao*AA11. A values given in MHz.

| | $g_{x,y,z}$ | $\lvert A_{x,y,z} \rvert$ |
|---|---|---|
| ***Bl*AA10** | 2.03, 2.10, 2.25 | 10, 60, 485 |

### *3.3.5.2 HERFD-XANES spectra of Cu(II) AoAA11 with chitin*

To test if the beam was sufficiently attenuated to minimise beam damage as described in Chapter 2.3, two consecutive HERFD-XANES spectra were measured in the same sample position in Cu(II) *Ao*AA11 (Figure 3.32). The two HERFD-XANES spectra show no significant differences attributable to photoreduction, therefore confirming that a single scan in each sample position can be measured and interpreted confidently.

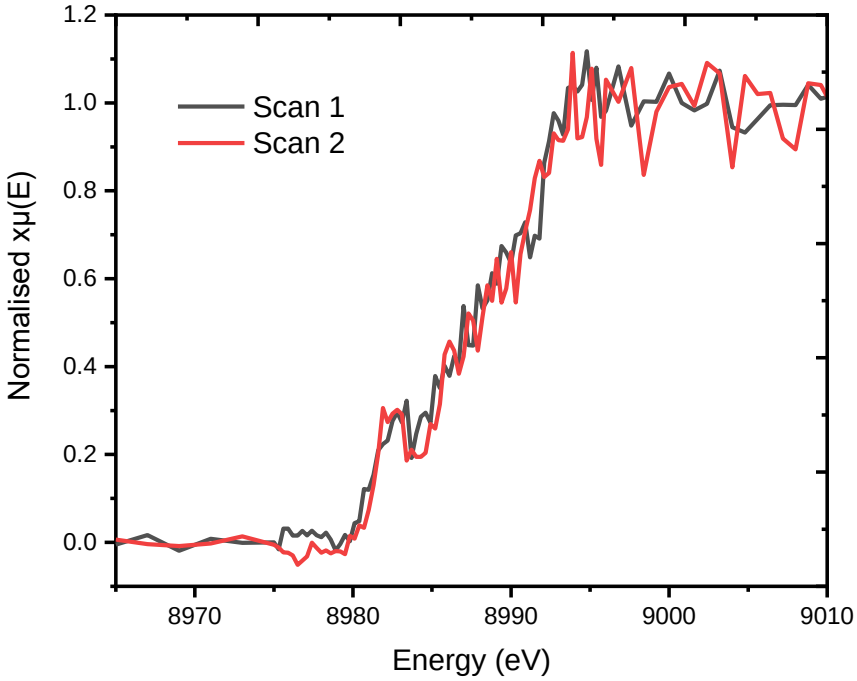


Figure 3.32: Two consecutive HERFD-XANES spectra recorded in the same sample position of Cu(II) *Ao*AA11.

The HERFD-XANES spectra of *Ao*AA11 had a lower signal to noise ratio than expected for the sample concentration (0.8 mM), the HERFD-XANES data was collected under the same conditions as the other LPMO samples which points to the concentration of the sample itself to be the issue. The concentration of this sample was measured before transportation to Diamond Light Source, at the same time at which the EPR was measured, the signal of which was commensurate with the concentration. When the sample was used at Diamond Light Source there were no signs of precipitation, leading to the hypothesis that an interaction between the Eppendorf the sample was stored in and Cu(II) *Ao*AA11 has reduced the concentration of Cu(II) in the sample measured by HERFD-XANES. Further investigation into this apparent loss of sample concentration needs to be undertaken.

Both the Cu(II) *Ao*AA11 and Cu(II) *Ao*AA11 with chitin spectra show typical characteristics of a Cu(II) HERFD-XANES spectrum including a 1s to $3d(x^2\text{-}y^2)$ dipole disallowed, quadrupole allowed transition at 8977.6(3) eV, and a rising edge feature consistent with a 1s to *4p* transition at 8982.6(3) eV. The addition of chitin results in a decrease in the intensity of the 1s to *4p* transition at 8982.6(3) eV (Figure 3.33).

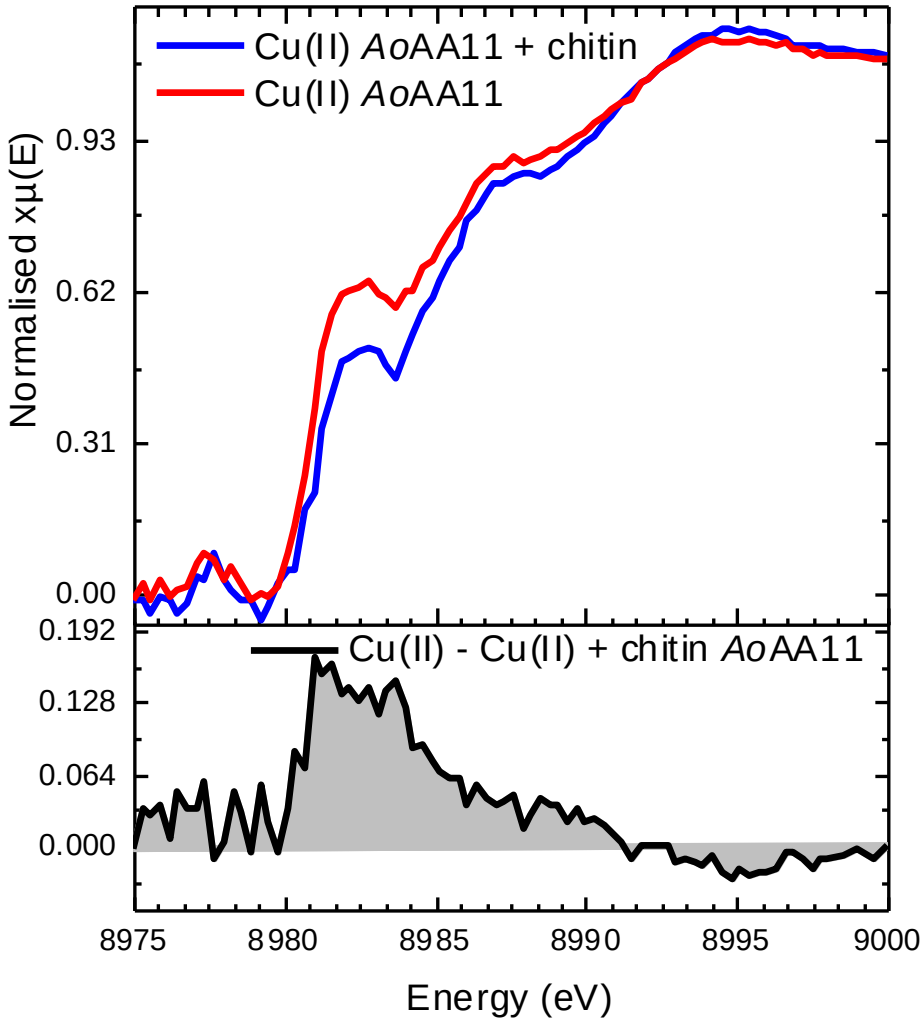


Figure 3.33: (Top) The HERFD-XANES spectra of Cu(II) *Ao*AA11 (red) and Cu(II) *Ao*AA11 with chitin (blue). (Bottom) The difference spectrum of Cu(II) and Cu(II) with chitin *Ao*AA11.

It is clear that chitin induces a structural change in the Cu(II) *Ao*AA11 active site. An increase in 1s to *4p* intensity has been shown in the previously discussed LPMO-substrate interactions to be commensurate with a decrease in coordination number or a change in copper geometry. However, a lack of crystallographic or other spectroscopic data means that the exact nature of this change cannot be discerned by HERFD-XANES alone.

#### *3.3.5.3 HERFD-XANES of Cu(I) AoAA11 with chitin*

The HERFD-XANES spectra of Cu(I) *Ao*AA11 and Cu(I) *Ao*AA11 with chitin show very similar spectral features to each other. Both the Cu(I) and Cu(I) with chitin *Ao*AA11 spectra have the absence of a 1s to $3d(x^2\text{-}y^2)$ pre-edge transition and have an intense rising edge transition at 8982.4(3) eV attributed to a 1s to *4p* transition. Whilst both the Cu(I) and Cu(I) with chitin *Ao*AA11 spectra are

very similar, there is a small reduction in the intensity of the 1s to *4p* transition at 8982.4(3) eV on the addition of chitin (Figure 3.34).

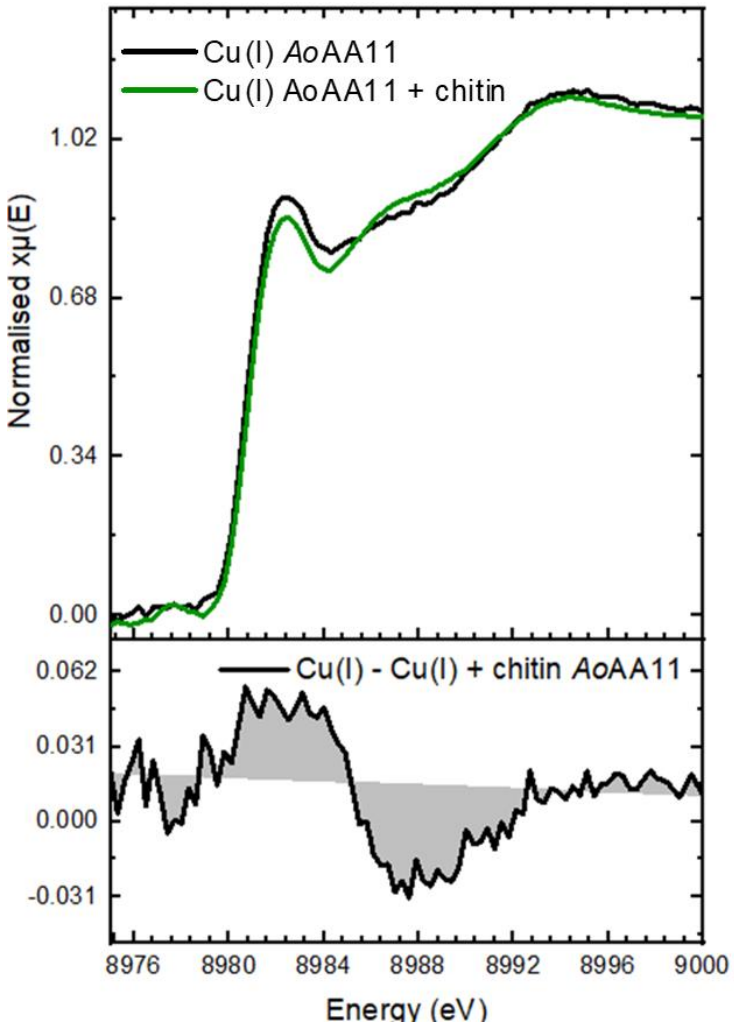


Figure 3.34: (Top) The HERFD-XANES spectra of Cu(I) *Ao*AA11 with chitin (green) and Cu(I) AoAA11 (black). (Bottom) The difference spectrum of Cu(I) and Cu(I) with chitin *Ao*AA11.

A decrease in 1*s* to *4p* transition intensity on the addition of chitin to Cu(I) *Ao*AA11 is the inverse of the change observed in the HERFD-XANES spectra of Cu(II) *Ao*AA11 on the addition of chitin. With such a small decrease in intensity of the 1*s* to *4p* transition on the addition of substrate to Cu(I) *Ao*AA11 it is unlikely that this change is due to a change in coordination number but perhaps could be induced by a change in geometry or bond lengths at the copper active site. Alternatively, a weak interaction of Cu(I) *Ao*AA11 with chitin could result in proportion of the sample undergoing a change in coordination number, giving a mix of species within the sample and a small change in the intensity of the 1s to *4p* transition. Whilst it is likely that chitin is causing a structural change in the

Cu(I) *Ao*AA11 active site, definitive conclusions of the structural effect the addition of substrate has on the Cu(I) *Ao*AA11 active site cannot be ascertained without further spectroscopic investigation.

#### *3.3.5.4 Summary*

The addition of chitin to both Cu(I) and Cu(II) *Ao*AA11 induces a structural change at the copper ion in the active site. However, without further spectroscopic of TD-DFT investigation it cannot be deduced exactly what these structural changes are.

## 3.4 Conclusions

This chapter set out to investigate the differences in LPMO interactions in the Cu(I) and Cu(II) oxidation states across different LPMOs and substrates. The findings of this chapter indicate that each of the LPMOs studied; *An*AA9, *Ls*AA9 Y164F, *Bl*AA10 and *Ao*AA11 undergo different changes in the primary coordination sphere of the copper active site on the addition of substrate including no change, a change in coordination number and a change in geometry (Table 3.9). In the case of *Ao*AA11, further investigation is required to decipher what changes occur, but it is clear that chitin induced a change at the active site in both the Cu(I) and Cu(II) oxidation states.

Table 3.9: the observed spectroscopic changes induced by the addition of substrate to different LPMOs.

| LPMO & Substrate | Cu(II) | Cu(I) |
|---|---|---|
| ***An*AA9 & PASC** | No change in EPR or HERFD-XANES | Increase in 1s to *4p* transition in HERFD-XANES. TD-DFT suggest this change is associated with a decrease in coordination number upon substrate addition. |
| ***Ls*AA9 Y164F & G6** | Change in XAS (XANES and EXAFS region) consistent with a decrease in coordination number. | Change in XAS (XANES and EXAFS region) consistent with a change in geometry at the copper ion. |
| ***Bl*AA10 & chitin** | Change in HERFD-XANES but no change in EXAFS region suggesting a geometric change. | Change in HERFD-XANES but no change in EXAFS region suggesting a geometric change. |
| ***Ao*AA11 & chitin** | An increase in 1s to *4p* intensity in HERFD-XANES. | A decrease in 1s to *4p* intensity in HERFD-XANES. |

The results presented in this chapter also showcase how HERFD-XANES and conventional XAS can be applied to the study of metalloprotein-substrate interactions.

The most significant changes in the XAS spectra (both conventional XAS and HERFD-XANES) were observed in the 1s to *4p* transitions. The 1s to *4p* transition is very responsive to changes in the primary coordination sphere namely changes in coordination number, symmetry, geometry and bond length. Whilst changes to the 1s to *4p* assigned peak are a good indicator of changes to the primary coordination sphere, it is not trivial to unambiguously assign the exact change in the primary coordination sphere.

The investigation into metal contaminants present in commonly used LPMO substrates highlights the need for rigorous testing of LPMO substrates before they are used for LPMO activity assays and spectroscopic characterisation.

Whilst CBMs were not included in the LPMO structures used in this study, XAS does not require long-range order and therefore in future studies could be utilised to study what interactions, if any, the CBM has with LPMO substrates.

# 4 Rapid freeze quenching to trap LPMO intermediates

## 4.1 Introduction

### 4.1.1 LPMO reaction with *m*-CPBA

The activation of C-H bonds in recalcitrant polysaccharides by the copper active site of LPMOs is performed via a largely uncharacterised mechanism. With an approximate polysaccharide C-H bond enthalpy of 95 - 100 kcal $mol^{-1}$ it is conjectured that the LPMO copper active site must form a high valence, strongly oxidising intermediate species.[59] The highly reactive nature of such a species would make it difficult to observe and characterise spectroscopically, however theoretical calculations suggest that the intermediate could be a singlet state (*S*=0) copper(III)-hydroxide or a triplet state (*S*=1) Copper(II)-oxyl.[1,12,153]

It is proposed that the first stage of the LPMO reaction mechanism involves the reaction in the Cu(I) oxidation state with an electron donor in the form of either peroxide or molecular oxygen.[154] *m*-CPBA is an oxidant which can react *via* both heterolytic and homolytic O-O bond cleavage reaction pathways (Figure 4.1).[155] The use of *meta*-chloro-perbenzoic acid (*m*-CPBA) as an oxygen atom shunt to force a redox enzyme reaction mechanism into producing a single species in the absence of substrate has previously been achieved in the study of P450 enzymes.[156]

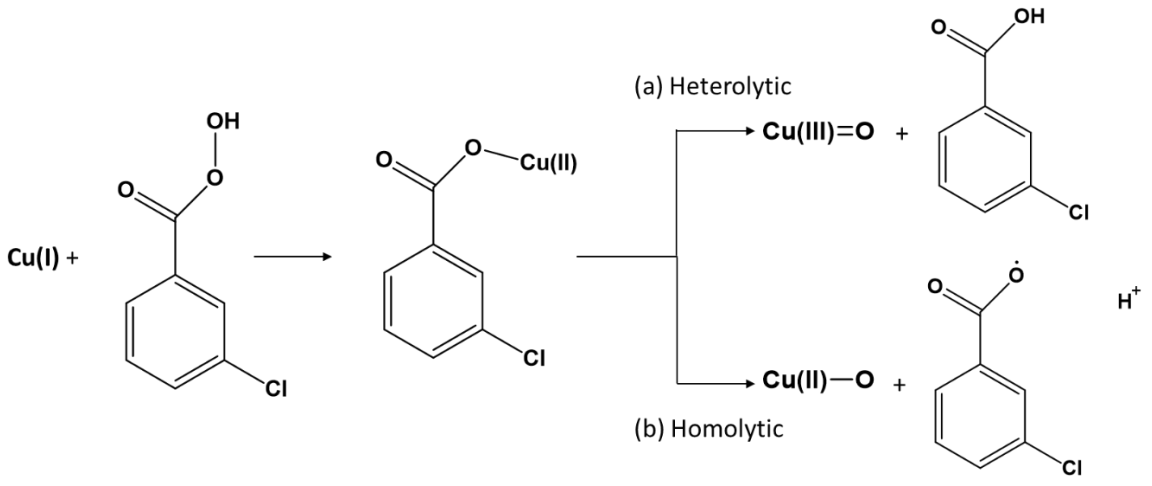


Figure 4.1: Reaction of Cu(I) with *m*-CPBA and the resulting products of the (a) homolytic reaction and (b) homolytic reaction.

An investigation into LPMO intermediates which sought to use *m*-CPBA as an oxygen atom shunt focused on the reaction of three Cu(I) AA9 LPMOs: *Ls*AA9, *Cv*AA9 and *Ta*AA9. The reaction of these

LPMOs with *m*-CPBA was monitored using stopped-flow UV-vis spectroscopy. The stopped-flow UV-vis results showed that *Ta*AA9 forms two optically distinct intermediates; the first with bands at 520 and 548 nm is characteristic of a tryptophanyl radical, and the second with bands at 420 nm is consistent with a tyrosyl radical similar to that of the Cu(II) tyrosyl radical characterised in the reaction of *Ls*AA9 with peroxide. [1,99,125] However, *Ls*AA9 and *Cv*AA9 LPMOs yielded different results; the first intermediate formed in 38.9 ms, decayed rapidly and gave an intense band at 361 nm (**Int1**). On decay **Int1** formed a second species resembling a tyrosyl radical with an absorbance band at 414 nm (**Int2**).[125] Using double mixing UV-vis stopped-flow experiments Zhao *et al* found that **Int1** and **Int2** are not formed in the LPMO reaction mechanism of oxidising the *Ls*AA9 substrate; cellopentaose (G5). Zhao *et al* also determined that **Int2** is a ferromagnetically coupled (*S* = 1) Cu(II)–tyrosyl complex (Figure 4.2), by hand freeze quenching the reaction at *ca*. 1s and measuring the sample using CW-EPR. The assignment of **Int2** as a tyrosyl radical was corroborated by stopped-flow experiments with the Y164F mutant which does not contain the tryptophan residue in the 164 position and did not show the formation of **Int2**.

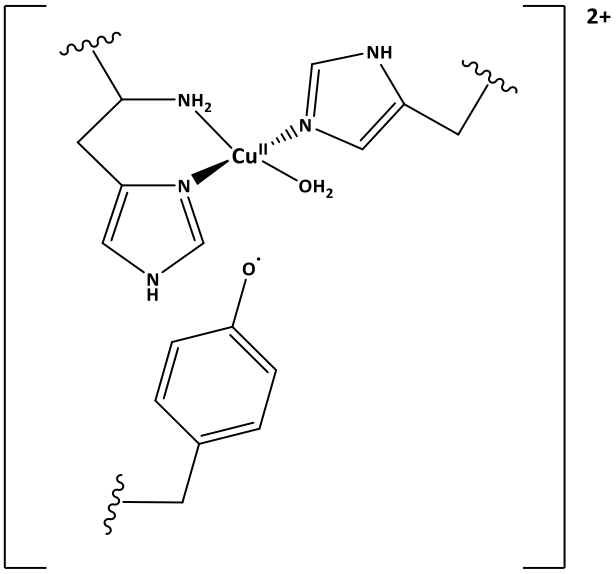


Figure 4.2: **Int2**; Cu(II)-tyrosyl LsAA9 complex expressed in *E. coli*.

Through stopped-flow it was found that **Int1** is formed in a greater quantity and forms/ decays at a slower rate in the Y164F mutant of *Ls*AA9 compared to the wild type (WT) (Figure 4.3). The rate of formation of **Int1** in Y164F is 29.9±0.05 $s^{-1}$ and in the WT is 38.9±0.1 $s^{-1}$.[125] **Int2** is not formed in the Y164F mutant due to the substitution of the tyrosine residue for phenylalanine.

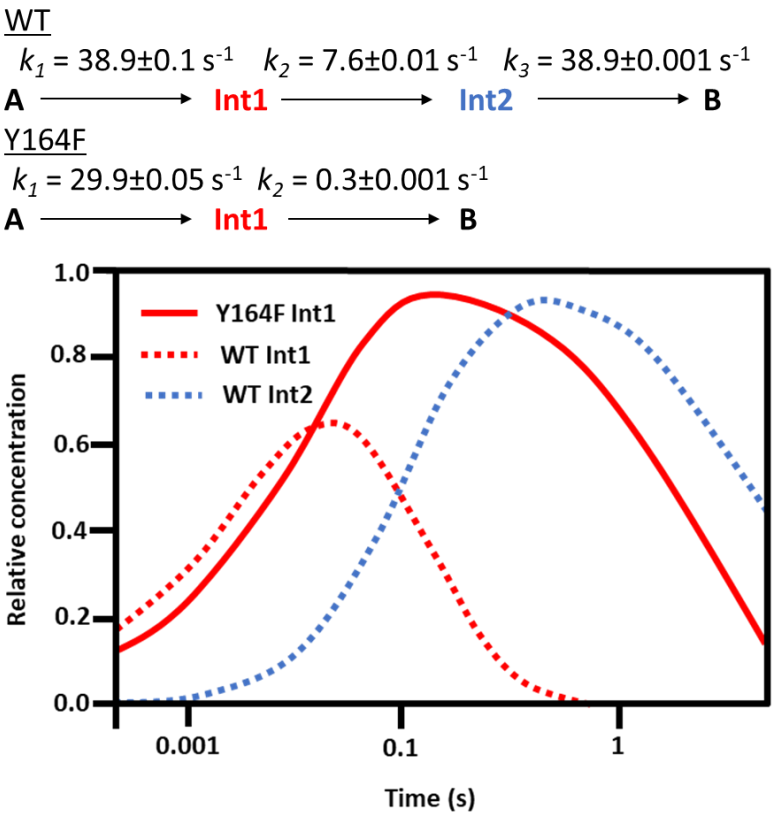


Figure 4.3: Reaction scheme for *Ls*AA9 WT and Y164F mutant with rate constants and a plot of the relative concentrations of Int1 (red) and Int2 (blue) formed by Cu(I) WT (dashed) and Cu(I) Y164F mutant (solid) *Ls*AA9 overtime, measured using UV-vis stopped flow. Figure adapted from Zhao *et al*.[125]

This chapter explains the process of characterising **Int1** which was identified by Zhao *et al*.

### 4.1.2 Freeze quenching method to trap Int1

Rapid freeze quenching is a technique used to isolate shorted lived intermediates on a millisecond timescale, first developed by R. C. Bray in 1961[157]. Reagents are mixed using a suitable flow rate and aged using a delay line before being ejected and rapidly frozen. The resulting frozen suspension is then packed into the receptacle of choice for spectroscopic analysis. Commonly, trapping and packing are undertaken in an isopentane/ liquid nitrogen bath at *ca.* −160 °C to maintain quenching of the reaction.[158]

There are several experimental considerations when using freeze quenching techniques to isolate a short-lived species. The ageing time is the time in which reagents are allowed to react before the reaction is quenched. The ageing time of the sample is dependent on the three stages; sample

mixing (which is determined by the flow rate, volume of the reagents and the time spent in the delay line), the ejection time which is the time between expulsion from the freeze quench to the freezing bath, and the freezing time (Equation 4.1). The freezing time is determined by three factors. The first factor is the magnitude of the difference between the initial reactant temperature and the freezing temperature; this can be reduced by cooling the reagents before mixing. In the BioLogic SFM 2000 system used for this work, cold water at *ca.* 3 °C was circulated through an umbilical cord which surrounds the internal syringes to reduce any temperature difference. The second factor is the time for the liquid to solid transition and the third factor is the time for sub-cooling of the frozen matter to the temperature of the cold bath. The latter two factors are largely dependent on the particle size of the frozen sample.

Whilst the ejection time is largely fixed at *ca.* 1 ms and the freezing time is around 4-5 ms in a liquid nitrogen/ isopentane bath, the sample mixing time is constrained by the limits of volume, flow rate and delay line parameters which are dependent on the model of freeze quench used and the viscosity of the solutions. In the example of the BioLogic SFM-2000 model, the flow rate must be between 0.5 and 5 ml/s to achieve turbulent mixing of the reagents, meaning the quickest ageing time that can be achieved is *ca.* 9 ms. However, the reactant volumes and flow rate also influence the size of the particles; when the flow rate is faster, larger frozen particles result, which in turn affects two things. Firstly, the size of the frozen particles affects the freezing time (which contributes to the overall ageing time); larger frozen particles take longer to freeze than smaller frozen particles. Secondly, larger frozen particles are significantly easier to pack into a suitable specimen holder for subsequent analysis (e.g. an EPR tube). This dichotomy requires a careful balance of obtaining a fast freezing time in order to trap the required species before reacting further, but also being able to pack the product effectively in order to be useful.

Equation 4.1

$$Aging\ time = \frac{reactants\ volume}{flow\ rate} + delay\ line\ time + \ ejection\ time + freezing\ time$$

The speed of freezing can also cause inconsistencies in the EPR data obtained. D. P. Ballou has suggested that in some compounds, particularly copper proteins, artifacts such as differing line shapes are observed in the EPR due to the rapid freezing of the sample and therefore the EPR should be interpreted with caution[159], this is particularly important for the study of LPMOs as they are mono-copper metallo-proteins.

Rapid freeze quenching to trap LPMO intermediates

The packing of the frozen sample into sample holders for spectroscopic studies (e.g. EPR) raises further experimental issues for consideration, and is the most challenging part of the freeze quenching process. The packing density is the volume of the frozen sample compared to the total sample volume, which has significant implications on the magnitude of the signal in EPR spectra and is highly irreproducible between freeze quenched samples.[160] Even with practice, the uncertainties in packing density between samples can range between 5 - 10 %, and between packing methods can vary between 40 – 60 %.[157,159,161–164] The "traditional" packing method is whereby the sample is ejected into an isopentane/ liquid nitrogen bath (*ca.* −150 °C) and is then packed into a sample tube that is fitted to a funnel suspended in a separate isopentane/ liquid nitrogen bath using a metal rod with a Teflon tip.[159] Variations of this method have been proposed such as the use of a vacuum attached to the bottom of the sample tube[164], or the use of copper wheels partially submerged in liquid nitrogen to freeze and crush the sample[163].

Another challenge pertaining to the preparation of freeze quenched samples is the loss of sample through poor packing efficiency. The packing efficiency is the amount of sample that can be packed in the sample tube compared to the amount of sample trapped. A proportion of the sample can easily be lost in the transfer from the freezing bath to the packing funnel as well as during the packing process through the smashing of the frozen particles and transfer into the sample tube. Using traditional methods of packing the packing efficiency is only *ca.* 20 %, meaning that five times as much volume of the product needs to be trapped to make a useful sample.[164] Poor packing efficiency means that freeze quenching is uneconomical, this is problematic in the study of metalloproteins because of the time required to produce large volumes/ concentrations.

Rapid freeze quenching has previously been employed to study a variety of protein intermediates and has previously been used to study intermediates formed in LPMOs.[98] A previous LPMO study combined rapid freeze quenching with EPR and MCD spectroscopy to characterise tyrosyl and tryptophanyl radicals which are formed on the addition of peroxide to Cu(I) *Hj*AA9, which the authors concluded are formed as part of a minor reaction pathway in the re-oxidation to Cu(II) in the absence of substrate.[98]

The following chapter documents the characterisation of **Int1** using rapid freeze quenching methods with EPR and X-ray spectroscopy.

## 4.2 Methods

### 4.2.1 Rapid freeze quench set up

The following series of experiments were undertaken to evaluate the capabilities of the BioLogic SFM-2000 instrument used in this study to establish the achievable experimental parameters.

#### *4.2.1.1 Methylene blue oxygen indicator*

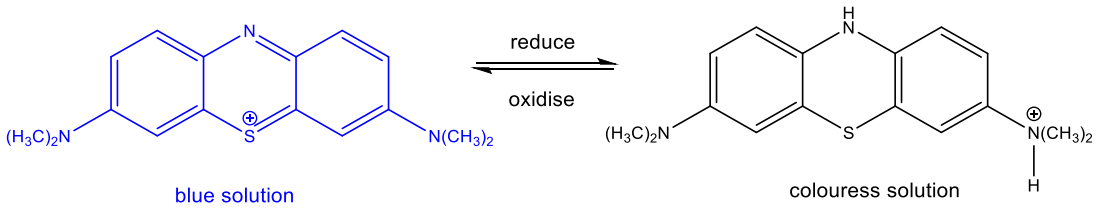


Figure 4.4: Scheme showing the reversible oxidation and reduction of methylene blue.

The development of a successful anaerobic rapid freeze quenching technique was assessed using the air-sensitive complex methylene blue. In the absence of oxygen, a dark blue solution of methylene blue in anaerobic water (1 mL, 0.25 mM) was titrated against a solution of ascorbic acid in anaerobic water (1.00 M) to give a colourless solution. One of the internal syringes of the freeze quench apparatus was flushed with anaerobic water and then loaded with the reduced methylene blue solution. The solution was allowed to sit in the internal syringe for five minutes before the solution was ejected. The UV-vis absorbance at 660 nm of the methylene blue solution ejected from the BioLogic SFM-2000 after different washing preparations was measured at various time points.

The internal syringe washing preparations tested were:

- no additional washing procedures
- washed with 6 mL degassed water
- washed with sodium bisulfite (1.00 x$10^{-4}$ M, 0.5 mL) followed by 6 x 2 mL degassed water

The results of these experiments are detailed in section 4.3.1.

## 4.2.2 Sample preparation

### *4.2.2.1 LsAA9 Y164F trapping*

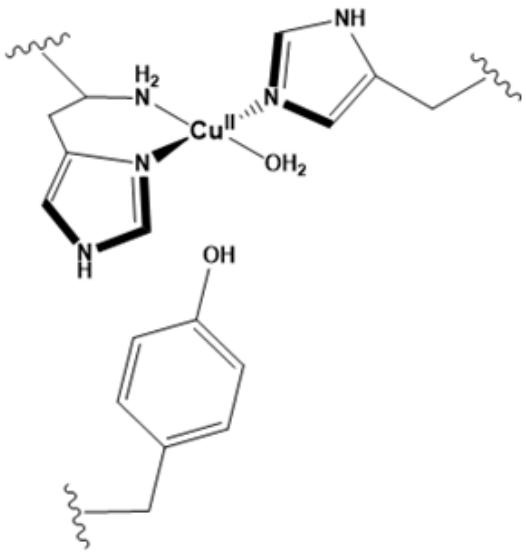


Figure 4.5: Active site structure of LsAA9 LPMO

*Ls*AA9 Y164F for the HERFD-XANES experiments was prepared by Dr Jingming Zhao and for the conventional XAS experiments was prepared following the method outlined in section 2.1.1. *Ls*AA9 Y164F (0.8 mM) in KPi buffer (1.5 mL, 50 mM, pH 6) was reduced using 0.8 equivalents of sodium ascorbate under anaerobic conditions to give a final concentration of Cu(I) LsAA9 Y164F of 0.64 mM. The Biologic SFM 2000 was flushed with a sodium bisulfite solution ($1.00 \times 10^{-4}$ M, 0.5 mL) and then degassed water and KPi buffer (12 mL) to achieve anaerobic conditions, Cu(I) LsAA9 Y164F (1.5 mL, 0.64 mM) was then loaded along with m-CPBA (15 µL, 64 mM) into separate syringes and cooled to 3 ˚C. The solutions were programmed to mix in a 1:1 molar ratio at 100 ms before being trapped either in liquid nitrogen for EPR measurements or onto a liquid nitrogen cooled aluminium sample holder for HERFD-XANES and conventional XAS measurements (Figure 4.11). The final copper concentration of the samples was approximately 0.63 mM.

## 4.3 Results and discussion

### *4.3.1* Oxygen contamination

The Cu(I) LPMO reaction with *m*-CPBA to form **Int1** occurs under anaerobic conditions, however, there are multiple sources of potential oxygen exposure in the freeze quench process (Figure 4.6). The first place the sample can be exposed to oxygen is in the external syringe, this risk is reduced by preparing the sample in the external syringe in an anaerobic glovebox. From the external syringe the solutions are then loaded into the internal syringes, which without intervention will contain air, once again exposing the sample to oxygen. Oxygen exposure also occurs during the flying time; once the sample is ejected it flows through air for approximately 1 ms at the flow rates used. To minimise oxygen exposure from the flying time the freezing bath in the sample collection receptacle should be held as close to the ejection nozzle as possible. The isopentane or liquid nitrogen bath commonly used to rapidly freeze the sample contains dissolved oxygen[165], which the sample is exposed to in the time it takes to freeze (freezing time of the sample is approximately 5 ms)[166].

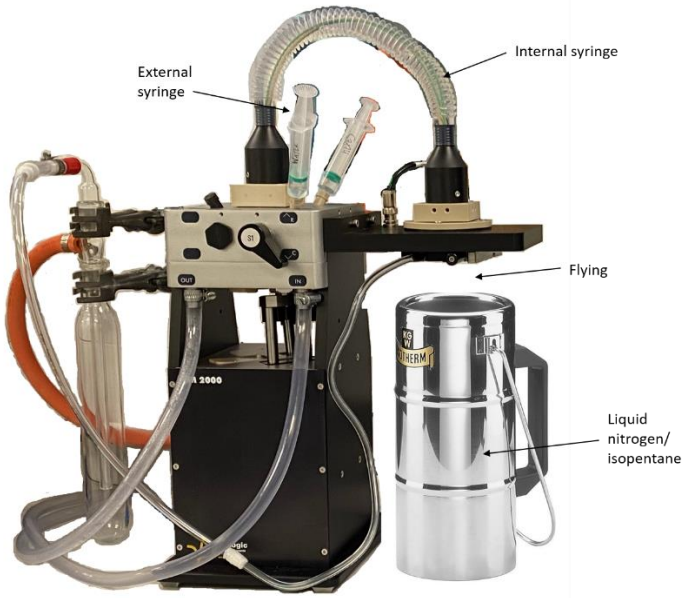


Figure 4.6: Diagram of freeze quench apparatus with the areas where the sample could be exposed to oxygen labelled.

Experimental conditions to reduce the sample's oxygen exposure in the internal syringe to create anaerobic conditions have been investigated. Methylene blue was chosen to be the indicator of oxygen exposure due to its reactivity with oxygen[167]. The reduced form of methylene blue (leuco methylene blue) is colourless and turns a deep blue on oxidation (Figure 4.4). The exposure to oxygen of partially reduced methylene blue was monitored by measuring the UV-vis absorbance at 660 nm[168–170] (Figure 4.7). It is clear that when the internal syringes are unwashed there is significant

oxygen contamination, with the UV-vis absorbance of the sample that has passed through the syringes higher than that of the methylene blue solution before it was reduced. When washed with degassed water (6 mL) there is a significant reduction in oxygen exposure as the solutions are not oxidised beyond that of the original oxidised methylene blue solution, however there is still oxygen contamination evidenced as the absorbance of these solutions are significantly higher than that of the reduced methylene blue solution before it is loaded into the freeze quench. The best conditions tested were found to be when the freeze quench was washed with an oxygen scavenger and then flushed with water, from shots three onwards the solutions were within error of the reduced solution before it was loaded into the freeze quench.

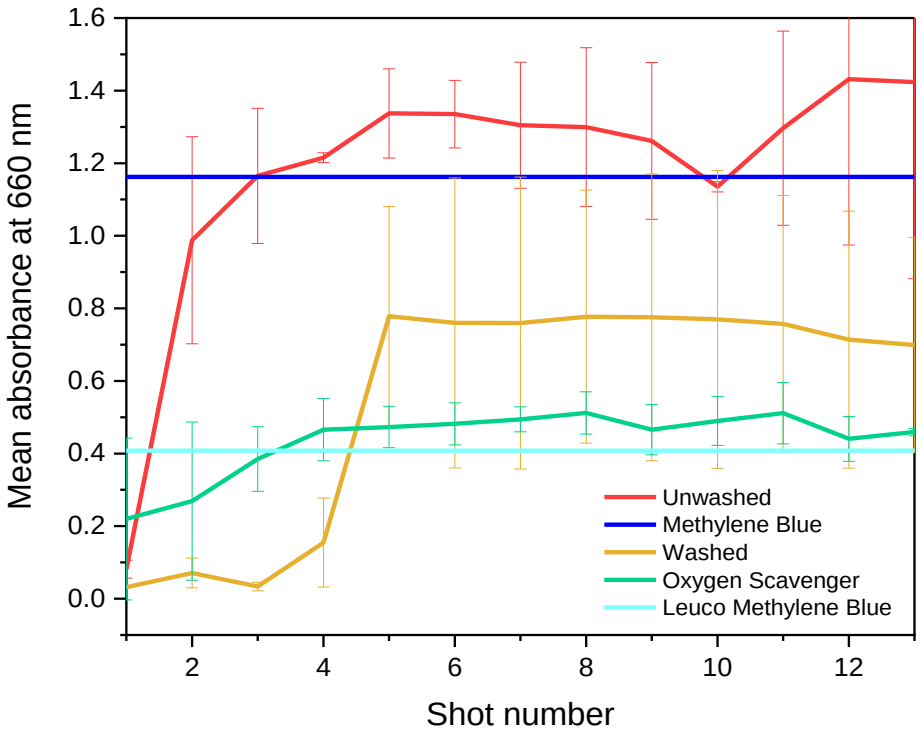


Figure 4.7: Graph showing the mean and standard deviation UV-vis absorbance at 660 nm over three repeats shots of reduced methylene blue from the freeze quench when the freeze quench was: unwashed (red), washed with 6 mL degassed water (yellow) and washed with sodium bisulfite ($1.00 \times 10^{-4}$ M, 0.5 mL) and 6 x 2 mL degassed water (green). The absorption (660 nm) of the methylene blue solution before it was reduced (dark blue) and the leuco methylene blue solution before it was loaded into the freeze quench (cyan) are also plotted.

Rapid freeze quenching to trap LPMO intermediates

The oxygen scavenger used in this experiment was sodium bisulfite ($NaHSO_3$). Sodium bisulfite is used as an oxygen scavenger in a variety of applications such as the prevention of oxidation of foods, drugs and sewerage systems[171–174]. Sodium bisulfite dissociates into sodium and sulfite ions in water, which then react with oxygen to produce hydrogen and sulfite ions as described in Scheme 4.1[175].

Scheme 4.1

$$NaHSO_{3(aq)} \leftrightarrow Na^{+}_{(aq)} + HSO_3^{-}{}_{(aq)}$$

$$HSO_3^{-}{}_{(aq)} \leftrightarrow SO_3^{2-}{}_{(aq)} + H^{+}_{(aq)}$$

$$2SO_3^{2-}{}_{(aq)} + O_{2(g)} \leftrightarrow 2SO_4^{2-}{}_{(aq)}$$

$$2HSO_3^{-}{}_{(aq)} + O_{2(g)} \rightarrow 2SO_4^{2-}{}_{(aq)} + 2H^{+}_{(aq)}$$

The first two shots in all the previously described experiments have a lower absorbance at 660 nm than the standard methylene blue solution ($t = -7.80$, $p < 0.01$) (Figure 4.8). The third shot of methylene blue solution onwards has the same absorbance at 660 nm within error as the standard solution ($t = -1.53$, $p > 0.05$). Based on the relative volumes used i.e. 12 mL of degassed water to flush out the oxygen scavenger and 100 µL shots, the likely cause of the discrepancy in UV-vis absorbance is dilution rather than oxygen scavenger contamination. The first two shots likely contain residual solvent used to flush the internal syringes and this is due to the discrepancy between the volume of solvent injected into the system and the volume that the software recognises as being in the system. As a result of this finding, it can be concluded that the first two shots of any further freeze quenching experiments using this system should be discarded and any interpretation of data from the first three shots should be made with caution.

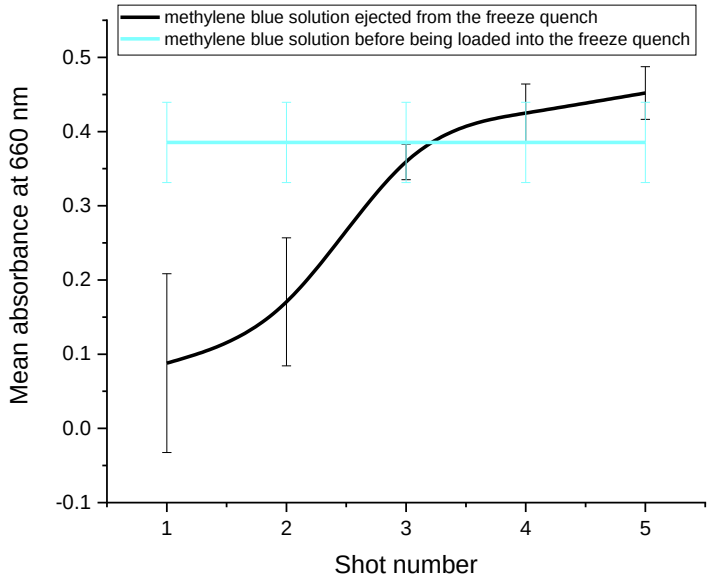


Figure 4.8: Mean absorbance at 660 nm and standard deviation of leuco methylene blue ejected from the freeze quench at increasing shot numbers, averaged over nine experiments with the time between shots varying between 2 and 15 minute intervals (black). The mean absorbance of the leuco methylene blue and standard deviation over 9 experiments is also plotted for reference (cyan).

The experiments described with methylene blue have established a method for reducing sample oxygen exposure in the Biologic SFM-2000 to facilitate rapid freeze quenching of anaerobic reactions, which has been used to trap **Int1**. The efficiency of rapid freeze quenched sample preparation has also been improved by establishing that the first two shots do not include the reaction products and should be discarded so as not to dilute the samples intended for spectroscopic characterisation.

### *4.3.2* Development of packing techniques

The packing process of freeze quenching is whereby the trapped frozen material is “packed” into the receptacle of choice for characterisation of the sample using various techniques. This aspect of the freeze quenching process is not trivial and can determine the quality of the data that can be recorded from the sample. To improve the quality of the data that can be obtained from the freeze quenched samples the packing process has been refined.

The “traditional” packing method is whereby the sample is ejected from the freeze quench into a liquid nitrogen/ isopentane bath, where it is frozen. Once frozen, the sample can be packed into

sample holders and the isopentane is then removed with a thin syringe. One of the problems encountered with the "traditional" packing method is that it results in a significant volume of isopentane trapped in the sample, as the samples are stored in liquid nitrogen causing the isopentane to freeze within the spaces in the frozen sample (Figure 4.9). Trapped isopentane in freeze quenched samples is known to create increased noise and affect the signal intensity when measured by EPR. To mitigate this issue, we decided to trap the samples directly in liquid nitrogen.

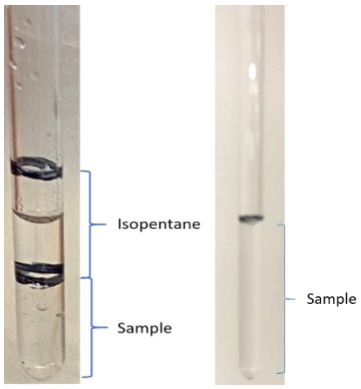


Figure 4.9: Melted freeze quenched EPR sample trapped in an isopentane bath (left) and melted freeze quenched sample trapped in liquid nitrogen (right).

To pack freeze quenched samples for XAS analysis using Lindemann tubes for use with a liquid nitrogen cryojet, an adapter to fit the packing funnel for EPR tubes was designed and manufactured (Figure 4.10). It was required that the adapter must be able to hold the significantly smaller XAS tubes securely in the same funnel that is designed to hold the EPR tubes, it must be able to withstand temperatures down to −200 °C and keep the XAS sample tube at the temperature of the bath it is suspended in. The XAS sample adapter has a larger hole where the sample tube sits which is drilled so that it is just long enough to hold the Lindemann tube to the correct depth. Then a smaller hole was drilled the rest of the way through the adapter to ensure the sample is immersed in the isopentane/ liquid nitrogen bath. The funnel adapter was made from Teflon (poly(1,1,2,2-tetrafluoroethylene)); the same material as the funnel and it is essentially chemically inert and maintains durability down to −268 °C. [176] A rubber ring was used to plug the gap between the XAS sample adapter and the Lindemann tube to prevent loss of frozen sample and to facilitate the packing process.

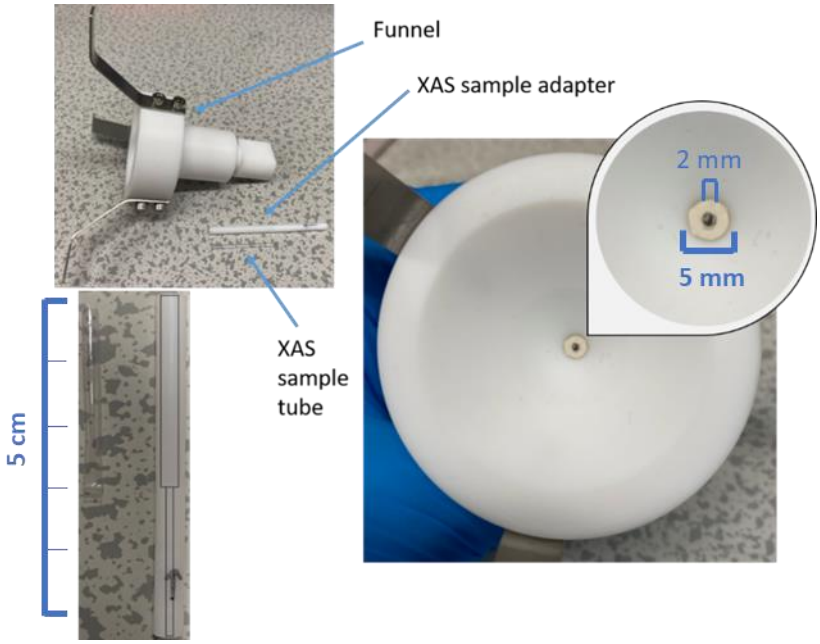


Figure 4.10: XAS sample adapter designed to allow freeze quenched XAS samples to be packed into Lindemann tubes using the funnel for packing EPR samples. Funnel, XAS sample adapter and XAS sample tube (top left) Lindemann tube and XAS sample adapter with markings to show where the adapter has been hollowed out in black (bottom left) and the above view of the XAS sample adapter fitted into the funnel with a rubber ring to prevent the frozen sample from being lost (right).

In the XAS experiments where a liquid helium cryostat was used, the freeze quenched samples needed to be packed into pure aluminium disk sample holders. To pack the freeze quenched samples, the aluminium plates were submerged in liquid nitrogen for a few minutes and then quickly and carefully held with tweezers under the freeze quench ejection port (*ca*. 1 cm from the ejection port), and the sample ejected directly onto the plate where it freezes within a few milliseconds (Figure 4.11). The sample holder containing a shot of frozen sample was then submerged in liquid nitrogen before the process was repeated until the sample holder had a good coverage of the frozen sample.

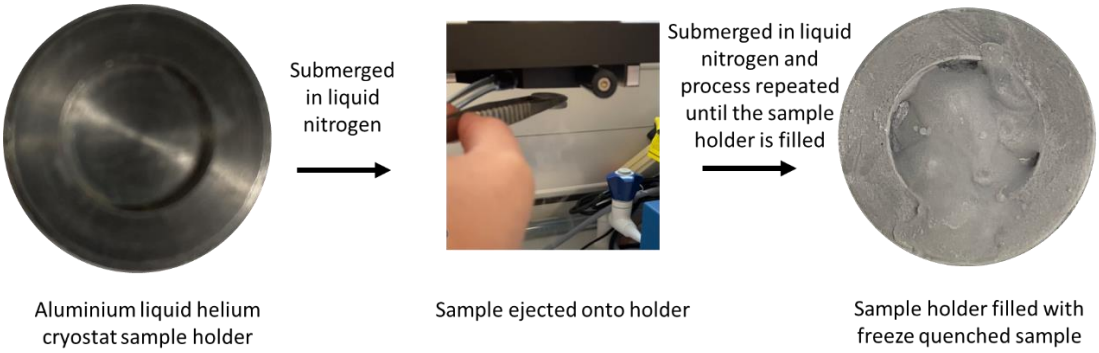


Figure 4.11: Preparation of rapid freeze quenched sample for measurement in a liquid helium cryostat.

### 4.3.3 Spectroscopic characterisation of rapid freeze quenched AA9 histidyl-radical

The work described in this chapter has been published in Zhao, J. *et al.* Mapping the Initial Stages of a Protective Pathway that Enhances Catalytic Turnover by a Lytic Polysaccharide Monooxygenase. *J Am Chem Soc* **145**, (2023). This chapter details the characterisation of **Int1** through rapid freeze quenching to prepare samples for spectroscopic analysis using EPR, HERFD-XANES, and XAS. The characterisation of **Int1** follows from the identification of **Int1** and **Int2** as part of an LPMO oxidative damage protection mechanism and the characterisation of **Int2** which was completed by collaborators in the experiment.

The AA9 LPMO used for the following experiments was *Ls*AA9 Y164F mutant, in which tyrosine in the 164 position is substituted for phenylalanine (Figure 4.12). The *Ls*AA9 Y164F mutant was used because of its slower rate of formation (29.9±0.05 $s^{-1}$ *Vs*. 38.9±0.1 $s^{-1}$) and decay of **Int1** as well as increased accumulation of **Int1** compared to the *Ls*AA9 WT (Figure 4.3). A slower rate of formation/ decay and increased accumulation of **Int1** in *Ls*AA9 Y164F means that there is a greater chance of trapping **Int1** by rapid freeze quenching.

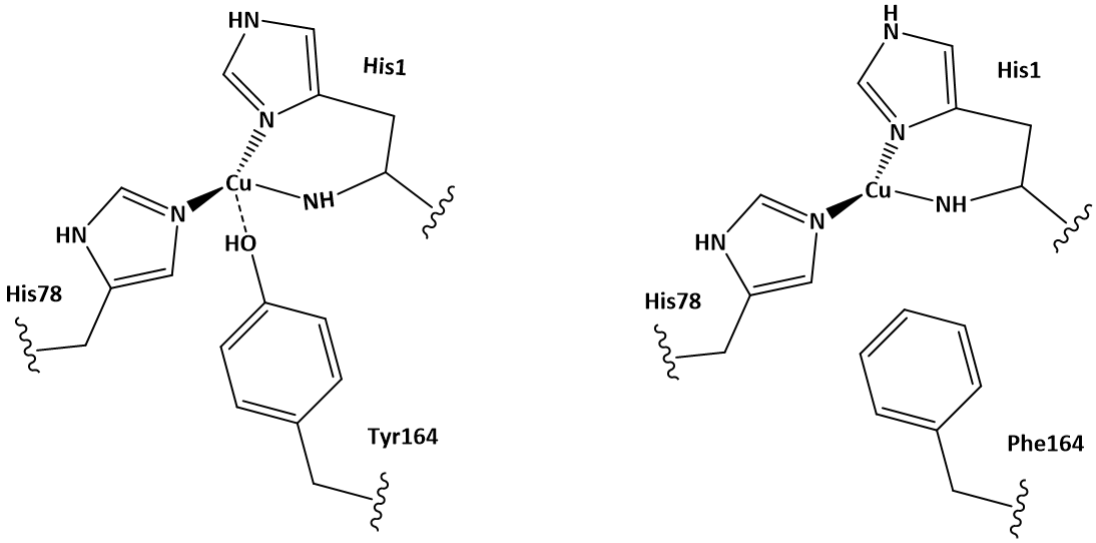


*Ls*AA9 WT *Ls*AA9 Y164F

Figure 4.12: Active site structure of *Ls*AA9 WT (*left*) and LsAA9 Y164F mutant (*right*).

#### *4.3.3.1 CW-EPR of Int1*

CW-EPR of the Cu(II) *Ls*AA9 Y164F resting state was recorded to ensure consistent protein preparation between samples and copper loading of the protein. The EPR spectrum is also used to check that there is no free copper that would interfere with spectroscopic measurements and as a standard with which to compare intermediate species. The Cu(II) *Ls*AA9 Y164F spectrum shows a single Cu(II) species with spin Hamiltonian parameters $g_z = 2.265$, $A_z = 445$ MHz, which is consistent with a type II copper site as defined by Peisach-Blumberg (Figure , Table 4).[51] The *g*-values for Cu(II) *Ls*AA9 Y164F are $g_1 < g_2 << g_3$ which is consistent with a spectral envelope with significant $d(x^2\text{-}y^2)$ SOMO character, alluding to sigma donation in the equatorial plane. Whilst accurate determination of $g_1$ and $g_2$ values was not possible, the fact that an accurate simulation could only be achieved when $g_1 \neq g_2$, suggests the presence of $d(z^2)$ mixing. These Hamiltonian parameters are comparable to those of other Cu(II) LPMOs.[32,88]

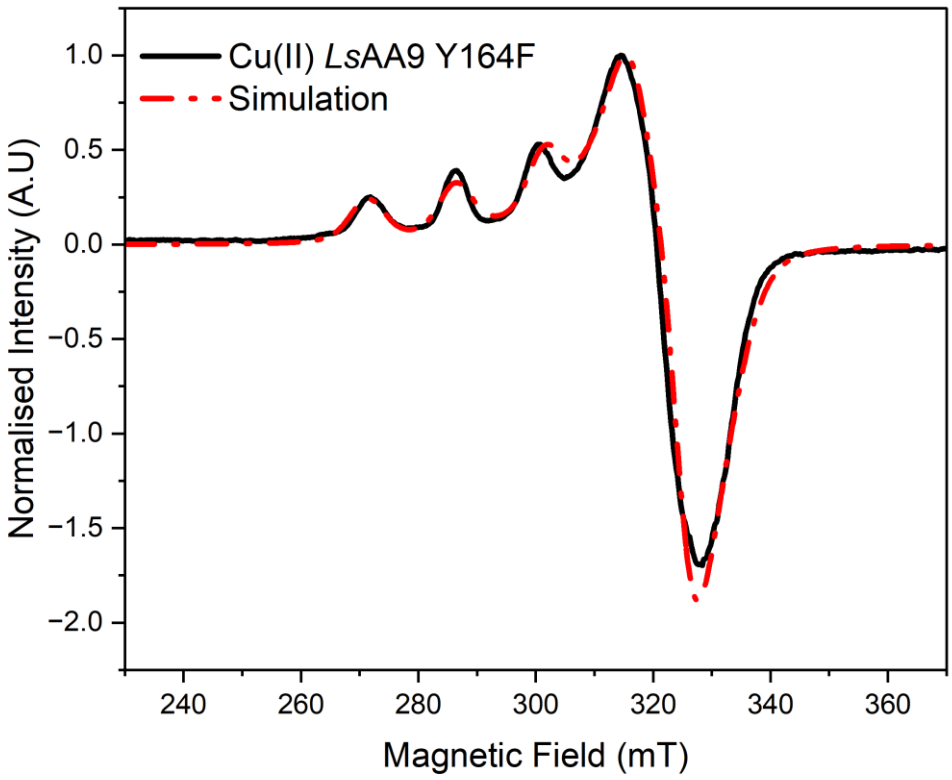


Figure 4.13: CW-EPR spectrum of Cu(II) LsAA9 Y164F (black) measured at 150 K, plotted with the simulated spectrum from EasySpin using the Spin-Hamiltonian parameters in Table 4.1 (red).

Table 4.1: Spin-Hamiltonian parameters used for the simulated CW-EPR spectrum of Cu(II) *Ls*AA9 Y164F

| | **A ($^{63,65}$Cu)† / MHz** | ***g*-tensor†** |
|---|---|---|
| **Cu(II) *Ls*AA9 Y164F** | \|[45 58 445]\| | [2.022 2.099 2.264] |

† Accurate determination of $g_x$, $g_y$, $|A_x|$ and $|A_y|$ values was not possible because of the nature of the perpendicular region, although satisfactory simulation could be achieved with the reported values.

To characterise **Int1**, rapid freeze quenched *Ls*AA9 Y164F **Int1** samples were studied using EPR, HERFD-XANES, and conventional XAS to determine the oxidation state and electronic structure of **Int1**. CW-EPR showed that **Int1** is EPR silent. The sample was annealed to confirm the presence of *Ls*AA9 Y164F in the sample, as the sample was warmed above 220 K a Cu(II) signal consistent with

the Cu(II) *Ls*AA9 Y164F signal appeared (Figure 4.14). The EPR spectrum of **Int1** showed no signals that would be commensurate with a triplet state, this combined with **Int1** being EPR silent, leads to the conclusion that **Int1** is likely to be $S = 0$ spin-singlet.

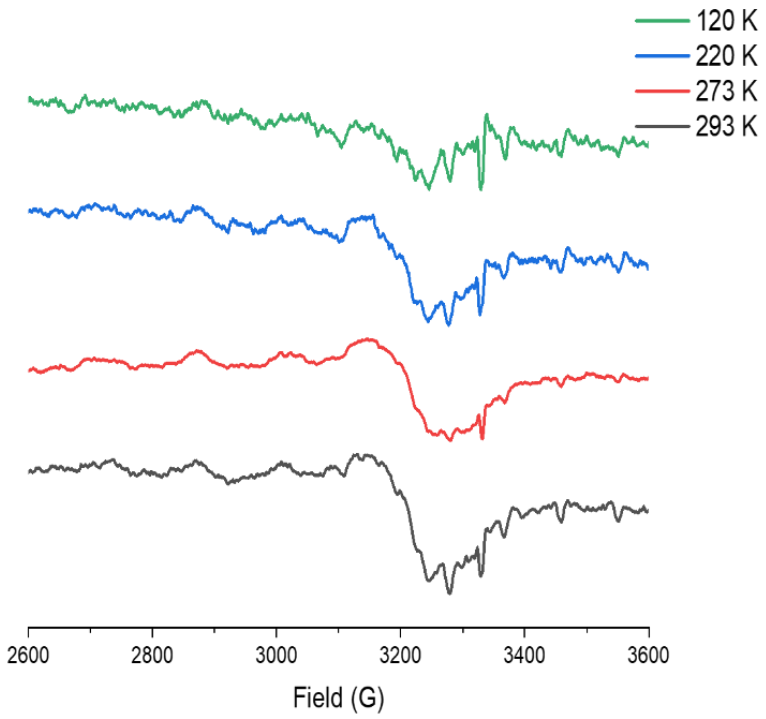


Figure 4.14: CW-EPR spectra of **Int1** annealed between 120 K and 193 K.

#### *4.3.3.2 HERFD-XANES of Int1*

Preliminary HERFD-XANES experiments to determine how to minimize the effects of photoreduction whilst maintaining a suitable signal-to-noise ratio in the freeze quenched and Cu(I)/Cu(II) *Ls*AA9 Y164F samples were undertaken. The samples were measured in a liquid helium cryostat at 10 K and each scan was measured in a new position within the frozen sample to limit beam damage, as described in Section 2.3. As Figure 4.15 shows, under these conditions, there is no significant difference in the position of the Cu K-edge, which will be used to determine the oxidation state of Int1, nor are there changes in the pre-edge when two consecutive scans are taken in the same sample position. However, the second scan shows a small increase in the intensity of the rising edge peak associated with the 1s to *4p* transition at *ca*. 8982.2 eV as a result of beam damage. Therefore, under these conditions, we can be confident in the assignment of oxidation states and pre-edge features from our subsequent measurements but care must be taken in the interpretation of changes in the rising edge 1s to *4p* region.

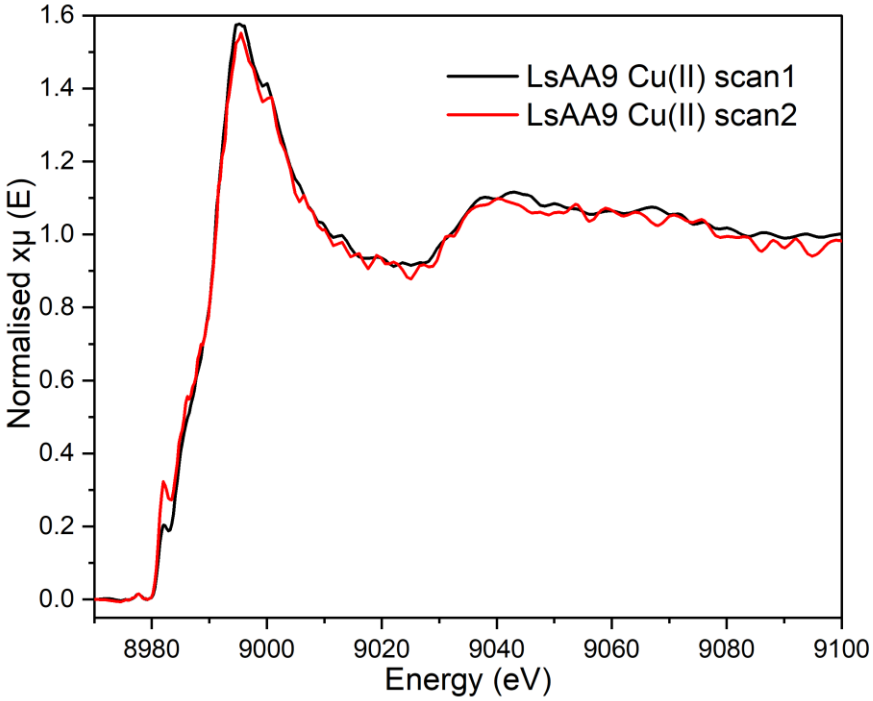


Figure 4.15: HERFD-XANES spectra taken consecutively in the same sample position.

The Cu(I), Cu(II) and **Int1** HERFD-XANES spectra are a merge of 40 spectra taken in different sample positions (Figure 4.16). The Cu(I) and Cu(II) *Ls*AA9 Y164F HERFD-XANES spectra were measured as standards for comparison with **Int1**. The differences in the Cu(I) *Ls*AA9 Y164F and Cu(II) *Ls*AA9 Y164F spectra are commensurate with literature spectral features of Cu(I) and Cu(II) complexes respectively (Figure ). The Cu(II) *Ls*AA9 Y164F HERFD-XANES spectrum shows the K-edge position at 8977.5(3) eV, and a dipole disallowed, quadrupole-allowed 1s–*3d*($x^2$–$y^2$) transition at 8977.6(3) eV, which is consistent with that of literature Cu(II) assignments and previous LPMO XAS data.[1,117,151] Conversely, the K-edge position of the Cu(I) *Ls*AA9 Y164F HERFD-XANES is lower in energy than the Cu(II) K-edge at 8980.8(3) eV, and an intense rising edge 1s to *4p* transition at 8982.0(3) eV and a less intense white line comparatively to that of Cu(II) can be seen.

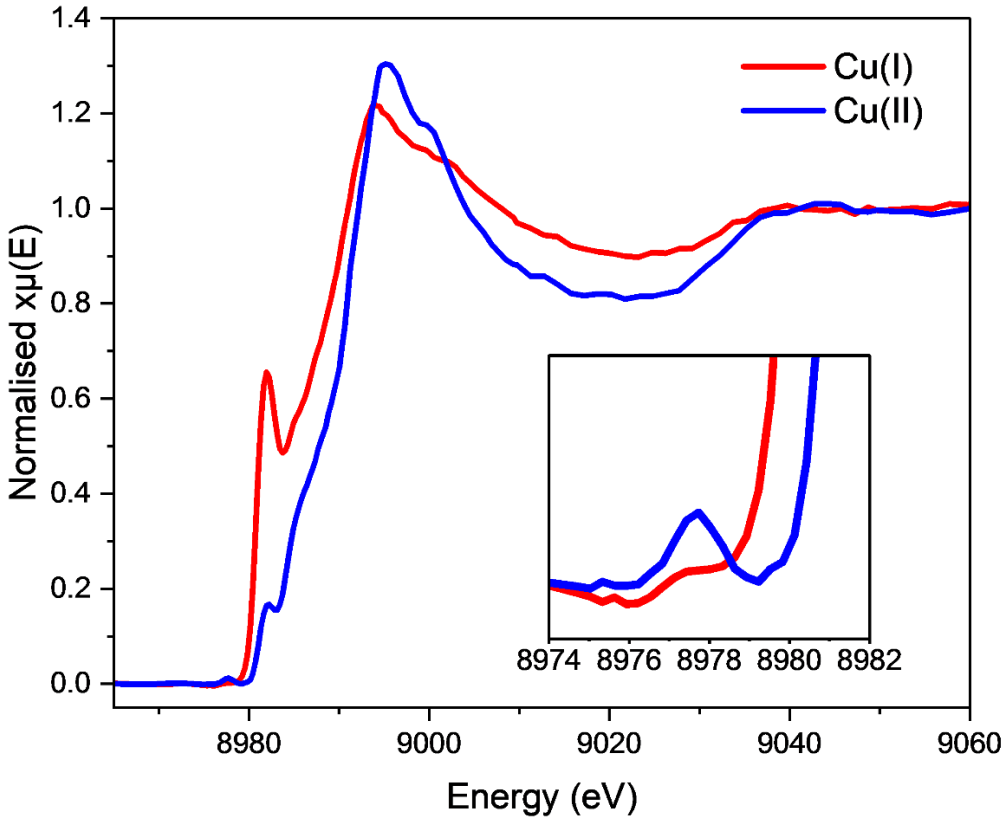


Figure 4.16: Cu(I) and Cu(II) *Ls*AA9 Y164F HERFD-XANES spectra, with an inset spectrum showing the pre-edge region.

The HERFD-XANES spectrum for **Int1** *Ls*AA9 Y164F shows a 1s to *3d* pre-edge transition in the same position as Cu(II) *Ls*AA9 Y164F at 8977.5(3) eV and is therefore commensurate with a Cu(II) oxidation state, but it has a further pre-edge peak at 8979.2(3) eV of similar intensity. **Int1** has an edge position of 8985.8(3) eV and a rising edge feature at 8981.9(3) eV. The rising edge feature in **Int1** is more intense than that of Cu(II) *Ls*AA9 Y164F and could arise from unreacted Cu(I) *Ls*AA9 Y164F present in the sample (Figure 4.17).

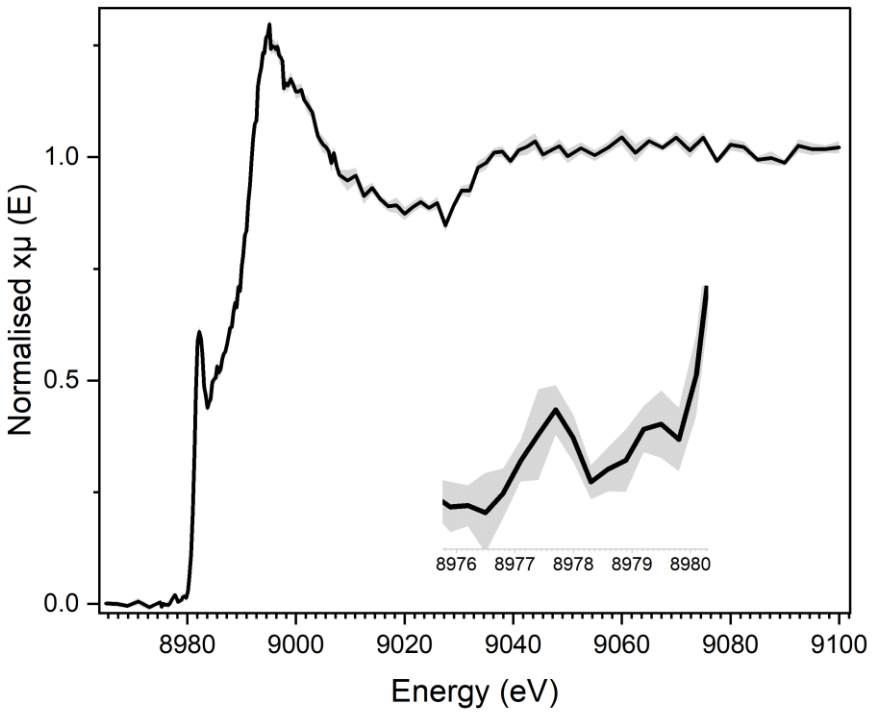


Figure 4.17: HERFD-XANES spectrum of **Int1** *Ls*AA9 Y164F. The inset show a zoom on the pre-edge region, plotted with the standard error.

#### *4.3.3.3 DFT of **Int1***

The HERFD-XANES of **Int1** suggests that Int1 is in the Cu(II) oxidation state. Further investigation into the double pre-edge transitions using TD-DFT along with the spectroscopic data recorded on Int1; UV-vis, EPR, and HERFD-XANES was undertaken to gain further information about **Int1** structure. Firstly, the pre-edge region can only be fit using a Gaussian and Lorentzian further confirming the presence of the double pre-edge peaks (Figure ). The peaks in the pre-edge region were fit using Larch[177] by fitting a baseline curve that follows the absorption edge, the baseline did not account for the two pre-edge peaks that were identified and therefore they were then fitted with appropriate models.

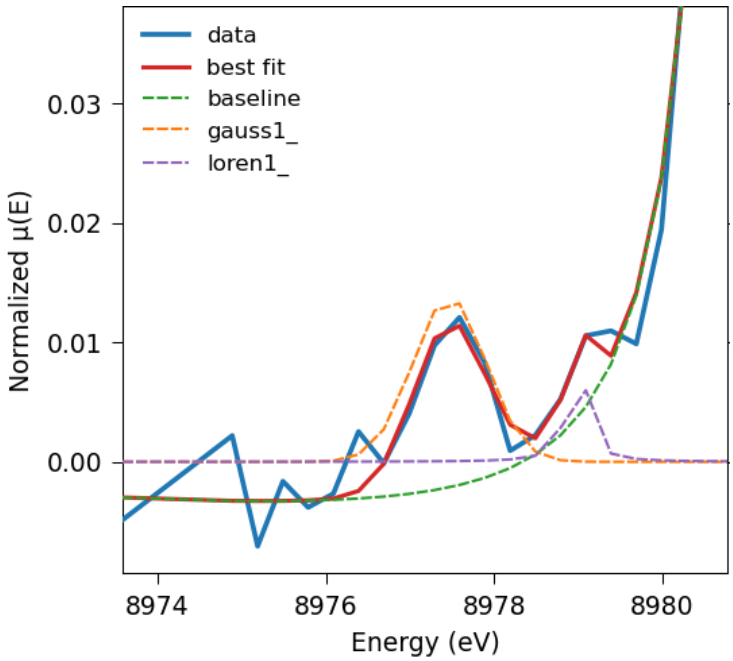


Figure 4.18: **Int1** HERFD-XANES pre-edge region plotted with fit using Gaussian and Lorentzian peaks.

The second pre-edge peak in the **Int1** HERFD-XANES spectrum most likely arises from a dipole-forbidden Cu 1s to a metal or ligand LUMO/SUMO transition in the Cu(II) oxidation state. This could be achieved through a radical ligand directly coordinated to the Cu(II) ion resulting in the ligand-based SOMO having metal character. A similar weak pre-edge transition has previously been observed using XAS of a Cu(II)-tyrosyl complex which was assigned to a Cu 1s-to-ligand charge transfer transition, though a tyrosyl complex can be ruled out in **Int1** as the tyrosine residue is not present in the Y164F mutant.[1] A Cu(II)-organic radical complex would also correspond to the EPR spectra of **Int1** which shows is EPR silent, despite an assignment of a Cu(II) oxidation state eluding to an *S* = 0 radical coupled Cu(II) ion. **Int1** gives an intense UV-vis absorption peak at 361 nm which is consistent with literature values of Cu(II)-imidazolyl complexes and Cu(II)-histidyl complexes which show UV-vis absorption peaks at *ca*. 360 nm, as well as isolated imidazolyl radicals which show peaks *ca*. 365 nm.[178–180] The conclusions from the experimental spectroscopic data that **Int1** is a Cu(II)-histidyl radical species, were confirmed through TD-DFT calculations. The output from TD-DFT calculations performed in collaboration with Dr. Peter Lindley showed two pre-edge peaks with equal intensity and an energy separation similar to that of the **Int1** HERFD-XANES experimental data (Figure 4.19).[125]

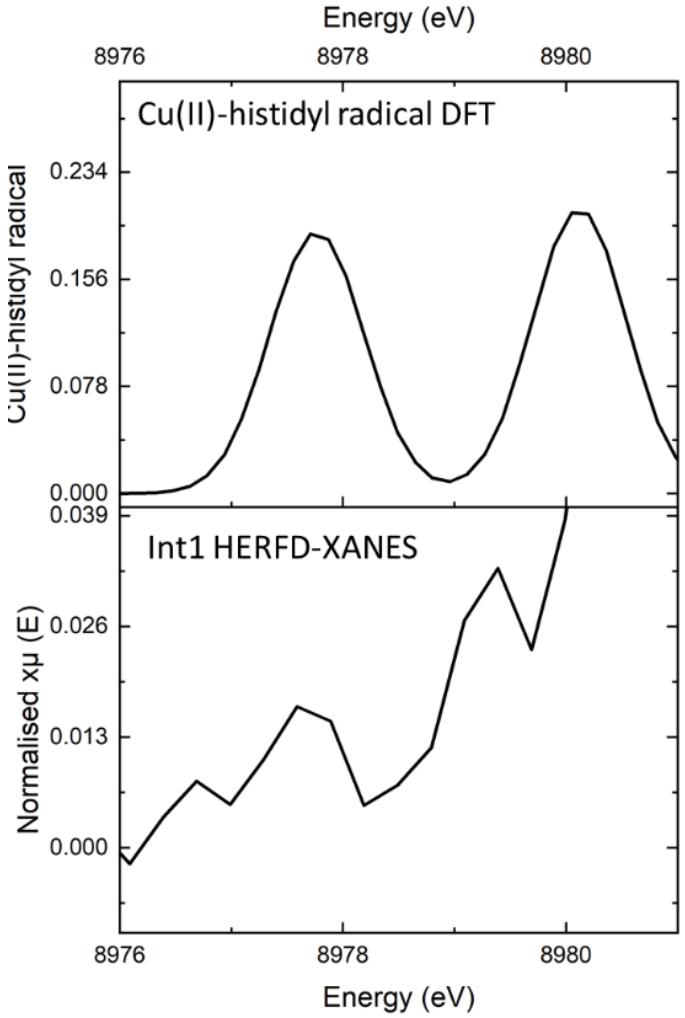


Figure 4.19: TD-DFT simulations of a Cu(II)-histidyl radical from Zhao *et al* [125] (*top*) and **Int1** HERFD-XANES pre-edge features.

#### *4.3.3.4 XAS of **Int1***

To further validate the conclusions extracted from the analysis of the EPR, HERFD-XANES, UV-vis data, and the TD-DFT calculations that **Int1** is a Cu(II)-histidyl radical, conventional XAS spectrum was recorded to ascertain structural information on the active site from the analysis of the EXAFS region. Whilst the aim of this experiment was to collect EXAFS on **Int1**, the XANES region recorded, although lacking the energy resolution required to observe the double pre-edge peaks, was in good agreement with the HERFD-XANES spectrum confirming consistency between the samples (Figure ). The Cu K-edge of **Int1** is at 8985.4(3) eV and shows a rising edge feature at 8982.2(3) eV as was also evident in the HERFD-XANES I**nt1** spectrum.

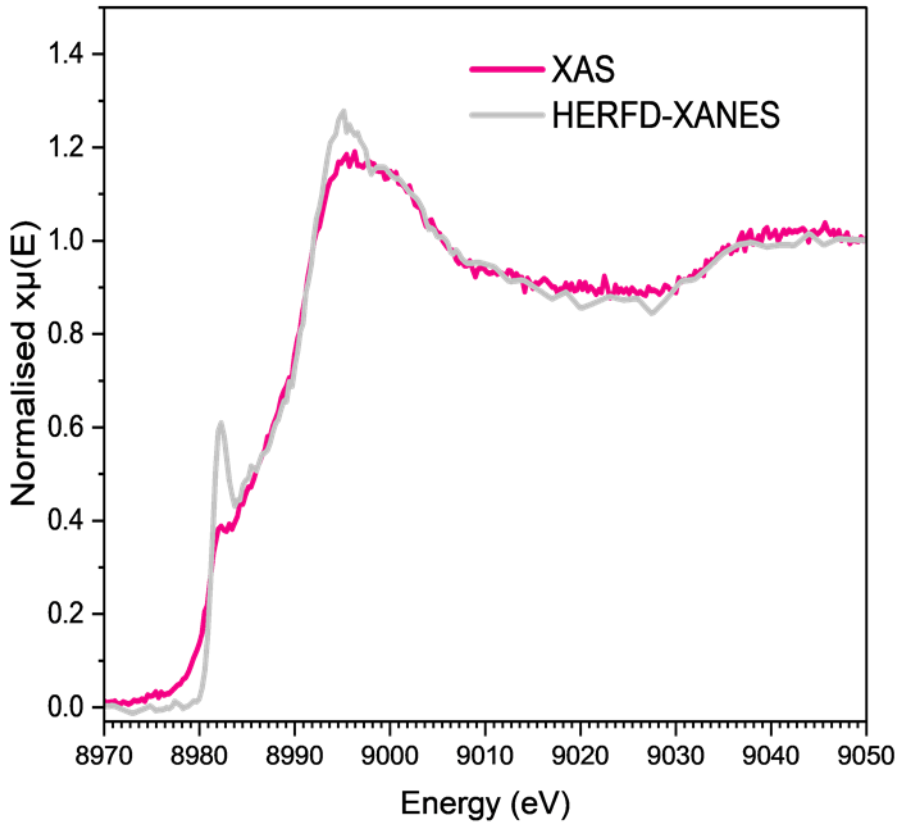


Figure 4.20: Comparison of the HERFD-XANES and the conventional XAS spectra of **Int1** *Ls*AA9 Y164F.

The comparison of the extracted EXAFS signal of Cu(I), Cu(II) and **Int1** *Ls*AA9 Y164F and the corresponding Fourier transform shows that there are slight structural differences between these three samples (Figure 4.21). **Int1** appears to have a structure most similar to that of Cu(II) *Ls*AA9 Y164F. All three of the samples display a double peak at *ca*. 4 $Å^{-1}$, this feature has previously been observed in imidazole complexes and has been coined a "camel-back", which arises from high frequency oscillations because of backscattering from atoms in the imidazole ring outside of the first coordination shell.[181] As such it stands to reason that this feature is observed in the *Ls*AA9 Y164F spectra as a result of the histidine brace.

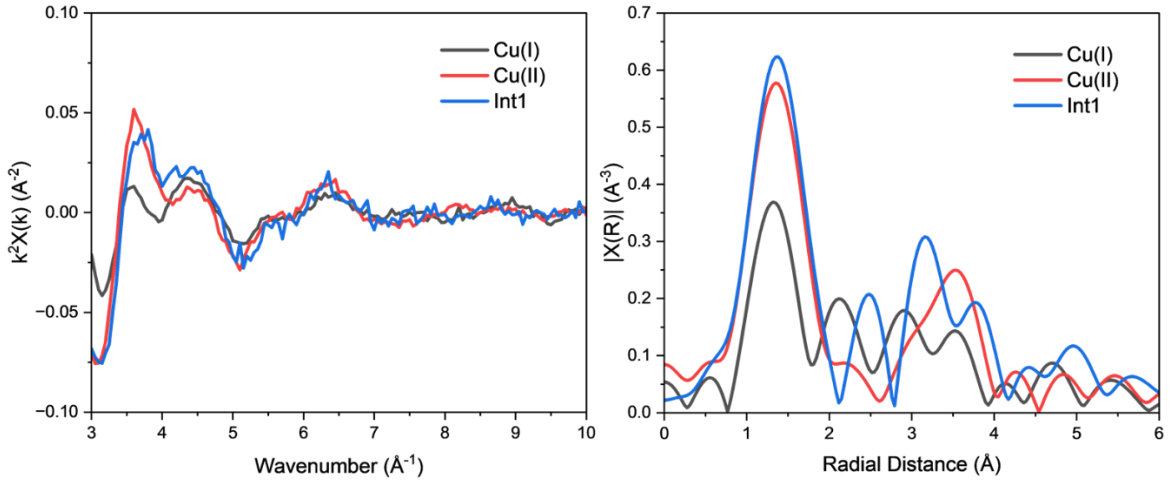


Figure 4.21: Comparison of the Cu(I), Cu(II) and **Int1** *Ls*AA9 Y164F extracted EXAFS signals in $k^2$ (*left*) and the corresponding magnitude of their Fourier transforms (k-range 3.4 – 9.3 $Å^{-1}$)(*right*).

Due to the low signal-to-noise ratio of these data sets, only a first shell fit could be undertaken with any confidence, so this was used to compare the first coordination sphere; coordination number and average bond lengths of ligands formally bonded to the copper ion.

The EXAFS fit of Cu(I) *Ls*AA9 Y164F was performed in R space. The results of the fit suggests that the copper centre is surrounded by three nitrogen ligands with an average bond length of 1.89(3) Å. This most likely corresponds to the histidine brace motif and is commensurate with other Cu(I) AA9 structures (Figure 4.22, Table 4.2). [182]

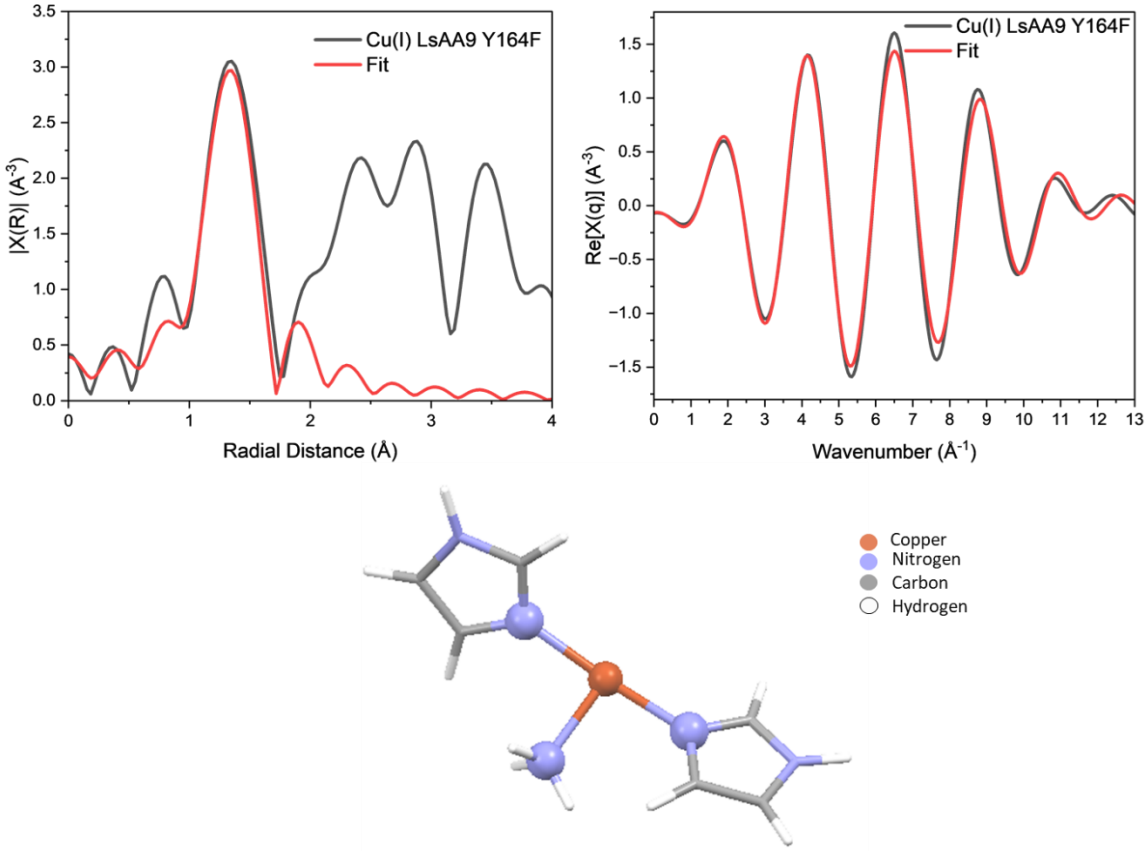


Figure 4.22: Copper K-edge magnitude of the Fourier transform from extracted EXAFS for Cu(I) *Ls*AA9 Y164F (k-range 3.4 – 9.3 Å$^{-1}$)(top *left*), q-space (R-range 1.01 – 1.87 Å) (*top right*) and the model used in the fitting (*bottom*). Experimental data is plotted in black and the corresponding fit is plotted in red, the fits were performed in R-space using the parameters in Table 4.2. The atoms used in the fit are represented as ball and stick.

The EXAFS fit of Cu(II) *Ls*AA9 Y164F was performed in R space. The results of the fit suggest that the copper centre is surrounded by nitrogen (oxygen) atoms with an average bond length of 1.89(3) Å (Figure 4.23, Table 4). Based on other Cu(II) AA9 structures this most likely corresponds to a copper ion with the conserved histidine brace motif as well as an oxygen-based ligand; OH or $H_2O$.[182]

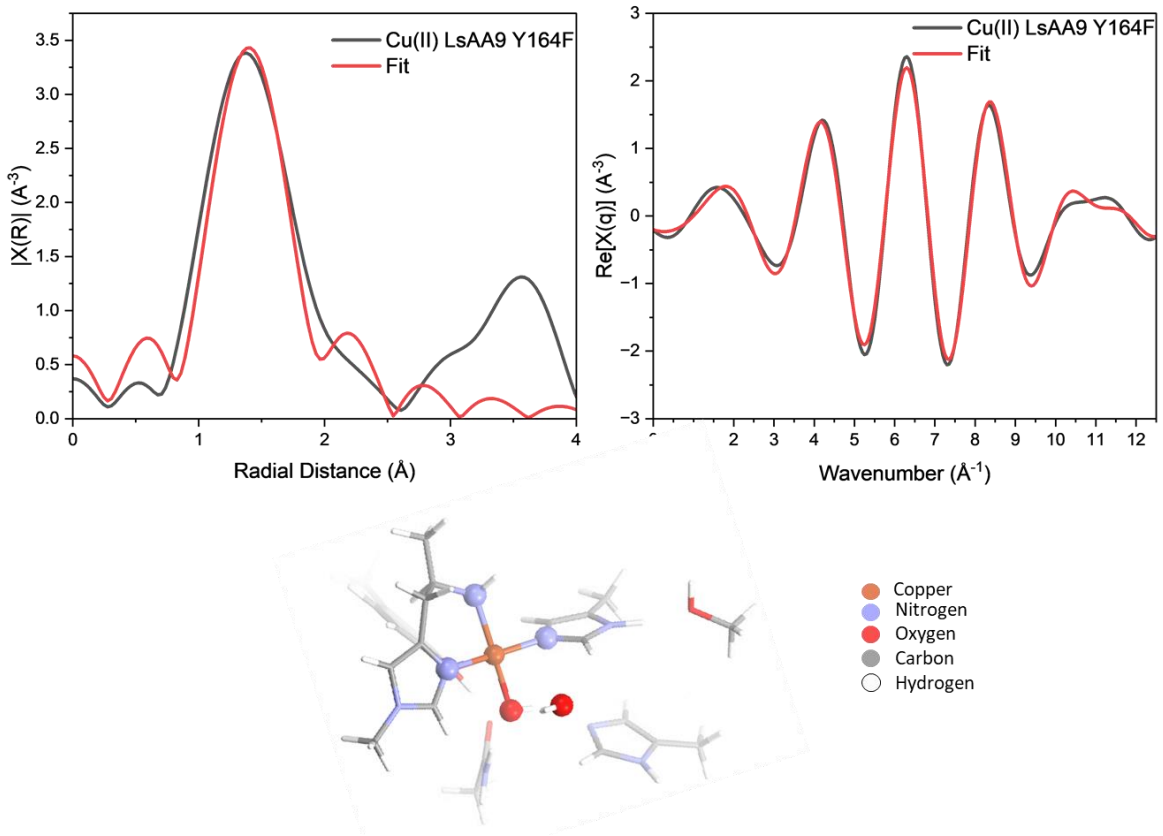


Figure 4.23: Copper K-edge magnitude of the Fourier transform from extracted EXAFS for Cu(II) *Ls*AA9 Y164F (k-range 3.4 – 9.3 $Å^{-1}$)(top *left*), q-space (R-range 1.16 – 2.00 Å) (*top right*) and the model used in the fitting (*bottom*). Experimental data is plotted in black and the corresponding fit is plotted in red, the fits were performed in R-space using the parameters in Table 4.2. The atoms used in the fit are represented as ball and stick.

The results of the EXAFS fit for **Int1** in R-space suggest **Int1** has a structure similar to that of Cu(II) *Ls*AA9 Y164F with four by nitrogen (oxygen) ligands with an average bond length of 1.95(4) Å (Figure 4.24, Table 4.2). This conforms with the copper coordination number of the TD-DFT optimised structure of the Cu(II)-histidyl radical which consisted of a Cu(II) ion bound to three nitrogen atoms through a histidine brace, and an OH ligand. The average Cu-N/O bond length in the TD-DFT optimised structure of Cu(II)-histidyl radical is 1.96 Å, which is consistent with the average bond length from the EXAFS fit for **Int1**.

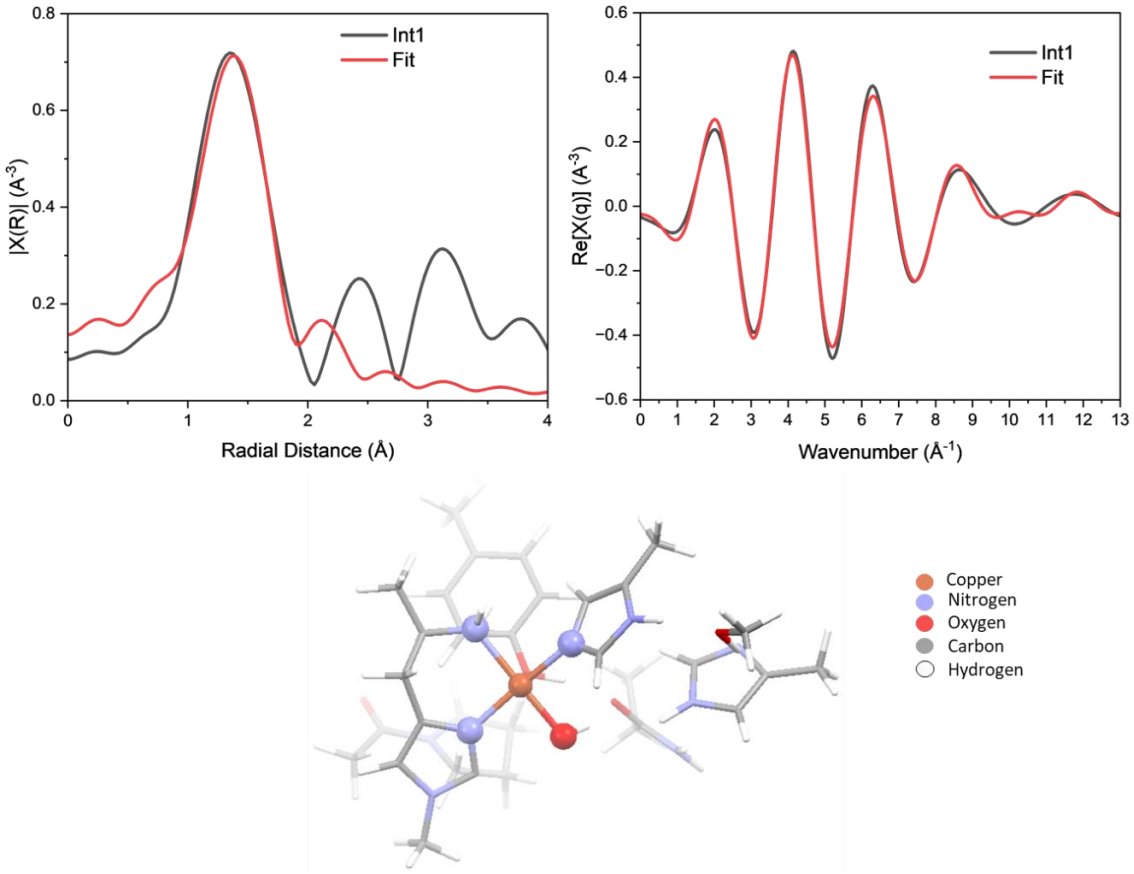


Figure 4.24: Copper K-edge magnitude of the Fourier transform from extracted EXAFS for **Int1** *Ls*AA9 Y164F (k-range 3.4 – 9.3 Å$^{-1}$) (top *left*), q-space (R-range 1.10 – 2.02 Å) (*top right*) and the model used in the fitting (*bottom*). Experimental data is plotted in black and the corresponding fit is plotted in red, the fits were performed in R-space using the parameters in Table 4.2. The atoms used in the fit are represented as ball and stick.

The EXAFS fit for **Int1** corroborates the evidence from TD-DFT, UV-vis, EPR and HERFD-XANES in the assignment of **Int1** as a Cu(II)-histidyl radical species.

Table 4.2: Best fit parameters obtained from the EXAFS fits of Cu(I), Cu(II) and **Int1** LsAA9 Y164F. The S0$^2$ value was fixed at 0.902 for all fits.

| | **N and path** | **R-space fitting range** | **R / Å** | **$\sigma^2$ / Å$^2$** | **$\Delta E_0$ / eV** |
|---|---|---|---|---|---|
| **Cu(I) *Ls*AA9 Y164F** | 3 Cu-N | 1.01 – 1.87 Å | 1.93±0.03 | 0.008±0.002 | -5±4 |
| **Cu(II) *Ls*AA9 Y164F** | 4 Cu-N/O | 1.16 – 2.00 Å | 1.89±0.03 | 0.009±0.001 | -11±5 |
| **Int1** | 4 Cu-N/O | 1.10 – 2.02 Å | 1.95±0.04 | 0.010±0.003 | -5±4 |

## 4.4 Conclusions

The analysis of the HERFD-XANES, EPR, UV-vis, and EXAFS, and the TD-DFT calculations are in agreement in the conclusion that **Int1** can be characterised as a Cu(II)-histidyl radical species. This assignment completes Zhao *et al*'s proposed mechanism for LPMO radical dissipation, whereby **Int1** is formed as part of a pathway to move radicals from the LPMO active site (Figure 4.25). The formation of a potent oxidising LPMO intermediate has the potential to cause damage such as oxidative cleavage of bonds on adjacent amino acids within the enzyme, which can lead to a loss of catalytic activity.[12,183,184] This protective mechanism reduces oxidative damage suffered by the LPMO copper active site incurred by the formation of high valence species during the LPMO reaction mechanism, which allows for increased turnover. This is a significant finding as the highly conserved histidine brace motif has not shown a particular function in LPMOs until now. Although **Int 1** has not been shown to be included in the catalytic cycle of LPMOs, studies have shown that an artificial metalloenzyme based on the LPMO structure with a histidine brace demonstrate catalytic activity on polysaccharides which indicate that the histidine brace is involved in this mechanism.[185] Similar histidine brace motifs can be found in other redox enzymes; therefore these conclusions may be of significance in the wider study of redox active proteins.

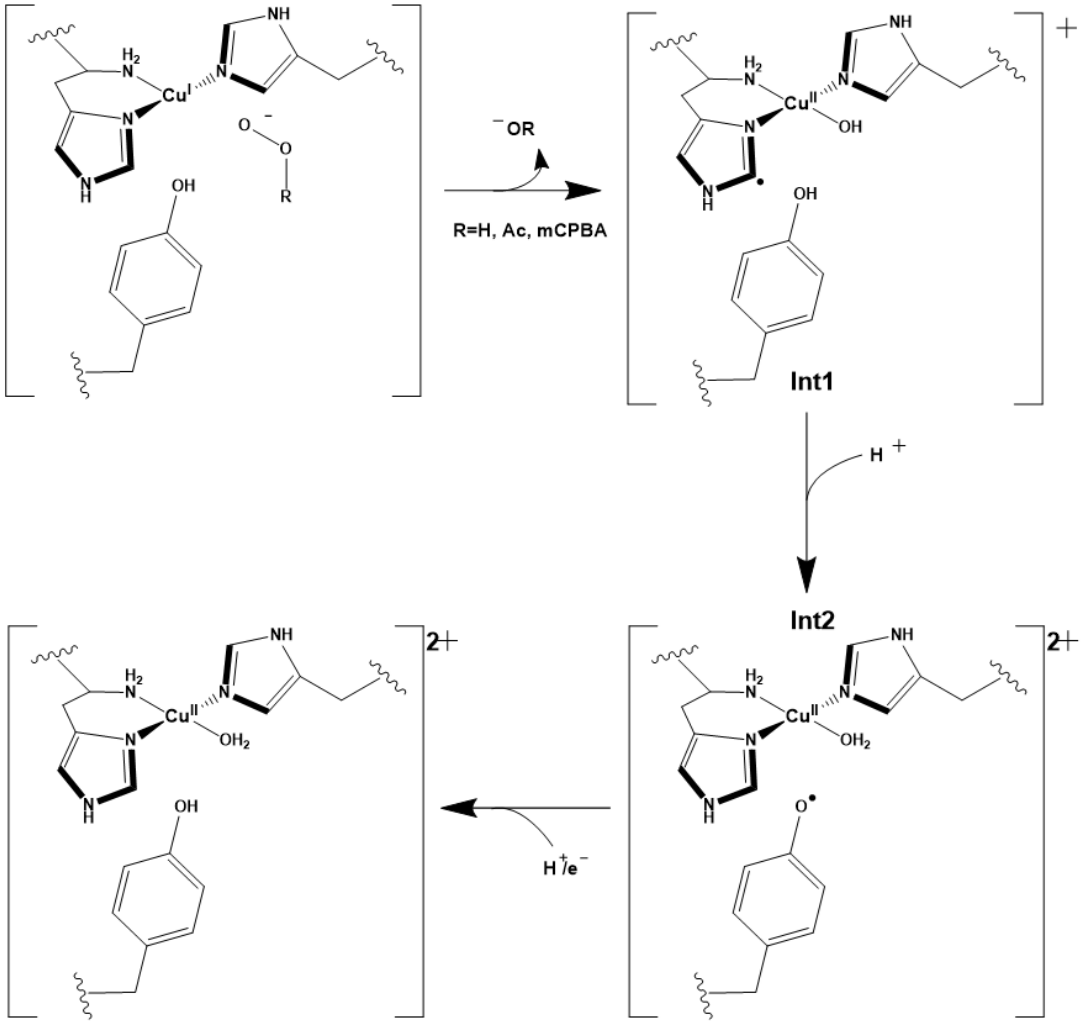


Figure 4.25: Radical dissipation pathway of *Ls*AA9, featuring **Int1** which has been characterised as a Cu(II)-histidyl radical.

The characterisation of **Int1** has proven the efficacy of the anaerobic rapid freeze quenching method and sample preparations for EPR data collection and X-ray spectroscopy. Furthermore, the characterisation of **Int1** demonstrates a method and the validity of using HERFD-XANES for characterisation of metalloprotein intermediates and particularly radical species due to its enhanced resolution in comparison to conventional XAS. The combination of EPR, EXAFS and HERFD-XANES has enabled the determination of the electronic and structural features of a Cu(II)-histidyl radical LPMO species.

# 5 X-ray induced photoreactions in LPMOs

## 5.1 Introduction

Photoreactions involve the absorption of a photon by a molecule resulting in an electronically excited state, therefore it is possible to induce a photochemical reaction using X-rays. The photochemical reaction of photoreduction has been used in previous metalloprotein investigations using synchrotron X-rays to induce a change in the metal oxidation state.[186–189] Photodamage, a form of photoreaction can be detrimental to spectroscopic and crystallographic measurements because a sample which has undergone a photoreaction is no longer structurally or electronically representative of the sample intended to be measured. This chapter will explore the photoreactions LPMOs undergo for two purposes; to observe the effects of photoreactions in LPMOs to inform the interpretation and experimental set ups for future spectroscopic and crystallographic studies of LPMOs, but also to explore if photoreactions can be used advantageously to gain insights into structural and electronic effects in LPMOs during the generation of intermediates.

Photoreactions in a sample can occur globally or specifically. Specific photoreactions occur at the point in the sample which is irradiated whereas global photoreactions are experienced throughout the sample irrespective of where in the sample is irradiated. Photoreactions can be further sub-categorised into primary, secondary, and tertiary reactions.

Primary photoreactions are specific and involve a direct inelastic interaction between the photons from the X-ray beam and atoms in the sample, this can cause bonds to break and the ejection of an electron through photoelectric, Compton and Auger effects. Primary photoreactions correlate linearly with X-ray dose, which follows Stark-Einstein Law which states a linear relationship such that for each quantum of photons absorbed one molecule reacts (Equation 5.1). Primary photoreactions can occur up to a limit of $1x10^7$ Gy, at which point secondary and tertiary photoreactions dominate.[190]

Equation 5.1

$$\Delta E_{mol} = N_A h v$$

Where $N_A$ is Avogadro's number, $h$ is Planck's constant, and v is frequency

Secondary photoreactions can be specific or global, these reactions result from interactions with the radiolytic products from the photolysis of solvents, most prevalently water (Scheme 5.1).[191,192]

X-ray induced photoreactions in LPMOs

Secondary photoreactions are dependent on the nature of the solvent used as well as the temperature and the presence of free radical scavengers.

Scheme 5.1

$$H_2O + h\nu \rightarrow H_2O^+ + e_{(aq)}^-$$

$$H_2O^+ \rightarrow H^+ + HO\bullet$$

Tertiary photoreactions are global and involve long range effects within the sample due to a build-up of reactive species formed by primary and secondary reactions.

Photoreactions can occur oxidatively or reductively. Photooxidation can occur as a result of secondary reactions through the production of hydroxyl radicals which can perform hydrogen atom abstraction reactions. Hydrogen atom extraction reactions are temperature dependant and significantly contribute towards tertiary reactions. More commonly, photoreactions can be photoreductive either through direct reaction with photons or through reaction with solvated electrons, resulting in reduction of the copper metal ion in the case of LPMOs.

As redox metalloproteins; LPMOs are susceptible to photoreduction, particularly in the Cu(II) oxidation state. Furthermore, as LPMO X-ray spectroscopy samples are predominantly comprised of water there is a high chance of solvated electrons forming when the sample is irradiated with X-rays.

X-ray spectroscopy of dilute redox systems requires a careful balance of using enough photon flux density to collect data with a suitable signal to noise ratio, whilst also limiting sample exposure to an excessive X-ray dose which could lead to photoreactions, altering the electronic and geometric structures collected in the data. Due to the move to developing beamlines with more brilliant beams, more insertion devices and consequently greater photon flux density, unwanted photoreactions are becoming more problematic (Figure 5.1). X-ray spectroscopy is a useful tool to investigate the oxidation state and active site structure of LPMOs, however LPMO susceptibility to photoreactions which can alter the copper oxidation state as well as lengthen/ break bonds means that preliminary experiments must include photoreduction checks. To curb the rate of photoreactions within the samples measured in the previous chapters several measures were taken including use of cryogenic temperatures (10 K), attenuation of the X-ray beam and collecting

spectra in different positions within the sample. A multifaceted approach is required as it has been shown that even in measurements at 4 K photoreduction can occur in copper metalloenzymes.[193] X-ray crystallography is also widely used to investigate the structure of LPMOs, although prolonged exposure to X-rays also causes potential for oxidation state and structural changes to occur within the LPMO during this collection time which can lead to incorrect interpretations of LPMO structures.[33,62,194] According to PDB deposited structures, LPMO crystal diffraction data is usually collected at 100 K, but from the information available on PDB it is not possible to work out the X-ray dose the LPMO crystal has received making it difficult to determine how likely the LPMO is to have undergone a photoreaction during the collection period.

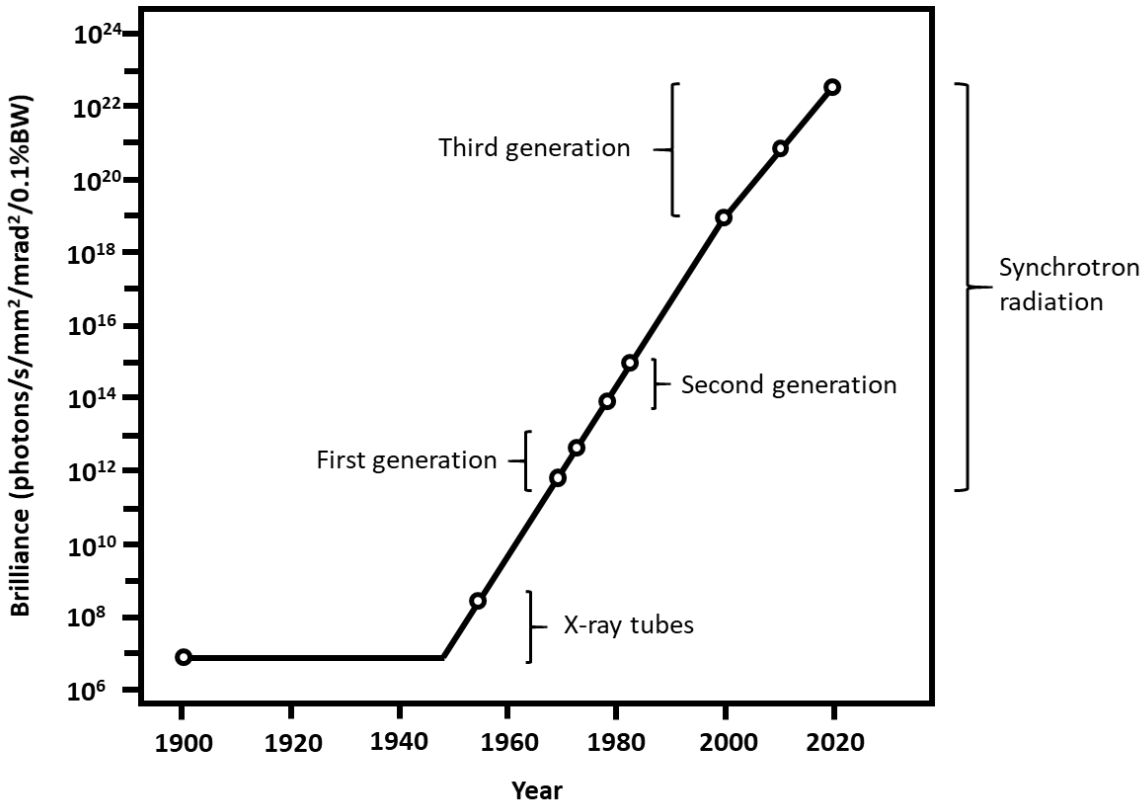


Figure 5.1: Increase in X-ray beam brilliance over time showing the drive for X-ray sources with greater photon flux.

Photoreduction studies of LPMOs have previously been conducted both using X-ray spectroscopy and crystallography. XAS of the copper K-edge of Cu(II) *Ba*AA10 before and after X-ray exposure showed an increase in intensity at 8982 eV, producing a spectrum commensurate with chemically reduced Cu(I) *Ba*AA10.[33] A crystallographic study of LPMO photoreduction involved taking snapshots of the photoinduced reaction of Cu(II) *Efa*AA10 as a progressively greater X-ray dosage

was applied. The starting Cu(II) four coordinate trigonal bipyramidal *Efa*AA10 structure consisted of a histidine brace and two exogenous water ligands, with continued X-ray exposure there was a reduction in electron density of the two water ligands and after *ca*. $1x10^6$ Gy of accumulated radiation both water ligands were lost. The change in coordination number from five to three also resulted in a change in conformation to a T-shaped geometry.[62]

A previous study of a copper-amyloid *β* complex used XAS to observe the changes induced in the Cu(II) structure with increasing X-ray beam exposure.[186] The findings showed that at 10 K an electronic change associated with an oxidation state change of Cu(II) to Cu(I) was observed but there was no change in the spatial organisation of the ligands around the copper ion. Through partial thermal relaxation a geometric change was observed and allowed the characterisation of a so called "in-between" state, an intermediate between the Cu(I) and Cu(II) states which facilitates the significant change in the first shell geometry of these two oxidation states.

Radiation damage of heme proteins has been comprehensively researched.[195–197] One such experiment utilised X-ray radiation to generate unstable intermediates in crystals under cryogenic conditions (88 K) in the heme enzyme cytochrome P450. In this experiment a low radiation dose crystal structure of the Fe(III) structure was collected before the crystal was exposed to the X-ray beam for 3 h which resulted in photoreduction of the enzyme to Fe(II). Thermal relaxations and subsequent re-freezing of the Fe(II) species resulted in a reaction with oxygen to give a dioxygen intermediate which was previously thought to be too unstable to be measured through X-ray diffraction.[198]

This chapter investigates photoreactions over a range of LPMO genomic families; *An*AA9, *Bl*AA10 and *Ao*AA11.

## 5.2 Methods

### 5.2.1 Copper Kα HERFD-XANES to study photoreactions

All LPMO samples were produced and purified following the procedures described in section 2.1. X-ray spectroscopy measurements were made following a modified version of the HERFD-XANES data collection method described in section 2.3.1 on I20-Scanning at Diamond Light Source. The modifications to this method include the removal of the attenuation filters meaning that the photon flux was *ca*. $5x10^{12}$ photons/s at the Cu K-edge energy, with a bandwidth of 1.25 eV. The copper K-edge HERFD-XANES spectra of the samples Cu(II) *Bl*AA10, Cu(II) *An*AA9 and Cu(II) *An*AA9 with chitin were time resolved based on the length of time taken for a single scan (463 s). Thermal relaxation of some of the samples (indicated in the results and discussion section) was undertaken by increasing the temperature of the liquid helium cryostat to the stated temperature for the stated amount of time before the temperature was once again reduced to 10 K to take the next HERFD-XANES measurement.

The Cu(I) and Cu(II) standards and "0s" spectra for each of the LPMOs studied were measured without any modifications to the method outlined in section 2.3.1 in order to measure the samples under conditions that mitigate photoreactions.

XAS and HERFD-XANES samples were prepared by making a slurry with the discussed LPMOs and their respective substrates before freezing in pure aluminium liquid helium cryostat holders. Cu(I) samples were achieved by adding stoichiometric quantities of ascorbate before the addition of substrate. The concentrations of the X-ray spectroscopy LPMO samples were as follows:

- HERFD-XANES of *An*AA9 was measured on 0.65 mM samples.
- XAS of *Ls*AA9 was measured on 0.8 mM samples.
- XAS and HERFD-XANES of *Bl*AA10 were measured on 0.8 mM samples.
- HERFD-XANES of *Ao*AA11 was measured of 0.8 mM samples.

The X-ray dose of the samples was calculated using the following equations:

$$\text{Power (W)} = 1.60219x10^{-16} \times \text{Flux (ph/s)}$$

$$\text{Energy (J)} = \text{Power (W)} \times \text{Time (s)}$$

$$\text{X-ray dose (Gy)} = \text{Energy (J)} / \text{Mass of matter (kg)}$$

The flux on I20-Scanning at Diamond Light Source at 10 keV is $5x10^{12}$ ph/s, which gives a power of 8 mW. Each of the HERFD-XANES scans took 463 s, which means the energy per scan is 3.7 J. Given the area of the beam and the thickness of the sample, the mass of matter is *ca*. $2.4x10^{-7}$ kg which means that an X-ray dose *ca.* $3.3x10^{4}$ Gy is delivered to the sample for every second of X-ray exposure.

### 5.2.2 Data processing

#### *5.2.2.1 Merging and normalisation*

The merging and normalisation of the copper K-edge HERFD-XANES spectra was undertaken in Athena (v 0.9.26) which is part of the Demeter software package.[132]

#### *5.2.2.2 Linear combination fitting*

Linear combination fitting (LCF) of the copper K-edge HERFD-XANES spectra was undertaken in Larch using the merged and normalised data processed in Athena.[132,177]

#### *5.2.2.3 Singular value decomposition and multivariate curve resolution - alternating least squares*

Singular value decomposition (SVD) was used to predict the number of "pure" components in the photoreaction series of copper K-edge HERFD-XANES data using the program Fastosh. The results of SVD were used to inform multivariate curve resolution-alternate least squares (MCR-ALS) analysis of the copper K-edge HERFD-XANES photoreaction series of data to extract the predicted HERFD-XANES spectra of the "pure" components in the system. MCR-ALS analysis was performed using Fastosh.[199]

## 5.3 Results and discussion

### 5.3.1 *An*AA9

HERFD-XANES of Cu(II) *An*AA9 with and without PASC was measured with increasing X-ray dose over time to investigate the electronic and structural effects during X-ray exposure.

#### *5.3.1.1 Cu(II) AnAA9 HERFD-XANES*

HERFD-XANES at the copper K-edge of Cu(II) *An*AA9 measured over time in the same sample position resulting in progressively increasing X-ray dose at the sample shows three distinct photoreactions take place (Figure 5.2). The initial spectrum recorded is consistent with a Cu(II) spectrum with a 1s to *3d* pre-edge peak at 8977.8(3) eV, a weak shoulder attributed to a 1s to *4p* transition on the rising edge at 8982.7(3) eV and an intense white line. As more HERFD-XANES spectra are recorded over time and thus as the X-ray dose at the sample increases, the 1s to *4p* transition increases in intensity and the intensity of the white line decreases, documenting the first photoreaction observed in the sample. The second photoreaction occurs at *ca*. 3954 s of X-ray exposure (X-ray dose *ca*. $1.3 \times 10^8$ Gy), where a sudden decrease in the intensity of the 1s to *4p* rising edge peak occurs culminating in a broad rising edge feature and a further decrease in white line intensity. Following from this, further expose to the X-ray beam results in an increase in intensity of the rising edge feature and little change in the white line intensity, demonstrating the third photoreaction which occurs.

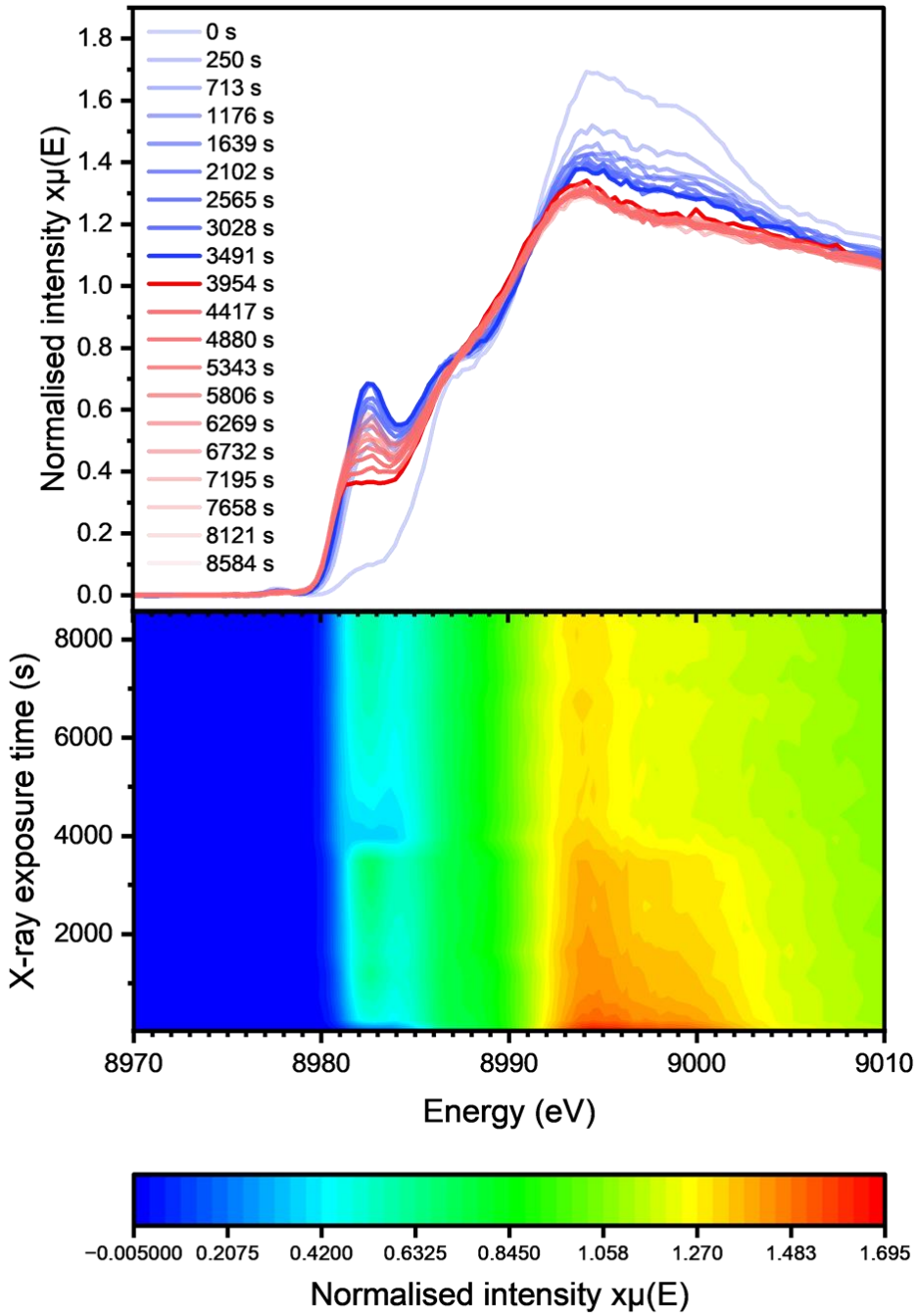


Figure 5.2: (Top) copper K-edge HERFD-XANES spectra of Cu(II) *An*AA9 with increasing X-ray beam exposure. (Bottom) contour map showing the change in normalised intensity of different regions in the copper K-edge HERFD-XANES spectra of Cu(II) *An*AA9 with increasing X-ray exposure.

After measuring the spectra in Figure 5.2 in one position a further copper K-edge HERFD-XANES spectrum was measured in a new position of the Cu(II) *An*AA9 LPMO which was found to show no significant difference to the first Cu(II) *An*AA9 spectrum recorded in the X-ray exposed position,

indicating that the photoreaction observed is local and therefore likely to be a primary or secondary photoreaction (Figure 5.3).

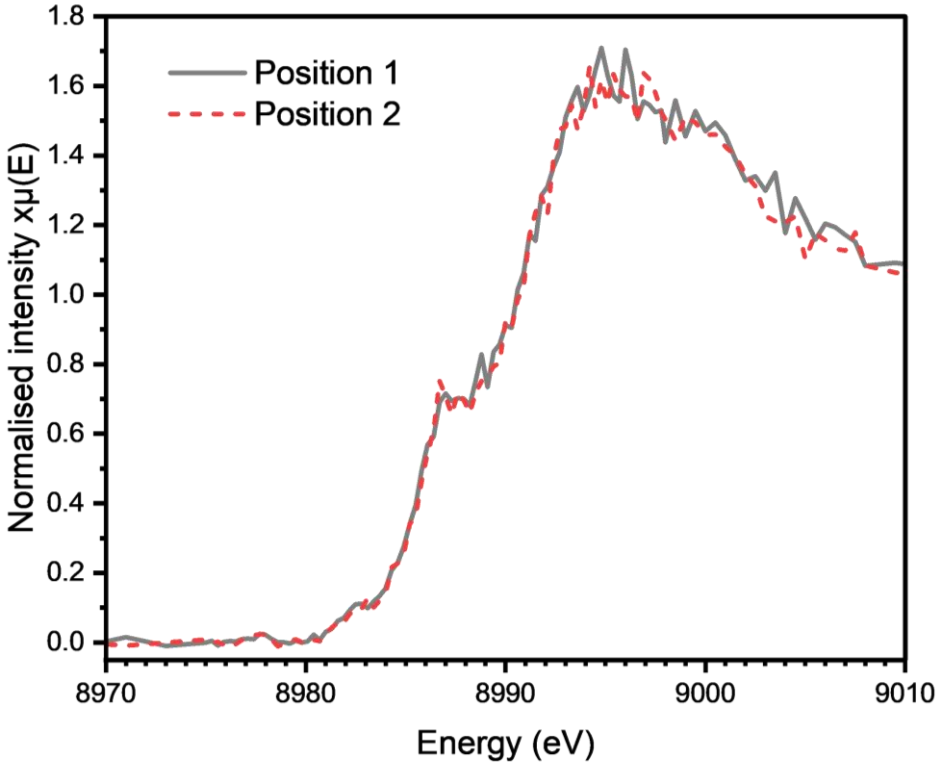


Figure 5.3: Copper K-edge HERFD-XANES of Cu(II) *An*AA9 measured in Position 1 which was then exposed to a high X-ray dose (*ca*. 2.8x10$^3$ Gy), and at a new sample position; Position 2.

The first photoreaction takes place roughly up to the threshold of 1x10$^7$ Gy above which secondary and tertiary photoreactions dominate, which means the first photoreaction observed is likely to be a primary photoreduction reaction.[190] The subsequent photoreactions are observed above this threshold which means that they are likely to be either secondary or tertiary mechanisms. The assignment as a specific photoreaction rather than a global photoreaction means that the subsequent photoreactions must be secondary.

Linear combination fitting of the spectra plotted in Figure 5.2 shows that in the first 3491 s (1.2x10$^8$ Gy) the copper K-edge HERFD-XANES spectra display increasingly more Cu(I) *An*AA9 similarity than Cu(II) *An*AA9 similarity and fits with reasonable R-factors can be achieved (Figure 5.4). These linear combination fits are in accordance with the suggestion that the first photoreaction observed over 3941 s of X-ray beam exposure in Cu(II) *An*AA9 is a primary photoreduction reaction. As the Cu(II) *An*AA9 sample is further exposed to the X-ray beam beyond 3491 s up to 8584 s (2.9x10$^8$ Gy) the R-factor for the linear combination fits increases significantly indicating that a good fit cannot be

achieved with only Cu(I) and Cu(II) *An*AA9 as standards. The poor linear combination fits from 3491 s onwards evidence that a further photoreaction occurs and another species other than Cu(I) *An*AA9 or Cu(II) *An*AA9 is present. The linear combination fits in the first 3491 s show a largely linear correlation between the time the sample is exposed to the X-ray beam and the proportion of the sample that is made up of Cu(I) *An*AA9. It should also be noted that whilst an increasing concentration of Cu(I) *An*AA9 is observed in the sample, the sample never becomes 100 % Cu(I) *An*AA9.

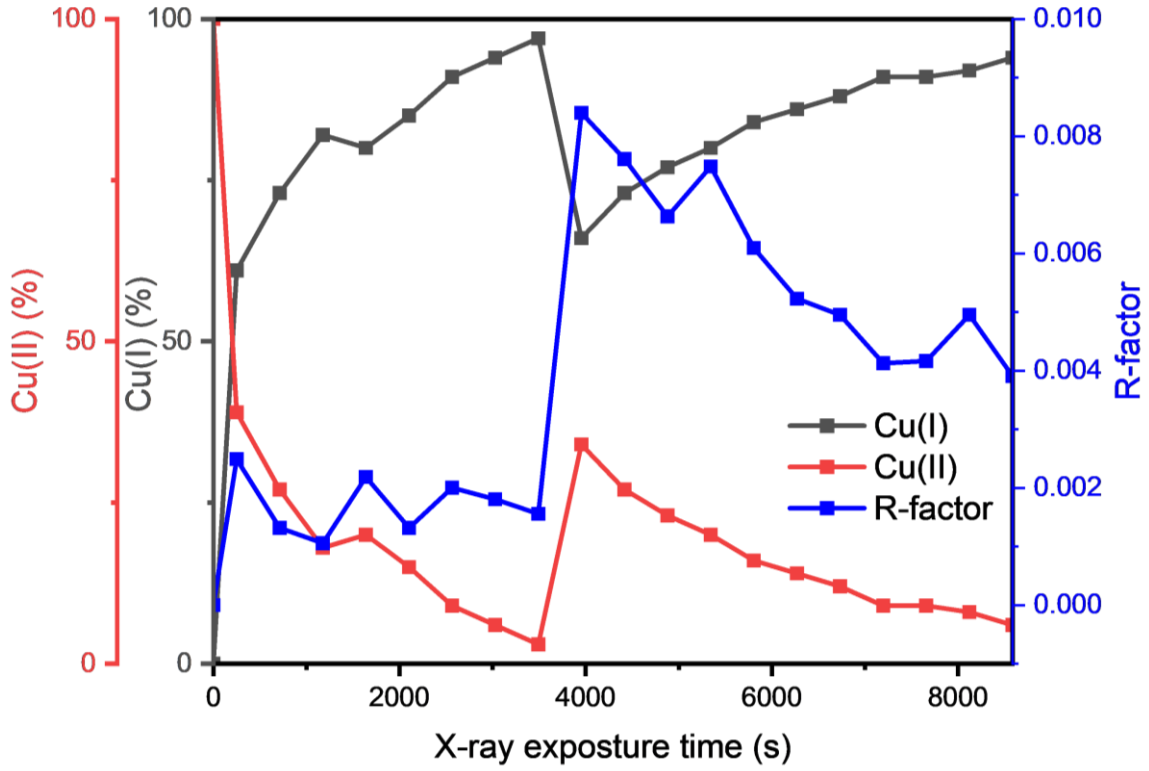


Figure 5.4: Best fit values for linear combination fits of the copper K-edge HERFD-XANES spectra plotted in figure 5.1 using a combination of Cu(I) *An*AA9 and Cu(II) *An*AA9 (left Y-axis), plotted with the R-factor values for the linear combination fits (right axis).

The observation that three photoreactions are occurring in this process is confirmed by singular value decomposition (SVD) which suggests that there are three components in the system. With this knowledge, Multivariate Curve Resolution - Alternating Least Squares (MCR-ALS) was used to extract the three “pure” spectral components from this dataset (Figure 5.5). The results of MCR-ALS show that one of the components in the system is consistent with Cu(II) *An*AA9, the second component in the system is comparable to Cu(I) *An*AA9 and the third component is currently uncharacterised.

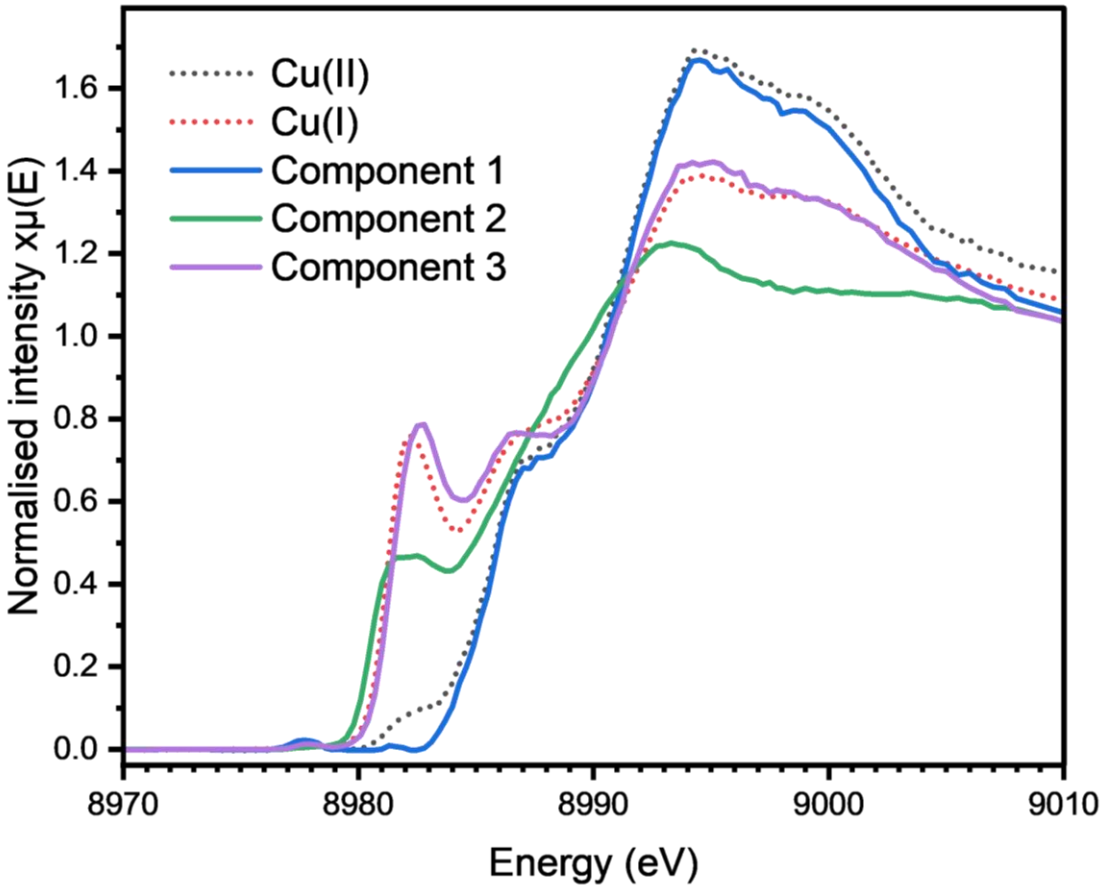


Figure 5.5: Experimental copper K-edge HERFD-XANES spectra of Cu(I) and Cu(II) *An*AA9 (dotted lines) and the three components from the series of spectra plotted in Figure 5.1 isolated by MCR-ALS.

The spectral shape of Component 2 is similar to that of a literature reported copper peptide "in-between" state characterised by Falcone *et al*; a three coordinate copper structure with mixed Cu(I)/ Cu(II) oxidation state (Figure 5.6). Both the copper K-edge XAS spectrum of the "in-between" state and the copper K-egde HERFD-XANES spectrum of Component 2 shows a 1s to *4p* intensity between that of the Cu(I) and Cu(II) spectra which broadens to a lower energy, as well as a significant decrease in the white line intensity. Therefore, it could be suggested that if Component 2 is structurally similar to the copper-amyloid *β* complex in the "in between" state, Component 2 could be a three coordinate Cu(I)/(II) complex coordinated to the histidine brace.

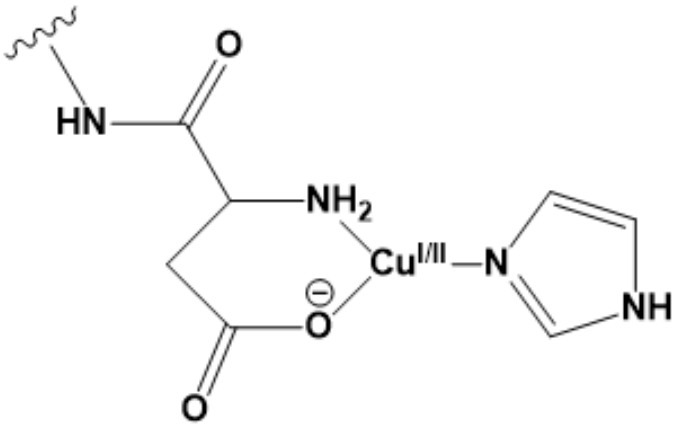


Figure 5.6: Proposed structure of copper-amyloid *β* complex in the "in between" state with a Cu(I)/(II) ion.[186]

### *5.3.1.2 Cu(II) AnAA9 with PASC HERFD-XANES*

A similar trend is also observed on irradiation of Cu(II) *An*AA9 in the presence of substrate (PASC). As previously discussed in Chapter 3, copper K-edge HERFD-XANES and cw-EPR suggest that there is not an interaction between Cu(II) *An*AA9 and PASC but that there is an interaction in the Cu(I) oxidation state. An experiment was undertaken to observe the effects of irradiating Cu(II) *An*AA9 in the presence of PASC to a Cu(I) oxidation state and then warming the sample for a short period of time before lowering the temperature and measuring the copper K-edge HERFD-XANES spectrum to see if there is an interaction with PASC (Figure 5.7).

The photoreactions which occur on the irradiation of Cu(II) *An*AA9 with PASC are firstly shown by a decrease in white line intensity and an increase in the intensity of the 1s to *4p* rising edge transition from 0 s to a maximum at 1639 s ($5.5 \times 10^7$ Gy), this is followed by a sharp decrease in 1s to *4p* intensity and broadening of the peak after 2102 s ($7.0 \times 10^7$ Gy) of beam exposure. The intensity of the 1s to *4p* transition then increases again up to 5343 s of exposure time ($1.8 \times 10^8$ Gy) and remains constant up to 8584 s of exposure time ($2.9 \times 10^8$ Gy). At this point the sample was warmed to 150 K for three minutes and then cooled back to 10 K to observe any changes in copper coordination geometry. After warming the sample, the intensity of the 1s to *4p* peak once again dropped and broadened, giving a similar spectrum to that at 2102 s of X-ray exposure. As previously observed, after further X-ray exposure the 1s to *4p* once again grew in intensity between 9047 s and 12751 s of exposure time ($3.0 \times 10^8$ Gy – $4.3 \times 10^8$ Gy). At this point, the sample was then warmed to 250 K for three minutes and then cooled to 10 K before data collection in the same sample position was continued. Once again a decrease in the 1s to *4p* intensity was observed, this time to the lowest intensity measured since the spectrum at 0 s. For a further time, as X-ray exposure was continued

between 13241 s and 16918 s ($4.4x10^8$ Gy – $5.6x10^8$ Gy) there was in increase in the intensity of the 1s to *4p* transition and further decrease in the intensity of the white line.

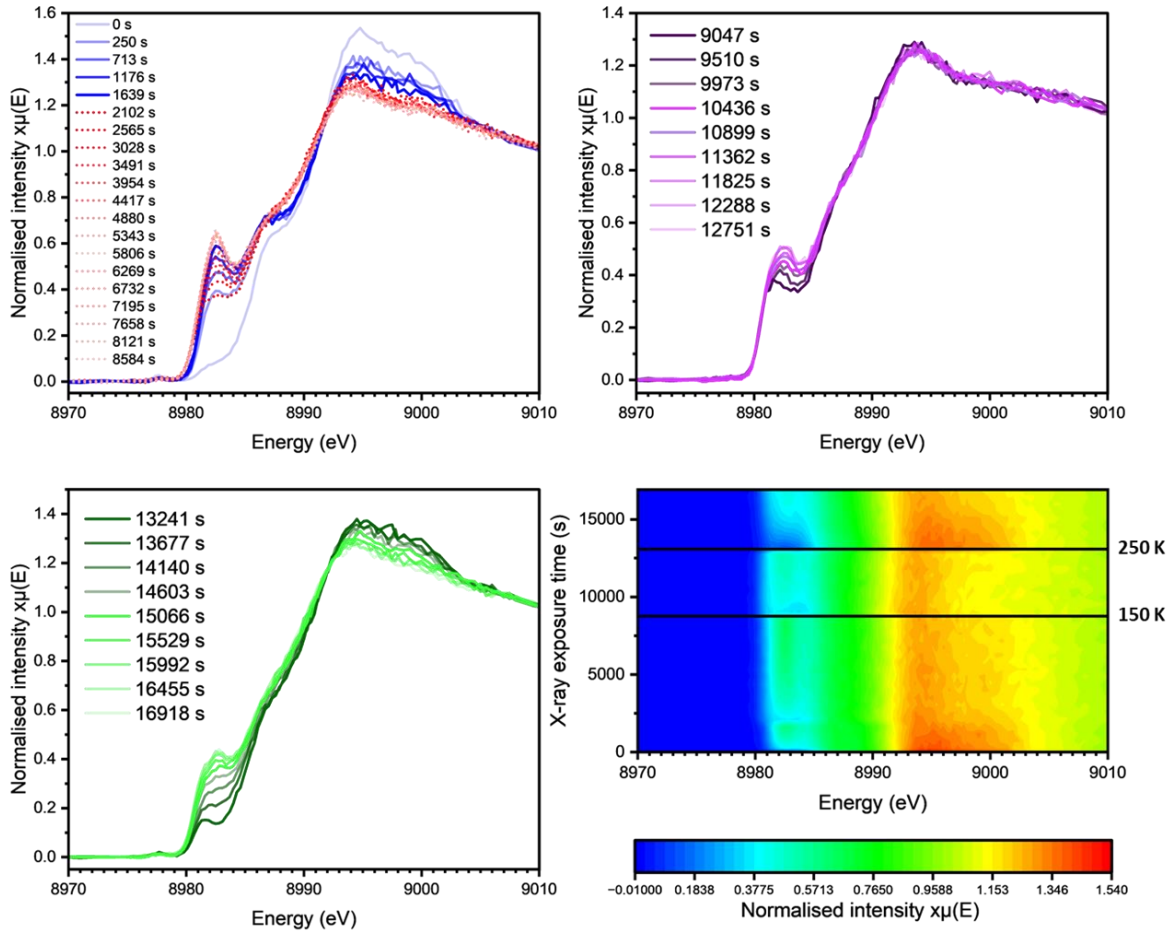


Figure 5.7: Copper K-edge HERFD-XANES of Cu(II) *An*AA9 with PASC measured in the same sample position. *Top left:* spectra measured over 0 s – 8584 s of X-ray exposure. *Top right*: spectra after the sample was warmed to 150 K for three minutes measured with 9047 s – 12751 s of X-ray exposure. *Bottom left:* spectra after the sample was warmed to 250 K for three minutes measured with 13241 s – 16918 s of X-ray exposure. *Bottom right:* contour map showing the change in normalised intensity of different regions in the copper K-edge HERFD-XANES spectra of Cu(II) *An*AA9 with PASC with increasing X-ray exposure, with the temperature change points indicated.

A further copper K-edge HERFD-XANES measurement was made in a new sample position after the spectra in Figure 5.6 were collected to investigate whether the photoreactions observed in the first sample position are specific or global. The spectrum measured in the second sample position shows no significant difference from the spectrum measured in the first sample position before irradiation

and therefore it can be concluded that the photoreactions observed are specific and not global (Figure 5.8).

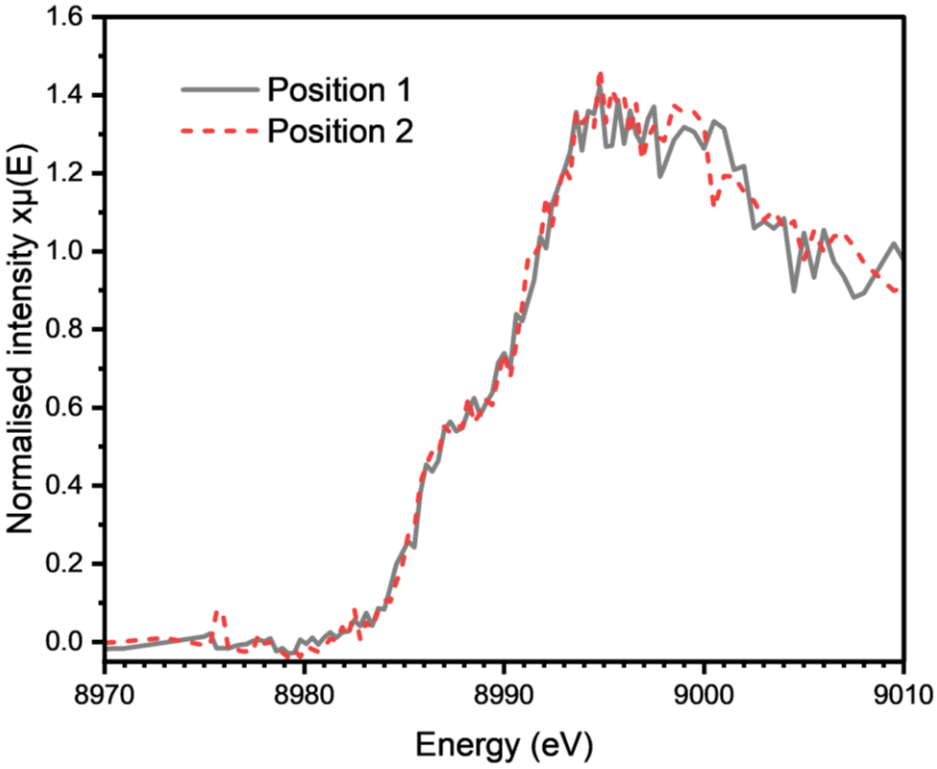


Figure 5.8: Copper K-edge HERFD-XANES of Cu(II) *An*AA9 with PASC measured in Position 1 which was then exposed to a high X-ray dose ($5.6 \times 10^8$ Gy), and at a new sample position; Position 2.

As the photoreactions observed are specific rather than global, they must be primary or secondary. The first photoreaction observed is in accordance with a primary photoreaction as it occurs roughly up to the threshold of $1 \times 10^7$ Gy above which secondary and tertiary photoreactions dominate. This threshold loosely corresponds to the X-ray dose in which the subsequent photoreactions occur, meaning that the subsequent photoreactions are likely to be secondary or tertiary and given there are no signs of global photoreactions they are likely to be secondary photoreactions.

Linear combination fits of the spectra plotted in Figure 5.7 show that good fits (based on the R-factor) can be achieved using a combination of Cu(I) *An*AA9 with PASC and Cu(II) *An*AA9 with PASC for the spectra recorded between 0s and 1693 s. The linear combination fits for the spectra recorded between 0s and 1693 s are in accordance with a primary photoreduction reaction resulting in an increasing proportion of the sample aligning with Cu(I) *An*AA9. From 1693 s onwards there is a significant increase in the R-factor which suggests that the linear combination fits for the

spectra recorded over these times were not as good. After 1693 s the percentage of Cu(I) and Cu(II) *An*AA9 in each of the fits fluctuates but there is consistently a greater proportion of Cu(I) than Cu(II) in the sample until the thermal relaxation of the sample at 13241 s, at which point the linear combination fits suggest there is a greater proportion of Cu(II) than Cu(I) in the sample.

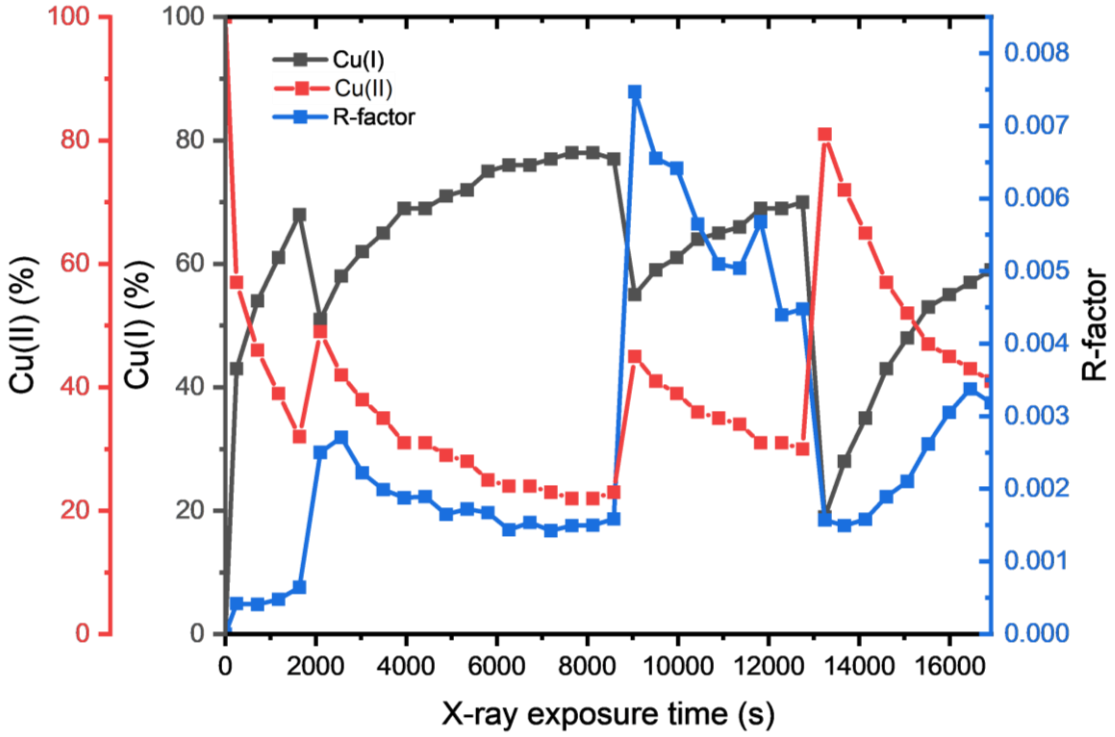


Figure 5.9: Best fit values for linear combination fits of the copper K-edge HERFD-XANES spectra plotted in figure 5.7 using a combination of Cu(I) *An*AA9 with PASC and Cu(II) *An*AA9 with PASC (left Y-axis), plotted with the R-factor values for the linear combination fits (right axis).

SVD of this dataset, over all the time points measured (0s – 16918 s), also gave three components which were extracted using MCR-ALS (Figure 5.10). The spectrum of component 1 from MCR-ALS is comparable the copper K-edge HERFD-XANES spectrum of Cu(II) *An*AA9 with PASC. The spectrum of component 2 from MCR-ALS appears to lie between the HERD-XANES spectra of Cu(I) *An*AA9 with and without PASC, suggesting that this spectrum is representative of a reaction beginning to occur between Cu(II) *An*AA9 which has been photoreduced to Cu(I) *An*AA9 and PASC. From the investigation into the interaction of PASC with Cu(I) *An*AA9 detailed in Chapter 3, it is suggested that the addition of PASC to Cu(I) *An*AA9 a change in coordination number from 3.5 to 3 occurs *via* the loss of a labile exogenous ligand (OH/ $H_2O$) which results in an increase in 1s to *4p* intensity in the copper K-edge HERFD-XANES spectrum. Given this understanding, component 2 could be showing a lengthening of the Cu(I) bond to the exogenous ligand without breaking the bond, or it

could be that component 2 is a mixture of 3.5 and 3 coordinate Cu(I) *An*AA9 structures induced by the presence of PASC but perturbed by the lack of kinetic energy at 10 K. Component 3 is structurally distinct from the standards measured and is similar to that of the uncharacterised component identified in the photoreactions of Cu(I) *An*AA9.

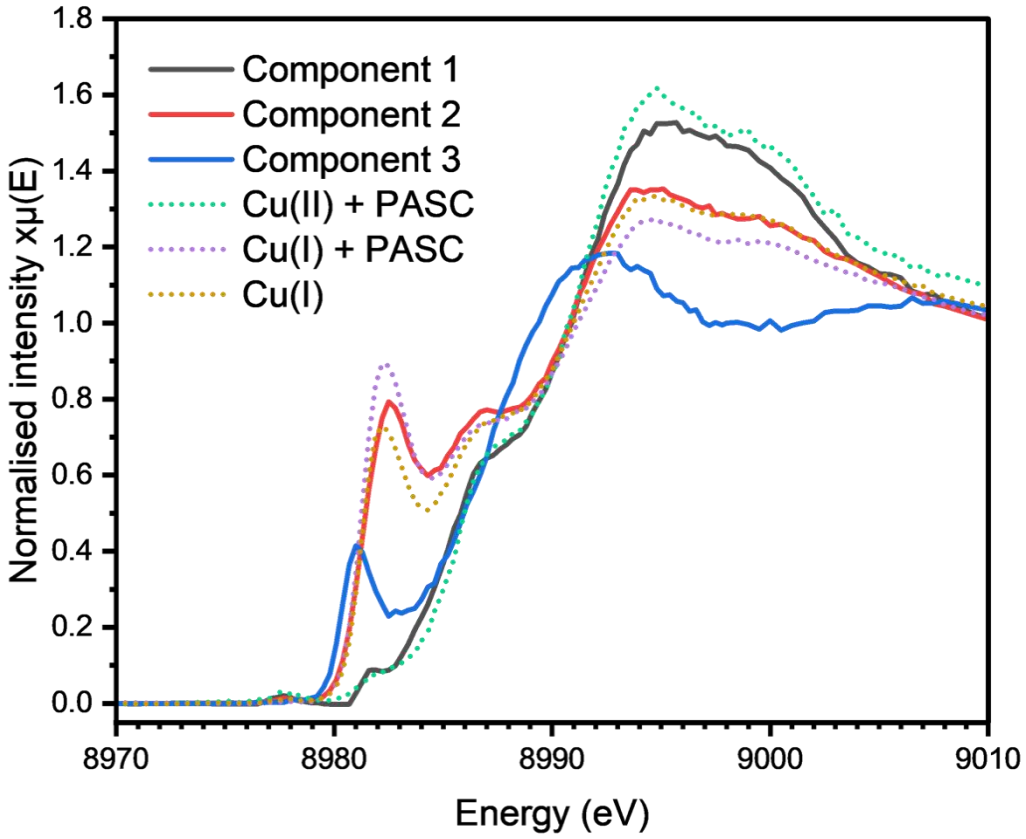


Figure 5.10: Experimental copper K-edge HERFD-XANES spectra of Cu(I) *An*AA9, Cu(II) *An*AA9 with PASC and Cu(I) *An*AA9 with PASC (dotted lines) and the three components from the series of spectra plotted in Figure 5.6 isolated by MCR-ALS.

#### *5.3.1.3 Summary*

Continuous X-ray exposure of both Cu(II) *An*AA9 with and without PASC resulted in photoreactions measured by copper K-edge HERFD-XANES. Both samples showed a similar trend of an increase in 1s to *4p* intensity to give spectra commensurate with a change in oxidation state from Cu(II) to Cu(I), in the case of Cu(II) *An*AA9 with PASC the 1s to *4p* intensity continued to increase suggesting that the presence of PASC resulted in an interaction in the photoreduced Cu(I) oxidation state. After photoreduction from Cu(II) to Cu(I) in both *An*AA9 samples there was a sudden decrease in 1s to *4p* intensity giving a component which has not been characterised. In both *An*AA9 samples the

photoreactions observed were found to be specific rather than global and laxly corresponds to the $1x10^7$ Gy threshold in which below this dose a primary photoreduction reaction is observed and above which different photoreactions occur which are likely to be secondary photoreactions.

### 5.3.2 *Bl*AA10

Copper K-edge HERFD-XANES spectra of Cu(II) *Bl*AA10 were measured with increasing X-ray exposure over time to gain insights into any photoreactions that may take place.

#### *5.3.2.1 Cu(II) BlAA10 HERFD-XANES*

Copper K-edge HERFD-XANES spectra of *Bl*AA10 measured consecutively in the same sample position showed evidence of photoreactions occurring over time (Figure 5.11). From the initial Cu(II) *Bl*AA10 HERFD-XANES spectrum several spectral changes occur in the first instance; there is a reduction in the intensity of the 1s to *3d* associated peak in the pre-edge, an increase in the intensity of the 1s to *4p* assigned transition in the rising edge and a decrease in white line intensity. The changes observed in the first instance are typically associated with a change in oxidation state from Cu(II) to Cu(I), indicating a photoreduction reaction is taking place. The first photoreaction observed occurs in the first 463 s ($1.5x10^7$ Gy) of X-ray exposure and is maintained up to 926 s ($3.1x10^7$ Gy) of X-ray exposure before a second photoreaction occurs. After 1389 s ($4.6x10^7$ Gy) of X-ray exposure the intensity of the rising edge peak attributed to the 1s to *4p* transition gradually decreases in intensity and broadens to a lower energy. Between 2778 s – 4630 s ($9.3x10^7$ Gy – $1.5x10^8$ Gy) there are no significant changes in the HERFD-XANES copper K-edge spectrum, even after thermal relaxation. Before the scan at the 2167 s timepoint the sample was warmed to 100 K for one minute before being cooled back to 10 K for the next HERFD-XANES spectrum measurement. Before the scan at the 4630 s timepoint the sample was warmed to 200 K for one minute before the sample was cooled back to 10 K to measure the HERFD-XANES spectrum. Neither of the 100 K and 200 K temperature changes afforded a change in the copper K-edge HERFD-XANES spectra showing that the species formed is not spatially constrained by temperature up to 200 K.

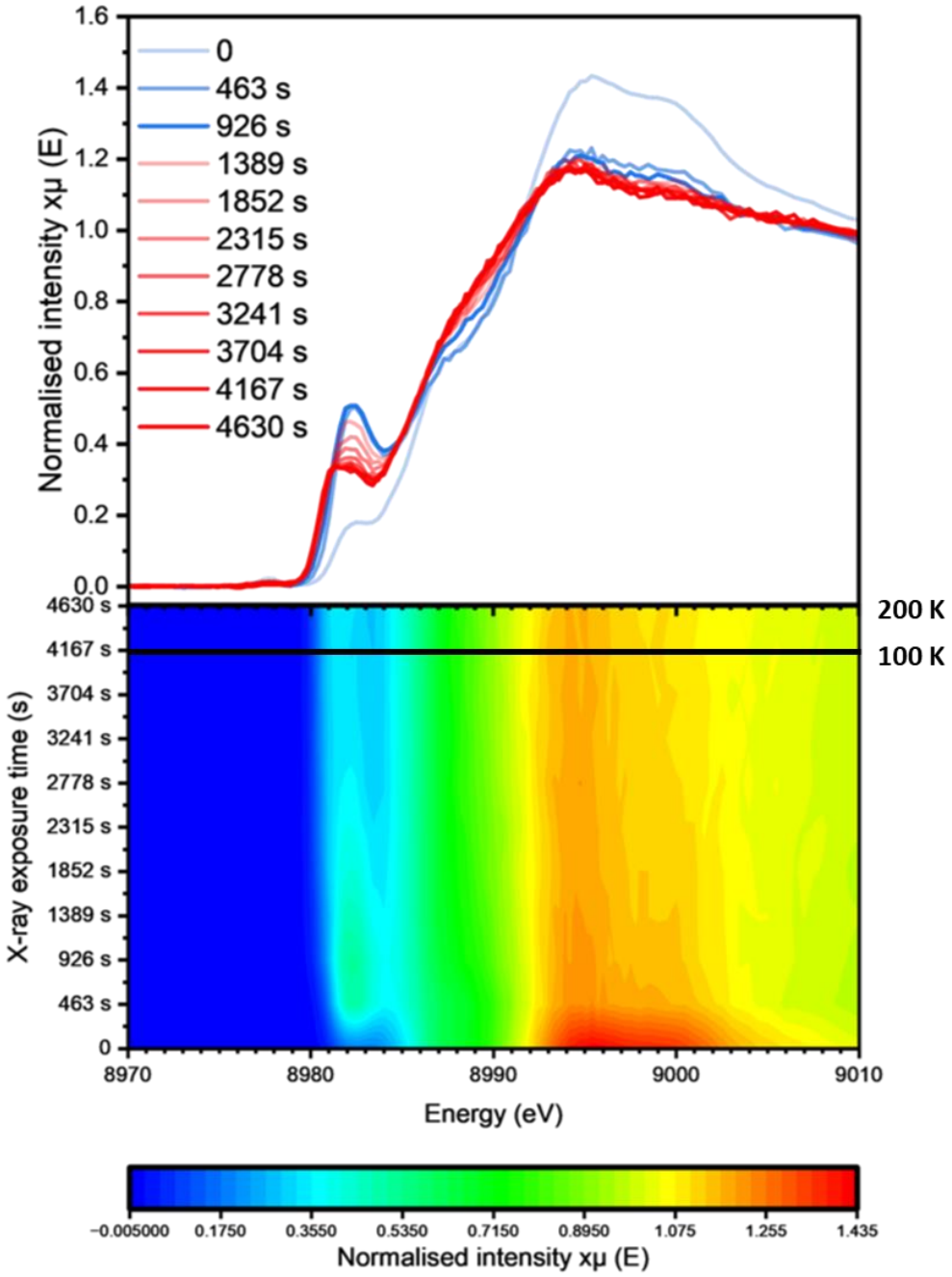


Figure 5.11: (Top) copper K-edge HERFD-XANES spectra of Cu(II) *Bl*AA10 with increasing X-ray beam exposure. (Bottom) contour map showing the change in normalised intensity of different regions in the copper K-edge HERFD-XANES spectra of Cu(II) *Bl*AA10 with increasing X-ray exposure. Spectra measured after thermal relaxation (4167s – 4630 s) are marked on the contour map.

To test if the photoreactions observed in Cu(II) *Bl*AA10 were specific or global, a further copper K-edge HERFD-XANES spectrum was measured in another sample position (Figure 5.12). The spectra

in Position 1 and Position 2 are not significantly different and therefore the photoreactions observed in Cu(II) *Bl*AA10 are specific and not global.

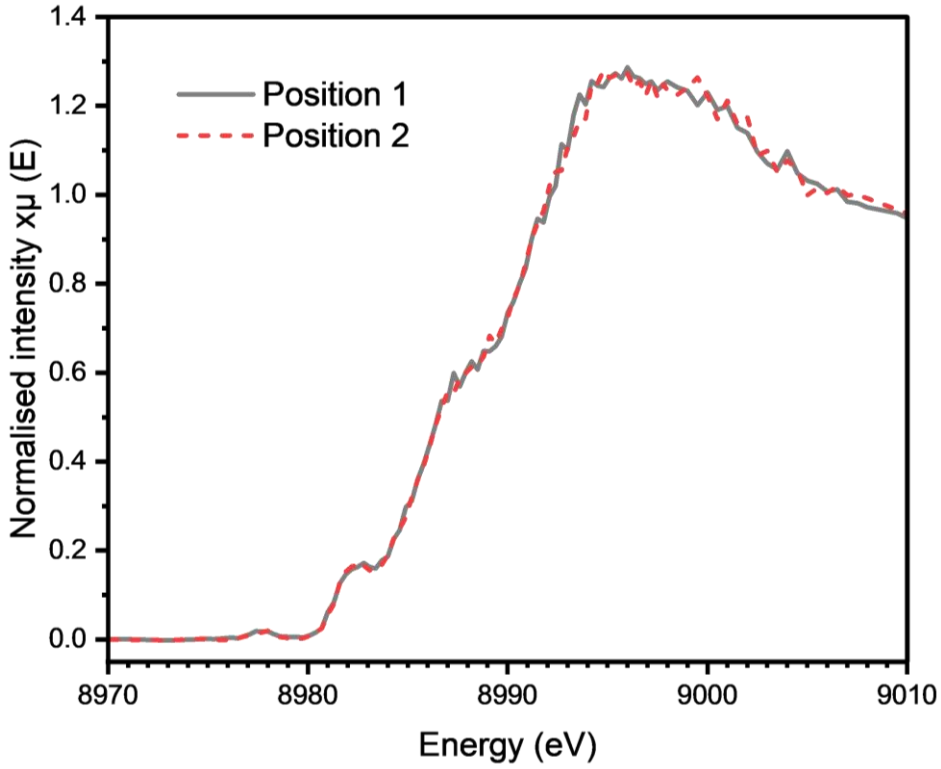


Figure 5.12: Copper K-edge HERFD-XANES of Cu(II) *Bl*AA10 measured in Position 1 which was then exposed to a high X-ray dose, and a new sample position; Position 2.

Linear combination fitting of the spectra plotted in Figure 5.10 show that the best fit initially is with Cu(II) *Bl*AA10 and then with an increasing percentage of Cu(I) *Bl*AA10, which then remains fairly consistent but the R-factor for the fits increases substantially with time (Figure 5.13). This means that the first two spectra are well represented by a change from Cu(II) *Bl*AA10 to Cu(I) *Bl*AA10, consistent with a specific primary photoreduction reaction. However, overtime and as the X-ray radiation dose increases the spectra cannot be well described by the Cu(I) and Cu(II) *Bl*AA10 standards and therefore there must be another component in the system as a result of a further photoreaction.

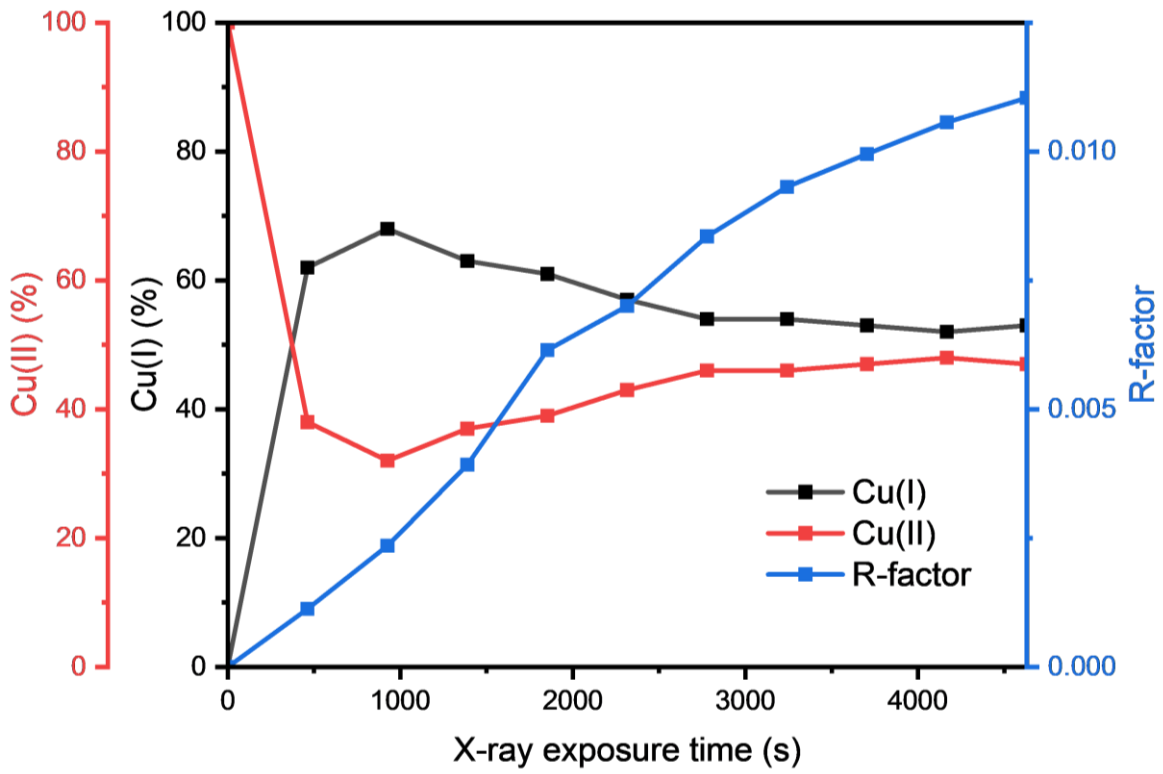


Figure 5.13: Best fit values for linear combination fits of the copper K-edge HERFD-XANES spectra plotted in figure 5.11 using a combination of Cu(I) *Bl*AA10 and Cu(II) *Bl*AA10 (left Y-axis), plotted with the R-factor values for the linear combination fits (right axis).

SVD of the X-ray irradiated Cu(II) *Bl*AA10 HERFD-XANES series of data show there are three components in this system. The spectra of the three components were extracted using MCR-ALS (Figure 5.14). The HERFD-XANES spectrum of component 1 is comparable to that of Cu(II) *Bl*AA10. The HERFD-XANES spectrum of component 3 is most similar to that of Cu(I) *Bl*AA10 but has significantly lower rising edge 1s to *4p* peak intensity. This suggests in the first photoreaction there is an oxidation state change but the exogenous ligand is not lost. Component 2 is similar to the uncharacterised components found in the photoreactions of Cu(II) *An*AA9 with and without substrate, but it is still not clear what this component is.

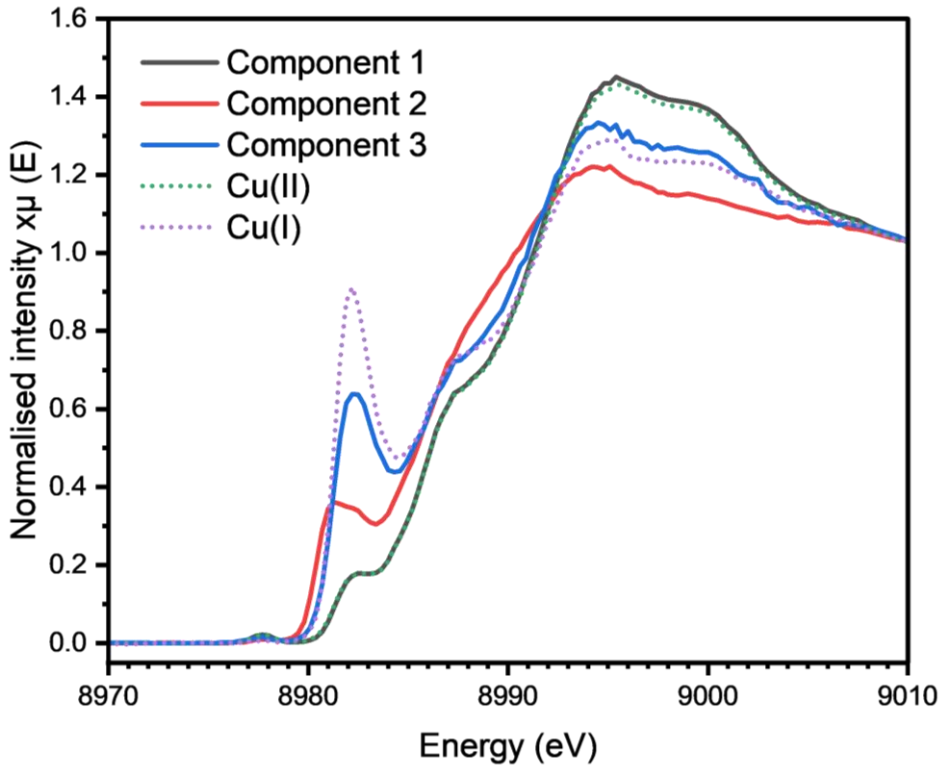


Figure 5.14: Experimental copper K-edge HERFD-XANES spectra of Cu(I) *Bl*AA10 and Cu(II) *Bl*AA10 (dotted lines) and the three components from the series of spectra plotted in Figure 5.11 isolated by MCR-ALS.

#### *5.3.2.2 Summary*

Prolonged X-ray exposure of Cu(II) *Bl*AA10 resulted in the occurrence of two distinct photoreactions as measured by copper K-edge HERFD-XANES spectroscopy. The first photoreaction is consistent with a photoreduction of Cu(II) *Bl*AA10 to Cu(I) *Bl*AA10. The second photoreaction produced an uncharacterised species which is similar to the uncharacterised species formed in the photoreactions of *An*AA9. This species did not change upon thermal relaxation and is formed through a specific photoreaction.

### 5.3.3 *Ao*AA11

Copper K-edge HERFD-XANES of Cu(II) *Ao*AA11 with and without chitin were recorded before and after being irradiated with the X-ray beam on I20-Scanning to observe photoinduced changes. Because of the unexpectedly poor signal to noise ratio of the *Ao*AA11 copper K-edge HERFD-XANES spectra, rather than measuring the changes in the HERFD-XANES spectra over time during X-ray exposure the sample was irradiated and several spectra in different sample positions were measured and merged.

### *5.3.3.1 Cu(II) AoAA11 HERFD-XANES*

The copper K-edge HERFD-XANES spectrum of Cu(II) *Ao*AA11 after an X-ray dose of 1.5x10$^7$ Gy becomes more similar to the HERFD-XANES spectrum of Cu(I) *Ao*AA11 than Cu(II) *Ao*AA11 suggesting a photoreduction reaction has been induced (Figure 5.15). Compared to the pure Cu(II) *Ao*AA11 HERFD-XANES spectrum, the HERFD-XANES spectrum of Cu(II) *Ao*AA11 with 1.5x10$^7$ Gy X-ray dose shows a reduction in the intensity of the 1s to *3d* transition at 8977.8(3) eV, a decrease in white line intensity and an increase in the rising edge peak associated with a 1s to *4p* transition combined with a shift to a lower energy. Whilst the Cu(II) *Ao*AA11 after 1.5x10$^7$ Gy HERFD-XANES spectrum is more similar to the Cu(I) *Ao*AA11 HERFD-XANES spectrum than the Cu(II) *Ao*AA11 HERFD-XANES spectrum, the white line intensity and 1s to *4p* peak intensity are lower in Cu(II) *Ao*AA11 1.5x10$^7$ Gy spectrum. Furthermore, the 1s to *4p* peak in the Cu(II) *Ao*AA11 1.5x10$^7$ Gy spectrum has shifted to a lower energy compared to the 1s to *4p* transition in both the Cu(I) and Cu(II) *Ao*AA11 spectra.

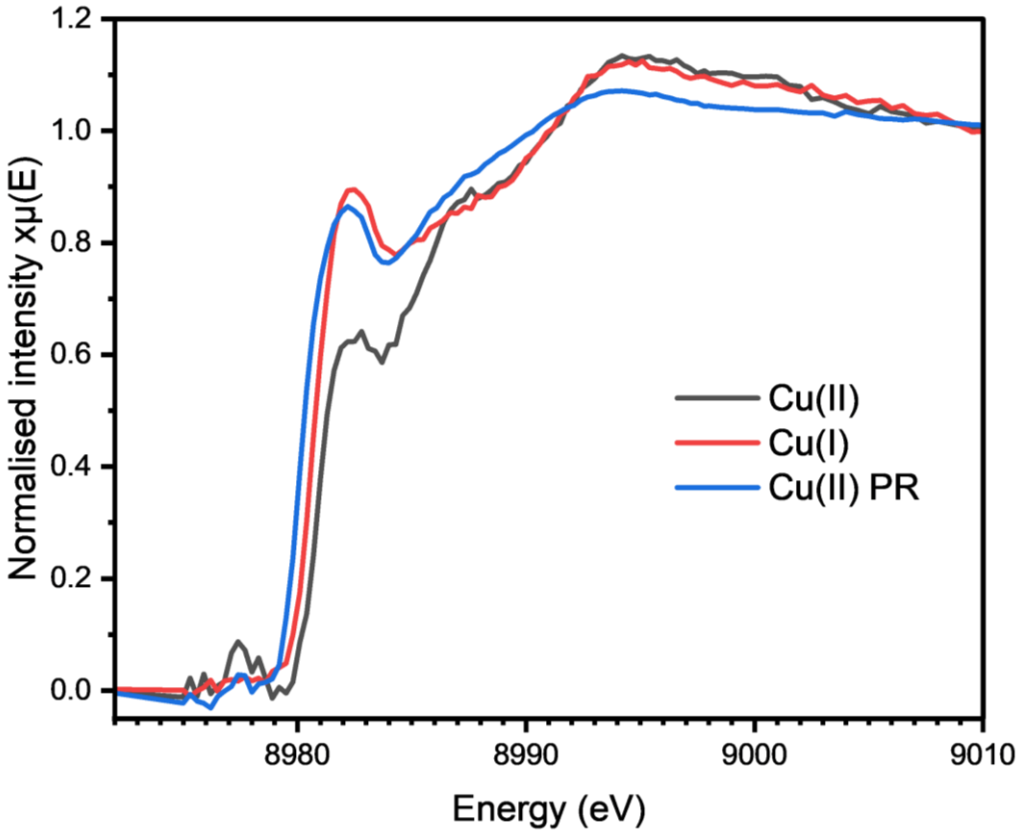


Figure 5.15: Copper K-edge HERFD-XANES of Cu(I) (*red*) and Cu(II) *Ao*AA11 (*grey*) and Cu(II) *Ao*AA11 after an X-ray dose of 1.5x10$^7$ Gy (*blue*).

A copper K-edge HERFD-XANES spectrum of Cu(II) *Ao*AA11 was measured in a sample position that had not previously been exposed to the X-ray beam after the photoreaction spectra were measured to test if the photoreactions observed were specific or global (Figure 5.16). The signal to noise ratio of the data is not very high, but within the noise we can conclude that there is no difference between the HERFD-XANES spectra measured before irradiation of the sample and in a "fresh" sample position, suggesting that the photoreaction observed is specific and not global.

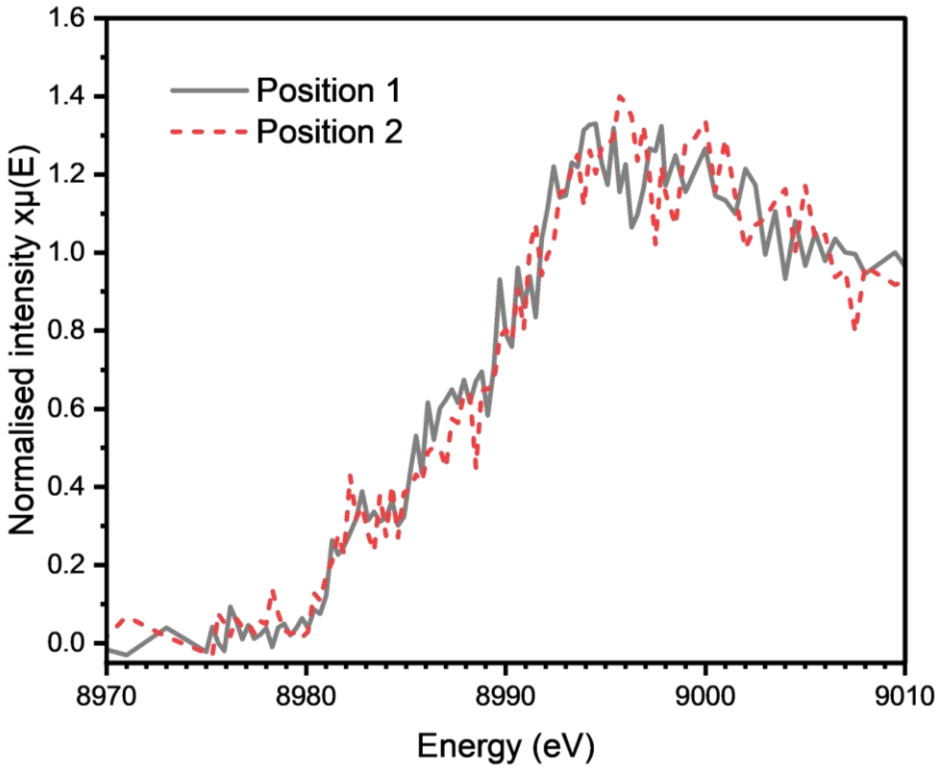


Figure 5.16: Single HERFD-XANES scans of the copper K-edge of Cu(II) *Ao*AA11 measured in Position 1 which was then exposed to an X-ray dose of $1.5 \times 10^7$ Gy, and at a new sample position; Position 2.

Linear combination fitting of Cu(II) *Ao*AA11 which has been exposed to a $1.5 \times 10^7$ Gy X-ray dose gives the best fit with a majority Cu(I) *Ao*AA11 standard and less than 1 % of the Cu(II) *Ao*AA11 standard, which suggests that the species observed is in the Cu(I) oxidation state and therefore a photoreduction reaction has occurred.

### *5.3.3.2 Cu(II) AoAA11 with chitin HERFD-XANES*

The findings of Chapter 3 suggest that chitin induces a change that is measurable in the copper K-edge HERFD-XANES of Cu(II) *Ao*AA11. This section aims to investigate the effect the presence of chitin has on the photoreactions of Cu(II) *Ao*AA11.

Copper K-edge HERFD-XANES of Cu(II) *Ao*AA11 with chitin that has been exposed to an X-ray dosage of 1.5x10$^7$ Gy is more similar in line shape to Cu(I) *Ao*AA11 with chitin than Cu(II) *Ao*AA11 with chitin (Figure 5.17). Excessive exposure of Cu(II) *Ao*AA11 with chitin to the X-ray beam results in significant changes in the rising edge 1s to *4p* transition, with an increase in intensity compared to Cu(II) *Ao*AA11 with chitin (although lower in intensity than Cu(I) *Ao*AA11 with chitin) and a shift to lower energy to 8981.8(3) eV compared to 8982.5 eV in both Cu(I) and Cu(II) *Ao*AA11 with chitin. The changes observed due to a photoreaction in Cu(II) *Ao*AA11 with chitin was also found to be a local photoreaction rather than global, suggesting this is a primary or secondary photoreaction.

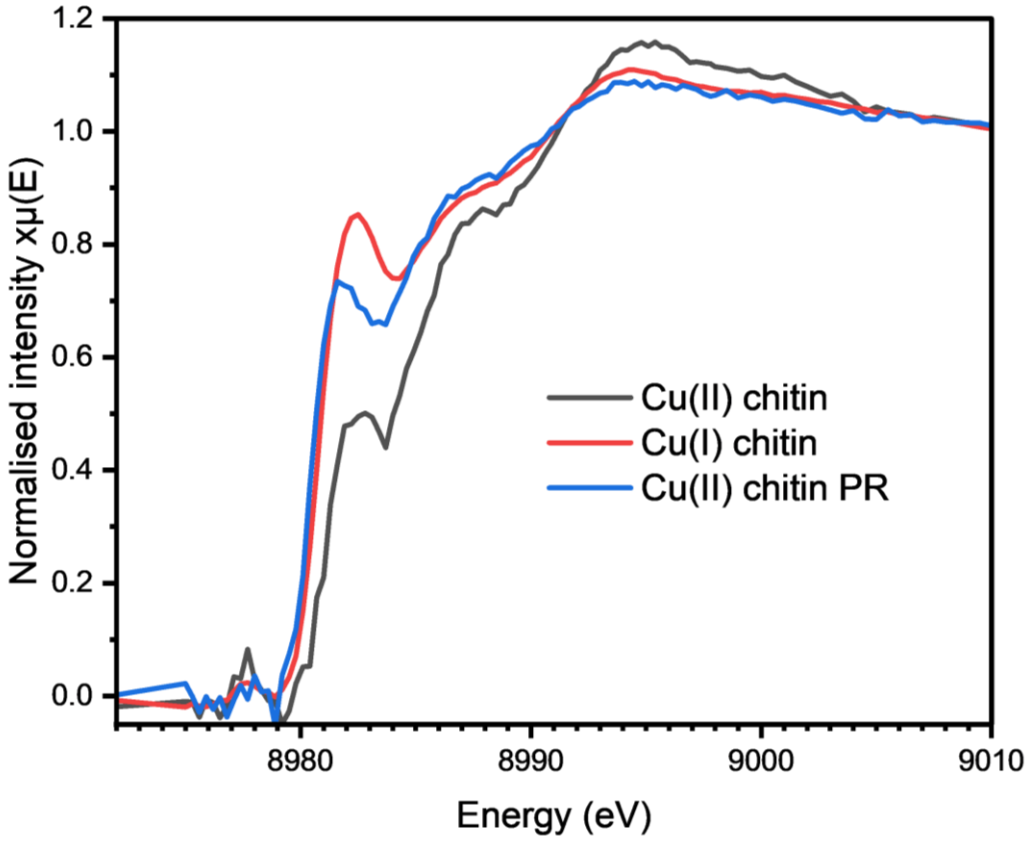


Figure 5.17: Copper K-edge HERFD-XANES of Cu(I) (*red*) and Cu(II) (*grey*) *Ao*AA11 with chitin and Cu(II) *Ao*AA11 with chitin which has been given an X-ray dose of 1.5x10$^7$ Gy (*blue*).

Linear combination fitting of the Cu(II) *Ao*AA11 with chitin after a 1.5x10$^7$ Gy X-ray dose HERFD-XANES spectrum gives a best fit with 77 % Cu(I) *Ao*AA11 with chitin standard and 23 % Cu(II) *Ao*AA11 with chitin standard. Whilst the HERFD-XANES spectrum of Cu(II) *Ao*AA11 with chitin after a 1.5x10$^7$ Gy X-ray dose is consistent with a majority Cu(I) *Ao*AA11 sample, the linear combination fit suggests

there is significantly more Cu(II) *Ao*AA11 after the same X-ray dose in the presence of chitin than in the absence of chitin. This finding points to the idea that the Cu(II) *Ao*AA11 interaction with chitin may be having a "protective" effect which slows the rate of photoreduction compared to Cu(II) *Ao*AA11 in the absence of chitin.

A copper K-edge HERFD-XANES spectrum measured within the same Cu(II) *Ao*AA11 sample after the photoreaction spectra were measured but in a sample position that had not been irradiated showed no significant difference to the HERFD-XANES spectra recorded in the sample positions before excessive irradiation, which confirms that the photoreaction observed is specific rather than global (Figure 5.18). As these spectra are single spectra recorded in different positions rather than a merge of spectra there is a poor signal-to-noise ratio, however as previously discussed, the signal-to-noise ratio is worse than expected (based on the other LPMO samples) for the concentration.

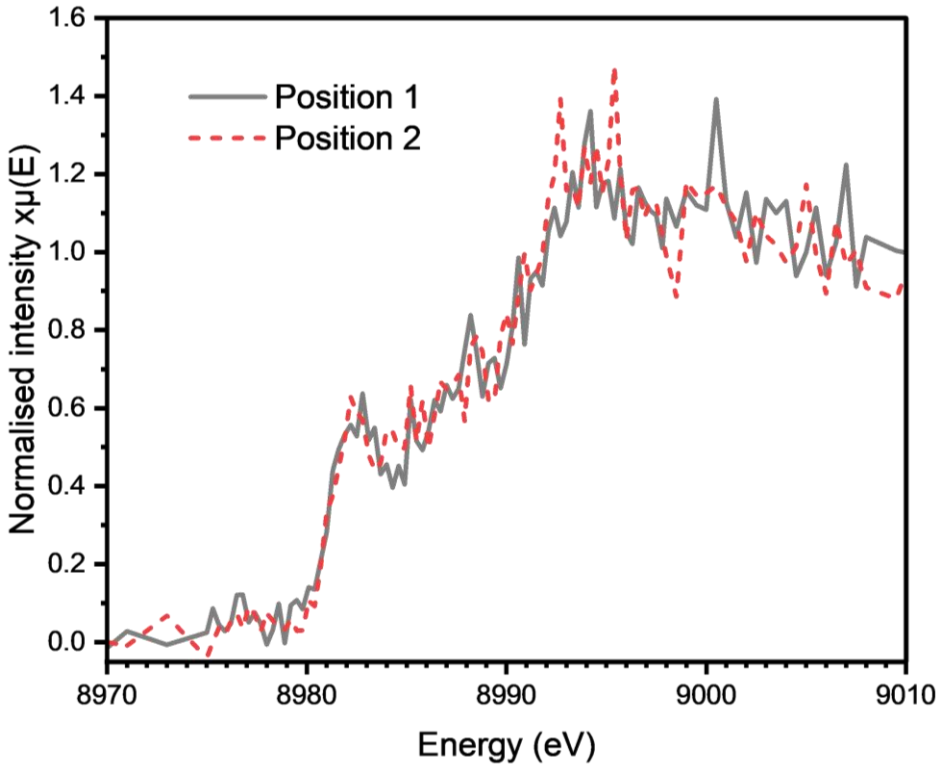


Figure 5.18: Copper K-edge HERFD-XANES of Cu(II) *Ao*AA11 with chitin measured in Position 1 which was then exposed to a high X-ray dose, and at a new sample position; Position 2.

When the copper K-edge HERFD-XANES spectra of Cu(II) *Ao*AA11 after $1.5 \times 10^7$ Gy X-ray dose both with and without chitin are compared they have similar line shapes but the 1s to *4p* rising edge transition of Cu(II) *Ao*AA11 is significantly more intense than that of Cu(II) *Ao*AA11 with chitin

(Figure 5.19). From this it can be deduced that whist Cu(II) *Ao*AA11 undergoes a similar photoreaction both in the presence and absence of chitin, they result in different products.

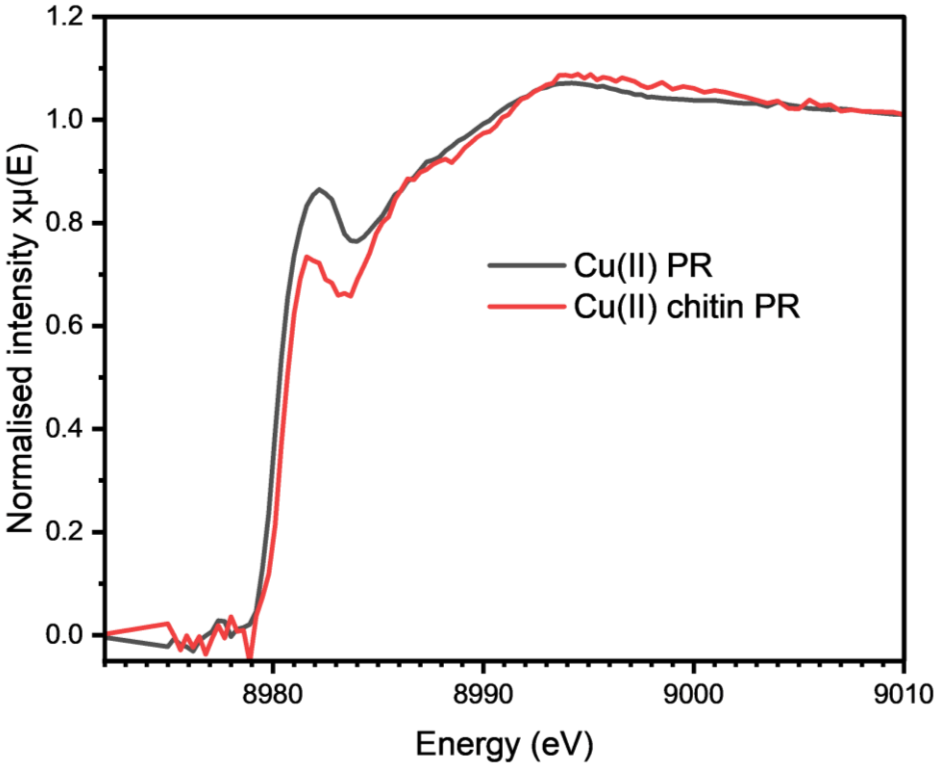


Figure 5.19: Copper K-edge HERFD-XANES of Cu(II) *Ao*AA11 after 1.5x10$^7$ Gy X-ray dose (black) and Cu(II) *Ao*AA11 with chitin after 1.5x10$^7$ Gy (red).

### *5.3.3.3 AoAA11 Pink species*

Once the Cu(II) *Ao*AA11 samples both with and without chitin had been exposed to an X-ray dose of 1.5x10$^7$ Gy a colour change was observed (Figure 5.20). The samples were initially blue (due to the concentration of Cu(II), but after excessive X-ray beam exposure the sample positions that were exposed to the beam had undergone a colour change to pink.

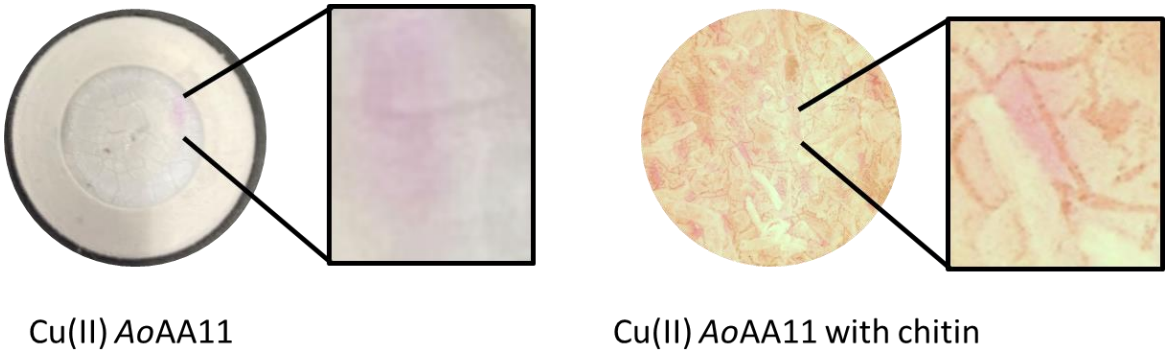


Figure 5.20: Cu(II) *Ao*AA11 samples with (right) and without (left) chitin showing the colour change that occurs where the samples have been exposed to the X-ray beam.

The copper K-edge HERFD-XANES spectrum of both Cu(II) *Ao*AA11 with and without chitin after a $1.5x10^7$ Gy X-ray dose are consistent with a sample with a mostly Cu(I) oxidation state, therefore it can be deduced that the "pink species" formed by X-ray beam exposure is in the Cu(I) oxidation state. As to further characterisation of the "pink species", further spectroscopic measurements need to be undertaken such as UV-vis stopped flow with reductants to investigate if this species can be produced chemically and if the formation of UV-vis bands can give clues as to the nature of the pink species. If the pink species can be generated through a reaction with chemical reductants then this also paves the way for further spectroscopic characterisation through EPR etc. In the absence of further spectroscopic data on the pink species literature data can be used to postulate its identity.

Lindley *et al* observed the formation of an LPMO species with a pink colour in Cu(II) *Bl*AA10 at pH 10.5. UV-vis and EPR spectroscopy was used to assign this species as a four coordinate Cu(II) species in which the Cu-$NH_2$ ligand as part of the histidine brace has been deprotonated to give a Cu-$NH^-$ azanide ligand (Figure 5.21). Lindley *et al* suggest this mechanism occurs after the deprotonation of an exogenous water ligand as well as the deprotonation and de-coordination of -$NH_2$ as a result of internal proton transfer from an exogenous water ligand. They suggest that the pink colour change observed arises due to a ligand to metal charge transfer (LMCT) from the coordination of $NH^-$ to Cu(II).[88]

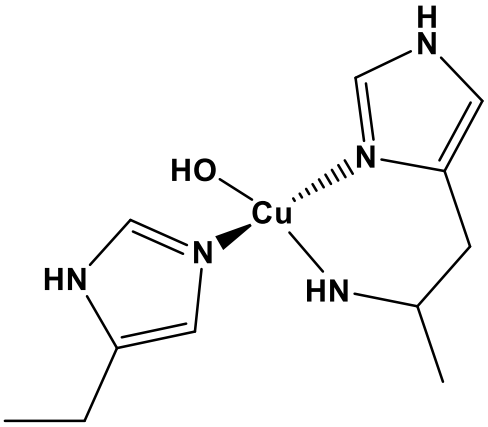


Figure 5.21: Cu(II) active site structure of *Bl*AA10 at pH 10.5 determined through EPR and UV-vis by Lindley *et* al.[88]

It is plausible that *via* a secondary photoreaction in which the photolysis of water from the solvent generates a proton and hydroxyl radical that the -$NH_2$ histidine brace group could be deprotonated to -$NH^-$ resulting in the copper coordination of an azanide group and thus giving the pink colour change observed. This change could be commensurate with the observed change in the 1s to *4p* transition peak intensity after *Ao*AA11 beam exposure as this peak is known to be reactive to changes in the copper primary coordination sphere. Alternatively, the observed change in the 1s to *4p* associated peak of the beam exposed *Ao*AA11 sample could be attributed to a change in oxidation state from Cu(II) to Cu(I). A change in oxidation state of the copper ion would be contradictory to the characterisations of the pink species found by Lindley *et al* at pH 10.5 in *Bl*AA10 which did not result in a change in oxidation state and therefore the structure proposed in Figure 5.21 is in the Cu(II) oxidation state. In the case of a change in oxidation state the pink species reported by Lindley *et al* may not be comparable to the pink species found in *Ao*AA11 and therefore other alternate explanations must be explored.

Another reported species to be considered when evaluating the possible structure of the pink species resulting from photoreduction is the Cu(II)-tyrosyl radical species characterised by Paradisi *et al* which was found to be purple in colour (Figure 5.22).[1] The "purple species" was formed in *Ls*AA9 and whilst similar in colour the purple species shows distinct differences to the pink species in *Ao*AA11. The purple species was formed oxidatively through the addition of peroxide and was found to be in the Cu(II) oxidation state, whereas the copper K-edge HERFD-XANES of the pink species is consistent with a Cu(I) oxidation state suggesting that the pink species is resultant of a photoreduction reaction. Furthermore the literature XAS spectrum of the purple species demonstrated a white line intensity between that of the Cu(I) and Cu(II) *Ls*AA9 oxidation states,

whereas the HERFD-XANES spectra of the pink species in *Ao*AA11 shown in Figure 5.19 has a white line intensity lower than both Cu(I) and Cu(II) *Ao*AA11.

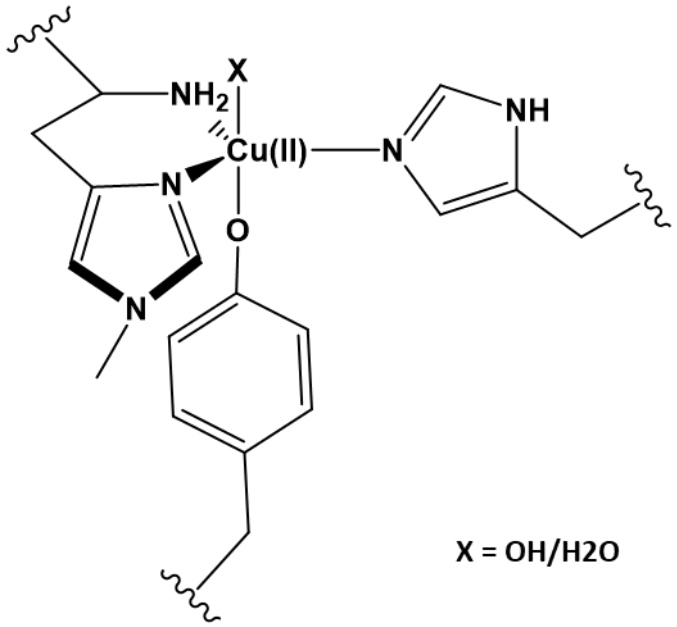


Figure 5.22: *Ls*AA9 “purple species” Cu(II)-tyrosyl radical structure characterised by Paradisi *et al*.[1]

An alternative explanation for the pink colour of the photo-ionised *Ao*AA11 species could be the formation of a tryptophanyl radical. There is precedent for peptides which contain neutral tryptophanyl radicals to be pink as a result of cation-π interations.[200] The *Ao*AA11 structure has a tryptophan residue *ca.* 5.9 Å from the copper active site. Using eMap, the most probable electron channel to produce a tryptophan radical was predicted to be an electron transfer from the copper ion to a tyrosine residue (Y140) and then to a tryptophan residue (W130) (Figure 5.23).

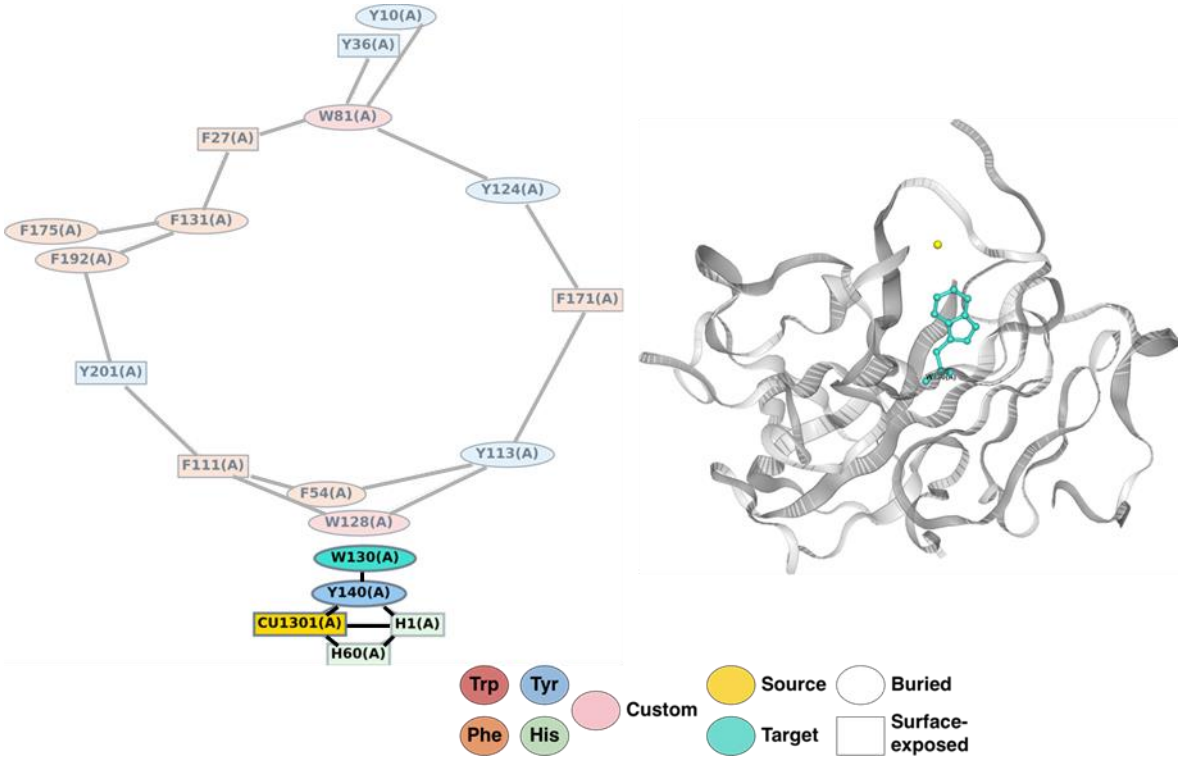


Figure 5.23: (Left) predicted electron transfer channel to generate a tryptophan radical in *Ao*AA11. (Right) *Ao*AA11 crystal structure (PDB: 4MAI) showing the copper ion in yellow and the nearest tryptophan residue (W130) in cyan. The images in this figure were generated on eMap.[201]

The predicted electron transfer channels to generate a tryptophan radical in *Ls*AA9 and *Ba*AA10 (used as a representative structure of *Bl*AA10 as there is not currently a *Ba*AA10 structure deposited in PDB) show that the generation of a tryptophan in these LPMOs is less probable than in *Ao*AA11 which would provide an explanation as to why a pink colour change was not observed after prolonged beam exposure in the *Ls*AA9 and *Bl*AA10 samples (Figure 5.24). In *Ls*AA9 the nearest tryptophan residue (W5) to the copper ion is *ca.* 10.2 Å away and the generation of a tryptophan radical from the copper ion would most likely involve an electron transfer channel *via* a histidine (H66) and a tyrosine (Y65) residue. In AA10 the nearest tryptophan residue (W187) to the copper ion is *ca*. 6.2 Å away and the most probable electron transfer channel from the copper ion would involve electron transfer from phenylalanine (F196) to tryptophan (W187).

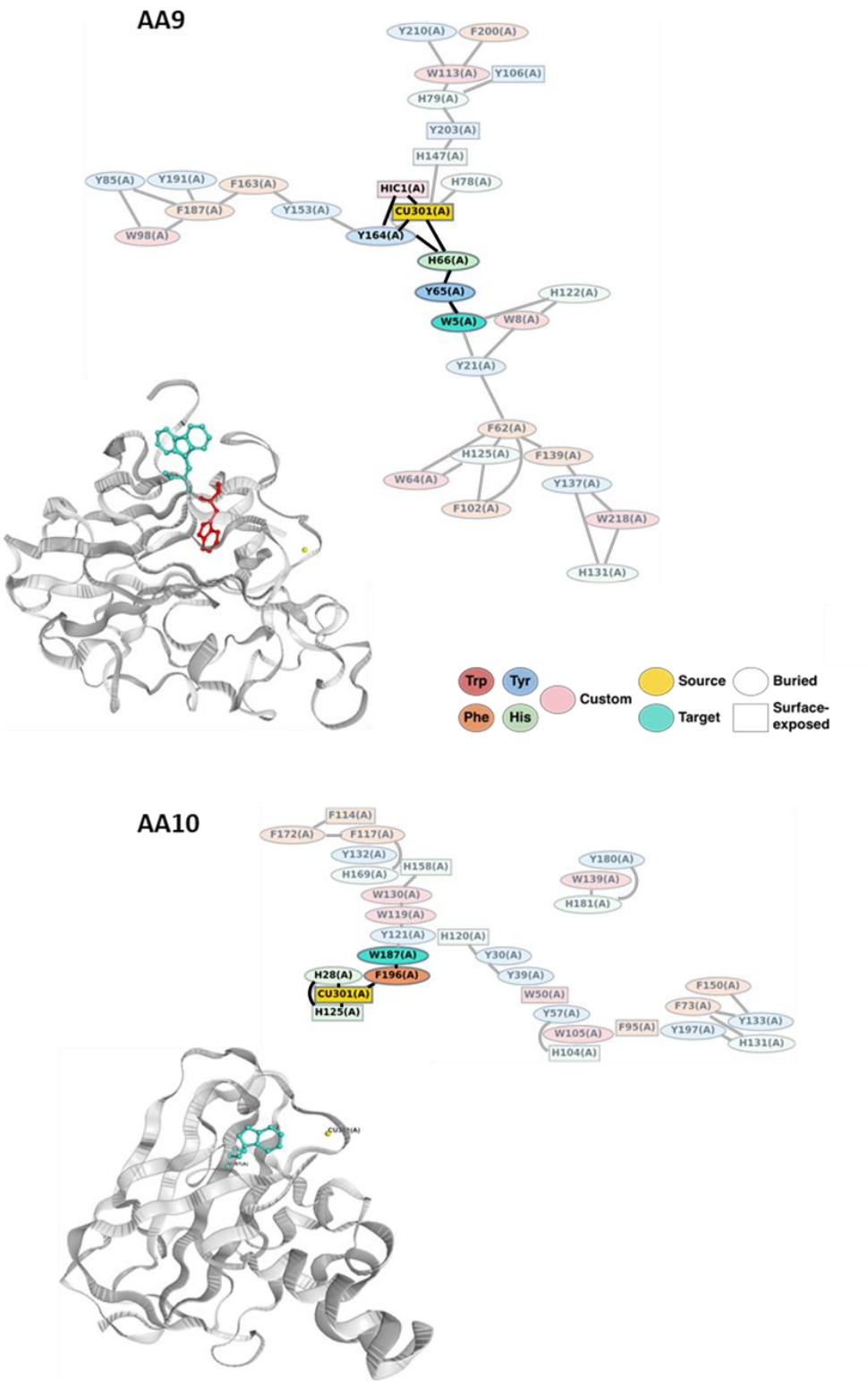


Figure 5.24: The predicted electron transfer channel to generate a tryptophan radical in *Ls*AA9 (PDB: 5N04) and *Ba*AA10 (5IJU) and their crystal structures showing the copper ion in yellow and the nearest tryptophan residues in cyan and red. The images in this figure were generated on eMap.[201]

The suggestion that the pink species formed on photoreduction of Cu(II) *Ao*AA11 is a tryptophanyl radical could be examined in future work by observing the changes induced by X-ray beam exposure to *Ao*AA11 mutants in which the two closest tryptophan residues are substituted. If the pink species is in fact a tryptophanyl radical a pink species should not form in the mutants.

## 5.4 Conclusions

Photoreactions can be induced in LPMO using X-ray beams at 10 K which lead to significant structural and electronic changes at the Cu(II) LPMO active site. All of the photoreactions observed across the three different LPMOs were specific photoreactions rather than global which means that they were either primary or secondary photoreactions.

Both the photoreactions of *An*AA9 (with and without PASC) and *Bl*AA10 gave similar reaction profiles with the first photoreaction observed being in accordance with a photoreduction reaction from the Cu(II) oxidation state and structure to a state with a HERFD-XANES spectrum similar to the Cu(I) oxidation state and structure. A second photoreaction then occurs in which a HERFD-XANES spectrum consistent with an unknown component emerges (Figure 5.25). The difference between the *Bl*AA10 and *An*AA9 photoreactions is that a third photoreaction is observed in the *An*AA9 samples where the unknown component appears to reform the Cu(I) *An*AA9-like structure as the X-ray dose is increased and changes are observed upon thermal relaxation. Whereas in *Bl*AA10 the unknown component appears to be more stable and does not change as either the X-ray dose nor the temperature is increased.

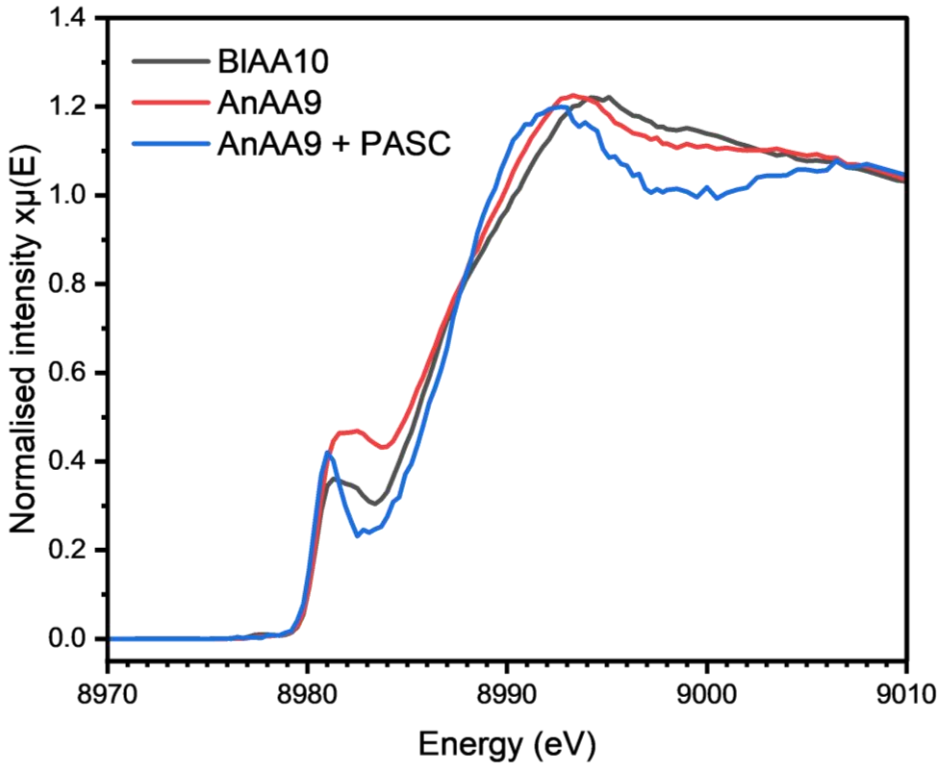


Figure 5.25: Predicted copper K-edge HERFD-XANES of the unassigned "pure" photoreaction components from MCR-ALS of the *Bl*AA10, *An*AA9 and *An*AA9 with PASC photoreaction datasets.

It should also be noted that in all of the photoreaction experiments presented in this chapter, the Cu(II) resting states of each LPMO were never photoreduced to the point of giving the same copper K-edge HERFD-XANES spectrum as the chemically reduced Cu(I) LPMO oxidation states. Therefore it can be concluded that over the X-ray doses and temperatures measured in *An*AA9 (with and without PASC), *Bl*AA10 and *Ao*AA11 (with and without chitin) photoreduced Cu(I) structures are not equivalent to their chemically reduced Cu(I) structures. The difference between the photoreduced and chemically reduced LPMO structures is important to note in the design of future spectroscopic/ crystallographic studies.

The photoreaction studies also confirm that the spectra reported in the previous two chapters were collected below the radiation dose at which photoreactions can be observed. The HERFD-XANES spectra recorded on I20-scanning had a dose per scan of $2x10^5$ Gy, and the XAS spectra recorded on B18 had a dose per scan of $6x10^5$ Gy. Both of these sets of experiments delivered a dose per scan to the sample below the radiation dose at which photoreactions have been reported to occur in this chapter, which is on the order of $1x10^7$ Gy.

Future work includes further spectroscopic characterisation of the photoreaction intermediates identified in this chapter. EPR measurements of the irradiated samples would be useful to confirm the copper oxidation states and to identify/ characterise and radical species present, although preparation of an irradiated EPR sample would be challenging.

# 6 Final remarks

## 6.1 Research outcomes

One of the overarching aims of this thesis was to set out methods of using X-ray spectroscopy to study the structure and electronics of the copper active site of LPMOs using a dual beamline approach to obtain HERFD-XANES and conventional XAS, which could be applied more widely to other metalloproteins. The studies presented in this thesis outline three different sets of X-ray spectroscopy experiments conducted on LPMOs; an investigation into the structural and electronic effects of substrate interactions, using rapid freeze quenching to trap short lived intermediates which can be characterised using X-ray spectroscopy, and the effects of X-ray irradiation induced photoreactions. The interpretation of the X-ray spectroscopy data collected was greatly facilitated by TD-DFT calculations which rely on good models based on crystal structures and EPR spectroscopy. It was investigated whether the activity differences between different genomic classes of LPMOs would result in structural/ electronic differences in the presence of substrate or induced by X-ray irradiation which could give insight into the LPMO mechanism of action. The LPMOs studied span over three different genomic classes of LPMO; AA9, AA10 and AA11, each of which showed spectroscopically measurable differences in their interactions with substrates and photoreactions. Not only were differences in the substrate interactions of different genomic classes of LPMOs compared, but also in different strains of LPMO within the same genomic group; *Ls*AA9 and *An*AA9.

Chapter 3 focuses on the use of HERFD-XANES spectroscopy and conventional XAS to obtain insights into the substrate interactions of *An*AA9 with PASC, *Ls*AA9 (Y164F) with G6, *Bl*AA10 with chitin and *Ao*AA11 with chitin in both their Cu(I) and Cu(II) oxidation states. The results of this study demonstrate the value of using two beamlines/ X-ray spectroscopy techniques to gain a fuller understanding of structural changes at the copper active site. The copper K-edge is very sensitive to changes in geometry and coordination number and these changes can be observed through the improved energy resolution that HERFD-XANES offers. In addition, the collection of EXAFS data using conventional XAS and QEXAFS to prevent sample damage over the longer energy range required facilitated the distinction between changes in the copper K-edge arising due to geometric/ coordination number/ bond length changes. Through the collection of HERFD-XANES and conventional XAS data across the LPMOs studied, it has been shown that each interacts differently with their respective substrates. In the Cu(II) oxidation state all of the LPMOs examined showed different outcomes on the addition of their respective substrates with *An*AA9 showing no change, *Ls*AA9 (Y164F) showing a decrease in coordination number, *Bl*AA10 showing a change in geometry.

In the Cu(I) oxidation state the addition of their respective substrates resulted in a decrease in coordination number in *An*AA9 and a change in geometry in both *Ls*AA9 (Y164F) and *Bl*AA10. The changes in the *Ao*AA11 HERFD-XANES spectra on addition of chitin cannot yet be confidently assigned without the collection of further spectroscopic data.

In Chapter 4 the results of the characterisation of a Cu(II) histidyl radical AA9 species which forms part of an oxidative damage repair mechanism is presented. The approach taken to characterise this radical LPMO species was the culmination of developing an anaerobic rapid freeze quenching technique combined with the use of the dual beamline approach to collect HERFD-XANES and EXAFS, a successful combination which could be applied to an array of metalloproteins and inorganic materials to gain insights into their reactivity. This chapter also highlights the importance of using a multifaceted and collaborative approach to the characterisation of LPMO intermediates through the use of cw-EPR, stopped flow spectroscopy, TD-DFT and activity assays.

The conclusions from Chapter 5 show the importance of being vigilant when setting up any reactions with LPMOs (or any dilute metalloproteins) that will be exposed to X-ray radiation as they are prone to unwanted photoreactions. A notable observation is that the photoreduction of Cu(II) LPMOs does not necessarily give a structure equivalent to a chemically reduced Cu(I) LPMO structure. Beyond the photoreduction reaction which is initially observed in the three LPMOs investigated, further X-ray exposure resulted in a structural change forming an uncharacterised species in *Bl*AA10 and *An*AA9 with and without PASC. In *Ao*AA11 a “pink species” formed both with and without chitin. The formation of these species shows firstly that different LPMOs undergo different photoreactions, but also that X-ray beams can be used to form new species of LPMO at cryogenic temperatures.

## 6.2 Future work

A considerable amount of work has been done within the LPMO community to gain insights into LPMOs which has led to the ongoing discovery of new LPMOs, new LPMO functions and information on their mechanisms, but with each valuable new discovery in LPMOs it raises more questions. The work presented in this thesis is no exception and whilst useful conclusions have been reached, it has also provided scope for further research.

For a more complete characterisation of the substrate interactions of *Ls*AA9, *Bl*AA10 and *Ao*AA11 in the way the characterisation of the substrate interactions of *An*AA9 have been presented more

spectroscopic information in the form of EPR for the Cu(II) oxidation states and crystal structures for the Cu(I) oxidation states would be useful. Furthermore, more TD-DFT calculations on the effects of different ligands, coordination numbers and geometries would be valuable but with so many possible combinations it is important to have good crystal structures to base models and hypotheses on. Furthermore, collection of more EXAFS repeats could improve the quality of the data and allow for fitting beyond the first shell. EXAFS for *An*AA9 and *Ao*AA11 with and without substrate would also be interesting to see to confirm the assignments of the *An*AA9-substrate structures and to gain further information on the *Ao*AA11-substrate structures. It is also noted that the measured concentration of the *Ao*AA11 samples is not commensurate with the quality of the HERFD-XANES data collected and therefore an investigation into how the sample has become more dilute (without precipitation) is essential for future *Ao*AA11 experiments using this method. The EPR and UV-vis spectra of the Cu(II) AA11 sample measured in the laboratory in the days prior to the synchrotron experiments were commensurate with the expected concentration, with no visible precipitation of the sample it is plausible that the lack of copper signal in the HERFD-XANES is due to an interaction with the Cu(II) AA11 sample and plastic Eppendorf it was stored in. The results of this chapter demonstrate that insights into the substrate interaction of LPMOs in the Cu(I) and Cu(II) oxidation states can be studies using X-ray spectroscopy and therefore this technique can be more widely apply to other LPMOs and other LPMO-substrate combinations to gain further insight.

The results of Chapter 4 outline a technique for preparing anaerobically freeze quenched intermediate samples which can be measured using EPR and X-ray spectroscopy. This method can be applied to other reactions and developed to be able to trap anaerobic freeze quenched samples that can be measured using other spectroscopic techniques. The HERFD-XANES results show how sensitive the copper K-edge pre-edge region is, so much so that it can be used in conjunction with TD-DFT to characterise radical species; this could be utilised more widely in the study of other copper systems.

The collection of EXAFS data to monitor photoreactions would allow for the distinction between electronic and structural changes, especially to observe the effects, if any, of thermal relaxation. EXAFS data in addition with TD-DFT calculations could also be used to characterise the “pure” components in the photoreaction mechanisms identified by MCR-ALS. Again, the issue of the concentration of the *Ao*AA11 samples must be resolved in order to collect high quality data going forward. Once this is achieved further investigation to try and characterise the pink species using stopped flow UV-vis spectroscopy to monitor the reaction and inform anaerobic rapid freeze

quenching to prepare samples which can be analysed using EPR. Furthermore, the hypothesis that the pink species is a tryptophan radical can be tested by mutating the tryptophan residues identified to be closest to the copper active site.

# List of Abbreviations

| | |
|---|---|
| AA | Auxiliary activity |
| CAZy | Carbohydrate active enzyme database |
| CBM | Carbohydrate-binding module |
| CDH | Cellobiose dehydrogenase |
| cw-EPR | Continuous wave electron paramagnetic resonance |
| DFT | Density functional theory |
| DMP | 2,6-dimethoxyphenol |
| EPR | Electron paramagnetic resonance |
| EXAFS | Extended X-ray absorption fine structure |
| GH | glycoside hydrolases |
| $Glc_6$ | Cellulose hexasaccharide |
| HERFD | High energy resolution fluoresence detected |
| HSQC | Heteronuclear single quantum coherence |
| LCF | Linear combination fitting |
| LMCT | Ligand to metal charge transfer |
| LPMO | Lytic polysaccharide monooxygenase |
| MCD | Magnetic circular dichroism |
| *m*-CPBA | *meta*-chloro-perbenzoic acid |
| MCR-ALS | Multivariate curve resolution - alternating least squares |
| NMR | Nuclear magnetic resonance |
| PASC | Phosphoric acid swollen cellulose |
| PDB | Protein database |
| polyXG | Polymeric xyloglucan |
| SOMO | Singularly occupied molecular orbital |
| UV-vis | Ultraviolet – visible |
| XANES | X-ray absorption near edge structure |
| XAS | X-ray absorption spectroscopy |
| XG14 | Xyloglucan oligomers |
| XRD | X-ray diffraction |

# Bibliography


1. Paradisi, A. *et al.* Formation of a Copper(II)-Tyrosyl Complex at the Active Site of Lytic Polysaccharide Monooxygenases Following Oxidation by H2O2. *J. Am. Chem. Soc.* **141**, 18585–18599 (2019).
2. Saloheimo, M., Nakari-SETÄLÄ, T., Tenkanen, M. & Penttilä, M. cDNA cloning of a Trichoderma reesei cellulase and demonstration of endoglucanase activity by expression in yeast. *Eur J Biochem* **249**, (1997).
3. Sunna, A., Gibbs, M. D. & Bergquist, P. L. A novel thermostable multidomain 1,4-β-xylanase from 'Caldibacillus cellulovorans' and effect of its xylan-binding domain on enzyme activity. *Microbiology (N Y)* **146**, (2000).
4. Suzuki, K., Suzuki, M., Taiyoji, M., Nikaidou, N. & Watanabe, T. Chitin binding protein (cbp21) in the culture supernatant of serratia marcescens 2170. *Biosci Biotechnol Biochem* **62**, (1998).
5. Kolbe, S., Fischer, S., Becirevic, A., Hinz, P. & Schrempf, H. The Streptomyces reticuli α-chitin-binding protein CHB2 and its gene. *Microbiology (N Y)* **144**, (1998).
6. Schnellmann, J., Zeltins, A., Blaak, H. & Schrempf, H. The novel lectin-like protein CHB1 is encoded by a chitin-inducible Streptomyces olivaceoviridis gene and binds specifically to crystalline α-chitin of fungi and other organisms. *Mol Microbiol* **13**, (1994).
7. Eriksson, K. E., Pettersson, B. & Westermark, U. Oxidation: An important enzyme reaction in fungal degradation of cellulose. *FEBS Lett* **49**, (1974).
8. Quinlan, R. J. *et al.* Insights into the oxidative degradation of cellulose by a copper metalloenzyme that exploits biomass components. *Proc Natl Acad Sci U S A* **108**, (2011).
9. Horn, S. J., Vaaje-Kolstad, G., Westereng, B. & Eijsink, V. G. H. Novel enzymes for the degradation of cellulose. *Biotechnology for Biofuels* vol. 5 Preprint at https://doi.org/10.1186/1754-6834-5-45 (2012).
10. Vaaje-Kolstad, G. *et al.* An oxidative enzyme boosting the enzymatic conversion of recalcitrant polysaccharides. *Science (1979)* **330**, 219–222 (2010).

11. Ciano, L., Davies, G. J., Tolman, W. B. & Walton, P. H. Bracing copper for the catalytic oxidation of C–H bonds. *Nat Catal* **1**, 571–577 (2018).

12. Bissaro, B. *et al.* Oxidative cleavage of polysaccharides by monocopper enzymes depends on H2O2. *Nat Chem Biol* **13**, (2017).

13. Sabbadin, F. *et al.* Secreted pectin monooxygenases drive plant infection by pathogenic oomycetes. *Science (1979)* **373**, (2021).

14. Himmel, M. E. *et al.* Biomass recalcitrance: Engineering plants and enzymes for biofuels production. *Science* vol. 315 Preprint at https://doi.org/10.1126/science.1137016 (2007).

15. Ramos, M. D. N., Milessi, T. S., Candido, R. G., Mendes, A. A. & Aguiar, A. Enzymatic catalysis as a tool in biofuels production in Brazil: Current status and perspectives. *Energy for Sustainable Development* vol. 68 Preprint at https://doi.org/10.1016/j.esd.2022.03.007 (2022).

16. Walton, P. H. & Davies, G. J. On the catalytic mechanisms of lytic polysaccharide monooxygenases. *Current Opinion in Chemical Biology* vol. 31 Preprint at https://doi.org/10.1016/j.cbpa.2016.04.001 (2016).

17. Klemm, D., Heublein, B., Fink, H. P. & Bohn, A. Cellulose: Fascinating biopolymer and sustainable raw material. *Angewandte Chemie - International Edition* vol. 44 Preprint at https://doi.org/10.1002/anie.200460587 (2005).

18. Goller, C. C. & Romeo, T. Environmental influences on biofilm development. *Current Topics in Microbiology and Immunology* vol. 322 Preprint at https://doi.org/10.1007/978-3-540-75418-3_3 (2008).

19. Updegraff, D. M. Semimicro determination of cellulose inbiological materials. *Anal Biochem* **32**, (1969).

20. Roberts, J. C. Lignin biodegradation and transformation. *Trends Biochem Sci* **7**, (1982).

21. Percival Zhang, Y. H., Cui, J., Lynd, L. R. & Kuang, L. R. A transition from cellulose swelling to cellulose dissolution by o-phosphoric acid: Evidence from enzymatic hydrolysis and supramolecular structure. *Biomacromolecules* **7**, (2006).

22. Gibson, L. J. The hierarchical structure and mechanics of plant materials. *Journal of the Royal Society Interface* vol. 9 Preprint at https://doi.org/10.1098/rsif.2012.0341 (2012).

23. Wilhelmi, A. E. Principles of biochemistry. *Endocrinology* **56**, (1955).

24. Tang, W. J., Fernandez, J. G., Sohn, J. J. & Amemiya, C. T. Chitin is endogenously produced in vertebrates. *Current Biology* **25**, (2015).

25. Sanjanwala, D. *et al.* Polysaccharide-based hydrogels for medical devices, implants and tissue engineering: A review. *International Journal of Biological Macromolecules* vol. 256 Preprint at https://doi.org/10.1016/j.ijbiomac.2023.128488 (2024).

26. Drula, E. *et al.* The carbohydrate-active enzyme database: Functions and literature. *Nucleic Acids Res* **50**, (2022).

27. Lombard, V., Golaconda Ramulu, H., Drula, E., Coutinho, P. M. & Henrissat, B. The carbohydrate-active enzymes database (CAZy) in 2013. *Nucleic Acids Res* **42**, (2014).

28. Levasseur, A., Drula, E., Lombard, V., Coutinho, P. M. & Henrissat, B. Expansion of the enzymatic repertoire of the CAZy database to integrate auxiliary redox enzymes. *Biotechnol Biofuels* **6**, (2013).

29. Forsberg, Z. *et al.* Structural and functional characterization of a conserved pair of bacterial cellulose-oxidizing lytic polysaccharide monooxygenases. *Proc Natl Acad Sci U S A* **111**, (2014).

30. Forsberg, Z. *et al.* Cleavage of cellulose by a cbm33 protein. *Protein Science* **20**, (2011).

31. Chu, X.-M. *et al.* Quinoline and quinolone dimers and their biological activities: An overview. *Eur. J. Med. Chem.* **161**, 101–117 (2019).

32. Gregory, R. C. *et al.* Activity, stability and 3-D structure of the Cu(II) form of a chitin-active lytic polysaccharide monooxygenase from: Bacillus amyloliquefaciens. *Dalton Transactions* **45**, 16904–16912 (2016).

33. Hemsworth, G. R. *et al.* The copper active site of CBM33 polysaccharide oxygenases. *J Am Chem Soc* **135**, (2013).

34. Courtade, G. *et al. H, 13 C, 15 N Resonance Assignment of the Chitin-Active Lytic Polysaccharide Monooxygenase BlLPMO10A from Bacillus Licheniformis*. www.cazy.org.

35. Forsberg, Z. *et al.* Comparative study of two chitin-active and two cellulose-active AA10-type lytic polysaccharide monooxygenases. *Biochemistry* **53**, (2014).

36. Zhang, H., Zhao, Y., Cao, H., Mou, G. & Yin, H. Expression and characterization of a lytic polysaccharide monooxygenase from Bacillus thuringiensis. *Int J Biol Macromol* **79**, (2015).

37. Manjeet, K., Madhuprakash, J., Mormann, M., Moerschbacher, B. M. & Podile, A. R. A carbohydrate binding module-5 is essential for oxidative cleavage of chitin by a multi-modular lytic polysaccharide monooxygenase from Bacillus thuringiensis serovar kurstaki. *Int J Biol Macromol* **127**, (2019).

38. Forsberg, Z. *et al.* Structural and functional analysis of a lytic polysaccharide monooxygenase important for efficient utilization of chitin in Cellvibrio japonicus. *Journal of Biological Chemistry* **291**, (2016).

39. Gardner, J. G. *et al.* Systems biology defines the biological significance of redox-active proteins during cellulose degradation in an aerobic bacterium. *Mol Microbiol* **94**, (2014).

40. Vaaje-Kolstad, G. *et al.* Characterization of the chitinolytic machinery of enterococcus faecalis V583 and high-resolution structure of its oxidative CBM33 enzyme. *J Mol Biol* **416**, (2012).

41. Ghatge, S. S. *et al.* Multifunctional cellulolytic auxiliary activity protein HcAA10-2 from Hahella chejuensis enhances enzymatic hydrolysis of crystalline cellulose. *Appl Microbiol Biotechnol* **99**, (2015).

42. Forsberg, Z. *et al.* Structural determinants of bacterial lytic polysaccharide monooxygenase functionality. *Journal of Biological Chemistry* **293**, (2018).

43. Wu, M. *et al.* Crystal structure and computational characterization of the lytic polysaccharide monooxygenase GH61D from the basidiomycota fungus Phanerochaete chrysosporium. *Journal of Biological Chemistry* **288**, (2013).

44. Hemsworth, G. R., Henrissat, B., Davies, G. J. & Walton, P. H. Discovery and characterization of a new family of lytic polysaccharide monooxygenases. *Nat. Chem. Biol.* **10**, 122–126 (2014).

45. Wang, D., Li, J., Wong, A. C. Y., Aachmann, F. L. & Hsieh, Y. S. Y. A colorimetric assay to rapidly determine the activities of lytic polysaccharide monooxygenases. *Biotechnol Biofuels* **11**, (2018).

46. Vu, V. V., Beeson, W. T., Span, E. A., Farquhar, E. R. & Marletta, M. A. A family of starch-active polysaccharide monooxygenases. *Proc Natl Acad Sci U S A* **111**, (2014).

47. Lo Leggio, L. *et al.* Structure and boosting activity of a starch-degrading lytic polysaccharide monooxygenase. *Nat. Commun.* **6**, 5961 (2015).

48. Couturier, M. *et al.* Lytic xylan oxidases from wood-decay fungi unlock biomass degradation. *Nat. Chem. Biol.* **14**, 306–310 (2018).

49. Sabbadin, F. *et al.* An ancient family of lytic polysaccharide monooxygenases with roles in arthropod development and biomass digestion. *Nat. Commun.* **9**, 756 (2018).

50. Filiatrault-Chastel, C. *et al.* AA16, a new lytic polysaccharide monooxygenase family identified in fungal secretomes. *Biotechnol. Biofuels* **12**, 55 (2019).

51. Peisach, J. & Blumberg, W. E. Structural implications derived from the analysis of electron paramagnetic resonance spectra of natural and artificial copper proteins. *Arch Biochem Biophys* **165**, (1974).

52. Jagadeeswaran, G., Veale, L. & Mort, A. J. Do Lytic Polysaccharide Monooxygenases Aid in Plant Pathogenesis and Herbivory? *Trends in Plant Science* vol. 26 Preprint at https://doi.org/10.1016/j.tplants.2020.09.013 (2021).

53. Frommhagen, M., Westphal, A. H., van Berkel, W. J. H. & Kabel, M. A. Distinct substrate specificities and electron-donating systems of fungal lytic polysaccharide monooxygenases. *Frontiers in Microbiology* vol. 9 Preprint at https://doi.org/10.3389/fmicb.2018.01080 (2018).

54. Frandsen, K. E. H. *et al.* The molecular basis of polysaccharide cleavage by lytic polysaccharide monooxygenases. *Nat. Chem. Biol.* **12**, 298–303 (2016).

55. Phillips, C. M., Beeson, W. T., Cate, J. H. & Marletta, M. A. Cellobiose Dehydrogenase and a Copper-Dependent Polysaccharide Monooxygenase Potentiate Cellulose Degradation by Neurospora crassa . *ACS Chem Biol* **6**, (2011).

56. Isaksen, T. *et al.* A C4-oxidizing lytic polysaccharide monooxygenase cleaving both cellulose and cello-oligosaccharides. *Journal of Biological Chemistry* **289**, (2014).

57. Westereng, B. *et al.* Simultaneous analysis of C1 and C4 oxidized oligosaccharides, the products of lytic polysaccharide monooxygenases acting on cellulose. *J Chromatogr A* **1445**, (2016).

58. Hu, J., Arantes, V., Pribowo, A., Gourlay, K. & Saddler, J. N. Substrate factors that influence the synergistic interaction of AA9 and cellulases during the enzymatic hydrolysis of biomass. *Energy Environ Sci* **7**, (2014).

59. Gao, J., Thomas, D. A., Sohn, C. H. & Beauchamp, J. L. Biomimetic reagents for the selective free radical and acid-base chemistry of glycans: Application to glycan structure determination by mass spectrometry. *J Am Chem Soc* **135**, (2013).

60. Petrović, D. M. *et al.* Methylation of the N-terminal histidine protects a lytic polysaccharide monooxygenase from auto-oxidative inactivation. *Protein Science* **27**, (2018).

61. Zhang, L., Koay, M., Maher, M. J., Xiao, Z. & Wedd, A. G. Intermolecular Transfer of Copper Ions from the CopC Protein of Pseudomonas syringae. Crystal Structures of Fully Loaded Cu I Cu II Forms. (2006) doi:10.1021/ja058528x.

62. Gudmundsson, M. *et al.* Structural and electronic snapshots during the transition from a Cu(II) to Cu(I) metal center of a lytic polysaccharide onooxygenase by x-ray photoreduction. *Journal of Biological Chemistry* **289**, 18782–18792 (2014).

63. Mazurkewich, S., Seveso, A., Hüttner, S., Brändén, G. & Larsbrink, J. Structure of a C1/C4-oxidizing AA9 lytic polysaccharide monooxygenase from the thermophilic fungus Malbranchea cinnamomea. *Acta Crystallogr D Struct Biol* **77**, (2021).

64. Hemsworth, G. R., Henrissat, B., Davies, G. J. & Walton, P. H. Discovery and characterization of a new family of lytic polysaccharide monooxygenases. *Nat Chem Biol* **10**, 122–126 (2014).

65. Muderspach, S. J. *et al.* Further structural studies of the lytic polysaccharide monooxygenase Ao AA13 belonging to the starch-active AA13 family . *Amylase* **3**, (2019).

66. Borisova, A. S. *et al.* Structural and functional characterization of a lytic polysaccharide monooxygenase with broad substrate specificity. *Journal of Biological Chemistry* **290**, (2015).

67. Simmons, T. J. *et al.* Structural and electronic determinants of lytic polysaccharide monooxygenase reactivity on polysaccharide substrates. *Nat Commun* **8**, (2017).

68. Peciulyte, A. *et al.* Redox processes acidify and decarboxylate steam-pretreated lignocellulosic biomass and are modulated by LPMO and catalase. *Biotechnol Biofuels* **11**, (2018).

69. Frandsen, K. E. H., Poulsen, J. C. N., Tovborg, M., Johansen, K. S. & lo Leggio, L. Learning from oligosaccharide soaks of crystals of an AA13 lytic polysaccharide monooxygenase: Crystal packing, ligand binding and active-site disorder. *Acta Crystallogr D Struct Biol* **73**, (2017).

70. Crouch, L. I., Labourel, A., Walton, P. H., Davies, G. J. & Gilbert, H. J. The Contribution of Non-catalytic Carbohydrate Binding Modules to the Activity of Lytic Polysaccharide Monooxygenases. *Journal of Biological Chemistry* **291**, 7439–7449 (2016).

71. Chalak, A. *et al.* Influence of the carbohydrate-binding module on the activity of a fungal AA9 lytic polysaccharide monooxygenase on cellulosic substrates. *Biotechnol Biofuels* **12**, 206 (2019).

72. Czjzek, M. & Ficko-Blean, E. Probing the complex architecture of multimodular carbohydrate-active enzymes using a combination of small angle X-ray scattering and X-ray crystallography. in *Methods in Molecular Biology* vol. 1588 (2017).

73. O'Dell, W. B., Bodenheimer, A. M. & Meilleur, F. Neutron protein crystallography: A complementary tool for locating hydrogens in proteins. *Arch Biochem Biophys* **602**, (2016).

74. Bacik, J. P. *et al.* Neutron and Atomic Resolution X-ray Structures of a Lytic Polysaccharide Monooxygenase Reveal Copper-Mediated Dioxygen Binding and Evidence for N-Terminal Deprotonation. *Biochemistry* **56**, (2017).

75. Caldararu, O., Oksanen, E., Ryde, U. & Hedegård, E. D. Correction: Mechanism of hydrogen peroxide formation by lytic polysaccharide monooxygenase. *Chem Sci* **10**, (2019).

76. O'Dell, W. B., Agarwal, P. K. & Meilleur, F. Oxygen Activation at the Active Site of a Fungal Lytic Polysaccharide Monooxygenase. *Angewandte Chemie - International Edition* **56**, (2017).

77. Schröder, G. C., O'Dell, W. B., Webb, S. P., Agarwal, P. K. & Meilleur, F. Capture of activated dioxygen intermediates at the copper-active site of a lytic polysaccharide monooxygenase. *Chem Sci* **13**, 13303–13320 (2022).

78. Berman, H., Henrick, K. & Nakamura, H. Announcing the worldwide Protein Data Bank. *Nature Structural Biology* vol. 10 Preprint at https://doi.org/10.1038/nsb1203-980 (2003).

79. Antholine, W. E. Low Frequency EPR of Cu2+ in Proteins. in *Biomedical EPR, Part A: Free Radicals, Metals, Medicine, and Physiology* (2006). doi:10.1007/0-387-26741-7_14.

80. Malmström, B. G., Reinhammar, B. & Vänngård, T. Two forms of copper (II) in fungal laccase. *BBA - General Subjects* **156**, (1968).

81. Garajova, S. *et al.* Single-domain flavoenzymes trigger lytic polysaccharide monooxygenases for oxidative degradation of cellulose. *Sci Rep* **6**, (2016).

82. Hemsworth, G. R., Ciano, L., Davies, G. J. & Walton, P. H. Production and spectroscopic characterization of lytic polysaccharide monooxygenases. in *Methods in Enzymology* vol. 613 (2018).

83. Theibich, Y. A., Sauer, S. P. A., Leggio, L. Lo & Hedegård, E. D. Estimating the accuracy of calculated electron paramagnetic resonance hyperfine couplings for a lytic polysaccharide monooxygenase. *Comput Struct Biotechnol J* **19**, (2021).

84. Vu, V. V. & Ngo, S. T. Copper active site in polysaccharide monooxygenases. *Coordination Chemistry Reviews* vol. 368 Preprint at https://doi.org/10.1016/j.ccr.2018.04.005 (2018).

85. Ciano, L. *et al.* Insights from semi-oriented EPR spectroscopy studies into the interaction of lytic polysaccharide monooxygenases with cellulose. *Dalton Transactions* **49**, (2020).

86. Bissaro, B., Isaksen, I., Vaaje-Kolstad, G., Eijsink, V. G. H. & Røhr, Å. K. How a Lytic Polysaccharide Monooxygenase Binds Crystalline Chitin. *Biochemistry* **57**, (2018).

87. Courtade, G. *et al.* Mechanistic basis of substrate-O2 coupling within a chitin-active lytic polysaccharide monooxygenase: An integrated NMR/EPR study. *Proc. Natl. Acad. Sci. U. S. A.* **117**, 19178–19189 (2020).

88. Lindley, P. J., Parkin, A., Davies, G. & Walton, P. H. Mapping the protonation states of the histidine brace in an AA10 lytic polysaccharide monooxygenase using CW-EPR spectroscopy and DFT calculations. *Faraday Discuss* (2021) doi:10.1039/d1fd00068c.

89. Marion, D. An introduction to biological NMR spectroscopy. *Molecular and Cellular Proteomics* vol. 12 Preprint at https://doi.org/10.1074/mcp.O113.030239 (2013).

90. Cavalli, A., Salvatella, X., Dobson, C. M. & Vendruscolo, M. Protein structure determination from NMR chemical shifts. *Proc Natl Acad Sci U S A* **104**, (2007).

91. Bertini, I. & Pierattelli, R. Copper(II) proteins are amenable for NMR investigations. in *Pure and Applied Chemistry* vol. 76 (2004).

92. Aachmann, F. L., Sørlie, M., Skjåk-Bræk, G., Eijsink, V. G. H. & Vaaje-Kolstad, G. NMR structure of a lytic polysaccharide monooxygenase provides insight into copper binding, protein dynamics, and substrate interactions. *Proc Natl Acad Sci U S A* **109**, (2012).

93. Courtade, G., Forsberg, Z., Heggset, E. B., Eijsink, V. G. H. & Aachmann, F. L. The carbohydrate-binding module and linker of a modular lytic polysaccharide monooxygenase promote localized cellulose oxidation. *Journal of Biological Chemistry* **293**, (2018).

94. Courtade, G. *et al.* Interactions of a fungal lytic polysaccharide monooxygenase with β-glucan substrates and cellobiose dehydrogenase. *Proc Natl Acad Sci U S A* **113**, (2016).

95. Gill, S. C. & von Hippel, P. H. Calculation of protein extinction coefficients from amino acid sequence data. *Anal Biochem* **182**, (1989).

96. Breslmayr, E. *et al.* A fast and sensitive activity assay for lytic polysaccharide monooxygenase. *Biotechnol Biofuels* **11**, 79 (2018).

97. Kittl, R., Kracher, D., Burgstaller, D., Haltrich, D. & Ludwig, R. Production of four Neurospora crassa lytic polysaccharide monooxygenases in Pichia pastoris monitored by a fluorimetric assay. *Biotechnol Biofuels* **5**, 79 (2012).

98. Jones, S. M., Transue, W. J., Meier, K. K., Kelemen, B. & Solomon, E. I. Kinetic analysis of amino acid radicals formed in H2O2-driven CuI LPMO reoxidation

implicates dominant homolytic reactivity. *Proc Natl Acad Sci U S A* **117**, (2020).

99. Singh, R. K. *et al.* Detection and Characterization of a Novel Copper-Dependent Intermediate in a Lytic Polysaccharide Monooxygenase. *Chemistry - A European Journal* **26**, (2020).
100. Andersson, L. A. Magnetic Circular Dichroism, Theory. *Encyclopedia of Spectroscopy and Spectrometry* 1400–1406 (1999) doi:10.1016/B978-0-12-374413-5.00332-8.
101. magnetic circular dichroism. *The IUPAC Compendium of Chemical Terminology* (2008) doi:10.1351/GOLDBOOK.MT06778.
102. Landrum, G. A., Ekberg, C. A. & Whittaker, J. W. A ligand field model for MCD spectra of biological cupric complexes. *Biophys J* **69**, (1995).
103. Hansson, H. *et al.* High-resolution structure of a lytic polysaccharide monooxygenase from Hypocrea jecorina reveals a predicted linker as an integral part of the catalytic domain. *Journal of Biological Chemistry* **292**, (2017).
104. Gaber, B. P., Miskowski, V. & Spiro, T. G. Resonance Raman Scattering from Iron(III)- and Copper(II)-Transferrin and an Iron(III) Model Compound. A Spectroscopic Interpretation of the Transferrin Binding Site. *J Am Chem Soc* **96**, (1974).
105. Tomimatsu, Y., Kint, S. & Scherer, J. R. Resonance Raman spectroscopy of iron (III) - ovotransferrin and iron (III) - human serum transferrin. *Biochem Biophys Res Commun* **54**, (1973).
106. Tang, S. P. W., Spiro, T. G., Mukai, K. & Kimura, T. Resonance Raman scattering and optical absorption of adrenodoxin and selena-adrenodoxin. *Biochem Biophys Res Commun* **53**, (1973).
107. Loehr, J. S., Freedman, T. B. & Loehr, T. M. Oxygen binding to hemocyanin: A resonance raman spectroscopic study. *Biochem Biophys Res Commun* **56**, (1974).
108. Dunn, J. B. R., Shriver, D. F. & Klotz, I. M. Resonance Raman studies of the electronic state of oxygen in hemerythrin. *Proc Natl Acad Sci U S A* **70**, (1973).

109. Long, T. V. & Loehr, T. M. The Possible Determination of Iron Coordination in Nonheme Iron Proteins Using Laser-Raman Spectroscopy. Rubredoxin. *Journal of the American Chemical Society* vol. 92 Preprint at https://doi.org/10.1021/ja00724a072 (1970).

110. Spiro, T. G. & Strekas, T. C. Resonance Raman spectra of hemoglobin and cytochrome c: inverse polarization and vibronic scattering. *Proc Natl Acad Sci U S A* **69**, (1972).

111. Siiman, O., Young, N. M. & Carey, P. R. Resonance Raman Spectra of "Blue" Copper Proteins and the Nature of Their Copper Sites. *J Am Chem Soc* **98**, (1976).

112. MacEdo, S. *et al.* Can soaked-in scavengers protect metalloprotein active sites from reduction during data collection? *J Synchrotron Radiat* **16**, (2009).

113. Bearden, J. A. & Burr, A. F. Reevaluation of X-ray atomic energy levels. *Rev Mod Phys* **39**, (1967).

114. Holbrook, R. D., Galyean, A. A., Gorham, J. M., Herzing, A. & Pettibone, J. Overview of Nanomaterial Characterization and Metrology. in *Frontiers of Nanoscience* vol. 8 (2015).

115. Cruz, I. F., Freire, C., Araújo, J. P., Pereira, C. & Pereira, A. M. Multifunctional Ferrite Nanoparticles: From Current Trends Toward the Future. in *Magnetic Nanostructured Materials: From Lab to Fab* (2018). doi:10.1016/B978-0-12-813904-2.00003-6.

116. Ferrando, R. Synthesis and experimental characterization of nanoalloy structures. in *Frontiers of Nanoscience* vol. 10 (2016).

117. Kau, L.-S. *et al. X-Ray Absorption Edge Determination of the Oxidation State and Coordination Number of Copper: Application to the Type Site in Rhus Vernicifera Lacease and Its Reaction With*. *Biochim. Biophys. Acta* vol. 109 https://pubs.acs.org/sharingguidelines (1987).

118. Tomson, N. C. *et al.* Re-evaluating the Cu K pre-edge XAS transition in complexes with covalent metal-ligand interactions. *Chem Sci* **6**, (2015).

119. McCleverty, J. A. & Meyer, T. J. *Comprehensive Coordination Chemistry II : From Biology to Nanotechnology*. (Elsevier Pergamon, 2004).

120. Kjaergaard, C. H. *et al.* Spectroscopic and computational insight into the activation of O2 by the mononuclear Cu center in polysaccharide monooxygenases. *Proc. Natl. Acad. Sci. U. S. A.* **111**, 8797–8802 (2014).

121. Munzone, A. *et al.* Integrated Experimental and Theoretical Investigation of Copper Active Site Properties of a Lytic Polysaccharide Monooxygenase from *Serratia marcescens*. *Inorg Chem* **63**, 11063–11078 (2024).

122. Rehr, J. J. & Albers, R. C. Theoretical approaches to x-ray absorption fine structure. *Rev Mod Phys* **72**, (2000).

123. Hayama, S. *et al.* The scanning four-bounce monochromator for beamline I20 at the Diamond Light Source. *J Synchrotron Radiat* **25**, (2018).

124. Diaz-Moreno, S. *et al.* The Spectroscopy Village at Diamond Light Source. *J Synchrotron Radiat* **25**, (2018).

125. Zhao, J. *et al.* Mapping the Initial Stages of a Protective Pathway that Enhances Catalytic Turnover by a Lytic Polysaccharide Monooxygenase. *J Am Chem Soc* **145**, (2023).

126. Terrasan, C. R. F. *et al.* Deletion of AA9 Lytic Polysaccharide Monooxygenases Impacts A. nidulans Secretome and Growth on Lignocellulose. *Microbiol Spectr* **10**, (2022).

127. Courtade, G., Le, S. B., Sætrom, G. I., Brautaset, T. & Aachmann, F. L. A novel expression system for lytic polysaccharide monooxygenases. *Carbohydr Res* **448**, (2017).

128. Stoll, S. & Schweiger, A. EasySpin, a comprehensive software package for spectral simulation and analysis in EPR. *Journal of Magnetic Resonance* **178**, (2006).

129. Hayama, S. *et al.* Photon-in/photon-out spectroscopy at the I20-scanning beamline at diamond light source. *Journal of Physics Condensed Matter* **33**, (2021).

130. Johann, H. H. Die Erzeugung lichtstarker Röntgenspektren mit Hilfe von Konkavkristallen. *Zeitschrift für Physik* **69**, (1931).

131. Plackett, R. *et al.* Merlin: A fast versatile readout system for Medipix3. in *Journal of Instrumentation* vol. 8 (2013).

132. Ravel, B. & Newville, M. ATHENA, ARTEMIS, HEPHAESTUS: Data analysis for X-ray absorption spectroscopy using IFEFFIT. in *Journal of Synchrotron Radiation* vol. 12 (2005).

133. Harris, P. V. *et al.* Stimulation of lignocellulosic biomass hydrolysis by proteins of glycoside hydrolase family 61: Structure and function of a large, enigmatic family. *Biochemistry* **49**, (2010).

134. Bey, M. *et al.* Cello-oligosaccharide oxidation reveals differences between two lytic polysaccharide monooxygenases (Family GH61) from Podosporaanserina. *Appl Environ Microbiol* **79**, (2013).

135. Beeson, W. T., Phillips, C. M., Cate, J. H. D. & Marletta, M. A. Oxidative cleavage of cellulose by fungal copper-dependent polysaccharide monooxygenases. *J Am Chem Soc* **134**, (2012).

136. Li, X., Beeson IV, W. T., Phillips, C. M., Marletta, M. A. & Cate, J. H. D. Structural basis for substrate targeting and catalysis by fungal polysaccharide monooxygenases. *Structure* **20**, (2012).

137. Tandrup, T. *et al.* Oligosaccharide Binding and Thermostability of Two Related AA9 Lytic Polysaccharide Monooxygenases. *Biochemistry* **59**, (2020).

138. Jagadeeswaran, G., Gainey, L., Prade, R. & Mort, A. J. A family of AA9 lytic polysaccharide monooxygenases in Aspergillus nidulans is differentially regulated by multiple substrates and at least one is active on cellulose and xyloglucan. *Appl Microbiol Biotechnol* **100**, (2016).

139. Fenton, H. J. H. LXXIII. - Oxidation of tartaric acid in presence of iron. *Journal of the Chemical Society, Transactions* vol. 65 Preprint at https://doi.org/10.1039/CT8946500899 (1894).

140. Wang, D. *et al.* Novel Two-Step Process in Cellulose Depolymerization: Hematite-Mediated Photocatalysis by Lytic Polysaccharide Monooxygenase and Fenton Reaction. *J Agric Food Chem* **70**, (2022).

141. Bissaro, B. *et al.* Fenton-type chemistry by a copper enzyme: molecular mechanism of polysaccharide oxidative cleavage. *bioRxiv* (2016).

142. Bissaro, B. & Eijsink, V. G. H. Lytic polysaccharide monooxygenases: enzymes for controlled and site-specific Fenton-like chemistry. *Essays in Biochemistry* vol. 67 Preprint at https://doi.org/10.1042/EBC20220250 (2023).

143. Wang, B., Zhang, X., Fang, W., Rovira, C. & Shaik, S. How Do Metalloproteins Tame the Fenton Reaction and Utilize •oH Radicals in Constructive Manners? *Acc Chem Res* **55**, (2022).

144. Li, F. *et al.* Lytic polysaccharide monooxygenases promote oxidative cleavage of lignin and lignin–carbohydrate complexes during fungal degradation of lignocellulose. *Environ Microbiol* **23**, (2021).

145. Mohammed, A. S. A., Naveed, M. & Jost, N. Polysaccharides; Classification, Chemical Properties, and Future Perspective Applications in Fields of Pharmacology and Biological Medicine (A Review of Current Applications and Upcoming Potentialities). *Journal of Polymers and the Environment* vol. 29 Preprint at https://doi.org/10.1007/s10924-021-02052-2 (2021).

146. Qi, X. *et al.* Removal of copper ions from water using polysaccharide-constructed hydrogels. *Carbohydr Polym* **209**, (2019).

147. Zhao, C. *et al.* Polysaccharide-based biopolymer hydrogels for heavy metal detection and adsorption. *Journal of Advanced Research* vol. 44 Preprint at https://doi.org/10.1016/j.jare.2022.04.005 (2023).

148. Barikani, M., Oliaei, E., Seddiqi, H. & Honarkar, H. Preparation and application of chitin and its derivatives: A review. *Iranian Polymer Journal (English Edition)* vol. 23 Preprint at https://doi.org/10.1007/s13726-014-0225-z (2014).

149. Østby, H. *et al.* Impact of Copper Saturation on Lytic Polysaccharide Monooxygenase Performance. *ACS Sustain Chem Eng* **11**, (2023).

150. Tandrup, T. *et al.* Changes in active-site geometry on X-ray photoreduction of a lytic polysaccharide monooxygenase active-site copper and saccharide binding. *IUCrJ* **9**, (2022).

151. Sano, M., Komorita, S. & Yamatera, H. XANES spectra of copper(II) complexes: correlation of the intensity of the 1s .fwdarw. 3d transition and the shape of the complex. *Inorg Chem* **31**, 459–463 (1992).

152. Blackburn, N. J. *et al.* X-ray Absorption Edge Spectroscopy of Copper(I) Complexes. Coordination Geometry of Copper(I) in the Reduced Forms of Copper Proteins and Their Derivatives with Carbon Monoxide. *Inorg Chem* **28**, (1989).

153. Torbjörnsson, M., Hagemann, M. M., Ryde, U. & Hedegård, E. D. Histidine oxidation in lytic polysaccharide monooxygenase. *Journal of Biological Inorganic Chemistry* **28**, (2023).

154. Kuusk, S. *et al.* Kinetic insights into the role of the reductant in H2O2-driven degradation of chitin by a bacterial lytic polysaccharide monooxygenase. *Journal of Biological Chemistry* **294**, (2019).

155. Hyun, M. Y. *et al.* Terminal and internal olefin epoxidation with cobalt(II) as the catalyst: Evidence for an active oxidant CoII-acylperoxo species. *Journal of Organic Chemistry* **77**, (2012).

156. Rittle, J. & Green, M. T. Cytochrome P450 compound I: Capture, characterization, and C-H bond activation kinetics. *Science (1979)* **330**, (2010).

157. Bray, R. C. Sudden freezing as a technique for the study of rapid reactions. *Biochem. J* **81**, 189–193 (1961).

158. Rondeau, R. E. Slush Baths. *J Chem Eng Data* **11**, 124–124 (1966).

159. Ballou, D. P. [7] Freeze-quench and chemical-quench techniques. in *Methods in Enzymology* vol. 54 85–93 (Academic Press, 1978).

160. Tsai, A. L., Berka, V., Kulmacz, R. J., Wu, G. & Palmer, G. An improved sample packing device for rapid freeze-trap electron paramagnetic resonance spectroscopy kinetic measurements. *Anal. Biochem.* **264**, 165–171 (1998).

161. Oellerich, S., Bill, E. & Hildebrandt, P. Freeze-Quench Resonance Raman and Electron Paramagnetic Resonance Spectroscopy for Studying Enzyme Kinetics: Application to Azide Binding to Myoglobin. *Appl. Spectrosc., AS* **54**, 1480–1484 (2000).

162. Georgieva, E. R. *et al.* Effect of freezing conditions on distances and their distributions derived from Double Electron Electron Resonance (DEER): a study of doubly-spin-labeled T4 lysozyme. *J. Magn. Reson.* **216**, 69–77 (2012).

163. Lin, Y., Gerfen, G. J., Rousseau, D. L. & Yeh, S.-R. Ultrafast microfluidic mixer and freeze-quenching device. *Anal. Chem.* **75**, 5381–5386 (2003).

164. Nami, F., Gast, P. & Groenen, E. J. J. Rapid Freeze-Quench EPR Spectroscopy: Improved Collection of Frozen Particles. *Appl. Magn. Reson.* **47**, 643–653 (2016).

165. Ballou, D. P. & Palmer, G. A. Practical rapid quenching instrument for the study of reaction mechanisms by electron paramagnetic resonance spectroscopy. *Anal. Chem.* **46**, 1248–1253 (1974).

166. Pievo, R. *et al.* A rapid freeze-quench setup for multi-frequency EPR spectroscopy of enzymatic reactions. *Chemphyschem* **14**, 4094–4101 (2013).

167. Galagan, Y., Hsu, S. H. & Su, W. F. Monitoring time and temperature by methylene blue containing polyacrylate film. *Sens Actuators B Chem* **144**, (2010).

168. Tayade, R. J., Natarajan, T. S. & Bajaj, H. C. Photocatalytic Degradation of Methylene Blue Dye Using Ultraviolet Light Emitting Diodes. *Ind. Eng. Chem. Res.* **48**, 10262–10267 (2009).

169. Height, M. J., Pratsinis, S. E., Mekasuwandumrong, O. & Praserthdam, P. Ag-ZnO catalysts for UV-photodegradation of methylene blue. *Appl. Catal. B* **63**, 305–312 (2006).

170. Lachheb, H. *et al.* Photocatalytic degradation of various types of dyes (Alizarin S, Crocein Orange G, Methyl Red, Congo Red, Methylene Blue) in water by UV-irradiated titania. *Appl. Catal. B* **39**, 75–90 (2002).

171. An, D. *et al.* Metagenomic Analysis Indicates Epsilonproteobacteria as a Potential Cause of Microbial Corrosion in Pipelines Injected with Bisulfite. *Front Microbiol* **7**, (2016).

172. Teumac, F. N. The history of oxygen scavenger bottle closures. in *Active Food Packaging* (1995). doi:10.1007/978-1-4615-2175-4_8.

173. Mayers, C. L. & Jenke, D. R. Stabilization of Oxygen-Sensitive Formulations via a Secondary Oxygen Scavenger. *Pharmaceutical Research: An Official Journal of the American Association of Pharmaceutical Scientists* **10**, (1993).

174. Lee, J. S., Jeong, S., Lee, H. G., Cho, C. H. & Yoo, S. R. Development of a Sulfite-Based Oxygen Scavenger and its Application in Kimchi Packaging to Prevent Oxygen-mediated Deterioration of Kimchi Quality. *J Food Sci* **83**, (2018).

175. Alef, K., Iglauer, S. & Barifcani, A. Effect of Dissolved Oxygen, Sodium Bisulfite, and Oxygen Scavengers on Methane Hydrate Inhibition. *J Chem Eng Data* **63**, (2018).

176. DuPont Fluoroproducts. *Properties Handbook*.

177. Newville, M. Larch: An analysis package for XAFS and related spectroscopies. in *Journal of Physics: Conference Series* vol. 430 (2013).

178. Das, A., Ahmed, J., Rajendran, N. M., Adhikari, D. & Mandal, S. K. A Bottleable Imidazole-Based Radical as a Single Electron Transfer Reagent. *Journal of Organic Chemistry* **86**, (2021).

179. Morozova, O. B. & Yurkovskaya, A. V. Reduction of transient histidine radicals by tryptophan: influence of the amino group charge. *Physical Chemistry Chemical Physics* **23**, (2021).

180. Bettelheim, A. & Faraggi, M. The reduction of Cu(II) complexes of histidine and histidyl peptides. A pulse radiolysis study. *Radiat Res* **72**, (1977).

181. A comparative assessment of the zinc–protein coordination in 2Zn–insulin as determined by X-ray absorption fine structure (EXAFS) and X-ray crystallography. *Proc R Soc Lond B Biol Sci* **219**, (1983).

182. Kjaergaard, C. H. *et al.* Spectroscopic and computational insight into the activation of O 2by the mononuclear Cu center in polysaccharide monooxygenases. *Proc Natl Acad Sci U S A* **111**, (2014).

183. Gray, H. B. & Winkler, J. R. Functional and protective hole hopping in metalloenzymes. *Chemical Science* vol. 12 Preprint at https://doi.org/10.1039/d1sc04286f (2021).

184. Loose, J. S. M. *et al.* Multipoint Precision Binding of Substrate Protects Lytic Polysaccharide Monooxygenases from Self-Destructive Off-Pathway Processes. *Biochemistry* **57**, (2018).

185. Liu, Y., Harnden, K. A., Van Stappen, C., Dikanov, S. A. & Lu, Y. A designed Copper Histidine-brace enzyme for oxidative depolymerization of polysaccharides as a model of lytic polysaccharide monooxygenase. *Proc Natl Acad Sci U S A* **120**, (2023).

186. Falcone, E. *et al.* Chasing the Elusive “In-Between” State of the Copper-Amyloid β Complex by X-ray Absorption through Partial Thermal Relaxation after Photoreduction. *Angewandte Chemie - International Edition* **62**, (2023).

187. Sigfridsson, K. G. V. *et al.* Rapid X-ray photoreduction of dimetal-oxygen cofactors in ribonucleotide reductase. *Journal of Biological Chemistry* **288**, (2013).

188. Pfanzagl, V. *et al.* X-ray–induced photoreduction of heme metal centers rapidly induces active-site perturbations in a protein-independent manner. *Journal of Biological Chemistry* **295**, (2020).

189. Corbett, M. C. *et al.* Photoreduction of the active site of the metalloprotein putidaredoxin by synchrotron radiation. *Acta Crystallogr D Biol Crystallogr* **63**, (2007).

190. Teng, T. Y. & Moffat, K. Primary radiation damage of protein crystals by an intense synchrotron X-ray beam. *J Synchrotron Radiat* **7**, (2000).

191. Gunter, T. E. Electron paramagnetic resonance studies of the radiolysis of H2O in the solid state. *J Chem Phys* **46**, (1967).

192. El Omar, A. K. *et al.* Time-dependent radiolytic yield of OH• radical studied by picosecond pulse radiolysis. *Journal of Physical Chemistry A* **115**, (2011).

193. Penner-Hahn, J. E., Murata, M., Hodgson, K. O. & Freeman, H. C. Low-temperature X-ray absorption spectroscopy of plastocyanin: Evidence for copper-site photoreduction at cryogenic temperatures. *Inorg Chem* **28**, (1989).

194. Sommerhalter, M., Lieberman, R. L. & Rosenzweig, A. C. X-ray crystallography and biological metal centers: Is seeing believing? *Inorganic Chemistry* vol. 44 Preprint at https://doi.org/10.1021/ic0485256 (2005).

195. Denisov, I. G., Makris, T. M. & Sligar, S. G. Cryoradiolysis for the study of P450 reaction intermediates. *Methods Enzymol* **357**, (2002).

196. Denisov, I. G., Makris, T. M. & Sligar, S. G. Formation and decay of hydroperoxo-ferric heme complex in horseradish peroxidase studied by cryoradiolysis. *Journal of Biological Chemistry* **277**, (2002).

197. Denisov, I. G., Makris, T. M. & Sligar, S. G. Cryotrapped Reaction Intermediates of Cytochrome P450 Studied by Radiolytic Reduction with Phosphorus-32. *Journal of Biological Chemistry* **276**, (2001).

198. Schlichting, I. *et al.* The catalytic pathway of cytochrome P450cam at atomic resolution. *Science (1979)* **287**, (2000).

199. Landrot, G. FASTOSH: A Software to Process XAFS Data for Geochemical & Environmental Applications. in *Proceedings of the Goldschmidt Abstracts* 1402 (Boston, MA, 2018).

200. Juszczak, L. J. & Eisenberg, A. S. The Color of Cation-Ï€ Interactions: Subtleties of Amine-Tryptophan Interaction Energetics Allow for Radical-like Visible Absorbance and Fluorescence. *J Am Chem Soc* **139**, (2017).

201. Tazhigulov, R. N., Gayvert, J. R., Wei, M. & Bravaya, K. B. eMap: A web application for identifying and visualizing electron or hole hopping pathways in proteins. *Journal of Physical Chemistry B* **123**, (2019).